

DOCTORAL THESIS

Developments Towards
Deriving Realistic Dynamic
Topography by Synergizing
High-Resolution Geoid with
Sea Level Data

Vahidreza Jahanmard

TALLINN UNIVERSITY OF TECHNOLOGY
DOCTORAL THESIS
3/2024

Developments Towards Deriving Realistic Dynamic Topography by Synergizing High-Resolution Geoid with Sea Level Data

VAHIDREZA JAHANMARD



TALLINN UNIVERSITY OF TECHNOLOGY

School of Engineering

Department of Civil Engineering and Architecture

This dissertation was accepted for the defence of the degree 21/12/2023

Supervisor: Prof. Artu Ellmann
School of Engineering
Department of Civil Engineering and Architecture
Tallinn University of Technology, Tallinn, Estonia

Co- Supervisor: Dr Nicole Camille Delpeche-Ellmann
School of Science
Department of Cybernetics, Laboratory of Wave Engineering
Tallinn University of Technology, Tallinn, Estonia

Pre-reviewer Prof. Kevin Ellis Parnell
School of Science
Department of Cybernetics, Laboratory of Wave Engineering
Tallinn University of Technology, Tallinn, Estonia

Opponents: Prof. Maaria Nordman
Department of Built Environment
Aalto University, Espoo, Finland

Dr. Tomas Torsvik
Geophysical Institute
University of Bergen, Bergen, Norway

Defence of the thesis: 02/02/2024, Tallinn

Declaration:

Hereby I declare that this doctoral thesis, my original investigation and achievement, submitted for the doctoral degree at Tallinn University of Technology has not been submitted for doctoral or equivalent academic degree.

Vahidreza Jahanmard



signature

Copyright: Vahidreza Jahanmard, 2024

ISSN 2585-6898 (publication)

ISBN 978-9916-80-100-0 (publication)

ISSN 2585-6901 (PDF)

ISBN 978-9916-80-101-7 (PDF)

DOI <https://doi.org/10.23658/taltech.3/2024>

Printed by Koopi Niini & Rauam

Jahanmard, V. (2024). *Developments Towards Deriving Realistic Dynamic Topography by Synergizing High-Resolution Geoid with Sea Level Data* [TalTech Press]. <https://doi.org/10.23658/taltech.3/2024>

TALLINNA TEHNIKAÜLIKOOL
DOKTORITÖÖ
3/2024

Merepinna realistliku dünaamilise topograafia saavutamise täppisgeoidi ja meretaseme andmete kooskasutamisel

VAHIDREZA JAHANMARD



Contents

Contents.....	5
List of Publications	7
Author’s Contribution to the Publications	8
Introduction	9
Scope and Objectives	13
Limitations.....	14
Structure.....	15
Abbreviations.....	16
Symbols.....	18
1 Derivation of Ocean Dynamic Topography	20
1.1 Observations of Dynamic Topography	20
1.2 Geoid-based Vertical Datum	21
1.3 Vertical Land Motion	22
1.4 Permanent Tide Systems	24
1.5 Dynamic Topography Modelling.....	25
1.6 Mean Dynamic Topography	26
2 Study Area, Data Sources and Preprocessing	27
2.1 Study Area	27
2.2 The Geoid Model	30
2.3 Tide Gauge Records.....	31
2.4 Satellite Altimetry Dynamic Topography.....	32
2.5 Airborne Laser Scanning point cloud.....	33
2.6 Hydrodynamic Model	34
3 Method I: Geoid-referenced Tide Gauges as Ground Truth	37
3.1 Theoretical Principles for Bias Computation	37
3.2 Hydrodynamic Model Correction	39
3.3 Comparative Assessment of HDM Bias Estimates Using Satellite Altimetry	41
4 Method II: Application of Machine Learning	46
4.1 Deep Neural Network for Modelling Error Prediction.....	46
4.1.1 Deep Learning Model Structure.....	48
4.1.2 Spatio-temporal Input Variables.....	50
4.1.3 Feature Selection	51
4.1.4 Deep Learning Model Performance.....	52
4.2 Vertical Reference Bias.....	54
4.3 Comparative Assessment	55
5 Airborne LiDAR Measurements.....	59
5.1 Directional Wave Spectrum.....	60
6 Discussion and Concluding Remarks	66
6.1 Summary of Results.....	66
6.2 Key Conclusions Presented for Defence.....	67
6.3 Recommendations for Further Research	69
List of Figures	70

List of Tables	73
References	74
Acknowledgements.....	84
Abstract.....	85
Lühikokkuvõte.....	86
Appendix 1	87
Appendix 2	107
Appendix 3	127
Appendix 4	141
Curriculum vitae.....	161
Elulookirjeldus.....	164

List of Publications

The thesis has been prepared based on the following peer-reviewed journal articles (indexed by SCOPUS and WOS):

- I **Jahanmard, V.**, Delpeche-Ellmann, N., Ellmann, A. (2021). Realistic Dynamic Topography Through Coupling Geoid and Hydrodynamic Models of the Baltic Sea. *Continental Shelf Research*, 222. doi:doi.org/10.1016/j.csr.2021.104421.
- II **Jahanmard, V.**, Delpeche-Ellmann, N., Ellmann, A. (2022). Towards Realistic Dynamic Topography from Coast to Offshore by Incorporating Hydrodynamic and Geoid Models. *Ocean Modelling*, 180. doi:10.1016/j.ocemod.2022.102124.
- III **Jahanmard, V.**, Varbla, S., Delpeche-Ellmann, N., Ellmann, A. (2022). Retrieval of directional power spectral density and wave parameters from airborne LiDAR point cloud. *Ocean Engineering*, 266. doi:10.1016/j.oceaneng.2022.112694.
- IV **Jahanmard, V.**, Hordoir, R., Delpeche-Ellmann, N., Ellmann, A. (2023). Quantification of Hydrodynamic Model Sea Level Bias Utilizing Deep Learning and Synergistic Integration of Data Sources. *Ocean Modelling*. doi:10.1016/j.ocemod.2023.102286.

Author's Contribution to the Publications

The author of this thesis contributed to the publications by:

- I** conceptualizing the study in cooperation with all the co-authors; developing the methodology with all co-authors; processing the data; conducting the analysis and validation of the results and drafting the manuscript in cooperation with all the co-authors; visualizing the manuscript.
- II** conceptualizing the study in cooperation with all the co-authors; developing the methodology with all co-authors; processing the data; conducting the analysis and validation of the results and drafting the manuscript in cooperation with all the co-authors; visualizing the manuscript.
- III** conceptualizing the study in cooperation with all the co-authors; developing the methodology; processing the data and conducting the analysis of the results; validating the results and drafting the manuscript in cooperation with all the co-authors; visualizing the manuscript.
- IV** conceptualizing the study with all co-authors; developing the methodology with the help of Dr Robinson Hordoïr; processing the data; conducting the analysis; validating the results and drafting the manuscript in cooperation with all the co-authors; visualizing the manuscript.

Introduction

Accurate and consistent quantification of sea level variation is of utmost importance for monitoring, forecasting, and planning of marine activities. In recent years, higher accuracy in sea level variations in both time and space dimensions has become important for various applications. For instance, improving our understanding of ocean weather and processes through the study of mesoscale and sub-mesoscale eddies requires a more accurate measurement of sea level variation that remains consistent over time (Durand et al., 2010; Bian et al., 2023). In addition, in the fields of navigation and marine engineering, an accuracy of a few centimetres is required, especially for determining the under-keel clearance as vessels enter into ports and shallow sea areas (Orseau et al., 2021; Zhang et al., 2022). Several sources of sea level data are available, including hydrodynamic models (HDM), tide gauges (TG), satellite altimetry (SA), Global Navigation Satellite Systems (GNSS) tide buoys and airborne laser scanning (ALS), each with its own set of advantages and disadvantages. Therefore, it is intuitive to realize that in order to obtain better accuracy and consistency from coastal to offshore requires the development of methodologies to synergize these data sources.

Previous studies have attempted to integrate sea level sources (Saraceno et al., 2008; Cheng et al., 2012; Chang et al., 2023), but their full potential was often limited by the absence of a common vertical reference datum. Advancements in sea level measurement technology, including improved accuracy and higher resolution, along with modelling, now paves the path so that instantaneous sea level modelling and forecasting can be achievable within accuracies of less than a few centimetres from coastal to offshore. Although several studies undertook extensive evaluations and comparative assessments between the sea level data sources for various purposes (Featherstone and Filmer, 2012; Ophaug et al., 2015; Schall et al., 2016; Andersen et al., 2018; Varbla et al., 2020 and 2021; Mostafavi et al., 2021 and 2023; Afrasteh et al., 2021 and 2023), there is a limited focus on integrating them for the determination of instantaneous enhanced dynamic topography (Slobbe et al., 2013).

In this research, the Baltic Sea region is chosen as a case study, where the objective of realizing chart datum with a standard uncertainty of less than 5 cm has been already initiated (Ågren et al., 2023). Although the synergy of data sources enables achieving higher accuracy, combining sea level sources still poses complexities due to several limitations, including: i) various spatial and temporal resolutions, ii) utilization of different vertical reference datums, and iii) diverse errors arising from the method of data collection (Jahanmard et al., 2022a and 2023a).

Tide gauge data stands out as the most historical and reliable source for representing sea levels in coastal areas, which often considered as the 'true' sea level (Adebisi et al., 2021). However, there are some limitations to their usage, including: i) TGs tend to have limited spatial coverage, primarily representing coastal areas, and their spatial distribution is often uneven and incomplete; ii) challenges may arise from the absence of a consistent vertical datum, especially when integrating TG measurements from multiple locations across different countries or communities; and iii) TGs measure relative sea level with respect to a fixed point on land called the TG benchmark, which in certain locations may be affected by vertical land motion, e.g. due to glacial isostatic adjustment (GIA). The TG benchmarks are usually connected (with different accuracies) to a national height network. Additionally, TG data may contain errors stemming from instrumentation, maintenance, and human factors, as well as biases caused by vertical

datum shifts or the lack of precise vertical reference unification among countries (Pytharouli et al., 2018; Gruber et al., 2022).

On the other hand, HDMs are capable of deriving sea level continuously, both spatially and temporally. This makes them ideal for integrating and consolidating various sea level datasets from the coast to offshore. However, HDMs have also some limitations, including: i) often lacking a well-defined vertical reference datum, whereas sea level derived from HDMs cannot be explicitly described in a 3D coordinate system (Slobbe et al., 2013); and ii) HDMs are driven by mathematical equations, which may contain errors stemming from computational errors, limitations in model resolution and parameterization schemes, time steps and modelling discretization, topography, and uncertainties in boundary conditions and forcing inputs (Hieronymus et al., 2017; Mardani et al., 2020). These limitations can introduce biases in HDMs compared to observations, both spatially and temporally (Jahanmard et al., 2023a).

In addition, SA is one of the most effective sea level determination techniques, which has seen significant technological advances over the last few decades. The basic concept is that the altimeter sends and receives radar pulses along the satellite's trajectory to measure the range. By knowing the altitude of the satellite above a reference ellipsoid, based on its orbit computation with respect to a geocentric reference frame, then sea surface height (SSH, i.e. the sea level relative to the reference ellipsoid) is determined by the difference between the altitude and the range (Figure 1). The reference ellipsoid is a mathematical approximation of the Earth's shape that is used in geodesy and satellite altimetry for its simplicity and to facilitate precise calculations and measurements. The extensive global coverage of SA measurements provides a fundamental resource for a wide range of applications, such as regional and global climate studies (Srinivasan and Tsontos, 2023) and marine gravity field (Li et al., 2022). Nevertheless, SA has some limitations, including: i) several instrumental and geophysical corrections are required to be applied to improve the range, some of which may be degraded by approaching land and inhomogeneity of radar backscattering; ii) sufficient spatial resolution, while lacking the required temporal resolution (e.g., Sentinel-3A has spatial along track resolution of 300 m and temporal resolution of 27 days); and iii) on approaching the coastal areas, the satellite signal can become contaminated by terrains causing inaccurate sea level measurements. With the latest missions and retracking algorithms, SA can achieve the resulting SSH accuracy up to 2–3 cm in the open ocean and up to 4 cm in coastal regions (Abdullah et al., 2023).

Sea surface topography can also be captured via the ALS technique by emitting laser pulses and registering returned reflections from the sea surface (Jahanmard et al., 2022c). The high pulse repetition rate, low beam divergence, and relatively slow platform speed enable covering a wide swath (from the nadir perpendicular to the flight direction). The dense and highly accurate 3D point cloud retrieved from the LiDAR sensor allows investigating sea surface variations and wind waves (Walsh et al., 1985). Although ALS observations are able to provide the most accurate instantaneous sea surface topography, this technique is relatively expensive compared to alternative approaches and is not suitable for long-term or continuous monitoring.

The shipborne GNSS data is also used for the determination of sea surface height (Nordman et al., 2018; Varbla et al. 2021). Installing a GNSS receiver on a ship is relatively straightforward, but deriving SSH from GNSS observations presents several challenges, such as determining geometrical connections between the GNSS antenna and the actual

sea surface. Additionally, retrieving sea surface from shipborne GNSS data lacks a necessary spatial and temporal resolution.

Synergizing diverse data sources for developing a seamless sea level determination system from coastal to offshore is challenging due to the use of different vertical reference surfaces and data sources with varying resolutions. To address this challenge, the key component that links and unifies all data sources is a geoid model as an equipotential surface of the Earth’s gravity field. The geoid model represents the shape of the equipotential ocean surface under the influence of the gravitational attraction and Earth’s rotation, in the absence of other influences such as winds and tides. This reference surface should ideally be used as the zero for sea level and allows the determination of dynamic topography (DT), which represents the realistic sea level variation. The SSH derived from various data sources, such as SA, GNSS, and ALS can be converted into DT using a suitable geoid model (see Figure 1).

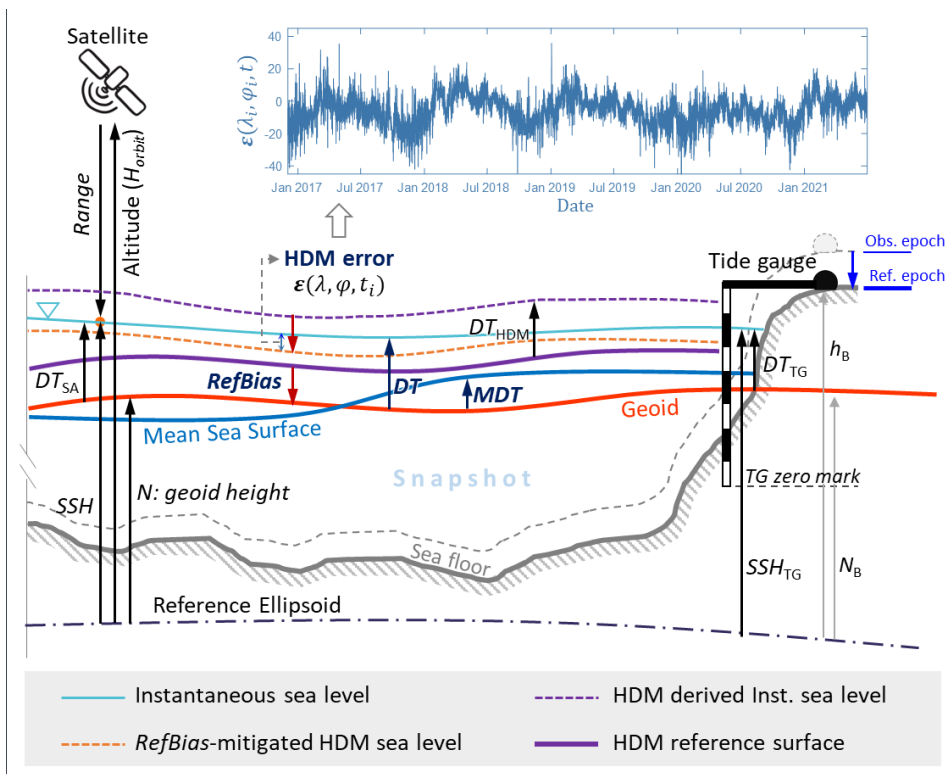


Figure 1. Schematic representations of the interrelation between various data sources, hydrodynamic parameters, and vertical reference surfaces. Refer to the main text body for the used symbols and abbreviations [from **Publication IV**].

Several global geoid models are available, such as the Earth Gravitational Model EGM08, yet they do not meet the required accuracy and spatial resolution for the determination of the realistic and accurate DT. For this purpose, high-resolution regional geoid models offer more practical solutions (Ågren et al., 2016; Ellmann et al., 2019). Regional geoid models are derived through inserting terrestrial gravity measurements and global geopotential models into modified Stokes’ formula (Stokes, 1849; Ellmann,

2005; Sjöberg & Bagherbandi, 2017). In many study areas, determining DT using high-resolution geoid models can be still challenging because of limited access to these models and the advanced measurements and expertise required for their development. However, notable achievements are observed in some regions and countries in the development of accurate geoid models for land and sea. For instance, the collaboration among Baltic Sea countries has resulted in the determination of a high-resolution geoid model known as NKG2015 (Ågren et al., 2016). This model facilitates advancements in marine studies and applications.

Dynamic topography represents a realistic quantification of the sea level variations with respect to an equipotential surface of Earth's gravity field, thus enabling better quantification and understanding of ocean currents, circulations, and heat and salinity transport (Wunsch and Stammer, 1998; Johannessen et al., 2014; Morrow et al., 2023). This parameter can be determined from two approaches: oceanographic and geodetic. In the geodetic applications, the calculation of the DT from SA measurements is obtained by subtracting the geoidal height N from the SSH, as follows:

$$DT_{SA} = SSH_{SA} - N = H_{orbit} - (Range + Cor) - N. \quad (1)$$

where H_{orbit} is the satellite's altitude, $Range$ represents the distance between the satellite and sea surface, and Cor represents various atmospheric, geophysical, and instrumental corrections.

For the oceanographic applications, DT is determined from physical ocean models or HDMs. Although HDMs use spherical coordinates (latitude φ , longitude λ , vertical component z) in their setup, they implicitly use a vertical datum that is adopting the constant geopotential W (Hughes and Bingham, 2008). Thus, the term DT is appropriate for modelled sea level; however, the value of W is often undisclosed, which indicates that there may be an offset required when compared to the geoid. This offset varies depending on the different HDMs and the selected zero reference point used for the height system of interest.

It is also important to note that HDMs can contain errors stemming from the model compilation setup, including input forcings, uncertainty in boundary conditions, bathymetry, modelling discretization, limitations in model resolution, and parameterization schemes. Therefore, the difference between HDM and observed data can be formulated by a combination of a bias due to the difference in zero level and the modelling errors.

Ideally and conventionally, two steps can be applied for vertical referencing HDMs to a particular geoid model: i) referring prescribed sea level along the open boundary to the geoid, and ii) assimilating instantaneous geoid-referenced observations into the HDM (Slobbe et al., 2013 and 2014). For this purpose, an accurate geoid model covering the entire HDM's domain is required. However, the marine geoid models may contain problematic regions (e.g., due to gravity data voids and/or inaccuracy), where their errors may reach a few decimetres (Varbla and Ellmann, 2023). While both the geoid and vertical referencing of the HDM can be realized through an iterative procedure (Slobbe et al., 2014), attaining a significant accuracy (i.e., a few centimetres) remains uncertain. This uncertainty is influenced by the chosen data assimilation technique and the approach adopted to converge toward a realistic DT during successive iterations.

As a result, this study develops two novel approaches. The first approach identifies the exact difference between HDMs and TG records, which is computed using a dense

network of geoid-referenced TG records and is assumed to measure the true sea level (**Publications I** and **II**). The bias is then propagated from coastal to offshore using conventional interpolation methods, such as linear and inverse distance weighted interpolation. This approach has some limitations especially on the potential vertical datum shifts between TGs and uncertainties in error interpolation away from the stations. On the other hand, the second approach uses machine learning to identify and predict modelling errors and then derive the bias of HDM's reference surface (**Publication IV**). For both approaches validation is made using SA data, which is particularly applicable to verify that the methods work in the offshore areas. A secondary deliverable of applying the two methods is that the synergy of the different sources allows in identification the problematic issues with the data sources and also where this may occur spatially and temporally. To the best of our knowledge, the developed methods is the first attempt at such a synergized exploration across the entire Baltic Sea. This study is the first step towards examining realistic dynamic topography, with the potential for similar developments to be adapted in other marine areas worldwide.

Scope and Objectives

A continuous model of accurate and consistent DT from the coast to the offshore region, with pre-defined uncertainty bounds, becomes important for various marine applications and serves as the motivation for this study. As mentioned earlier, various approaches and data sources derive sea level variations relative to different vertical references, each with its own limitations and strengths. Therefore, the main objective of this research is to develop a synergistic integration between sea level sources, utilizing a geoid reference surface to establish a link between them.

Firstly, in **Publications I** and **II**, the reference bias and modelling errors are treated as one integral bias in the HDM. Hence, the vertical reference unification and correcting of the HDM-derived DT are addressed simultaneously using a dense closed-loop network of geoid-referenced TGs as ground-truth observation.

Publication I represents the first attempt to combine the HDM and TG data by deriving time-domain bias at the location of TGs followed by determination of spatial-domain bias using bilinear interpolation. This concept is founded on the assumption that the spatial variation of the time-domain biases obtained at the TG stations is insignificant, as long as the HDM exhibits a high correlation with TGs, whereas the TG zero marks are accurately referred to an identical geoid-based vertical datum. This assumption is tested in **Publication I** by comparing two different HDMs and in **Publication II** by comparing different interpolation techniques along with an assessment using the SA-derived DT in the offshore area.

The primary limitation of the approach used in **Publications I** and **II** is that TG data are considered as ground-truth. Therefore, if the TG data contain errors or vertical datum shifts, they can propagate into the corrected HDM. This issue can be addressed by dividing the difference between modelled and observed DT into two main components: modelling error and vertical reference bias. A machine learning (ML) strategy was applied to determine HDM modelling error over time and space. After correcting the HDM, the vertical reference bias is determined by comparing the corrected HDM with the SA-based DT. **Publication IV** focuses on the application of a deep neural network to correct the HDM and quantifies the vertical reference bias using SA data. The study area in **Publication I** is the Gulf of Finland and the northern part of the Gulf of Riga. It is extended to the entire Baltic Sea region in **Publications II** and **IV**.

A comparative assessment between data sources in **Publications I** and **IV** reveals the inconsistency between data sources and highlights problematic regions. These regions demonstrate issues related to the geoid model, SA data, HDM errors, or a combination of these factors. In **Publication IV**, the ML-based HDM correction also allows the determination of the existing vertical datum shift between TGs.

The main objective of this study is to integrate modelled and observed data for the accurate determination of instantaneous dynamic topography. The corrected HDM has also been assessed via airborne laser scanning (ALS) observations. A study was conducted to explore the potential of utilizing dense ALS point cloud sea surface data for retrieving directional wave parameters. The results of this study were detailed in **Publication III**.

In summary, this study introduces two approaches for correcting HDM:

- **Method I:** utilizing a dense network of geoid-referenced TGs to determine the HDM bias over the course of time at the location of TGs and then spatially distributing this bias using interpolation techniques (**Publications I** and **II**).
- **Method II:** employing a deep neural network to determine the HDM errors and vertical referencing the HDM by the reference bias derived from comparison with SA data (**Publication IV**).

Additionally, this study evaluates the results achieved by correcting the HDM using ALS point cloud data and, as a secondary topic, presents an approach for retrieving the directional wave spectrum (**Publication III**).

Therefore, the objectives of this study are listed as follows:

- Develop a methodology to correct instantaneous dynamic topography derived from HDMs and unify the reference surface of the modelled and observed sea level data from diverse sources with respect to a specific geodetic reference system (**Publications I, II, and IV**).
- Compare multiple sea level datasets to evaluate the performance of the corrected HDM and quantify the accuracy and bias of the corrected instantaneous dynamic topography (**Publications II, and IV**).
- Identify inconsistencies and significant disparities between the datasets and the locations and frequency of occurrence (**Publications II, and IV**).
- Employ deep learning techniques to integrate HDM data and TG records, leveraging physical input variables and causal relationships to address HDM errors (**Publication IV**).
- Establish a methodology for retrieving directional wave spectra from airborne LiDAR point cloud data (**Publication III**).

Limitations

The presented investigations have certain limitations that need to be addressed:

1. For **Method I (Publications I, II)**, there are some limitations:
 - I. Adoption of the TG zero in a common vertical reference datum poses challenges, as it may not be available in most regions, especially when multiple countries/communities are involved.
 - II. The TGs must be rigorously connected to the national vertical datum, as the TG records may experience vertical datum shifts caused by various factors, such as natural disasters or insufficient maintenance. These shifts, along with the individual errors and uncertainties present in different TGs, can propagate into the corrected model.

- III. The method relies on interpolation techniques, necessitating a dense closed-loop TG network. As a result, it is more suitable for narrow seas or gulfs, as the interpolated values may become less reliable with increasing distance from the TG stations.
2. For **Method II (Publication IV)**:
 - I. The ML-based HDM correction requires additional efforts to address localized features that may be overlooked due to model generalization.
 - II. The deep neural network used solely relies on temporal causal convolution layers, which hinders the possibility of spatial feature learning and the utilization of spatial convolutions. This limitation makes it challenging to account for ocean features dependent on basin geometry, such as seiches.
3. The Baltic Sea region, which serves as the study area for this research, is a semi-enclosed sea with its specific characteristics. This region is an ideal study area for this examination due to its dense network of TGs with a common geoid-based chart datum and well-developed high-resolution geoid model, HDM, and vertical land movement model. However, the generalizability of these approaches requires testing in other regions of the world, where new challenges may arise.
4. In **Publication III**, while the capability to capture 3D point cloud data of sea surface topography provides deeper insights into surface ocean waves, ALS technology is relatively expensive compared to alternative approaches.

Structure

The dissertation is structured into sections that define the problem, address the requirements, and present the solutions in the form of two methods that were developed. To maintain conciseness, the sections focus on essential details and findings, while additional explanations are available in the corresponding publications. The following Section 1 provides the theoretical overview and principles for determining absolute dynamic topography using diverse sea level sources. In Section 2, the study area and datasets are reviewed. Section 3 presents the first method that provided to correct the HDM. This section is organized to express the background theory, implementation of the method, results, and discussion through a comparative assessment of available data sources. Section 4 then introduces the second method, which is based on machine learning strategies. This section provides an overview of the approach, defines a deep neural network for correcting the HDM, and concludes with results and discussion. In Section 5, sea surface topography derived from an airborne LiDAR point cloud is introduced for the evaluation of the corrected HDM, employing a low-pass filter. Furthermore, high-resolution ALS data also facilitates the determination of sea state, hence, this section continues by presenting a technique for deriving the wave spectrum from this dataset. In conclusion, Section 6 provides a comprehensive discussion and summary to wrap up the thesis.

Abbreviations

ALES	Adaptive Leading Edge Subwaveform
ALS	Airborne Laser Scanning
ASL	Absolute Sea Level
BSCD2000	Baltic Sea Chart Datum 2000
CERRA	Copernicus regional reanalysis for Europe
CMEMS	Copernicus Marine Environment Monitoring Service
Conv1D	One-dimensional convolutional layer
DL	Deep Learning
DT	(ocean) Dynamic Topography
ECMWF	European Centre for Medium-Range Weather Forecasts
EVRS	European Vertical Reference System
ERA5	ECMWF Reanalysis v5
ESA	European Space Agency
FES2014	Finite Element Solution tide model 2014
FFT	Fast Fourier Transform
GEBCO	General Bathymetric Chart of the Oceans
GIA	Glacial Isostatic Adjustment
GNSS	Global Navigation Satellite System
HBM-EST	Estonian implementation of the HIROMB-BOOS Model
HDM	Hydrodynamic Model
HIRLAM	High-Resolution Limited Area Model
HYPE	Hydrological Predictions for the Environment
IAG	International Association of Geodesy
IDW	Inverse Distance Weighted
IHO	International Hydrographic Organization
JONSWAP	Joint North Sea Wave Project
LAT	Lowest Astronomic Tide
MAD	Median Absolute Deviation
MDT	Mean Dynamic Topography
ML	Machine Learning
MSL	Mean Sea Level
MSS	Mean Sea Surface
NAP	Normaal Amsterdams Peil
NEMO	Nucleus for European Modelling of the Ocean
NKG	Nordic Geodetic Commission
NM	Nautical Mile
ReLU	Rectified Linear Unit
RMSE	Root Mean Square Error
RSL	Relative Sea Level
SA	Satellite Altimetry

SAR	Synthetic Aperture Radar
SMHI	Swedish Meteorological and Hydrological Institute
SSH	Sea Surface Height
SWOT	Surface Water and Ocean Topography
TG	Tide Gauge
VLM	Vertical Land Motion

Symbols

ASL	absolute sea level
$Bias$	bias between modelled and observed data for a certain period
$Bias_{CHDM}$	bias of corrected HDM
c	dimension of the input variable in the DL model
Cor	satellite altimetry corrections
d	dilation of causal convolution layers
DAC	dynamic atmospheric satellite altimetry correction
DT_{ALS}	dynamic topography from airborne laser scanning
DT_{HDM}	dynamic topography from hydrodynamic model
DT_{HDM}^C	dynamic topography from corrected hydrodynamic model
$DT_{HDM}^{C,Ref}$	dynamic topography from corrected and unified reference surface hydrodynamic model
$DT_{HDM@TG}$	dynamic topography from hydrodynamic model at location of TG station
DT_{RSL}	relative dynamic topography from tide gauge records
DT_{SA}	absolute dynamic topography from satellite altimetry
DT_{TG}	absolute dynamic topography from tide gauge records
DTC	dry tropospheric satellite altimetry correction
E	Instantaneous difference between HDM and TG records
fs	filter size of convolution layers
$G(k_s, \sigma)$	2D Gaussian filter with kernel size k_s and standard deviation σ
$H_{mean-tide}$	heights in mean-tide system
H_{orbit}	satellite's altitude
$H_{tide-free}$	heights in tide-free system
$H_{zero-tide}$	heights in zero-tide system
ice_frac	ice fraction variable
$iono$	ionospheric satellite altimetry correction
k	number of causal convolutional units
M	mask for transferring from HDM grid points to TG locations
MDT_p	mean dynamic topography for the period of p
$msdDT_{24}$	sea level variability for a period of a day
MSS_p	mean sea surface for the period of p
n	number of observations within a selected time span
nf	number of filters in convolution layers
N	geoid height, which is relative to a reference ellipsoid
$N_{mean-tide}$	geoid height in mean-tide system
$N_{zero-tide}$	geoid height in zero-tide system
OTC	ocean tide satellite altimetry corrections
p	a certain period of time
PT	pole tide satellite altimetry correction
q	index of the HDM grid points

R^2	coefficient of determination of prediction
<i>Range</i>	satellite's range
<i>RefBias</i>	vertical reference bias of hydrodynamic model
<i>RF</i>	receptive field of DL model
<i>RMSE</i>	root mean square error
<i>RMSE_{ε}</i>	root mean square error of predicted ε
<i>ROC</i>	radial orbit error satellite altimetry correction
<i>RSL</i>	relative sea level
<i>SDBias</i>	spatial-domain bias
<i>SLP</i>	sea level pressure variable
<i>SSB</i>	sea state bias satellite altimetry correction
<i>SSH_{ALS}</i>	sea surface height from airborne laser scanning
<i>SSH_{SA}</i>	sea surface height from satellite altimetry
<i>SSS</i>	sea surface salinity variable
<i>SST</i>	sea surface temperature variable
<i>SWH</i>	significant wave height variable
<i>t</i>	measurement time instant
<i>t₀</i>	reference epoch
<i>TDBias</i>	time-domain bias
<i>Uwind</i>	zonal wind speed variable
<i>VLM</i>	vertical land motion
<i>Vwind</i>	meridional wind speed variable
<i>w</i>	sliding window length for determination of <i>TDBias</i>
<i>W₀, W_{0E}</i>	potential value and Earth gravity field potential
<i>w_{Ekman}</i>	Ekman pumping velocity variable
<i>WTC</i>	wet tropospheric satellite altimetry correction
<i>x</i>	DL model input variables
<i>x_{inp}</i>	vectorised input variables
<i>x_{TG}</i>	DL model input variables at TG location
<i>X_s</i>	zonal wind stress variable
<i>Y_s</i>	meridional wind stress variable
ε	hydrodynamic modelling errors
$\hat{\varepsilon}$	predicted hydrodynamic modelling errors
η_p	Precipitation-induced water column variable
η_s	steric height variable
ξ	wind wave elevation
φ_{NAP}	geodetic latitude of NAP
φ, λ	geodetic coordinates: latitude and longitude
$\varphi_{TG_i}, \lambda_{TG_i}$	geodetic coordinates of TG stations
\mathcal{D}	distance between two geodetic coordinates
\mathcal{W}	vector of inverse distance weight

1 Derivation of Ocean Dynamic Topography

Several sea level data sources are available, each referring to a different vertical reference datum, and this diversity in reference datums complicates the integration between datasets. Therefore, adopting a particular geoid surface as an intermediate vertical reference datum presents a viable solution for integrating various sea level measurement approaches (Slobbe et al., 2014). The geoid surface represents the shape of the ocean surface influenced by gravitational attraction and Earth's rotation, excluding other factors like winds and tides. It is important to note that the geoid serves as a stable and static vertical reference datum, remaining constant over time, unlike Tidal datums, and it should ideally be considered as the zero reference for sea level measurements. Therefore, sea levels referenced to a geoid surface provide a physically meaningful and realistic measure of ocean dynamics known as DT. This section provides an overview and background theory of the DT derivation from various approaches. The study area and datasets used in this study will be introduced in Section 2.

1.1 Observations of Dynamic Topography

The most common observation techniques that provide instantaneous sea levels are tide gauge (TG) and Satellite altimetry (SA) datasets. Both sources offer complementary observations and are necessary to observe the complete spectrum of ocean dynamic processes (Cheng et al., 2012; Andersen et al., 2018). Satellite altimetry offers a time series over a sufficiently long period and adequate spatial resolution in open sea areas, however, lacks the required temporal resolution. Significant progress in coastal altimetry over the past decade also enables the observation of sea levels closer to the coast, with improved accuracy (Adebisi et al., 2021). On the other hand, TG records provide a long historical time series with sufficient temporal resolution. However, TG stations are spatially sparse, and their spatial coverage is limited to the coastal boundary.

The sea level obtained from SA observations is known as the absolute sea level (ASL), which is referenced to the Earth's centre of mass and remains unaffected by VLM. Contrastingly, TG stations are land-bounded and measure sea level relative to a nearby benchmark in the national vertical datum. Therefore, TG records is referred to as relative sea level (RSL), which includes both ASL and VLM accordingly (Wöppelmann et al., 2007):

$$RSL = ASL - VLM. \quad (2)$$

Derivation of the DT from SA observation relies on a geoid model, where the accuracy of the determined DT is contingent upon the accuracy of the utilized geoid model (Equation 1). At TG stations, instantaneous DT is directly measured if the TG zero mark coincides with a geoid-based chart datum (Jahanmard et al., 2022a). Otherwise, by utilizing nearby benchmarks with GNSS observations and a geoid model, one can derive DT from TG measurements, where the accuracy depends on the availability of reliable ties to the benchmark and geoid model at the TG location (Woodworth et al., 2015; Filmer et al., 2018). The TG and SA datasets used in this study are detailed in Subsections 2.3 and 2.4, respectively.

1.2 Geoid-based Vertical Datum

A height system definition comprises essential components: an origin, a vertical reference surface of the zero level, and a specific type of height measurement (Heiskanen and Moritz, 1967). The vertical reference datum of marine areas, including TGs, commonly relies on a chart datum, which typically represents tidal observation such as lowest astronomic tide (LAT) and mean sea level (MSL), or a physical model like the geoid as their reference surface (IHO, 2020). The tidal datums are most customarily used by several countries; however, they are no longer an ideal approach as they can vary over different time spans, whereas depending on the country/community, the sea level data may be referred to different definitions of vertical datums (Jahanmard et al., 2021a). For instance, this issue can lead to inconsistencies and incompatibilities in the Baltic Sea region (the study area for this research; described in Subsection 2.1), which is surrounded by nine countries. Therefore, pan-regional integration is essential in order to study this dynamic marine area effectively.

While tidal datums are based on sea level variations for a certain time span, geoid-based datums are realized using geoid models with a typical standard uncertainty of few centimetres. The use of a geoid-based datum offers the advantage of a stable reference surface, allowing for a seamless transition of the chart datum from land to offshore as well as enabling vertical datum unification between countries/communities (Schwabe et al., 2020; Ke et al., 2020).

The Baltic Sea countries have adopted national realizations of the European Vertical Reference System (EVRS), which defines the vertical datum as an equipotential surface where the Earth's gravity field potential remains constant:

$$W_0 = W_{0E} = Const., \quad (3)$$

and is set at the level of the Normaal Amsterdams Peil (NAP). Note that the EVRS is in the zero-tide permanent tide with reference epoch 2000.0 (Ihde et al., 2002). The differences between the national height systems range from a few millimetres up to a few centimetres (Varbla et al., 2022). Due to the significant influence of glacial isostatic adjustment (GIA) in this region (described in Subsection 1.3), the NKG2016LU VLM model is employed to adjust observations to the common reference epoch $t_0 = 2000.0$ (Vestøl et al., 2019).

Similarly, considerable efforts have been made to establish the Baltic Sea Chart Datum 2000 (BSCD2000) as a unified geoid-based chart datum (Liebsch et al., 2023) for hydrographic surveying, engineering, nautical charts, and sea level measurement in all countries surrounding the Baltic Sea. Consequently, the BSCD2000 also enables the establishment of a seamless height reference framework compatible with the national height systems (listed in Table 1) of the surrounding countries (Schwabe et al., 2020; Varbla et al., 2022).

Table 1. National height systems complying with BSCD2000, along with their regional geoid models and permanent tide systems.

Country	National height systems	National geoid model	Permanent tide system
Denmark	DRV90	DKgeoid12	tide-free system
Estonia	EH2000	EST-GEOID2017	zero-tide system
Finland	N2000	FIN2005N00	zero-tide system
Germany	DHHN2016	GCG2016	mean-tide system
Latvia	LAS2000,5	LV14	zero-tide system
Lithuania	LAS07	LIT15G	zero-tide system
Poland	PL-EVRS2007-NH	PL-geoid-2011	zero-tide system
Sweden	RH2000	SWEN17_RH2000	zero-tide system
Russia	BHS77 (Kronstadt)	--	mean-tide system

1.3 Vertical Land Motion

Tide gauges measure sea levels relative to fixed benchmarks on land and include any vertical land motions. The VLM values are not spatially constant, and to ensure accurate determination of the DT observed at coasts and comparability with SA measurements, it is necessary to consider the VLM correction for TG records (Santamaría-Gómez et al., 2012; Wöppelmann and Marcos, 2016; Pfeffer and Allemand, 2016).

Note that the VLM can be categorized into non-linear and linear motions. Non-linear VLM is influenced by various factors, such as tectonics, groundwater depletion, dam building, and settling of landfills, which have relatively short spatial scales and are challenging to model and account for (Raucoules et al., 2010; Fokker et al., 2018; Denys et al., 2020). The most important VLM in terms of rates is the GIA due to response of the solid Earth's surface to periods of glacier and polar cap loading/unloading, which is commonly expressed as a spatially dependent linear trend (Ostanciaux et al., 2012).

In the Baltic Sea region (study area; described in Subsection 2.1), vertical motions observed in Fennoscandia are primarily attributed to GIA, resulting in a mean sea level retreat as the crust rises faster than the sea level (Steffen and Wu, 2011). Therefore, the VLM must be compensated for TG records to the common reference epoch t_0 using a land uplift model as follows:

$$DT_{TG}(\varphi, \lambda, t) = DT_{RSL}(\varphi, \lambda, t) + VLM(\varphi, \lambda) \cdot (t - t_0), \quad (4)$$

where DT_{RSL} is obtained relative TG records, and DT_{TG} represents VLM-mitigated DT derived from TGs (i.e., absolute sea level). The most recent official VLM model used in the Baltic Sea region is NKG2016LU model (Vestøl et al., 2019).

Figure 2 shows the difference between relative and absolute DT measured by Spikarna TG station, located in the west of the Bothnian Sea (denoted in Figure 3), with a land uplift rate of 8.94 mm/year according to the NKG2016LU model. The station exhibits a long-term linear sea level trend of -6.7 mm/year for relative DT and 2.2 mm/year for absolute DT, indicating a significant influence of VLM at this location.

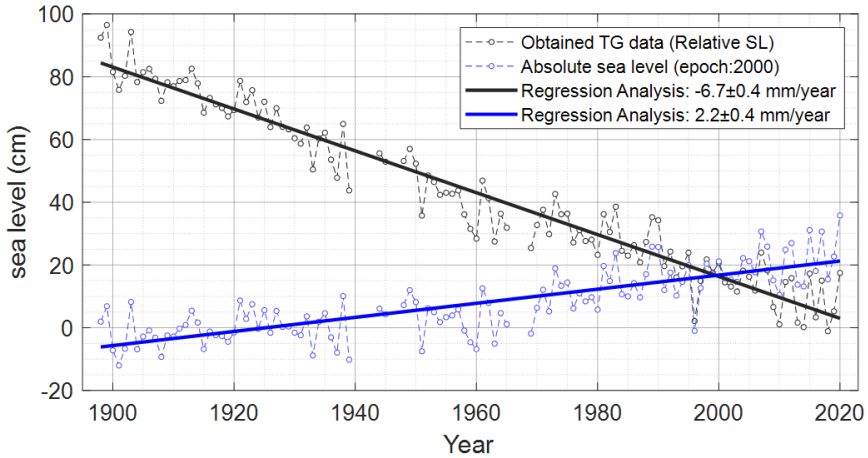


Figure 2. Relative and absolute DT from Spikarna station, located in the northwest of the Bothnian Sea, along with their linear trend [from **Publication II**].

Note that the geoid also rises in the Baltic Sea region due to the VLM and mass redistribution, however, the values of the geoid rise is relatively small (Figure 3). The maximum geoid rise in the northern part of the Baltic Sea region is approximately 0.6 mm/year, relative to reference epoch 2000.0, then the geoid rise would be 1.4 cm for 2021. Since DT refers to the difference between SSH and the geoid height, the geoid rise needs to be considered in precise applications (Jahanmard et al., 2022a and 2023a).

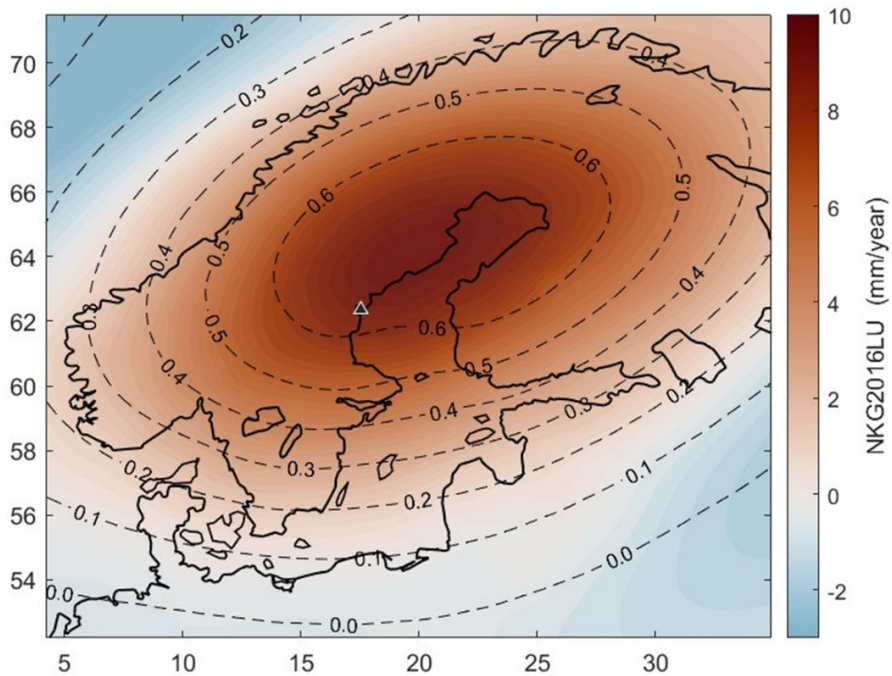


Figure 3. Rate of the vertical land movement (colormap) and geoid rise (dashed isolines) in the Baltic Sea region according to NKG2016LU. Black triangle denotes the location of Spikarna TG station.

1.4 Permanent Tide Systems

The time-averages of the gravitational forces exerted by the Sun and Moon, which give rise to tidal forces leading to ocean and earth tides, are not zero (Ekman, 1989; Mäkinen and Ihde, 2009). To address the permanent deformation caused by the permanent tide, the Earth's geometric shape (crust or topography) is described using two concepts: tide-free and mean-tide; whereas the gravity field is described using three concepts: tide-free, zero-tide, mean-tide (Mäkinen, 2021). Therefore, it is important to harmonize the permanent tide system of the datasets used.

In the tide-free system, all direct (i.e., tide-generating potential) and indirect (i.e., the deformation potential of the Earth) effects of the Sun and Moon are eliminated. In the mean-tide system, the permanent effect on the Earth's shape is considered, representing the long-term average shape under tidal forces. The SSH measured by SA is in the mean-tide system, as the tidal corrections do not remove the permanent tide (Mäkinen and Ihde, 2009). Therefore, since the mean-tide system is the most physically meaningful case for oceanographers and comparison with SA observations, all datasets are transformed to this permanent tide system.

In the International Association of Geodesy recommended (IAG, 1984) zero-tide system, the direct effect of tides is removed, but the indirect effects are retained. This results in the gravity field being generated solely by the Earth's masses and the centrifugal force (Mäkinen and Ihde, 2009). Regional gravimetric geoid models (e.g., NKG2015) are explicitly stated to be in the zero-tide system, which must be transformed into the mean-tide system before applying to SSH.

The transformations between the normal height differences and geoid height between the aforementioned permanent tide systems are presented by Ekman (1989). Since, TG records in the Baltic Sea region refer to NAP, they are transferred from the zero-tide to the mean-tide system accordingly (Varbla et al., 2022):

$$H_{mean-tide}(\varphi) = H_{zero-tide}(\varphi) + 0.2954(\sin^2(\varphi) - \sin^2(\varphi_{NAP})), \quad (5)$$

where φ_{NAP} is the latitude of NAP (52°22' 53") and the units are in meters. For Danish TGs that are in the tide-free system:

$$H_{mean-tide}(\varphi) = H_{tide-free}(\varphi) + 0.2954\gamma(\sin^2(\varphi) - \sin^2(\varphi_{NAP})), \quad (6)$$

where the coefficient $\gamma = 0.7$. Similar to Eq. 5, the conversion of geoidal heights to the mean-tide system is as follows:

$$N_{mean-tide}(\varphi) = N_{zero-tide}(\varphi) - 0.2954(\sin^2(\varphi) - \sin^2(\varphi_{NAP})), \quad (7)$$

The values of the conversion from the zero-tide and tide-free system to the mean-tide system are shown in Figure 4, according to Equations (5) and (6).

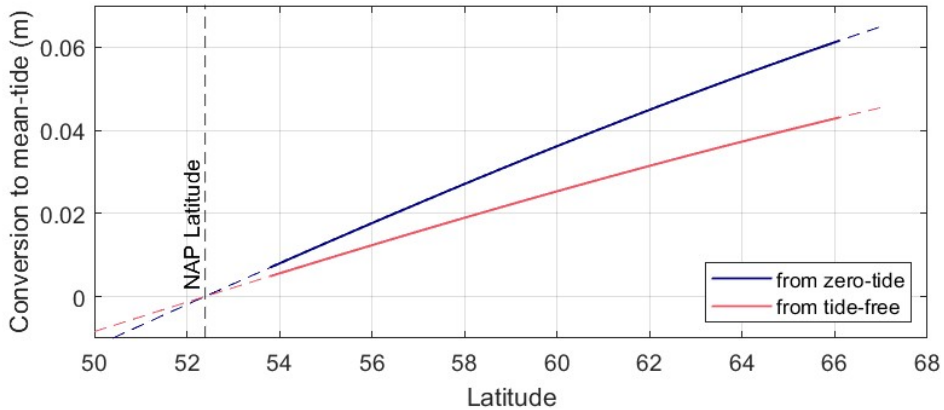


Figure 4. Differences of heights in the zero-tide and tide-free system and the mean-tide system in the Baltic Sea region, latitude from 54° to 66°.

1.5 Dynamic Topography Modelling

Hydrodynamic models are considered one of the most valuable sea level data sources due to their high resolution in both time and space, allowing for extensive spatial and temporal data coverage from coast to offshore. Nevertheless, they are not devoid of limitations, particularly in sea level determination, which is the main focus of this study. The foundation of HDMs lies in the governing equations of fluid dynamics, which are based on fundamental principles of physics, particularly the laws of conservation of mass, momentum, and energy. The most common set of equations used is the Navier-Stokes equations, the analytical solution of which is often extremely challenging. Thus, numerical methods and mathematical techniques, involving the discretization of continuous equations into a set of discrete equations, are employed to approximate and solve these equations. Hence, HDMs may contain modelling errors arising from assumptions, approximations, time steps and modelling discretization, limitations in model resolution, and parameterization schemes. Additionally, the models may have modelling errors inherited from various input sources, such as topography, atmospheric forcings, and river discharge (Mardani et al., 2020).

The second and important limitation is that HDMs typically lack a well-defined vertical reference surface, which hinders direct integration with other sea level data sources. In HDMs, it is common to set up the model using a spherical coordinate system with latitude, longitude, whereas vertical coordinates (z - height) are derived from the bathymetry dataset. However, the bathymetry is often considered as a control variable in the calibration process (Slobbe et al., 2013). Regardless of the vertical coordinate system utilized in the model, there will always be an implicit z coordinate for sea level determination.

It is important to note that since the models' dynamics are based on the assumption that gravity acts in the z -direction, the surface of the constant z represents surfaces of constant geopotential W (Hughes and Bingham, 2008). Consequently, the sea level derived from HDMs can be referred to as dynamic topography (DT_{HDM}). However, the potential values (W_0) of the HDMs' reference surface are still undisclosed, and the determination of the reference surface in HDMs is challenging due to the presence of modelling errors. In this regards, two approaches for correcting HDM relative to a

well-defined geodetic reference frame are presented in this study, which are described in Section 3 (see **Publications I** and **II** for more details) and Section 4 (see **Publication IV** for more details). The HDM datasets used in this study are detailed in Subsections 2.6.

1.6 Mean Dynamic Topography

The time-mean dynamic topography (MDT) can be derived by subtracting the geoid height from the time-mean sea surface (MSS) or calculated using ocean models based on estimated distributions of temperature, salinity, currents, etc. (Ekman and Mäkinen, 1996; Filmer et al., 2018). The former is the geodetic approach that is determined from TG records and SA data from the geodetic methods; the latter is the oceanographic approach that is computed from a global or regional ocean model. Therefore, in geodetic approach, the MDT for the period of p is:

$$MDT_p(\varphi, \lambda) = MSS_p(\varphi, \lambda) - N(\varphi, \lambda), \quad (8)$$

and in oceanographic approach, the MDT is determined as follows:

$$MDT_p(\varphi, \lambda) = \frac{1}{p} \sum_{t=1}^p DT_{HDM}(\varphi, \lambda, t). \quad (9)$$

Oceanographers are interested in MDT knowledge in order to study the ocean's geostrophic currents and ocean transports (e.g., Marshall et al., 1997; Krauss et al., 1991; Bingham et al., 2008; Armitage et al., 2018; Mintourakis et al., 2019; Knudsen et al., 2021;), and geodesists aim to unify or analyse height datums globally or locally (e.g., Rummel, 2002; Woodworth et al., 2012; Featherstone and Filmer, 2012; Slobbe et al., 2014; Afrasteh et al., 2023). In **Publication II**, the two approaches are employed to evaluate the HDM correction by comparing SA data and the corrected HDM. Additionally, the vertical reference bias of the HDM is determined by comparing geodetic and oceanographic MDTs in **Publication IV**.

2 Study Area, Data Sources and Preprocessing

Sea level datasets are gathered from various sources to determine the accurate absolute DT from coast to offshore area. In this dissertation, the Baltic Sea region is selected as the study area, and the instantaneous determination of DT is realized by correcting a high-resolution HDM by a network of TGs and utilizing the geoid as an intermediate reference surface. The corrected HDM is examined by the DT derived from the separation between SA data and a high-resolution geoid model. By comparing geodetic and oceanographic MDTs, it is possible to determine the vertical reference bias of the HDM relative to the EVRS (with the reference point of NAP and the reference epoch of 2000.0). The synergistic integration of data sources and approaches also facilitates the identification of problematic regions related to HDM, TG vertical datum shifts, SA data, and geoid model.

2.1 Study Area

The HDM correction and vertical reference unification is investigated in the Baltic Sea region, which is characterized as a micro-tidal semi-enclosed water body located in Northern Europe and surrounded by nine countries. The sea area is divided onto several sub-basins often defined by their geometry and bathymetry (see Figure 5 for the location Baltic Sea and its' sub-basins). Some of these sub-basins are often only slightly inter-connected (Lehmann and Hinrichsen, 2000).

An estuarine type of environment exists in this sea area, the freshwater flows from the numerous rivers of the surrounding countries, whilst the salty water from the Atlantic Ocean often intrudes through the narrow connection with the North Sea via the Danish Straits. This often leads to the formation of the strongly stratified water column, with the Baltic Sea being the world's second-largest estuarine water mass with an area of ca. 377,000 km² and average depth of 55 m. It is also quite common in the winter months for the Baltic Sea to become ice-covered, especially in the northern and eastern sections and also along coastal areas (Leppäranta and Myrberg, 2009).

The Baltic Sea is frequently chosen as an ideal research site for investigating global climate and environmental changes, thanks to extensive long-term monitoring programs on land and at sea (Reusch et al., 2018). Furthermore, owing to its semi-enclosed nature, surrounded by densely populated and highly industrialized countries, the Baltic Sea is highly sensitive to anthropogenic influences. This region is also considered to be one of the busiest maritime traffic areas in the world (Rytkönen et al., 2002). These characteristics make it necessary to have a realistic and continuous sea level data from coastal to offshore.

The Baltic Sea is a well-suited study area for evaluating the proposed methods due to the availability of key resources such as the high-resolution Nemo-Nordic model (Hordoir et al., 2019; Kärnä et al., 2021), a dense network of well-established TG stations with a common geoid-based reference datum (i.e., BSCD2000), a high-resolution geoid model NKG2015 (Ågren et al., 2016), and an accurate land uplift model NKG2016LU (Vestøl et al., 2019).

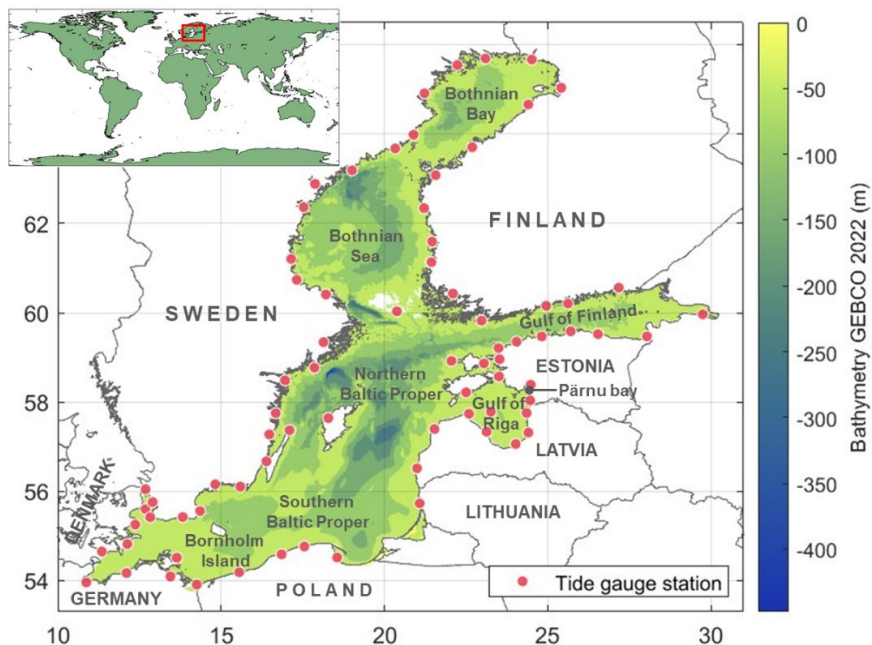


Figure 5. Baltic Sea region and its bathymetry sourced from GEBCO 2022 gridded bathymetry data¹. The dense network of used tide gauges is denoted by red circles.

Some general characteristics can be seen for both baroclinic and barotropic forces play a major role in the dynamics of the Baltic Sea. In general, the surface salinity decreases from west to east (ranging from 5 to 7 PSU) being influenced by freshwater river runoff and net precipitation, and exchange with saline water from the North Sea through the Danish Straits (Kniebusch et al., 2019). This often results in multi-structured seasonal and permanent thermocline and halocline at various depths (Liblik and Lips, 2019). Due to this layered structure, direct atmospheric forcing primarily affects the upper layer, which typically has a thickness of 40–80 meters (Soomere and Quak, 2013). For the bottom layer advection and mixing play a major role.

Winds over the Baltic Sea have a seasonal pattern. However, the dominant wind direction in this area is southwest, but it is quite common for northerly winds to also be prevalent (Soomere and Keevallik, 2001). The winter and autumn seasons tend to have the strongest winds and highest waves (Jakimavičius et al., 2018). Winds play an essential role in this region, causing the occurrence of free oscillations known as seiches, which can significantly contribute to sea level extremes (Suursaar et al., 2002).

For waves in general the long-term average significant wave height in the Baltic Proper is 1–1.5 m (Räämet and Soomere, 2010; Björkqvist et al., 2018). For other sub-basins, such as the Gulf of Finland, where ALS surveys were performed, it can be around 0.5–0.8 m, and the maximum significant wave height is 3.8 m with a return period of 100 years. However, the maximum significant wave height at the western entrance of the Gulf of Finland may reach values comparable with extreme wave heights in the Baltic Proper (about 10 m) during severe storms (Soomere et al., 2008). The geometry and bathymetry of the northern Baltic Proper can influence wave direction, particularly

¹ https://www.gebco.net/data_and_products/gridded_bathymetry_data/ [accessed 7 August 2023]

towards the Gulf of Finland. Consequently, wave periods in the gulf may be comparable to those in the Baltic Proper. Notably, there can be a deviation of up to 50° between wind and wave directions in the gulf (Pettersson et al., 2010). An examination of wind, waves, and surface currents reveals that wind and surface waves predominantly govern surface drift (Delpeche-Ellmann et al., 2021). Moreover, wind waves can also play a noticeable role in contributing to extreme sea levels (Staneva et al., 2016).

Currents in the Baltic Sea are mainly the result of four factors: wind stress at the sea surface, surface pressure gradients, horizontal gradients of thermohaline density, and tidal forces. Furthermore, the currents are influenced by Coriolis acceleration, topography, and friction, resulting in the formation of a general cyclonic circulation in this stratified system; however, this circulation can vary within the different layers. Up- and downwellings are also common in the Baltic Sea especially in the summer months. Winds blowing predominantly parallel to the coast from favourable directions induce up- and downwelling, which often results in vertical water displacement and mixing (Lehmann and Myrberg, 2008; Delpeche-Ellmann et al., 2017). Also, the internal (baroclinic) Rossby radius that defines the size of meso-scale circulation cells (meso-scale or synoptic eddies) varies from a radius of 1–10 km (Alenius et al., 1998). Unlike many global sea areas, astronomical tides in the Baltic Sea are negligible, less than 10 cm, due to its limited co-oscillation with the open ocean. However, under resonance conditions, locally generated tides may still play a role, and as a result, tidal variations could become noticeable (Weisse et al., 2021).

Several components affect the sea level in the Baltic Sea. For a long-term effect, the global sea level change (due to thermal sea water expansion and melting of glaciers) will influence the sea level. Whilst changes in temperature, precipitation and evaporation are mostly influenced on a decadal time scale. It has also been suggested that temperature and precipitation may contribute for 15% of the sea level variability in winter and approximately 35% in summer (Hünicke and Zorita, 2006).

Short-term influences (yearly, seasonal, daily, etc.), variations in the water balance are mainly occurring due to water exchange in the Danish Straits. For instance, saltwater intruding (driven by atmospheric conditions) from the Atlantic (Major Baltic inflow) may lead to notable sea level changes. As an example, the Baltic inflow in 1993 increased the mean sea level by 70 cm within 21 days (Matthäus and Lass, 1995). River runoff also affects the water balance, with the biggest freshwater contributor being the Neva River located on the eastern end of the Gulf of Finland (Myrberg and Soomere, 2013). The decrease in sea ice days also contributes to the sea level in the Baltic Sea (Rosentau et al., 2017). Localized events, occurring on much shorter time frames, such as weeks, days, and even hours, can impact sea levels. Most of these events are influenced by meteorological factors, e.g. particularly strong, anisotropic winds in the Baltic Sea (Soomere, 2003). For example, storm surges and coastal upwellings are quite prevalent in the Baltic Sea with a more or less seasonal trend (Suursaar and Sooäär, 2007; Delpeche-Ellmann et al., 2017). These drastic short-term sea level changes that can occur show the importance of obtaining accurate instantaneous DT measurements that are necessary to record and predict these incidents.

2.2 The Geoid Model

The official NKG2015 geoid model, the most recent high-resolution geoid model for the Baltic region (Ågren et al., 2016), is employed for the determination of DT derived from SA data. The model was developed by the Nordic Geodetic Commission with spatial resolution of $0.01^\circ \times 0.02^\circ$ and reference epoch of 2000.0. The NKG2015 coverage extends from 23°N to 73°N latitude and from 0°E to 34°E longitude. The geoid model was determined based on the least-squares modification of Stokes' formula with additive corrections (LSMSA) up to degree and order 300 using the GOCE/GRACE geopotential model. The geoid model is shown in Figure 6. The standard deviation of the NKG2015 in agreement with the control GNSS/levelling data is 2.85 cm.

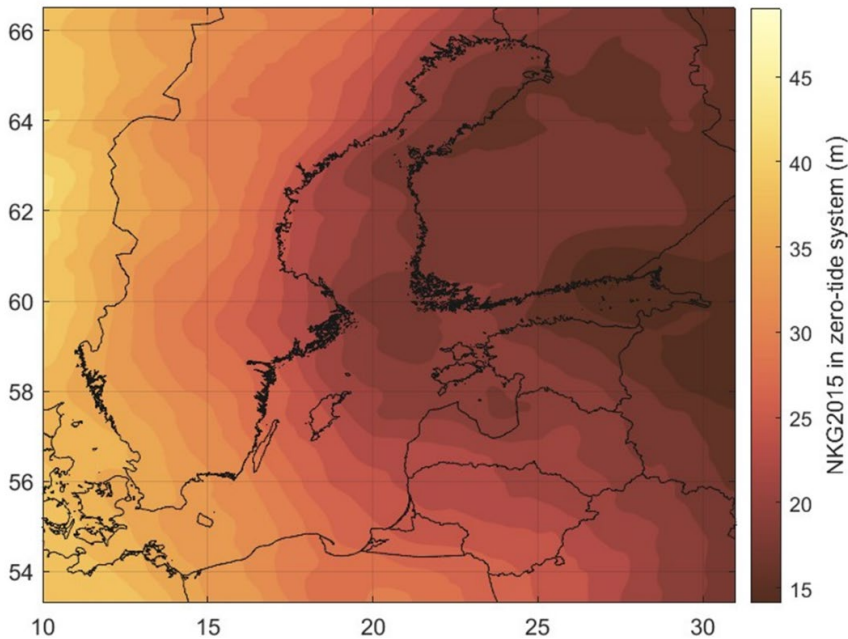


Figure 6. The NKG2015 geoid model in the zero-tide system.

The NKG2015 geoid heights are relative to the GRS80 reference ellipsoid. Accordingly, in this study, the GRS80 ellipsoid is adopted, and if necessary, the SA data (that could initially refer to some other reference ellipsoid, e.g. Topex/Poseidon) are transformed to this reference surface. Note that the NKG2015 model is in the zero-tide system, however, the officially released online model² contains a 'hybrid permanent tide system' correction, making it directly applicable to GNSS data. Therefore, this correction should be removed first, then the geoid model in the mean-tide system can be determined by Equation (7). In addition, the rate of geoid rise also needs to be accounted for due to the GIA-induced geoid rise in this region (Vestøl et al., 2019; see also Figure 3).

² https://www.isgeoid.polimi.it/Geoid/Europe/NordicCountries/nordic_baltic_countries_g.html [accessed 7 August 2023]

2.3 Tide Gauge Records

Tide gauge data serve as a base for correcting the HDM, which provides geoid-referenced sea level observations and can be considered as the ground-truth data (in **Method I**); as it is the most accurate source of high-temporal-resolution sea level variation, but may include errors and vertical datum shifts (in **Method II**). In this regard, hourly TG records were obtained from nine Baltic Sea countries: Estonia³, Latvia⁴, Lithuania⁵, Poland⁶, Germany⁷, Denmark⁸, Sweden⁹, Finland¹⁰, and Russia¹¹. Figure 5 shows the location of TG stations marked by red circles (see the **Publications I, II and IV** for more details about the used stations).

Since the Baltic Sea is under a strong influence of the GIA induced land uplift, it is essential to reduce TG benchmarks into a common time-epoch using a vertical land uplift model. In this region, this can be accomplished using the NKG2016LU model for the reference epoch 2000.0 (Vestøl et al., 2019). In addition, the common geoid-based chart datum BSCD2000 has been adopted to unify the reference surface of TG benchmarks in the Baltic Sea region with the reference point of the NAP (Schwabe et al., 2020). Therefore, according to the BSCD2000, the TG zero marks are consistent with their respective national height systems in the EVRS, with the exception of the Russian station, as indicated in Table 1. Given that the EVRS is a zero tidal system, it is essential to transform TG benchmarks to the mean-tide system before comparing them with the HDM sea level. Two exceptions exist for German and Danish stations, which employ mean-tide and tide-free systems, respectively.

In conclusion, to compare spatially distributed TG records with the HDM in terms of absolute values, the records need to be transformed into the mean-tide system using Equations (5) and (6). Furthermore, it is necessary to correct the TG readings to a common reference epoch of 2000.0 through the application of Equation (4) and the utilization of the NKG2016LU VLM model (see also Figure 3). **Method I** requires that missing TG data be addressed, and TG records be completed. Therefore, a machine learning (ML) based approach was employed to fill the gaps in TG data using neighbouring stations (Jahanmard et al., 2021b). In **Method II**, the only requirement is to account for the reduction of vertical land motion to a reference epoch. To determine HDM's reference bias using a network of TG data, it is essential to have a common geoid-based chart datum and to transform TG records to the mean-tide system.

³ <http://www.ilmateenistus.ee/meri/vaatlusandmed/kogu-rannik/kaart/> [accessed 7 August 2023]

⁴ <https://www.meteo.lv/hidrologija-datu-meklesana/> [accessed 7 August 2023]

⁵ <http://gamta.lt/> [accessed 7 August 2023]

⁶ <https://imgw.pl/> [accessed 7 August 2023]

⁷ <https://www.bsh.de/> [accessed 7 August 2023]

⁸ <https://kyst.dk/soeterritoriet/maalinger-og-data/vandstandsmaalinger/> [accessed 7 August 2023]

⁹ <https://www.smhi.se/data/oceanografi/ladda-ner-oceanografiska-observationer/> [accessed 7 August 2023]

¹⁰ <https://en.ilmatietaenlaitos.fi/download-observations> [accessed 7 August 2023]

¹¹ <http://www.emodnet-physics.eu/Map/DefaultMap.aspx> [accessed 7 August 2023]

2.4 Satellite Altimetry Dynamic Topography

Satellite altimetry is a widely recognized remote sensing technique employed for acquiring sea level measurements with respect to a reference ellipsoid across offshore and coastal region. The altimeter calculates the range by transmitting and receiving radar pulses along the satellite's path. By determining the accurate position and altitude of the platform in a geocentric reference frame, the SA mission derived SSH can be calculated by Equation (1).

In this study, the Sentinel-3A mission was employed to obtain along-track SSH observations, which were used to assess the HDM correction and ascertain the vertical reference bias of HDM. The trajectories of the Sentinel-3A mission over the Baltic Sea are visible in Figures 16 and 26. The SSH measurements operate in SAR mode based on the ALES+SAR retracker algorithm with a cycle period of 27 days and a spatial resolution of 300 m in high frequency data rate (20 Hz). The Synthetic Aperture Radar (SAR) mode is designed for high along-track resolution over flat surfaces, facilitating increased independent measurements in various areas including sea-ice thickness, coastal waters, ice sheet margins, land, and inland waters. The ALES+SAR is an empirical retracker developed as part of the ESA Baltic SEAL project and validated to assess its effectiveness in estimating sea level from signals acquired by the Sentinel-3A SAR altimeter (Passaro et al., 2022).

The determination of DT from SA data is performed by applying Equation (1) and the NKG2015 geoid model within the mean-tide system and utilizing an identical reference ellipsoid; where the atmospheric, geophysical, and instrumental corrections are embedded in the joint correction (*Cor*) term:

$$Cor = WTC + DTC + iono + SSB + DAC + OTC + SET + PT + ROC, \quad (10)$$

where *WTC* wet tropospheric correction;
DTC dry tropospheric correction;
iono ionospheric correction;
SSB Sea state bias correction;
DAC dynamic atmospheric correction;
OTC ocean tide corrections;
SET solid Earth tide;
PTC pole tide correction;
ROC radial orbit error correction;

Given the focus on instantaneous DT in this study, Equation (10) is employed with the exclusion of *DAC* and *OTC* corrections. Note also that the instantaneous TG readings do not contain these terms either. The SA data was sourced from Baltic+ SEAL datasets¹² (Passaro et al., 2021) for **Publication II** and from EUMETSAT data centre¹³ for **Publication IV**.

Satellite altimetry data may also include gross errors and outliers resulting from factors such as land contamination and the presence of sea ice (Mostafavi et al., 2023). The treatment of the SA data errors and outliers is conducted after the determination of DT and the removal of the geoid variation from SSH. Therefore, to mitigate errors arising

¹² <http://balticseal.eu/data-access/> [accessed 7 August 2023]

¹³ <https://www.eumetsat.int> [accessed 7 August 2023]

from land contamination, data points located within 5 km of the coastlines were excluded. Then, the gross errors beyond the ± 3 m range were eliminated, as DT variation exceeding 3 m is physically impossible in the study area and can distort the statistical parameters of SA data for detecting outliers. Finally, for each pass and cycle, outlier data is detected and removed by applying a moving median with a sliding window of one degree along the latitude and a threshold of three times the local scaled median absolute deviations. Figure 7a shows the data screening for a sample pass and cycle.

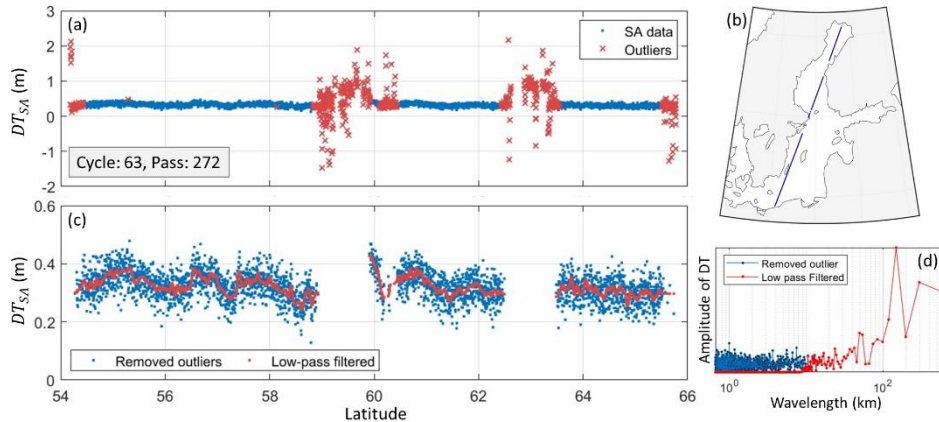


Figure 7. An illustration of the data screening for SA data: a) SA-derived DT for Cycle No. 63 (24-Sep-2020 09:42) and Pass No. 272 (denoted in b) and detected outliers. c) the clean SA data is represented in blue, and smoothed DT by applying the wavelet filtering method is shown in red. The frequency contents of the SA data are displayed in panel (d) [from **Publication IV**].

The 300 m spatial sampling rate of SA enables the derivation of a robust DT through the application of wavelet filtering to eliminate high-frequency features, including noise. These high frequency signals observed from the SA can be examined in future studies to determine their importance. For the purpose of this study, focused on validating the corrected HDM with a one-nautical-mile resolution, it is important to note that the model cannot accurately represent sea level variations with wavelengths shorter than about 10 km. Figure 7c shows a comparison between the cleaned and filtered SA data, and Figure 7d demonstrates the efficacy of high-frequency wavelength removal.

2.5 Airborne Laser Scanning point cloud

Airborne Laser Scanning (ALS) is a remote sensing technology that enables high-resolution mapping through active ranging. In this technique, a LiDAR (Light Detection and Ranging) sensor mounted on an aircraft emits short laser pulses and records the returning reflections from the Earth's surface. While measuring the distance from the sensor to a surface with signal return time, the sensor's position and direction on the aircraft are determined using a GNSS device and an inertial measurement unit. Therefore, the captured point cloud is accurately mapped with regard to desired coordinate system.

This technique is primarily employed for topographic mapping on dry lands with a vertical accuracy of 10 to 15 cm, depending on the measured surface and setup configuration (Hodgson and Bresnahan, 2004). However, ALS has advanced over the years and is now also used for marine applications, offering similar accuracy for sea

surface measurements (e.g., Sutherland et al., 2018; Varbla et al., 2021; Jahanmard et al., 2022c; Baker et al., 2023).

The capabilities of ALS, including its high pulse repetition rate, utilization of slow platform speed, and low beam divergence (resulting in a small-size and crisp footprint), enable the capture of dense and highly accurate point cloud data of the sea surface across a wide swath along the flight direction. As the ALS point cloud is accurately georeferenced by GNSS with respect to a reference ellipsoid, this technique provides precise observations of the instantaneous SSH surface, which can then be transformed into DT using a suitable marine geoid model. Furthermore, this technique is able to record high-frequency features of the sea surface due to its spatial resolution (e.g., 1×1 m), which makes it a valuable tool for measuring a wide range of waves. **Publication III** explores this dataset to retrieve the wind waves' parameters and their directional power spectral density.

The dataset used in this study was obtained from a marine ALS survey conducted on May 10, 2018, in the Gulf of Finland. This survey was performed using the Cessna Grand Caravan 208B aircraft operated by the Estonian Land Board. The aircraft was equipped with a LiDAR scanning system, RIEGL VQ-1560i, which operated with a pulse repetition rate of 1 MHz at a wavelength of 1064 nm. The dataset, along with more details, is available in Varbla et al. (2020). Figure 8 displays the location and a portion of the ALS-derived SSH surface from the 6th profile of this dataset that is used in this study.

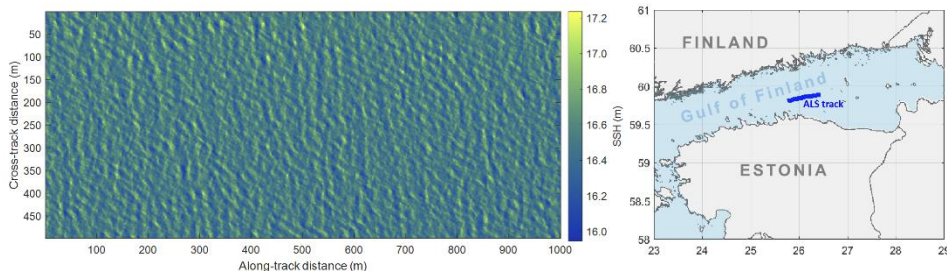


Figure 8. Image of the sea surface topography derived from ALS (first 1 km of the trajectory from west) with respect to the reference ellipsoid GRS-80 (left panel), and location of the flight trajectory on 10 May 2018, at 9:30 UTC in the Gulf of Finland (right panel).

The measured data corridor is about 1000–1200 m wide. In this study, the central 500 m wide data-strip is used, whereas the poor-quality data at the edges are disregarded (Varbla et al., 2021). The horizontal resolution is 1 m, which enables the extraction of surface features by a minimum wavelength of 5 m by considering 5 grid points to accurately define a feature without aliasing. Therefore, the highest wave frequency that may be observed is 3.5 rad/s, which makes it possible to derive wind waves from this dataset (e.g., Walsh et al., 1985; Jahanmard et al., 2022c; Baker et al., 2023). This is described in Section 5 and with more details in **Publication III**.

2.6 Hydrodynamic Model

Hydrodynamic models play a pivotal role in comprehending ocean dynamics, predicting natural disasters, assessing human impacts and climate change effects, designing resilient infrastructure, and optimizing shipping routes. Numerical modelling offers valuable insights into complex processes, including circulation patterns, sea level,

temperature, and salinity variations, stratification, and their impact on pollutant transport and water quality in the water body.

This numerical modelling relies on the Navier-Stokes equations, which are informed by meteorological and hydrological data to simulate the real world. HDMs are usually sufficient at features that the actual observations are limited, which is their resolutions in time and space from coast to offshore. However, there is no guarantee that HDMs do not deviate from reality due to potential modelling errors stemming from modelling limitations and uncertainties in inputs (Axell and Liu, 2016). Errors in HDMs can originate from factors such as bathymetry, temporal discretization, spatial resolution limitations, parameterization schemes, computational errors, and uncertainties in boundary conditions and forcing data (Mardani et al., 2020). In addition, HDMs typically lack a well-defined vertical reference datum, which is an obstacle to express uniquely the sea level derived from HDMs in a 3D coordinate system (Slobbe et al., 2013).

Two hydrodynamic models were selected to investigate the methodologies for determining realistic absolute DT by integrating observed and modelled sea levels. In **Publication I**, Nemo-Nordic model¹⁴ (Hordoir et al., 2019; Kärnä et al., 2021) with a horizontal resolution of 2 NM and HBM-EST model¹⁵ (Lagemaa et al., 2011) with a resolution of 0.5 NM were sourced for the period spanning 2014 and 2015 (see **Publication I** for more details regarding the HDMs). The spatial coverage of HBM-EST model is shown in Figure 9. In **Publications II** and **IV**, assimilated Nemo-Nordic model with a horizontal resolution of 1 NM was employed for the entire Baltic Sea region during the periods from December 2016 to April 2020 and from December 2016 to June 2021, respectively. The spatial domain of the Nemo-Nordic model is the Baltic and North Sea (see Figure 9).

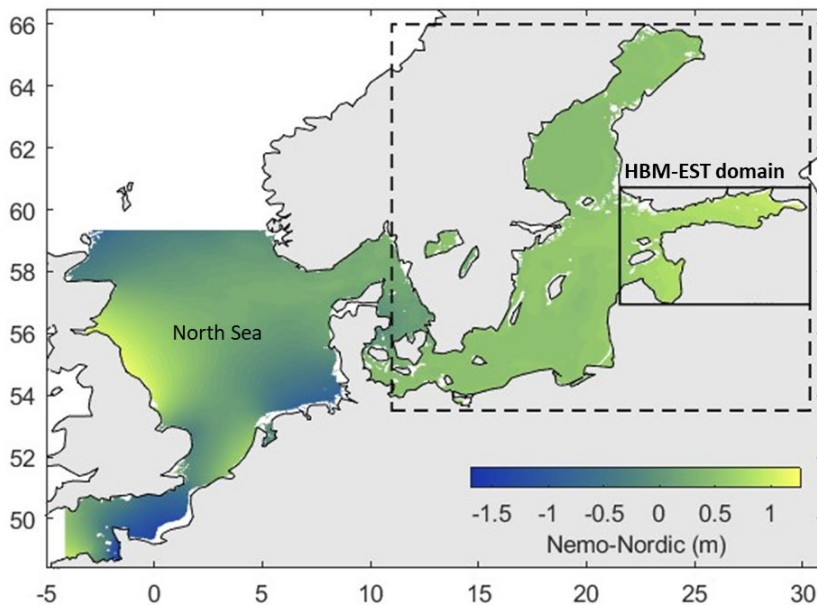


Figure 9. Nemo-Nordic model domain covers the Baltic Sea and the North Sea. The model domain of HBM-EST is denoted by a solid-line rectangle.

¹⁴ <https://www.smhi.se/> [accessed 7 August 2023]

¹⁵ <http://emis.msi.ttu.ee/download/> [accessed 7 August 2023]

The Nemo-Nordic model (NEMO NS01) was obtained from the Swedish Meteorological and Hydrological Institute¹⁶ (SMHI). This model is a 3D high-resolution ocean model of the Baltic and North Seas. It is based on the Nucleus for European Modelling of the Ocean (NEMO) ocean engine, which is a set of ocean modelling tools supported by a large community. The Nemo-Nordic model is used for both research and operational applications, including forecasting sea level, water temperature, salinity, velocity, sea ice concentration, and thickness (Hordoir et al., 2019; Kärnä et al., 2021). The model provides a 60-hour forecast every 6 hours through data assimilation of available observations. For this purpose, the meteorological forecast model Arome, the forecast model from ECMWF, and river data from the hydrological model HYPE are employed.

The Nemo-Nordic model has a horizontal resolution of 1 NM and uses a z* grid configuration with 56 vertical levels. However, the obtained dataset contains only surface parameters. The layer thickness is 1 m at the surface, increasing to 10 m at a depth of 75 m and 24 m at a depth of 700 m. The model uses GEBCO-2014¹⁷ bathymetry data, with the ambiguous vertical reference surface assumed to be the mean sea surface.

The model has two open boundaries, located in the English Channel (meridionally) and between Scotland and Norway (zonally). The sea level data along the open boundaries are prescribed from the CMEMS Northwestern Shelf forecast model.

The model uses SI3 sea ice model (NEMO Sea Ice Working Group, 2019) and landfast ice parametrization. The Nemo-Nordic is forced with the 3 km HIRLAM atmospheric forecast model data (Undén et al., 2002). River discharge data is derived from the E-HYPE daily mean (Arheimer et al., 2012). It has been shown that wind waves play a significant role in contributing to extreme sea levels (Staneva et al., 2016 and 2017). However, to our knowledge, Nemo-Nordic does not incorporate wind waves into its calculations. For more details about the model setup, please refer to Hordoir et al. (2019) and Kärnä et al. (2021).

¹⁶ <https://www.smhi.se/data/ladda-ner-data/ladda-ner-fran-gribarkiv/nemo-bs01> [accessed 7 August 2023]

¹⁷ https://www.gebco.net/data_and_products/gridded_bathymetry_data/ [accessed 7 August 2023]

3 Method I: Geoid-referenced Tide Gauges as Ground Truth

The implementation of BSCD2000 has unified the vertical reference for the extensive network of TGs along the coastline of the Baltic Sea. BSCD200 is the geoid surface with the zero level through the NAP (Schwabe et al., 2020). Using NKG2015 geoid model to derive DT from SA data enables a comparison with the TGs on a consistent equipotential reference surface. However, the reference surface of the HDM remains undisclosed, and the presence of modelling errors complicates the determination of this reference surface.

To integrate data sources, the HDM should be reduced to the same reference surface as observations, then the modelling errors can be treated by comparing with observed data. On the other hand, the modelling errors distort the accurate determination of the HDM's reference surface. Thus, as a primary step in the presence of a dense network of geoid-referenced TGs, the modelling errors and HDM's vertical reference bias can be considered as one integral bias. As a result, the HDM can be corrected using TG records for the narrow and limited Baltic basins. For the sake of consistency between sections and methods, minor adjustments have been applied to some equations and figures, as compared to the initial publications. For more detailed information, please refer to **Publications I and II**.

3.1 Theoretical Principles for Bias Computation

The difference between HDM and TG records illustrate temporal and spatial variations (see Figure 10). Temporal variations of the bias range from -20 cm to 50 cm, covering frequencies from high (e.g., half-day and daily) to low (e.g., seasonal and annual cycles). In addition, the HDM has a roughly 20 cm shift with respect to the TG records due to the difference in zero level, which also changes under influence of the HDM errors. The difference between HDM and TG records is determined as follows:

$$E(\varphi_{TG_i}, \lambda_{TG_i}, t) = DT_{HDM}(\varphi_{TG_i}, \lambda_{TG_i}, t) - DT_{TG}(\varphi_{TG_i}, \lambda_{TG_i}, t). \quad (11)$$

To correct the HDM, its bias is classified into time-domain bias (*TDBias*) and spatial-domain bias (*SDBias*). The *TDBias* is initially obtained by comparing HDM and TG records, and subsequently, the *SDBias* is determined using interpolation techniques. Utilizing a backward moving average method with a window length of w to determine the *TDBias* helps filter out high frequencies that are not of interest and also effectively eliminates potential spike errors in the TG records. Therefore:

$$TDBias(\varphi_{TG_i}, \lambda_{TG_i}, t) = \frac{1}{w} \sum_{t=(1-w)}^0 (E(\varphi_{TG_i}, \lambda_{TG_i}, t)). \quad (12)$$

In this study, window length of 6-hour is used (see **Publication I and II** for more details). Given the strong correlation that is observed between the Nemo-Nordic model and the TG records, it can be inferred for each time instant that the determined biases at stations do not have drastic changes by moving away from the TG stations.

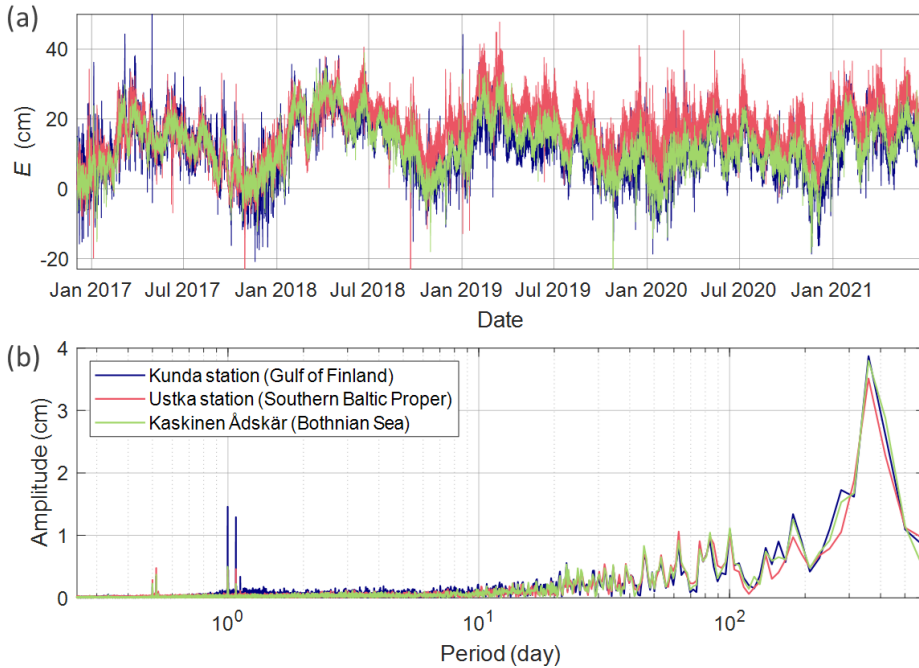


Figure 10. Difference between the Nemo-Nordic model and tide gauge records: a) time series at three sample stations. Location of the stations are denoted in Figure 12. b) Fast Fourier transform (FFT) of the records shown in panel (a). Please note that the HDM data until April 2020 were accessible for **Method I** [Modified from **Publication IV**].

Based on the limited distance between the network of TGs in the study domain, the $TDBias$ at each time instant can be propagated using an interpolation technique. Therefore, the $SDBias$ can be obtained as follows:

$$SDBias(\varphi, \lambda, t) = \text{Interp}(\varphi_{TG}, \lambda_{TG}, TDBias(\varphi_{TG_i}, \lambda_{TG_i}, t), \varphi, \lambda), \quad (13)$$

where Interp is an interpolation operator, and the $SDBias$ is estimated at the HDM's grid points. Finally, the corrected HDM is determined as follows:

$$DT_{HDM}^C(\varphi, \lambda, t) = DT_{HDM}(\varphi, \lambda, t) - SDBias(\varphi, \lambda, t). \quad (14)$$

Several interpolation techniques were examined, such as linear, inverse distance weighted, and thin plate spline, the results of which are detailed in **Publication II**. The differences between the use of different interpolation methods are negligible. For conciseness, only the results of the inverse distance weighted (IDW) method are presented in the sequel.

As a result, the corrected HDM can be evaluated using the DT derived from SA observations to assess the effectiveness of the HDM correction approach. Moreover, comparing all DT data sources in a common geodetic reference frame can reveal inconsistencies and highlight problematic regions requiring further investigation. Figure 11 shows a flowchart of the methodology for correcting HDM and comparing data sources.

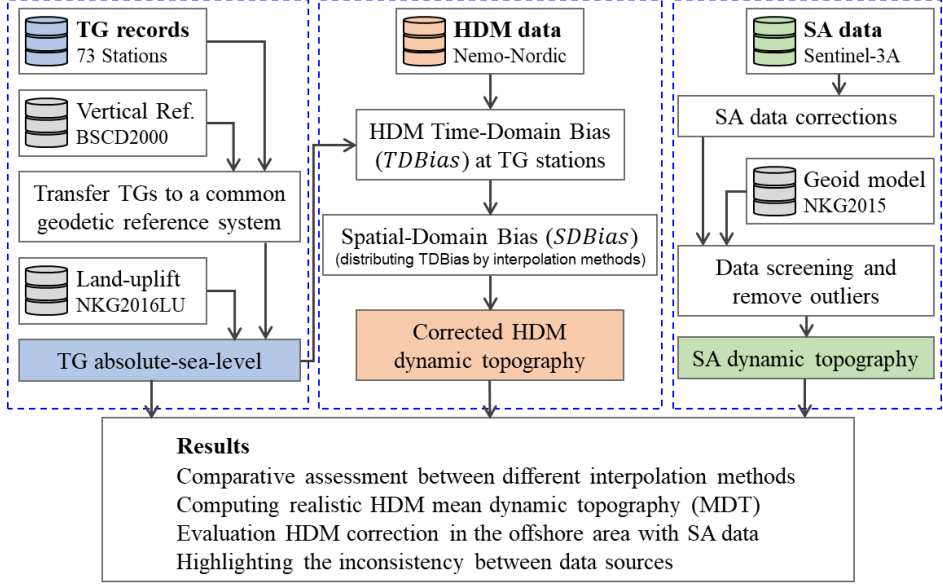


Figure 11. Flowchart of the HDM correction using a dense network of geoid-referenced TG records and comparative assessment of the datasets [from **Publication II**].

3.2 Hydrodynamic Model Correction

This method considers that the TG records represent the true absolute sea level relative to a common geoid surface. Therefore, Equation (12) was applied to obtain the *TDBias*s at 73 TG stations along the Baltic coastline. Figure 12a shows the spatial distribution of the *TDBias* for an arbitrary time instant (i.e., 5 June 2019, 12:00). The root mean squared error (*RMSE*) between the HDM and TG records, before and after correction, is calculated as follows:

$$RMSE(\varphi_{TG_i}, \lambda_{TG_i}) = \sqrt{\frac{1}{n} \sum_{t=1}^n \left(E(\varphi_{TG_i}, \lambda_{TG_i}, t) - Bias(\varphi_{TG_i}, \lambda_{TG_i}) \right)^2}, \quad (15)$$

where n is the number of observations within the selected time span, and *Bias* represents the average of the differences over the entire time period for each station:

$$Bias(\varphi, \lambda) = \frac{1}{n} \sum_{t=1}^n (E(\varphi, \lambda, t)). \quad (16)$$

Figure 12b and 12c illustrate the *RMSE* and *Bias* at the stations for original and corrected HDM. The corrected HDM at the stations can be computed using Equation (14) by employing *TDBias* instead of *SDBias*. The *RMSE* of the Nemo-Nordic model after correction is reduced by approximately a factor of three at the stations, which is within the range of 1 to 6 cm. The *Bias* of the original HDM with respect to TGs varies from 13 cm to 25 cm, which is reduced to zero after correction. The average of the *Bias* is 18.6 cm, with a standard deviation of 2.5 cm.

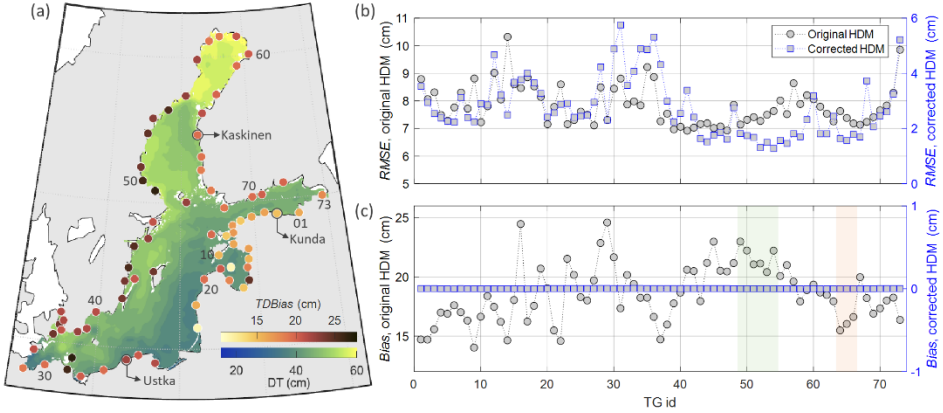


Figure 12. Comparing the HDM with the network of TGs. a) DT of the Nemo-Nordic model at a specific time instant (e.g., 5 June 2019, 12:00), along with the corresponding $TDBias$. b) RMSE of original and corrected HDM at TG stations. TG stations are numbered clockwise, starting from the easternmost Estonian TG station, as indicated in (a) for some stations. c) Bias of the HDM with respect to TG records.

The results demonstrate that the 6-hour window employed in Equation (12) effectively eliminates biases between HDM and TG records, and the remaining errors are limited to a standard deviation of 5 cm (see **Publication I** regarding the window selection). A larger window results in a larger post-correction RMSE and may not effectively eliminate systematic errors. Conversely, employing a smaller window can introduce high-frequency noise into spatial interpolation, and as a result, decrease the reliability of the interpolated $TDBias$ by increasing the distance from TG stations.

Using Equation (14) requires propagating the $TDBias$ over the HDM grid points at each time step. In **Publication II**, it has been demonstrated that the variability resulting from different interpolation methods is negligible (around 1.3 cm), and the IDW interpolation effectively interpolates the $TDBias$ over the grid points for each time step. Therefore, the surface of the HDM bias (i.e., $SDBias$) can be determined as follows:

$$SDBias(\varphi, \lambda, t) = \frac{\sum_{i=1}^m \mathcal{W}_i(\varphi, \lambda) \cdot TDBias(\varphi_i, \lambda_i, t)}{\sum_{i=1}^m \mathcal{W}_i(\varphi, \lambda)}, \quad \forall(\varphi, \lambda) \neq (\varphi_i, \lambda_i), \quad (17)$$

where \mathcal{W} represents the vector of inverse distance weight, computed by measuring the distance \mathcal{D} of each grid point from the TG stations:

$$\mathcal{W} = \frac{1}{\mathcal{D}^2}. \quad (18)$$

As a result, the corrected HDM is obtained using Equation (14). Figure 13 illustrates the original and corrected HDM for a sample time instant (i.e., 5 June 2019, 12:00), along with the corresponding $SDBias$. The $SDBias$ varies spatially from 11 cm to 28 cm for this time instant, with the largest bias occurring along the Swedish coastline and decreasing eastward. The notable observation in this figure is the abrupt variation in the $SDBias$ near some stations. This variation may imply a potential vertical datum shift at these stations; however, the IDW interpolation method has effectively damped this error in the vicinity of the stations.

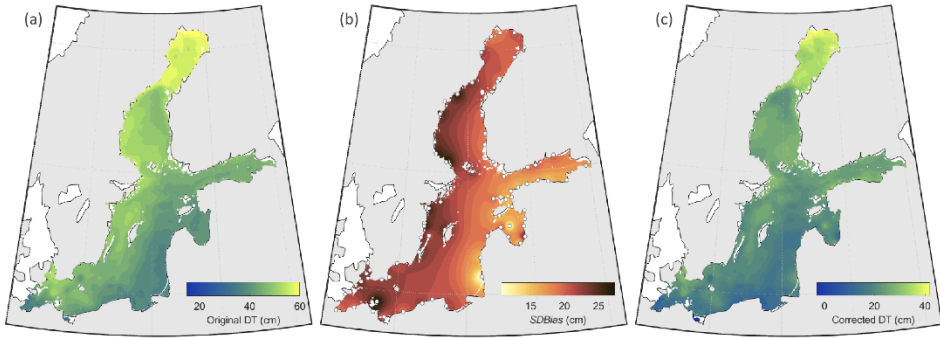


Figure 13. HDM correction for 5 June 2019, 12:00. a) instantaneous DT derived from the original Nemo-Nordic model, b) the corresponding SDBias obtained from 73 TG records, and c) corrected DT based on Equation (14).

3.3 Comparative Assessment of HDM Bias Estimates Using Satellite Altimetry

The corrected HDM, particularly in offshore regions, can be validated using SA data as an independent data source. Hence, conducting a comparative assessment between sea level data sources with both the original and corrected HDM can reveal the performance of the HDM correction process and highlight discrepancies among sea level measurement techniques.

For this purpose, the instantaneous DTs derived from the original/corrected HDM are extracted at the coordinates of the SA data points using bilinear interpolation in space and linear interpolation in time, corresponding to the time of SA. The SA data was available for the period from January 2017 to June 2019, including the winter months. The *Bias* between the HDM and SA data is determined along the SA tracks using Equation (16), where the E is the difference between the original/corrected HDM and SA measurements. Figure 14 shows the *Bias* of the original and corrected HDM with respect to SA data against the SA passes and cycles, along with the interquartile range to demonstrate the variability of the differences. In this figure, it can be observed that the HDM correction can reduce the HDM's reference surface to the specified geoid surface.

In Figure 14a, passes showing a significant *Bias* are situated in the vicinity of the coastline, which SA data are affected by land contamination, or located in the eastern part of the Gulf of Finland, where the geoid model lacks accuracy and contains an unrealistic undulation due to the gravity data voids (Varbla et al., 2023). This figure also demonstrates a reduction in the variability of differences between HDM and SA after applying the HDM correction. A significant reason can be seen in Figure 14b, where the original HDM demonstrates a seasonal discrepancy compared to the SA measurement, which is almost eliminated in the corrected HDM. During the winter months, both the *Bias* and interquartile ranges of the corrected HDM increase, which can be attributed to the presence of ice coverage in the northern and eastern parts of the Baltic Sea. In sea ice conditions, SA measurements include sea ice freeboard and are not accurate sea level measurements for comparison with HDM data. Therefore, the winter months should be discarded in this comparison.

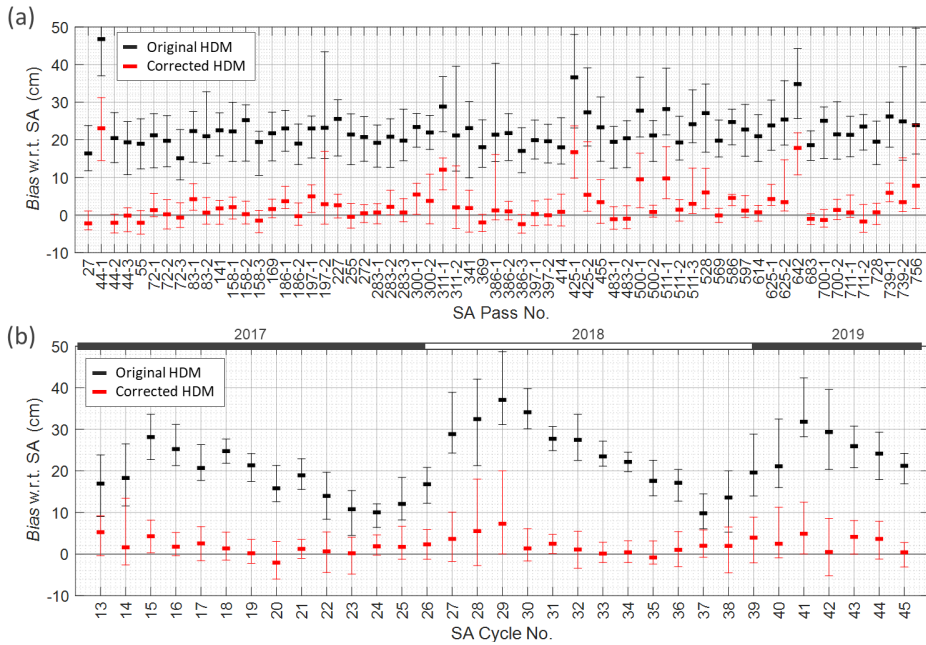


Figure 14. Existing Bias between the original and corrected HDM with respect to the SA measurements against the SA passes in (a) and cycles in (b). The bars demonstrate the distance between the first and third quartiles [Modified from **Publication II**].

Since the instantaneous SA measurements are utilized (meaning the *DAC* and *OTC* corrections are not applied), the temporal average of SA data does not precisely represent the MDT. Hence, the mean of SA data across cycles is denoted as *CycleMDT*, and it is derived through an inverse-variance weighted average (please see **Publication II** for more details). Figure 15 illustrates the *CycleMDT* along a selection of sample tracks extracted from the SA data, the original and corrected HDM, and nearby TGs. It is observed that the original HDM deviates from the SA and TG data by approximately 19 cm, which is due to the HDM’s vertical reference bias relative to the specified geoid surface.

Figure 15 also shows the negligible (spatial) variation of the corrected HDM in comparison to the original HDM, which indicates that the instantaneous corrections have effectively eliminated modeling errors and the HDM’s reference level has almost coincided with an equipotential surface. Therefore, the discrepancy of HDM can be categorized into two components: HDM modelling errors and vertical reference bias, which is tackled in the following section.

The significant discrepancy between the corrected HDM and SA measurement for pass number 414 (Figure 15e) indicates problems with the geoid model in the eastern part of the Gulf of Finland. The substantial undulation of the DT derived from SA data is not realistic for such a limited area. This unrealistic variation is also noticeable in Figure 14a, especially around Bornholm Island (i.e., latitude 54° to 56°) and in the Bothnian Sea (i.e., latitude 60° to 64°).

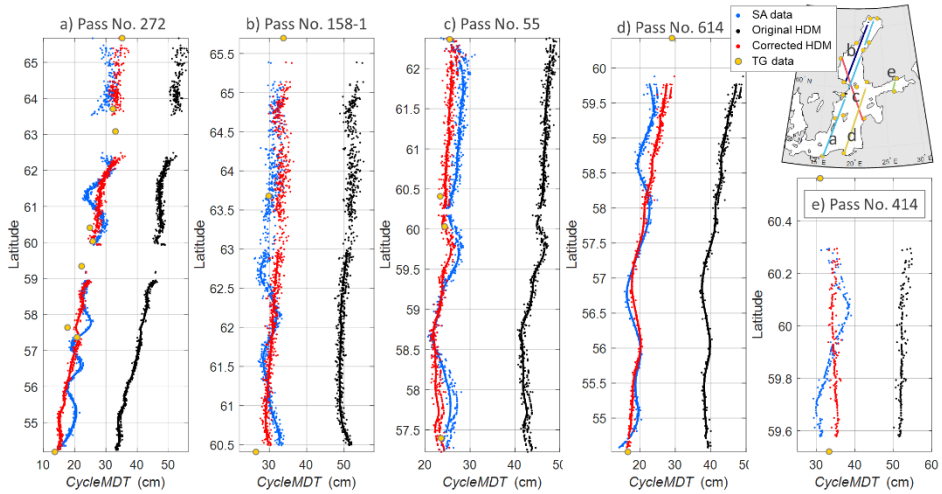


Figure 15. CycleMDT derived from the SA data, original and corrected HDM, and nearby TG records. The location of the selected passes is shown in the top-right panel [Modified from **Publication II**].

Spatial distribution of the *Bias* between the original/corrected HDM and SA data are shown in Figure 16 to highlight problematic areas. The *Bias* is determined at the SA data points, where the along-track data are gridded by latitude interval of 900 m (i.e., three observations at each cycle) and *Bias* is obtained with a threshold of 95% data presence. Comparison between the original and corrected HDM illustrates the average spatial correction. Note that the HDM correction in this method is forced by the network of TG observations, which might contain vertical datum shift. The mean of the *Biases* with respect to SA data after correction is almost zero with a standard deviation of 2.4 cm.

Furthermore, Figure 16b emphasizes problematic regions where the discrepancy between the corrected HDM and SA data is significant. Four regions showing noticeable patterns are indicated by green dashed rectangles. However, further investigations are necessary for discussing the sources of errors in other regions. The *Bias* in the Bothnian Bay arises from winter months when SA measurements are disrupted by ice coverage. The noticeable *Biases* observed in the eastern part of the Gulf of Finland, Bothnian Sea, and around Bornholm Island can be attributed to issues with the geoid model (Figure 15a and e; see also Jahanmard et al., 2022b).

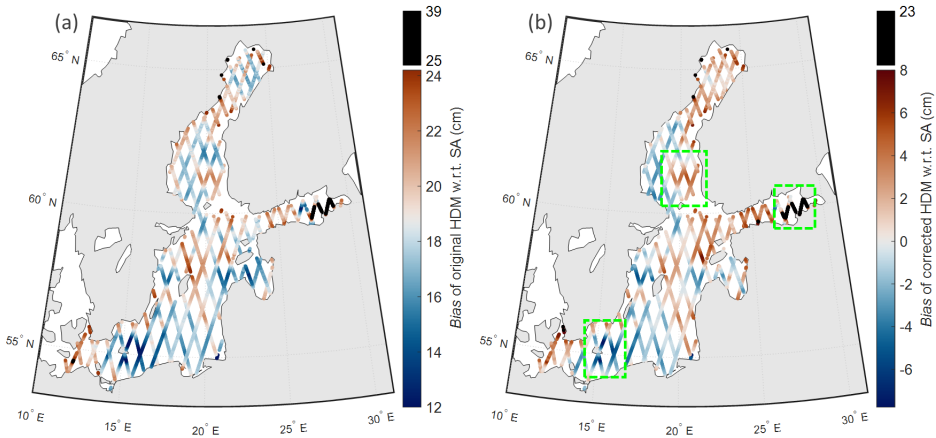


Figure 16. Spatial distribution of the Bias of the a) original and b) corrected HDM with respect to SA-derived DT. Green dashed rectangles denote noticeable patterns of differences [Modified from Publication II].

As a result, the instantaneous absolute DT can be derived through the correction of HDM using a network of geoid-referenced TG records. Therefore, a realistic MDT for a certain time period, which represents the corresponding ocean circulation patterns, can also be determined by calculating the temporal mean of the corrected DT. Figure 17 presents a comparison between the original and corrected annual MDTs, accompanied by the corresponding observed MDTs from TGs. For consistency in colour scales, the original MDT has been adjusted downward by 18.6 cm, which corresponds to the average Bias relative to the TG records. The corrected MDTs demonstrate enhanced consistency with observed MDTs at TG stations, and a noticeable change in the MDT patterns can be observed in 2019. Note that by reducing the period of MDT, such as to seasonal or monthly intervals, the discrepancy between the corrected and original MDT becomes more evident.

It is worth mentioning that the HDM correction using a closed-loop network of geoid-referenced TGs and interpolation techniques is vulnerable to any presence of tilts in height datums (caused by systematic errors in levelling data; Featherstone et al., 2012; Afrasteh et al., 2023) or vertical datum shifts among stations. For instance, in Figure 17, the MDT of a station situated in the middle of the Gulf of Riga displays a spike difference relative to the HDM, as well as its neighbouring stations. This discrepancy indicates a datum shift in the zero level of the TG records. Additionally, an eastward tilt in the zero level of TGs in the Bothnian Sea can be inferred by comparing HDM and TG data (refer to Figure 12c; Swedish and Finnish TG stations are highlighted in green and red colour, respectively), which is further supported by comparing the corrected HDM with SA data (see Figure 16b).

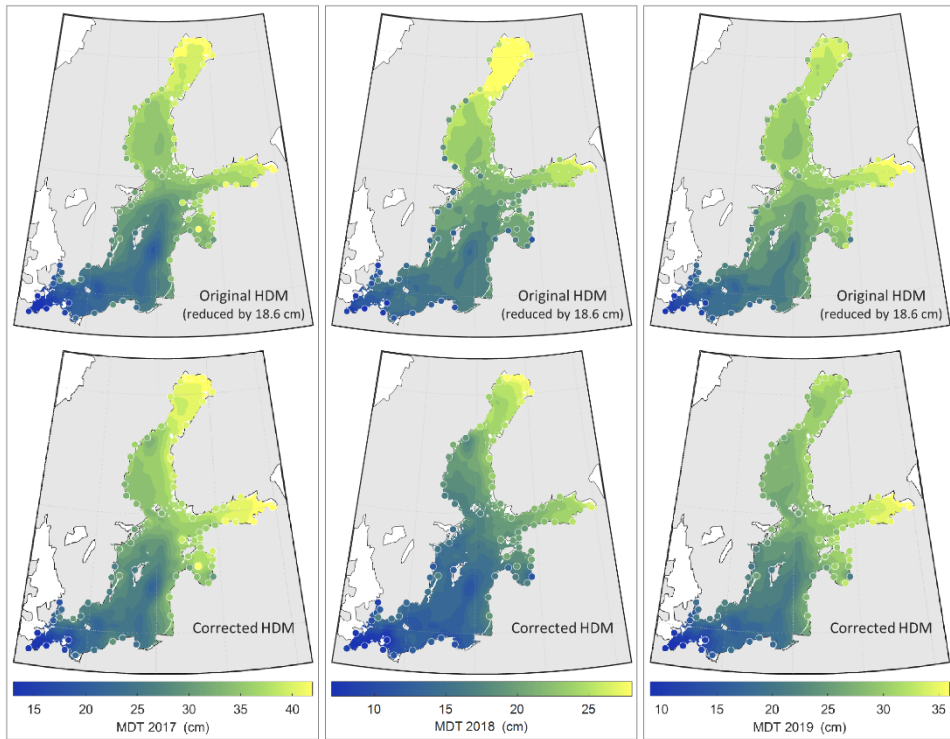


Figure 17. Annual mean dynamic topography shown for the original Nemo-Nordic model in the top row and the corrected HDM in the bottom row, along with the corresponding TG-based MDTs marked by circles. The original HDM has been adjusted by -18.6 cm to use consistent colour scaling with the corrected HDM for each year [Modified from **Publication II**].

In the following Section, an ML-based approach is used to eliminate the HDM modelling errors, in which the method is independent of the absolute values of TG records and can address the TG-related bias and errors by generalizing the HDM correction. Then, correcting HDM allows accurate determination of the vertical reference bias between HDM and the geoid surface of interest using SA measurements. Therefore, the HDM correction can also be performed in the absence of a common geoid-based reference for TG readings. Moreover, the ML-based approach can resolve the limitations of the interpolation, such as the necessity of a closed-loop network of TG stations and the uneven distribution of stations along the coastlines.

4 Method II: Application of Machine Learning

As inferred and mentioned above, the difference (E) between the modelled and observed DT (derived from Equation 11) includes two components: i) HDM modelling errors that can vary in a wide range of frequency, and ii) a bias due to difference between zero levels that is a constant value over time and space. Therefore:

$$E(\varphi, \lambda, t) = \varepsilon(\varphi, \lambda, t) + RefBias, \quad (19)$$

where ε represents the HDM errors and $RefBias$ is the bias between the HDM's reference surface and geoid surface of interest. The former, which is due to the modelling limitations, can be predicted across model domain by a deep learning (DL) model; and the latter is accurately determined by comparing the corrected HDM with the DT derived from SA measurements. For this purpose, a multivariate temporal causal convolutional network is employed. Note that the observations may also contain errors and biases, and the DL model has the capability to mitigate the influence of errors by generalizing the pattern it learns across different time periods and locations.

The fundamental idea is that the HDM modelling errors can be predicted based on temporal causal relationships between spatio-temporal input variables and computed errors in the TG stations. It is also expected that the DL model can be generalized spatially. Figure 18 presents the flowchart of **Method II** for correcting the HDM and comparing the sea level data sources.

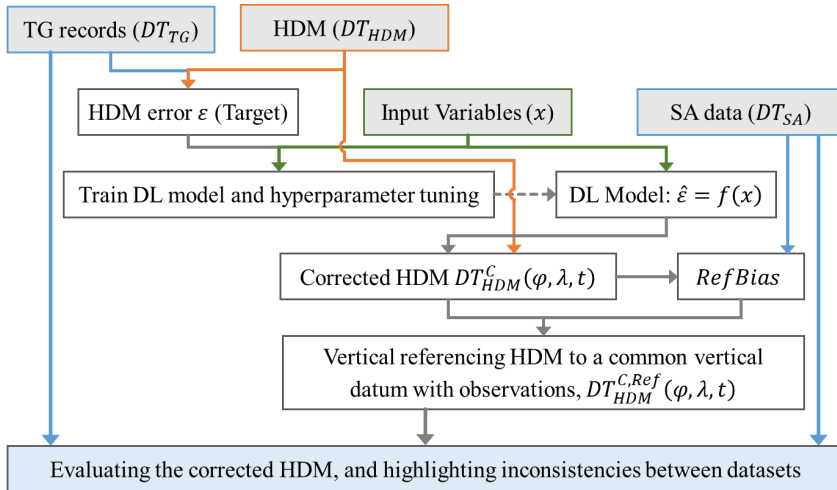


Figure 18. Flowchart of **Method II** for the HDM correction and vertical referencing it to a common vertical datum, as utilized for both SA and TG observations [Modified from **Publication IV**].

4.1 Deep Neural Network for Modelling Error Prediction

Tide gauges present continuous and high-frequency measurements of sea level, which are historically the most reliable source of sea level variations in a wide range of temporal features. However, they may suffer from datum shifts or even lack a common vertical datum to combine sea level records from multiple locations. Comparing the HDM-based DT with TG records at station locations on an hourly basis allows for the detection of

HDM errors (ε) across various frequencies (see Figure 10). Therefore, the HDM errors that will be served as the *target* values for the DL model training is obtained as follows:

$$\varepsilon_i(t) = \left(DT_{HDM@TG_i}(t) - DT_{TG_i}(t) \right) - Bias_i, \quad (20)$$

where *Bias* is computed by Equation (16), and $DT_{HDM@TG_i}$ represents DT derived from the HDM at the nearby *i*-th TG station, which is obtained as follows:

$$DT_{HDM@TG_i}(t) = \text{median}\left(M_i(\varphi, \lambda) \cdot DT_{HDM}(\varphi, \lambda, t)\right), \quad (21)$$

where M_i is a mask for *i*-th station, employed to extract HDM time series within a limited radius (e.g., 5 km) around the station. Accordingly, the input variables are also determined for each station by the M_i :

$$x_{TG_i}(c, t) = \text{median}\left(M_i(\varphi, \lambda) \cdot x(\varphi, \lambda, c, t)\right), \quad (22)$$

where *c* represents the dimension of the input variable (or channel). The input variables are described in Subsection 4.1.2.

The DL model is trained by a set of TG records for the available period to predict the HDM errors over the HDM grid points. Therefore, the predicted HDM errors is obtained from a pre-trained model as follows:

$$\begin{aligned} x_{inp}(c, t, q) &= \text{Vec}\left(x(\varphi, \lambda, c, t)\right), \\ \hat{\varepsilon}(q, t) &= \text{DLModel}\left(x_{inp}(c, t, q)\right)', \\ \hat{\varepsilon}(\varphi, \lambda, t) &= \text{Vec}^{-1}(\hat{\varepsilon}(q, t)) * G(ks, \sigma), \end{aligned} \quad (23)$$

where G is a 2D Gaussian filter with a kernel size of $ks = 5$ nautical miles and a standard deviation of $\sigma = 2.5$ nautical miles. This spatial filter is applied to suppress potential high-frequency noises that may arise from the individual determination of HDM errors at each grid point. By utilization of spatio-temporal input variables, the predicted HDM errors $\hat{\varepsilon}(q, t)$ can be calculated, where q are the indices of the HDM grid points within the study domain. The operator $\text{Vec}(\)$ is employed for vectorization, and the symbol $*$ represents the convolution operation.

Finally, the corrected HDM (DT_{HDM}^C) is obtained based on the Equations (11) and (19) as follows:

$$DT_{HDM}^C(\varphi, \lambda, t) = DT_{HDM}(\varphi, \lambda, t) - \hat{\varepsilon}(\varphi, \lambda, t). \quad (24)$$

Thus, by determining the *RefBias* through the comparison of DT_{HDM}^C and DT derived from SA observations and a specific geoid model, the reference surface of the corrected HDM can be unified with the observations as follows:

$$DT_{HDM}^{C,Ref}(\varphi, \lambda, t) = DT_{HDM}^C(\varphi, \lambda, t) - RefBias. \quad (25)$$

Figure 19 depicts the procedure of the HDM correction and its vertical referencing using the pre-trained DL model, TG records, and SA measurements.

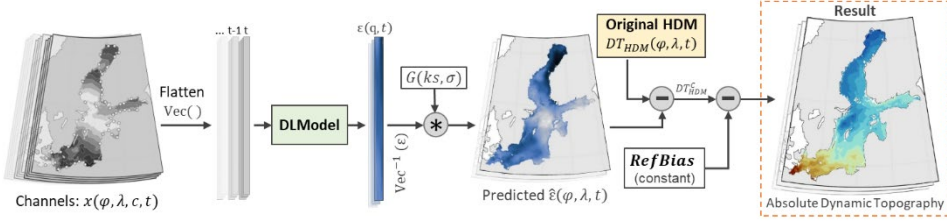


Figure 19. Utilizing the DL model to correct HDM dynamic topography and vertical reference the HDM to a specific geodetic reference frame [Modified from **Publication IV**].

During the DL training process, it's important to consider that TG stations are spatially sparsely distributed. This characteristic of TG observations hinders effective feature learning across the spatial dimension in machine learning approaches. Nevertheless, their high-resolution time series enables feature learning over the course of time using causal convolutional layers. The absence of the feature learning across spatial dimensions can lead to overfitting in this aspect, which requires controlling the DL model's generalization. Hence, employing a spatial-sample splitting strategy can effectively address this issue.

In this approach, a set of 50 tide gauge stations are used and partitioned into three subsets: 16 stations for training, another 16 for validation, and a remaining 18 for the test set (see Figure 22a). Therefore, the DL model will undergo training using the training set, while the model's spatial generalization will be controlled by the validation set, and the test set (along with the validation set) is used for evaluating the model's performance. The performance of the DL model is statistically examined by RMSE and R-Squared estimates, which are computed as follows:

$$RMSE_{\varepsilon} = \sqrt{\frac{1}{n} \sum_{t=1}^n (\hat{\varepsilon}(\varphi, \lambda, t) - \varepsilon(\varphi, \lambda, t))^2}, \quad (26)$$

and

$$R^2 = 1 - \frac{\sum_{t=1}^n (\hat{\varepsilon}(\varphi, \lambda, t) - \varepsilon(\varphi, \lambda, t))^2}{\sum_{t=1}^n \left(\varepsilon(\varphi, \lambda, t) - \frac{1}{n} \sum_{t=1}^n \varepsilon(\varphi, \lambda, t) \right)^2}, \quad (27)$$

where ε is the actual HDM errors (target) at the measurement point (φ, λ) , and $\hat{\varepsilon}$ represents the predicted HDM errors using the DL model.

4.1.1 Deep Learning Model Structure

A multivariate DL model employing a stack of dilated causal convolutional layers is utilized to predict the HDM errors (ε). The network is inspired by WaveNet (Oord et al., 2016), which is also used in a wide range of fields, such as ocean wave height prediction (Lou et al., 2022), wind speed forecasting (Rathore et al., 2021), and dynamic topography forecasting (Rajabi-Kiasari et al., 2023).

The DL model consists of k blocks of causal convolutional units, each containing two conv1D layers with parameters: filter size (fs), number of filters (nf), and dilation (d). The conv1D layer includes two trainable parameters: weights and biases, which are learned during training. Incorporating rectified linear unit (ReLU) activation functions after the conv1D layers enable the model to learn complex relationships between the

inputs and the output by adding nonlinearity to the model. The utilization of batch normalization layer between the conv1D and ReLU layers enhances accuracy and accelerates the training process. The utilization of batch normalization layer between the conv1D and ReLU layers enhances accuracy and accelerates the training process (Bjorck et al., 2018), and the inclusion of a dropout layer enables the prevention of overfitting and encourages the network to learn more robust and generalized representations (Baldi and Sadowski, 2013).

The internal structure of the DL model and the causal convolution blocks are shown in Figure 20. After passing through the convolutional units, the feature tensors are then input into the fully connected layers to compute the HDM errors using the final regression layer.

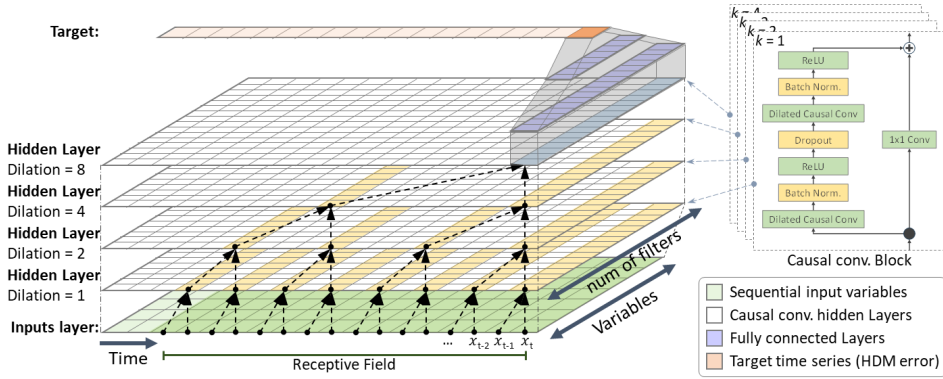


Figure 20. Internal structure of the DL model with $k = 4$, $fs = 2$, and $nf = 16$ for simplicity in display. The causal convolution blocks are shown on the right-hand side [from **Publication IV**].

Table 2 presents a summary of the DL model used and the selected hyperparameters. By employed $k = 5$ blocks of the causal convolutional unit with fs of 6 and nf of 32, the receptive field RF of the DL model is 156 time-steps (i.e., 6.5 days), accordingly:

$$RF = (fs - 1) \cdot (2^k - 1) + 1. \quad (28)$$

Table 2. Summary of the DL model and the chosen hyperparameters for training, with default values applied to the remaining parameters. C , T , and B represent dimensions of channel, time, and batch, respectively.

Layers	Output shape	Learnable parameters #	
Causal_conv_block ($k = 1$) $f_s: 6, n_f: 32$, and $d: 1$	$32(C) \times 1(T) \times 1(B)$	Weights: 7488 Bias: 64	Offset: 64 Scale: 64
Skip_conv1D $f_s: 6, n_f: 1$, and $d: 1$	$32(C) \times 1(T) \times 1(B)$	Weights: 224 Bias: 32	
Causal_conv_block ($k = 2 \sim 5$) $f_s: 6, n_f: 32$, and $d: 2^{k-1}$	$32(C) \times 1(T) \times 1(B)$	Weights: 49152 Bias: 256	Offset: 256 Scale: 256
Fully_connected_1	$32(C) \times 1(T) \times 1(B)$	Weights: 1024 Bias: 32	
Layer_normalization_1	$32(C) \times 1(T) \times 1(B)$	Offset: 32 Scale: 32	
Dropout (probability of 0.2)	$32(C) \times 1(T) \times 1(B)$	--	
Fully_connected_2	$16(C) \times 1(T) \times 1(B)$	Weights: 512 Bias: 32	
Layer_normalization_2	$16(C) \times 1(T) \times 1(B)$	Offset: 16 Scale: 16	
Fully_connected_out	$1(C) \times 1(T) \times 1(B)$	Weights: 16 Bias: 1	
Regression_output	$1(C) \times 1(T) \times 1(B)$	--	
Number of layers: 49	Number of epochs: 200		
Total learnable parameters: 59553	Loss function: 0.5MSE (default)		
Optimizer: Adam	Learning rate: 0.001		
mini-batch size: 4			

4.1.2 Spatio-temporal Input Variables

To reconstruct ε across the HDM domain, identifying relevant spatio-temporal input variables (x) is essential. For selecting the variables, following key factors must be considered: i) relevance to the physical processes, ii) predictive capability for generalizing to new data, especially within the spatial domain, iii) channel availability, iv) data dimensionality, and v) addressing concerns related to regularization and overfitting.

In this study, sixteen spatio-temporal variables are sourced to predict the HDM errors over time and space. The variables are listed in Table 3 and include oceanic and atmospheric parameters, as well as some computed variables, all of which are obtained from the Nemo Nordic or other data sources. Further details regarding the variables and their calculations are detailed in **Publication IV**.

Prior to being fed the variables into the model, they were normalized. This normalization process enhances stability and facilitates faster convergence during training, which is particularly important when utilizing the Adam optimizer. In addition, in the following Subsection, a feature selection process is employed to identify variables that have significant contribution to the reconstruction of the HDM errors. As mentioned above, to avoid spatial overfitting, this feature elimination process is essential. However, deep learning approaches can reduce the impact of unrelated input variables and enhance generalization through feature learning (Sun et al., 2020).

Table 3. List of the input variables used for feature selection.

	Variable	units	Sourced resolution		Dataset
			Temporal	Spatial	
1	Zonal wind (U_{wind})	m/s	Hourly	1 NM	Nemo-Nordic
2	Meridional wind (V_{wind})	m/s	Hourly	1 NM	Nemo-Nordic
3	Sea surface temperature (SST)	°C	Hourly	1 NM	Nemo-Nordic
4	Sea surface salinity (SSS)	psu	Hourly	1 NM	Nemo-Nordic
5	Ice fraction (Ice_frac)	%	Hourly	1 NM	Nemo-Nordic
6	Zonal wind stress (X_s)	Pa	Computed hourly at the HDM grid points		
7	Meridional wind stress (Y_s)	Pa	Computed hourly at the HDM grid points		
8	Ekman pumping (w_{Ekman})	m/s	Computed hourly at the HDM grid points		
9	Sea surface pressure (SLP)	Pa	3-hourly	5.5 km	CERRA ¹⁸
10	Precipitation water col. (η_p)	cm	Hourly	0.25°	ERA5 ¹⁹
11	Significant wave height (SWH)	m	Hourly	2 km	Baltic Sea Wave Hindcast ²⁰
12	Semi-diurnal tide (M2)	cm	Computed hourly at		FES2014 ²¹
13	Diurnal tides	cm	the HDM grid points		
14	Low tides	cm			
15	Steric height changes (η_s)	cm	Computed hourly at the HDM grid points from monthly observations at BY15 station ²²		
16	Sea level variability ($msdDT_{24}$)	cm	Computed hourly at the HDM grid points		

4.1.3 Feature Selection

To ensure the robustness of the DL model in predicting HDM errors, excluding irrelevant input features that could cause overfitting is essential. For this purpose, a wrapper-type sequential feature elimination algorithm is employed to systematically eliminate and sort variables through multiple iterations (Guyon and Elisseeff, 2003). The algorithm starts by training the model with the set of all variables and then progressively removes individual variables based on specific elimination criteria. The criterion is a combination of the $RMSE_\epsilon$ (cf. Equation 26) from both training and validation sets.

The iterations of the feature elimination process are illustrated in Figure 21, which started with ‘none’, indicating the inclusion of all variables (see Table 3). In the second iteration, the algorithm removed the ‘ice_frac’ variable due to its lack of contribution to the HDM errors reconstruction at various locations. Furthermore, the utilization of ‘ice_frac’ is observed to cause overfitting at the training locations, as evidenced by the decline in the performance of the DL model on the validation set. The iterations continue until all variables have been removed from the set of input variables.

The results of all feature elimination steps are shown in Figure 21 sequentially from left to right, where the x-axis indicating the variable that is removed. The blue and red lines correspond to the $RMSE_\epsilon$ values of the training set and validation set, respectively. This visual representation facilitates the detection of overfitting, evident when the RMSE of the training set exceeds that of the validation set. To mitigate the influence of random variations in the iterations, the training process is repeated five times, and the average RMSE was adopted as the elimination criterion. Dotted lines in the figure show one

¹⁸ <https://doi.org/10.24381/cds.622a565a> [accessed 7 August 2023]

¹⁹ <https://doi.org/10.24381/cds.adbb2d47> [accessed 7 August 2023]

²⁰ <https://doi.org/10.48670/moi-00014> [accessed 7 August 2023]

²¹ <https://www.avisio.altimetry.fr/> [accessed 7 August 2023]

²² <https://sharkweb.smhi.se/> [accessed 7 August 2023]

standard deviation for both the training and validation sets, derived from the five training repetitions.

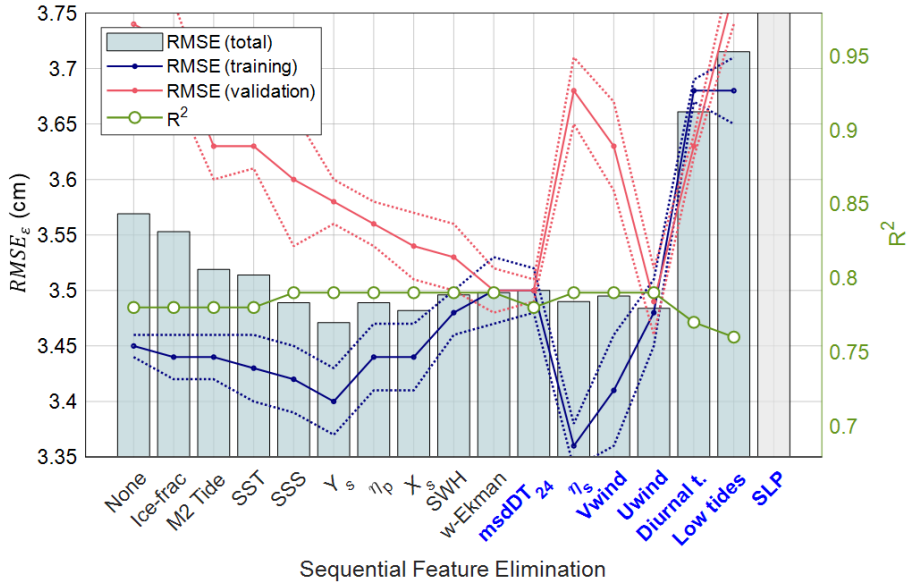


Figure 21. Sequential feature elimination for selecting optimal input variables. Variables are removed stepwise from left to right based on the elimination criterion. The solid blue and red lines are the average $RMSE_\epsilon$ resulting from five repeats of the training processes, with dotted lines representing one standard deviation from the average. The green line represents the R-Squared result of each elimination iteration. The variable set of the best solution is highlighted in blue font [from **Publication IV**].

According to Figure 21, the best set of variables includes: ‘msdDT₂₄’, ‘ η_s ’, ‘Uwind’, ‘Vwind’, ‘Diurnal tides’, ‘Low tides’, and ‘SLP’, where the $RMSE_\epsilon$ is 3.5 cm for both the training and validation sets and the R-Squared is 0.79. Note that additional new variables can be included in Table 3, and the feature elimination process can be repeated. While this approach is essential for training a spatially generalized DL model in this study, it could potentially lead to the exclusion of variables with localized effects or make the addition of localized variables more challenging.

4.1.4 Deep Learning Model Performance

The performance assessment of the DL model is conducted through the calculation of $RMSE_\epsilon$ and R-Squared values at all TG stations, including training, validation, and test sets. The structure of the DL model is outlined in Subsection 4.1.1, and the model is trained using the selected variables (as described in Subsection 4.1.3) on 16 training stations highlighted in blue in Figure 22a.

Figure 22b demonstrates the performance of predicted HDM errors based on Equations (26) and (27). The mean $RMSE_\epsilon$ and R-Squared values are 3.4 cm and 0.79, respectively. The training set shows a performance of 3.2 cm and 0.82, while the combination of validation and test set demonstrates a performance of 3.5 cm and 0.77. Evident patterns of significant $RMSE_\epsilon$ values are noticeable at some regions, such as the Gulf of Riga and Southwest of the Baltic Sea. These patterns may indicate issues with the DL model (e.g., the need for additional variables and the requirement to optimize

hyperparameters), TG problems (e.g., errors, vertical datum shifts over time, and the TG location compared to HDM data points; as TGs are utilized as truth values for evaluating DL model performance), and/or localized HDM errors that might not be considered during the generalization.

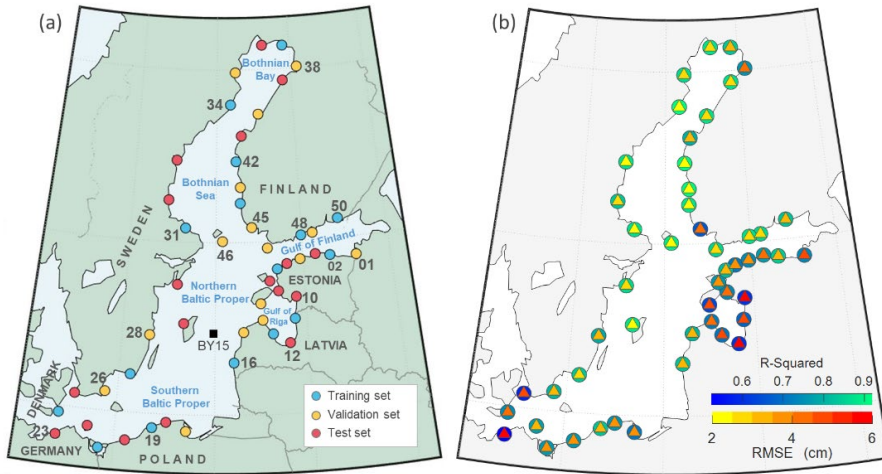


Figure 22. DL model performance. a) Location of tide gauge stations utilized in this study and their division into training, validation, and test sets. b) Performance of HDM error prediction at the tide gauge stations. Triangles and circles represent RMSE and R-Squared values, respectively, using separate colourbar [Modified from **Publication IV**].

The residuals between the target and predicted HDM errors (see Figure 23) imply that the DL model and input variables do not effectively address the high-frequency components (Daily and shorter periods) of the HDM errors. Hence, the significant $RMSE_{\varepsilon}$ values in specific regions indicate that the remaining HDM errors could be attributed to localized high-frequency events, such as resonance and seiche. Not only are these events not simulated by HDM modeling, but they also pose a challenge for the DL model to accurately predict the corresponding errors using input variables.

For instance, at station 10, resonance with the barotropic 5-hour seiche period of the Gulf of Riga can lead to amplitude growth in Pärnu Bay (Suursaar et al., 2002). In addition, the bathymetry and unique geometry of the Gulf of Riga (particularly at its main entrance Irbe Strait) induce distinct oscillations within this basin (Jönsson et al., 2008). These localized high-frequency oscillations degrade the performance of the DL model during the process of generalization. Similarly for station 23 in Eckernförde Bay, seiche-like oscillations strongly influence DT variations (Friedrichs et al., 1995) and cause challenges for predicting HDM errors. Station 45 is situated in an archipelago area; therefore, the HDM may have localized issues there that the generalized DL model for the entire Baltic Sea is not able to predict.

Figure 23 also presents the time series of actual and predicted HDM errors, along with their residuals and corresponding FFT for three sample stations 10, 26, and 31. At station 10, the HDM errors vary from -40 to 40 cm, while the residuals (i.e., remaining errors after HDM correction) range from -20 to 20 . This pattern of HDM errors being reduced by a factor of at least two is replicated in other stations. Note that the DL model effectively estimates low-frequency HDM errors, such as annual and seasonal cycles. Nonetheless, additional efforts are needed to address high-frequency errors.

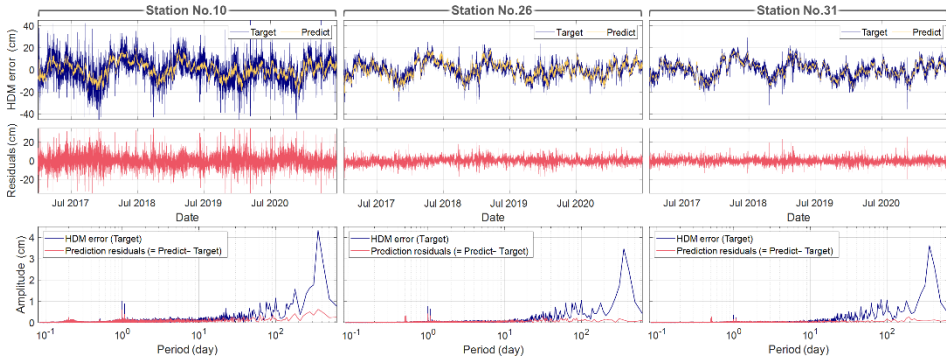


Figure 23. Time series of the actual (ε) and predicted HDM errors ($\hat{\varepsilon}$) at three sample stations (10, 26, and 31) in top row, residuals are in middle row, and the FFT of actual HDM errors and residuals in the bottom row [from **Publication IV**].

4.2 Vertical Reference Bias

The vertical Reference bias ($RefBias$) is the height difference between the potential surface (W_0) of the HDMS' reference surface and a particular geoid model. The determination of $RefBias$ allows for the adjustment of a HDM's zero level to a well-defined geodetic reference. Consequently, a direct comparison between modeled and observed DTs is facilitated in terms of absolute values. Additionally, the use of a common reference datum enables the systematic combination of various sources of sea level with a consistent physical definition.

The $RefBias$ can accurately be computed by taking the spatial median of the remaining bias, referred to as $Bias_{CHDM}$, between the corrected HDM and observed DT, as follows:

$$RefBias = spatialMedian(Bias_{CHDM}(\varphi, \lambda)). \quad (29)$$

Figure 24a shows histograms of the differences between the original/corrected HDM and TG records. The results indicate that the HDM correction not only successfully reduced the standard deviation of the HDM errors but also aligned the remaining errors after the HDM correction to a normal distribution. Therefore, the $Bias_{CHDM}$ determined both from TG stations and SA data points is represented in the Figure 24b histograms.

The $Bias_{CHDM}$ should ideally remain constant since both modeled and observed DT are referenced to the equipotential surface of the Earth. However, it is apparent that $Bias_{CHDM}$ values vary from 5 to 25 cm in the SA data points and from 13 to 21 cm in the TG stations. This variation arises from errors in several factors such as TG zero marks, geoid model, and near-coast SA measurements. Therefore, the $RefBias$ of the Nemo-Nordic model relative to TG and SA datasets is obtained as 16.2 ± 1.6 cm and 18.1 ± 2.9 cm, respectively. SA dataset offers a more robust estimation of the $RefBias$ due to its extensive spatial coverage compared to the TG stations. The $RefBias$ can be improved in accuracy by removing problematic areas from the analysis, resulting in a bias of 18.3 ± 1.9 cm.

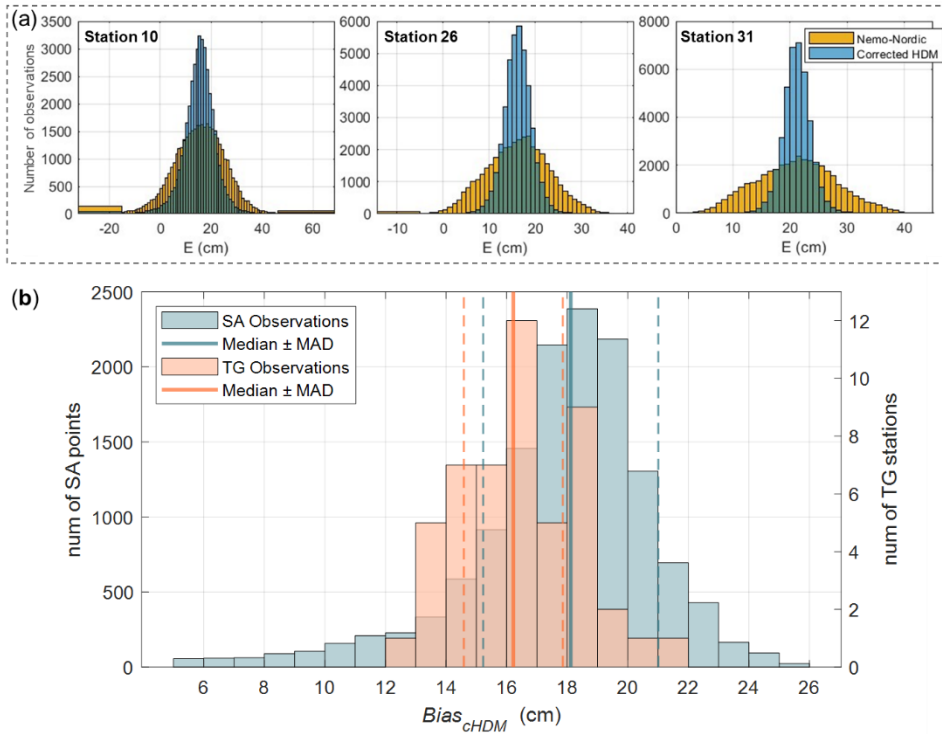


Figure 24. Bias between HDM and observations. a) Histogram of the difference between original/corrected HDM and TG measurements. b) Histogram of the $Bias_{CHDM}$ with respect to the TG and SA data [Modified from **Publication IV**].

4.3 Comparative Assessment

The correction and vertical referencing of the HDM are implemented as shown in Figure 19, aiming to calculate instantaneous absolute DT. A comparison of the instantaneous DT before and after the correction is presented in Figure 25 for a certain time instant (e.g., 18 August 2019, 10:00). In this figure, the original HDM is reduced by the *RefBias* to visualize solely the improvements resulting from the application of the ML-based correction to the HDM. The HDM error (ϵ) in this figure illustrates the values and pattern of the HDM correction for the corresponding time instant, with range of from 5 to 16 cm. The range and pattern of the HDM error vary over the course of time.

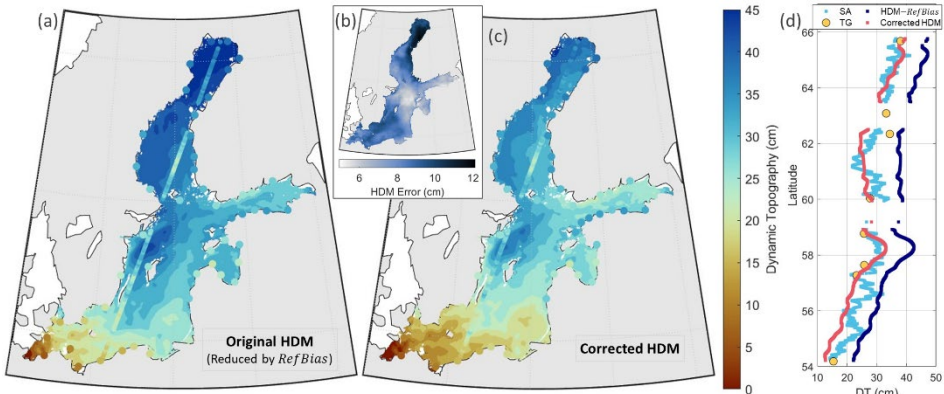


Figure 25. A sample time instant of HDM correction for 18-Aug-2019, at 10:00. a) original Nemo-Nordic model reduced by Ref Bias, along with TG readings and SA measurement (pass No. 272 and cycle No. 48) at the corresponding time instant, b) predicted HDM error based on Equation (23), c) the corrected HDM, and d) along the SA track comparison between modelled and observed DTs [Modified from **Publication IV**].

Figure 25d shows the differences between the original/corrected HDM along the SA track and observed DT measured by SA and nearby TGs. In this example, two significant discrepancies are observed between the corrected HDM and SA data, in the southern Baltic Sea (latitude 54° to 57°) and the Bothnian Sea (latitude 60° to 62°). Further investigations are required to provide a precise explanation for the former. However, it can more likely be imputed to an issue with the geoid model. The latter is due to deficiencies in the geoid model in this area. (Jahanmard et al., 2022a and 2023b; Varbla and Ellmann, 2023; Mostafavi et al., 2023). It can be inferred that such an enormous DT variation in the limited area is not realistic; and since these variations can be observed constantly over the SA cycles, the discrepancies can be attributed to the geoid model (see also Figure 15, Figure 16, and Figure 26).

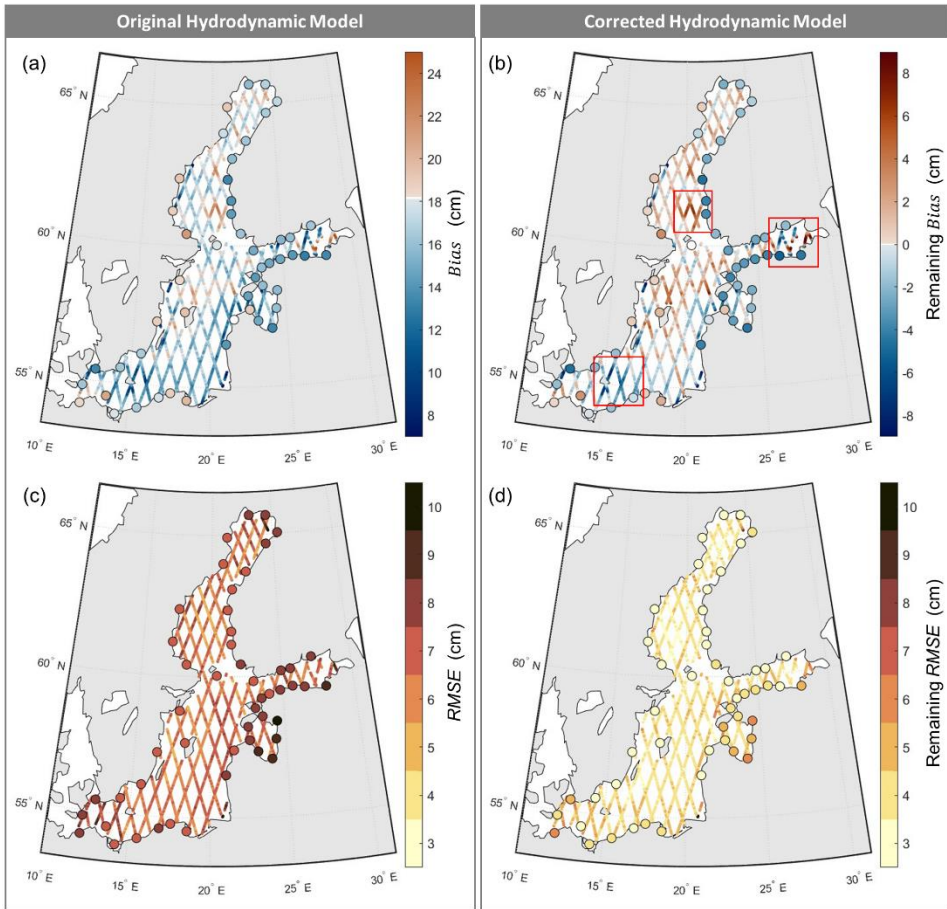


Figure 26. Spatial distribution of the a) Bias of the original HDM, b) Bias of the corrected HDM, c) RMSE of the original HDM, and d) RMSE of the corrected HDM [from **Publication IV**].

The *Bias* and *RMSE* of the differences between the original/corrected HDM and observations are presented in Figure 26. Both *Bias* and *RMSE* demonstrate a significant improvement in the corrected HDM. The *Bias* of corrected HDM (similar to Figure 16) reveals the problematic areas where inconsistencies are evident among various data sources. Three significant problematic areas are marked, the associated reasons and sources of errors were discussed above and Subsection 3.3. The spatial distribution of the *RMSE* before and after applying HDM correction (shown in Figure 26c and d) demonstrates the performance of the DL model in post-processing the HDM-derived DT. The spatial average of the *RMSE* for the original HDM is 7.6 cm and 6.5 cm with respect to TGs and SA data points, respectively. While these values for the corrected HDM are, respectively, 3.4 cm and 4.1 cm, which indicates a significant improvement in the modelled DT. However, more effort is still needed to address high-frequency errors, particularly in the Gulf of Riga. Moreover, the corrected HDM exhibits an average increase in the correlation coefficient compared to the TG records, rising from 0.93 to 0.98.

Figure 26b also displays the spatial distribution of the *Bias* between the TG records and corrected HDM, which indicates the shift between TG zero-mark relative to the HDM's reference surface. It is observed that the *Biases* along the coastlines of Finland

and Estonia are negative, while they are almost always positive along the Swedish coastline. This indicates that there could be a tilt from west to east between TG zero marks and HDM's reference surface. Moreover, the spike variations observed in the *Bias*, which do not align with neighbouring stations, indicate the presence of a vertical datum shift in those stations, such as stations with IDs 22, 25, 31, and also TG stations 42 to 44.

Figure 27 illustrates the spatial variations of the monthly mean of the HDM errors for the period from January 2017 to June 2021. This figure implies that a seasonal variation was not considered in the original model. The monthly mean error reaches its highest positive values during Spring (March, April, and May) and its lowest, negative values during Autumn (September, October, and November). The seasonal variation of the HDM errors may arise from a combination of factors, including the seasonal changes in wind patterns, freshwater runoff and ice melting, and steric effect.

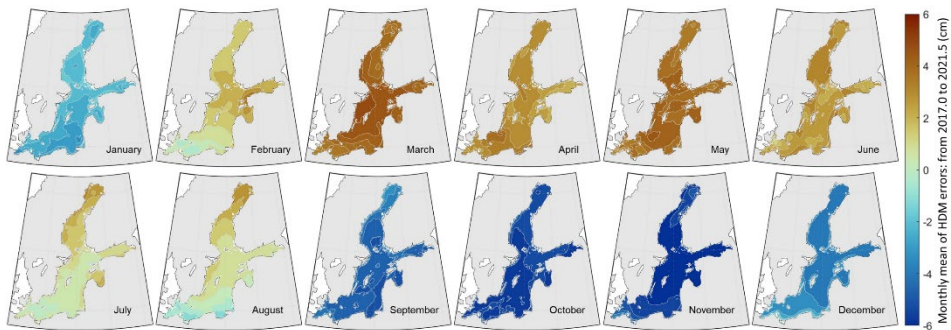


Figure 27. Monthly mean of the HDM errors (ϵ) for the period from January 2017 to June 2021.

5 Airborne LiDAR Measurements

The unique horizontal resolution of the ALS dataset allows for the retrieval of a broadband of spatial scales of sea surface processes. However, unlike SA measurements, which are regularly collected at a fixed repeat cycle, this measurement technique can only provide a snapshot of the sea surface topography at a specific time instant. Hence, although the ALS technique cannot consistently capture long-term sea surface variability or be available at all desired times, it can serve as a valuable observation method for gaining insights into high-frequency processes in both near-shore and offshore areas. Furthermore, ALS observations can serve as an additional data source for investigating problematic regions through conducting of ALS surveys over marine areas.

This section aims to demonstrate (i) the potential use of ALS observations for validating corrected HDM-derived DT and (ii) the utilization of ALS point clouds to determine the sea state parameters and directional power spectral density of wind waves. To compare ALS point cloud data with HDM data, the first step is transforming the ALS-derived SSH into DT using the geoid model, as follows:

$$DT_{ALS} = SSH_{ALS} - N. \quad (30)$$

To eliminate high-frequency sea surface fluctuations from DT, a low-pass filter is applied. In this study, a wavelet filter was applied to separate the high-frequency wind waves that are not considered in the HDM computations. Note that the HDM has a horizontal resolution of one nautical mile, meaning it can accurately depict only features larger than 5 NM (i.e., 9.26 km). Figure 28a illustrates a comparison between DTs derived from ALS and original/corrected HDM along the flight track at the observation epoch (i.e., 10 May 2018, at 9:30). Since the flight direction changed in the middle of the track, this figure presents the first 21 km of the track, during which the flight azimuth was 71.2°. The comparison indicates that the ALS observations validate the corrected HDM. Nevertheless, the HDM offers a smoother surface compared to the ALS results, which can be due to the HDM's lower spatial and temporal resolutions.

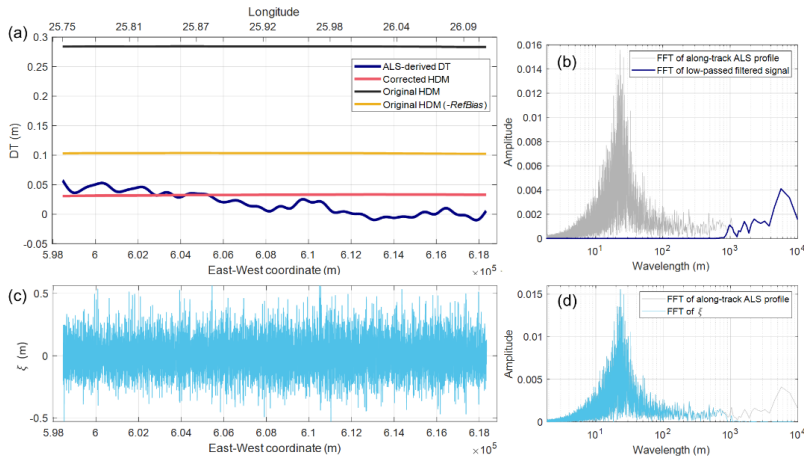


Figure 28. Decomposing ALS data and comparing with HDM. a) DT derived from ALS and original/corrected HDM along the flight track observation epoch 10 May 2018, at 9:30. b) FFT of the ALS profile along the track, along with the low-pass filtered signal (shown in panel a). c) High-frequency signal recorded by ALS, which indicates the wind-generated wave fluctuations, and its FFT in panel (d).

Figure 28b displays the FFT of the ALS profile before (grey line) and after (dark blue) applying the wavelet filter, which eliminates fluctuations with wavelengths less than 1 km. The residual between the ALS profile and filtered signal reveals wind-generated waves, which is shown in Figure 28c and will be discussed in Subsection 5.1.

Figure 29 overlays sea surface topography from the ALS campaign and the corrected HDM to reveal discrepancies. Note that the HDM surface is inherently smoother than ALS observations due to its limitations in spatial and temporal resolution. Therefore, the corrected HDM exhibits good agreement with ALS observations, yielding an RMSE of 1.8 cm. To calculate the RMSE between the HDM and ALS point cloud, the corrected HDM data were extracted at the coordinates of ALS data points using bilinear interpolation in space and linear interpolation in time.

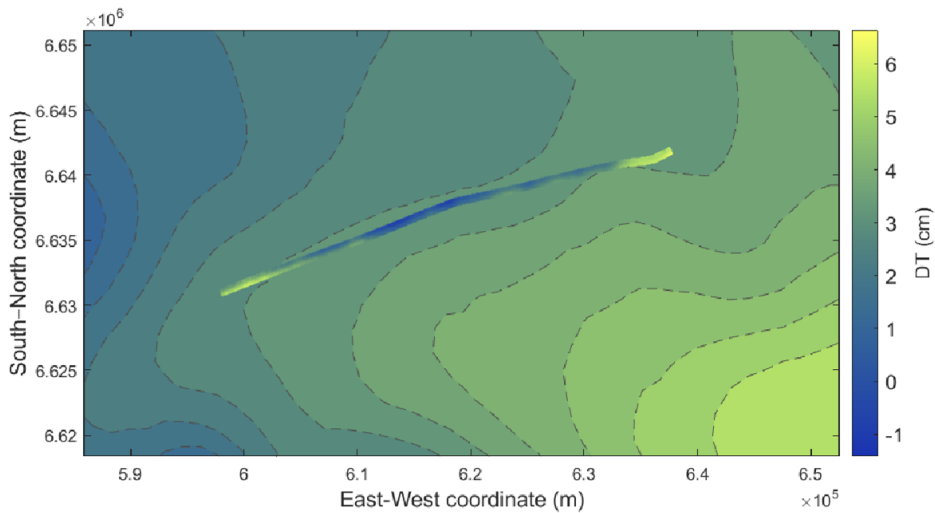


Figure 29. Overlay of DTs from the ALS point cloud and the corrected HDM at the observation epoch, in L-EST97 coordinate system.

5.1 Directional Wave Spectrum²³

High-resolution ALS data acquisition (1×1 m) enables the determination of the wavenumber spectrum, defining wave propagation direction and wavelength (Hwang et al., 1998; Walsh et al., 1985). This section introduces the retrieval of directional wave spectra from the ALS point cloud as a potential source of wind wave observations over a wide area (please see **Publication III** for mere details).

Figure 30 displays the steps and flowchart for obtaining directional wave spectra and wave parameters from airborne LiDAR point cloud. For this purpose, the ALS data are segmented into limited areas (1×1 km) to compute the directional wavenumber spectrum since wave direction may change due to variations in wind regime and water depth. As a scale of 10 km and 30 min or longer may be desirable for considering homogeneous (i.e., spatial invariance) and stationary (i.e., temporal invariance) wave processes for field observations, the statistical stability of the computed wave spectra

²³ The symbols used in this section are not included in the table of Symbols to avoid the use of non-conventional symbols in wave theory and potential symbol-conflict with other sections.

should be examined. Moreover, in this study, rather than using 2D FFT, 1D periodograms of wave records are determined in various directions. This approach enables the examination of the statistical stability of wave spectra for each direction, especially when the record lengths vary due to the ALS limited data corridor width. Therefore, the wave record $\xi(x)$ (similar to Figure 28c) are extracted for 12 azimuthal directions, from 0° to 165° with a 15° step.

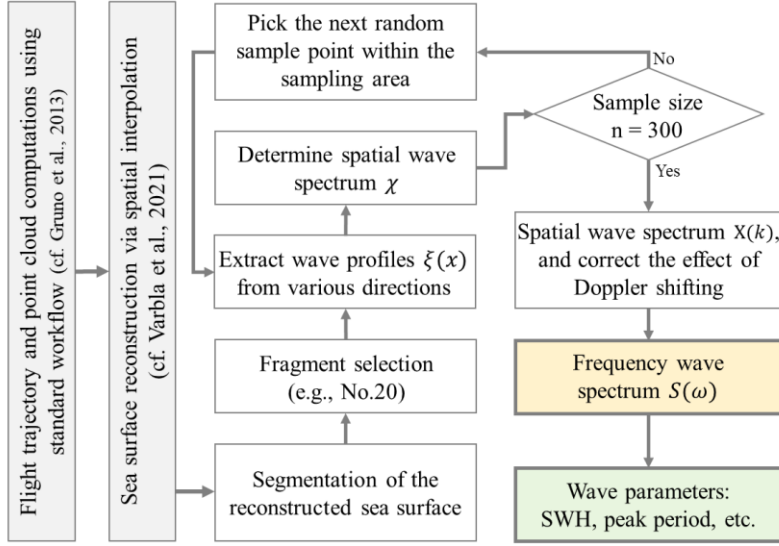


Figure 30. Flowchart of the retrieval of directional wave spectra from the ALS point cloud [Modified from **Publication III**].

Therefore, the wavenumber power spectral density of a stationary process is computed by averaging 1D periodograms for each direction of interest (Bartlett, 1948; Welch, 1967). For this purpose, the discrete Fourier transform Y_m of the wave records $\xi(x)$ is determined as follows:

$$Y_m = \sum_{n=1}^N \xi_n e^{-ik_m n \delta x} \delta x = \delta x \sum_{n=1}^N \xi_n e^{-\frac{2\pi i m n}{N}}, \quad (31)$$

where N is the number of samples with sampling interval of δx , and k is the wavenumber vector with a size of m :

$$k_m = \frac{2\pi i m}{N \delta x}, \quad m = 1, 2, \dots, N. \quad (32)$$

As a result, the one-sided wavenumber power spatial density χ_θ of wave record $\xi(x)$ for a selected direction θ is determined as follows:

$$\chi_\theta(k) = \frac{2}{2\pi N \delta x} |Y_m|^2, \quad (33)$$

Before applying Equation (31), using a cosine taper data window is beneficial for mitigating discontinuities at the two endpoints of the records (Liu and Frigaard, 1999). In addition, to maintain consistent wavenumber resolution across different directions,

zero padding was applied to both ends of the wave profiles. Eventually, the directional wavenumber power spectral density function X is obtained as follows:

$$X(k, \theta) = \frac{1}{s} \sum_{i=1}^s \chi_{\theta_i}(k), \quad (34)$$

where s represents the number of samples required to satisfy the statistical stability of the wave spectral density. In this regard, a random sampling is used to produce parallel wave spectra for each direction. To determine the required number of samples, an experiment was conducted to assess the statistical stability of $X(k, \theta)$ for various sample sizes. This experiment was repeated $R = 100$ times for s values from 1 to 1000, and for each s , the standard error SE of the spectrum's peaks $X(k_p)$ as a criterion of the statistical stability is determined as follows:

$$SE = \sqrt{\frac{\sum_{i=1}^R (X_i(k_p, \theta) - \mu)^2}{R}}, \quad (35)$$

where μ is the mean of R repetitions of the experiment. Figure 31 shows the results of this experiment for direction 75° as an example. By considering all directions, a sample size of 300 was deemed suitable for the current study.

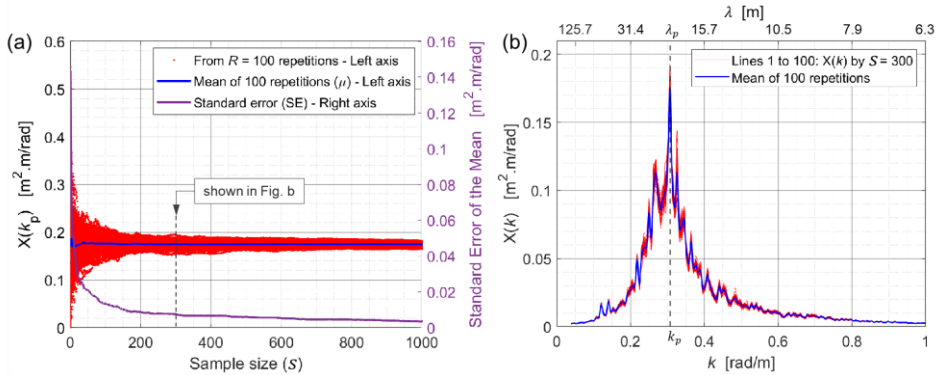


Figure 31. Statistical stability of the wave spectral density. a) Standard errors (Equation 35) against various sample sizes for a selected fragment and wave direction 75° . b) Wavenumber spectra corresponding to the sample size of 300 [from **Publication III**].

Because the measurements have been taken on a moving platform, the wavenumber spectra are calculated using the encountered wavenumber (k_e). Therefore, the Doppler effect can introduce a shift between the computed and true wavenumber (Δk). Hence, the wavenumber should be adjusted according to the aircraft's speed (v_a) and the angle of difference between the flight direction and the wave spectrum (α) as follows (Walsh et al., 1985):

$$\Delta k = \frac{\sqrt{g \cdot \tanh(kd/k)}}{v_a \cdot \cos(\alpha)}, \text{ and } \Delta k = k_e - k, \quad (36)$$

where d represents water depth, which is approximately 70 m in the study area, and g is the acceleration of gravity. The aircraft's speed was ca. 62 m/s, and the flight azimuth was 71.5° , which changed slightly along the flight track.

To determine frequency wave spectra $S(\omega)$ from Equation (34), one can employ the dispersion relation, which defines the relationship between wave frequency ω and wavenumber k :

$$\omega = \sqrt{kg \cdot \tanh(kd)}. \quad (37)$$

The frequency spectrum represents the distribution of wave energy over frequency at a fixed location, while the wavenumber spectrum represents this distribution over wavenumber or wavelength. Since wave frequencies propagate at different speeds, the dispersion relation links the wavenumber spectrum and frequency spectrum. As a result, the frequency spectrum can be determined as follows:

$$S(\omega, \theta) = X(k(\omega), \theta) \cdot \frac{dk(\omega)}{d\omega}. \quad (38)$$

Therefore, calculating the wavenumber power spectral density for 12 directions from each segment of the ALS point cloud (Equation 34) enables the determination of directional frequency power spectral density, as illustrated in Figure 32. The peak of wave energy is observed at $\theta_d = 72^\circ$, representing the dominant wave direction. This direction almost agrees with measurements from a nearby buoy²⁴ (approximately 40 km from the ALS profile) and the WAM model²⁵, which recorded dominant directions of 86.5° and 82.5° , respectively. Also, the ALS-derived peak period ($T_p = 2\pi/\omega_p$) is 3.63 s, compared to 3.65 s measured by the buoy and 3.56 s by the model.

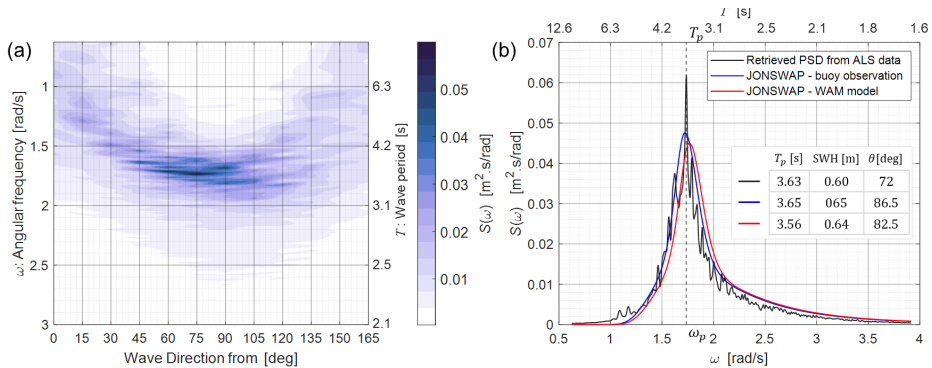


Figure 32. Frequency wave spectrum for a segment in the middle of the ALS track: a) in different direction, b) in the dominant direction. The power spectral density derived from the ALS point cloud, the buoy, and the WAM model is compared in panel (b) [Modified from **Publication III**].

In Figure 32b, the wave spectrum of the dominant wave direction retrieved from the ALS data is compared with the JONSWAP standard wave spectrum related to the sea state measured by the buoy and WAM model. This comparison demonstrates a good agreement among the various techniques used for measuring the sea state. Moreover, the significant wave height of the ALS measurement can theoretically be defined based on the zero moment (m_0), which represents the area under the spectral curve, using the formula $SWH = 4\sqrt{m_0}$. Thus, it is evident that there is also a good agreement among

²⁴ Suomenlahti wave buoy, obtained from: <https://ilmatiiteenlaitos.fi> [accessed 7 August 2023]

²⁵ <https://doi.org/10.48670/moi-00014> [accessed 7 August 2023]

data sources in terms of SWH , with a value of 0.6 m for ALS data, compared to 0.65 m for the buoy and 0.64 m for the model. Also, the peak period (T_p) derived from ALS point cloud is 3.63 s, compared to 3.65, and 3.56 s for the buoy, and WAM model, respectively.

The wavelength corresponding to the peak period, as derived from Equation (34), is 20.55 meters. This value represents deep water conditions for the sea state by considering a depth of 70 m. Therefore, the dominant wave directions and wavelengths of each ALS point cloud fragment are computed and illustrated in Figure 31. The computed wavelengths vary between 17.9 and 25.1 m (which is 21.3 m on average) along the trajectory, decreasing towards the eastern direction.

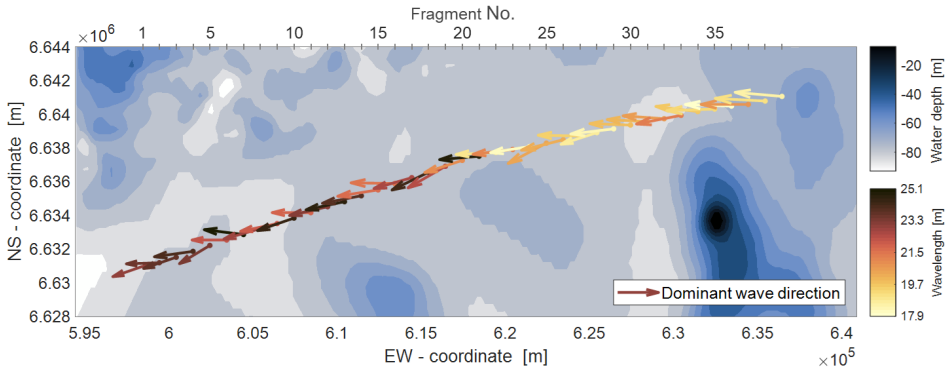


Figure 33. Dominant wave directions and wavelengths derived from ALS point cloud along the flight trajectory. The background contour represents the bathymetry obtained from GEBCO_2020 [Modified from **Publication III**].

Besides, a comparison of wave parameters derived from the LiDAR-based method and WAM model is illustrated in Figure 34. The model has a temporal resolution of hourly data and a spatial resolution of one nautical mile. For comparing two datasets, the WAM model obtained the coordinates of the fragments' centres at ALS flight time (i.e., 9:35 UTC) via bilinear interpolation in space and linear interpolation in time. This figure shows that the wave parameters derived from ALS data are supported by the modelled estimations along the flight trajectory. The mean and standard deviation of differences are a) 0.2 and 0.1 s for the peak period, b) -0.09 m and 0.03 m for the SWH , and c) -0.5° and 10.0° for dominant wave direction, respectively. Note that the WAM model produces smoother results, which could be attributed to limitations in the model's resolution and the wind model used to force the wave model. Additionally, ALS-derived parameters are based on instantaneous observations and the results are sensitive to local conditions.

The modelled parameters are also compared with the buoy data at the location of the buoy for a duration of 24 hours, as shown in the figure. This comparison shows the performance of the model relative to buoy observations with a mean and standard deviation of -0.1 and 0.23 s for the peak period, -0.12 and 0.05 m for the SWH , and 10.0° and 7.4° for the wave direction, respectively.

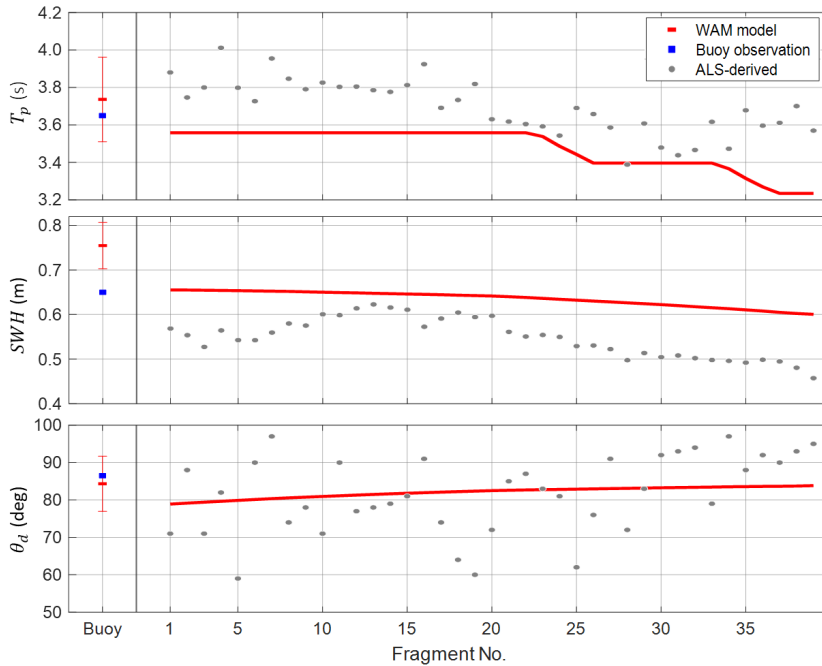


Figure 34. Comparing wave parameters peak period (top row), significant wave height (middle row), and wave direction (bottom row) derived from ALS point cloud and the WAM model. Comparison between the model and buoy observations for a period of 24 hours are also demonstrated [Modified from **Publication III**].

The results show that the possibility of retrieving directional power spectral density and wave parameters from ALS point cloud. For this purpose, the wavenumber spectra are computed from 12 directions using the periodogram method and a random sampling approach to satisfy the statistical stability of the spectra. Compared to the previous studies (e.g., Hwang et al., 2000a and b), this study introduces a method for retrieving the directional wave spectrum for each small ALS data fragment (i.e., 1×1 km), regardless of the angle between the dominant wave and flight directions, in a stand-alone manner.

Although ALS technology may be somewhat expensive compared to some alternative sensors, such as wave buoys, pressure sensors, and satellites, it provides the capability to capture 3D point cloud data from the spatial wave field. This capability offers a deeper insight and a better understanding of surface ocean waves, which is essential in the context of our changing climate and advancements in marine engineering and shipping.

6 Discussion and Concluding Remarks

6.1 Summary of Results

The vertical reference unification between the hydrodynamic models (HDMs) and observations facilitates the accurate and comprehensive determination of absolute dynamic topography by integrating diverse data sources. This unification has the potential to enhance the effectiveness of data assimilation for accurate sea level forecasting. Moreover, accurate and consistent sea level data are always important for understanding ocean weather and supporting applications like marine engineering, coastal management, optimal route planning based on under-keel clearance criteria in shallow waters, and autonomous shipping navigation.

In this dissertation, Section 1 reviewed various approaches and considerations for deriving dynamic topography (DT). Section 2 reviewed the study area and datasets used in this study. Among the different sea level data sources, HDMs are distinguished by their high spatial and temporal resolutions. However, they often lack a well-defined vertical reference datum, which hinders direct combination with other sea level data sources. In addition, HDMs are prone to modelling errors due to numerical limitations. Therefore, vertical referencing HDM and combining observed and modelled DT within a unified vertical reference system can enhance modelling and forecasting capabilities. However, modelling errors hinder the accurate determination of vertical reference in HDM. Conversely, the absence of a common vertical reference system between HDM and observations poses challenges in effectively identifying and rectifying modelling errors.

This study presented two approaches for correcting and vertical referencing of HDMs in Sections 3 and 4. In both approaches, a geoid surface is employed as an intermediate vertical reference datum. Since the geoid is an equipotential surface of Earth's gravity field, hence a physically meaningful reference surface for the determination of sea level, which can also be used seamlessly from land to offshore. In the geodetic applications, geoid surfaces are modelled by using gravity data. HDMs inherently utilize a similar concept for their reference surface, with simulated sea levels being relative to a geopotential reference surface. Therefore, utilizing high-resolution geoid models as a common reference surface for both observations and modelled sea level data is beneficial in establishing an integrated measurement system.

Section 3 discussed **Method I** used to correct HDM through a dense network of geoid-referenced TG records. In this approach, TG readings were considered as ground-truth and the HDM bias was determined in the location of TG stations. Then, the biases were propagated from stations into HDM grid points using interpolation techniques. This method is practical when dense network of TG stations is accurately in a common geoid-based chart datum. Additionally, because the model is directly corrected by the TGs, any errors in the TG records or zero marks can propagate into the corrected HDM. However, the corrected HDM demonstrates a good agreement with SA measurements. Furthermore, the method enabled the identification of inconsistencies between data sources and problematic areas, which can be explored in further research to improve the models used in this comparative assessment.

Certain shortfalls of **Method I** became the motivation to develop **Method II** using machine learning strategies, which were presented in Section 4. For this purpose, a multivariate deep neural network was introduced to predict HDM modelling errors, followed by an adjustment of HDM's reference surface using SA observations. Input

variables for predicting HDM errors were chosen using a wrapper feature selection method, and these selected inputs ($'msdDT_{24}'$, $'\eta_s'$, $'Uwind'$, $'Vwind'$, $'Diurnal\ tides'$, $'Low\ tides'$, and $'SLP'$) were generalized for the entire Baltic Sea. However, localized high-frequency HDM errors still require attention.

The DL model accurately predicted HDM modelling errors with RMSEs of 3.2 cm (R-Squared: 0.82) for the training set and 3.5 cm (R-squared: 0.77) for the test set. Nevertheless, addressing remaining HDM errors in specific areas, such as the Gulf of Riga and the entrance of the Baltic Sea, requires further efforts. Once the HDM was corrected by predicted HDM errors, the vertical reference bias of the HDM relative to the geoid model was determined as 18.3 ± 1.9 cm using SA measurements by excluding problematic areas.

Therefore, the instantaneous absolute DT was determined through a DL-based HDM correction and SA measurements. The corrected HDM presents a notable improvement relative to TG readings with an RMSE of 3.4 cm and a correlation coefficient of 0.98, in contrast to the original HDM, which had an RMSE of 7.6 cm and a correlation coefficient of 0.93. The RMSE of the corrected HDM in offshore was examined by SA measurement, which exhibited an improvement on average from 6.5 cm to 4.1 over the entire Baltic Sea. Moreover, the comparative assessment highlighted problematic areas, such as the eastern part of the Gulf of Finland, the Bothnian Sea, and southwest of the Baltic Sea (Bornholm), as well as possible vertical datum shifts between the network of the TG stations.

This study developed a methodology to correct instantaneous dynamic topography derived from the HDM with respect to the common vertical datum in the Baltic Sea region. The method also involved the unification of the reference surface among various sea level data sources, which enabled us to compare modelled and observed sea level data in terms of dynamic topography across time and space. Therefore, quantifying the accuracy and bias of the corrected instantaneous dynamic topography also allowed us to identify inconsistencies between datasets and problematic areas for further investigations. The presented methodology can be adopted in other marine areas worldwide to harmonize sea level measurements from different sources and approaches and achieve an appropriate level of accuracy in datasets.

6.2 Key Conclusions Presented for Defence

- All used diverse sea level datasets were transferred to a common vertical reference surface with consistent physical meaning (geoid: equipotential surface of Earth's gravity field), zero reference level (NAP), reference epoch (2000.0), and permanent tide system (mean-tide system).
- Two methods were developed to correct HDM-derived instantaneous sea level:
 - i) employing a dense network of geoid-referenced TGs, in which model discrepancies from observations are propagated spatially via conventional interpolation methods;
 - and ii) utilizing a DL model to investigate HDM modelling errors without considering vertical reference bias, thereafter, addressing the *RefBias* by SA data and a geoid model.

Method I:

- The method demonstrated that using a network of geoid-referenced TG records allows for a direct evaluation of the HDM-derived DT based on TG readings. It is also possible to spatially interpolate the discrepancies from stations to offshore areas when a close loop of TGs with limited distances is available.
- Based on a frequency analysis, it was observed that the HDM bias varies temporally with both high- and low-frequency components, along with spatial variations. Hence, to achieve uncertainties less than 5 cm across the Baltic Sea region, bias correction with a maximum window length of 6 hours is necessary.
- The corrected HDM demonstrates an average RMSE of 2.5 cm compared to TG records and a zero-bias agreement with SA data and RMSE of 2.4 cm for period of form January 2017 to June 2019.

Method II:

- The DL model accurately predicted HDM errors with RMSEs of 3.2 cm (R-squared: 0.82) for the training set and 3.5 cm (R-squared: 0.77) for the test set. Nevertheless, addressing remaining HDM errors in specific areas, such as the Gulf of Riga and the entrance of the Baltic Sea, requires further efforts.
- The vertical reference bias (*RefBias*) of the HDM relative to the NKG2015 geoid model was determined to be 18.1 ± 2.9 cm using SA measurements. This bias can be refined for accuracy by excluding problematic areas, resulting in a bias of 18.3 ± 1.9 cm.
- In contrast to the original HDM, which had an RMSE of 7.6 cm and a correlation coefficient of 0.93, the corrected HDM presents a notable improvement relative to TG readings with an RMSE of 3.4 cm and a correlation coefficient of 0.98. The RMSE of the corrected HDM in offshore was examined by SA measurements, which exhibited an improvement on average from 6.5 cm to 4.1 over the entire Baltic Sea.
- The corrected HDM reveals vertical datum shifts between the network of TG stations and highlights that the TG benchmarks at Latvian, Estonian, and Finnish stations are below the reference surface of the HDM.
- A comparative assessment in both methods identified problematic areas, including the eastern part of the Gulf of Finland, the Bothnian Sea, and the southwest of the Baltic Sea (Bornholm). These issues were attributed to the accuracy of the geoid model in the marine area, where the geoid model quality is questionable due to marine gravity data voids.
- Airborne LiDAR point cloud can serve as an additional observation data source for investigating problematic regions.
- The corrected HDM was also compared with the ALS point cloud at a specific time and location in the Gulf of Finland, revealing a strong agreement with an RMSE of 1.8 cm.
- The ALS point cloud data demonstrated the potential to observe sea state and retrieve directional wind wave spectra. This technique provides an observational approach to capture the spatial wave field, offering a deeper insight and a better understanding of surface ocean waves.

6.3 Recommendations for Further Research

Future research can explore various aspects of this study, including enhancing the performance of the DL model, investigating problematic areas to mitigate sources of errors, studying land/sea datum unification by comparing mean dynamic topography from both geodetic and oceanographic approaches, examining the circulation system of the Baltic Sea through the corrected HDM, and exploring applications such as accurate spatio-temporal sea level nowcasting and forecasting, as well as determining near-real-time under-keel clearance in navigation. The DL model performance has the potential to improve by collaborating with model developers and acquiring a better knowledge of the physical model outputs. In addition, including feature learning from spatial dimensions can improve the DL model performance. The DL model can also be employed in real-time alongside the hydrodynamic model to post-process the physical ocean model output, correcting the modelled dynamic topography using observed sea levels, and providing feedback to refine the physical ocean model.

Moreover, research can be conducted on the corrected HDM to investigate the circulation of the Baltic Sea in shorter time periods, such as seasonal circulations. The DL model has shown potential to reduce modelling errors of instantaneous DT with respect to observations with a high level of accuracy. The corrected DT can also reveal variations in other ocean parameters within the Baltic Sea, such as temperature and salinity. This can be particularly insightful at the entrance of the Baltic Sea, where saline water inputs from the North Sea interface with the freshwater inputs from the north and east of the Baltic Sea.

The study area utilized in this research was equipped with a favourable data set, with an essential component being the existence of a dense network of TGs around the Baltic Sea. In many marine areas, where such a dense network of TGs doesn't exist, which may make the implementation of the methods described challenging. A possible solution that can be explored is an adaption of the present methods. Instead of the TGs acting as the 'ground truth', it may be possible to utilize multi-mission SA with TG data in machine learning strategies, so that the SA measurements may also serve as 'ground truth' data. As SA data lack sufficient temporal resolution, the utilization of this method requires relying on the spatial variability of the DT for training the DL model, in contrast to the temporal variability considered in this study. With the advent of the Surface Water and Ocean Topography (SWOT) mission, new opportunities can arise for employing DL models to learn patterns from the observed surface of DT, which the DL model can also be used for correcting HDM. The SWOT data offers one of the most detailed views of the sea surface topography.

List of Figures

Figure 1. Schematic representations of the interrelation between various data sources, hydrodynamic parameters, and vertical reference surfaces. Refer to the main text body for the used symbols and abbreviations [from Publication IV].	11
Figure 2. Relative and absolute DT from Spikarna station, located in the northwest of the Bothnian Sea, along with their linear trend [from Publication II].	23
Figure 3. Rate of the vertical land movement (colormap) and geoid rise (dashed isolines) in the Baltic Sea region according to NKG2016LU. Black triangle denotes the location of Spikarna TG station.	23
Figure 4. Differences of heights in the zero-tide and tide-free system and the mean-tide system in the Baltic Sea region, latitude from 54° to 66°.	25
Figure 5. Baltic Sea region and its bathymetry sourced from GEBCO 2022 gridded bathymetry data. The dense network of used tide gauges is denoted by red circles. ...	28
Figure 6. The NKG2015 geoid model in the zero-tide system.....	30
Figure 7. An illustration of the data screening for SA data: a) SA-derived DT for Cycle No. 63 (24-Sep-2020 09:42) and Pass No. 272 (denoted in b) and detected outliers. c) the clean SA data is represented in blue, and smoothed DT by applying the wavelet filtering method is shown in red. The frequency contents of the SA data are displayed in panel (d) [from Publication IV].	33
Figure 8. Image of the sea surface topography derived from ALS (first 1 km of the trajectory from west) with respect to the reference ellipsoid GRS-80 (left panel), and location of the flight trajectory on 10 May 2018, at 9:30 UTC in the Gulf of Finland (right panel).	34
Figure 9. Nemo-Nordic model domain covers the Baltic Sea and the North Sea. The model domain of HBM-EST is denoted by a solid-line rectangle.	35
Figure 10. Difference between the Nemo-Nordic model and tide gauge records: a) time series at three sample stations. Location of the stations are denoted in Figure 12. b) Fast Fourier transform (FFT) of the records shown in panel (a). Please note that the HDM data until April 2020 were accessible for Method I [Modified from Publication IV].	38
Figure 11. Flowchart of the HDM correction using a dense network of geoid-referenced TG records and comparative assessment of the datasets [from Publication II].	39
Figure 12. Comparing the HDM with the network of TGs. a) DT of the Nemo-Nordic model at a specific time instant (e.g., 5 June 2019, 12:00), along with the corresponding <i>TDBias</i> . b) <i>RMSE</i> of original and corrected HDM at TG stations. TG stations are numbered clockwise, starting from the easternmost Estonian TG station, as indicated in (a) for some stations. c) <i>Bias</i> of the HDM with respect to TG records.....	40
Figure 13. HDM correction for 5 June 2019, 12:00. a) instantaneous DT derived from the original Nemo-Nordic model, b) the corresponding <i>SDBias</i> obtained from 73 TG records, and c) corrected DT based on Equation (14).	41
Figure 14. Existing <i>Bias</i> between the original and corrected HDM with respect to the SA measurements against the SA passes in (a) and cycles in (b). The bars demonstrate the distance between the first and third quartiles [Modified from Publication II].	42

Figure 15. *CycleMDT* derived from the SA data, original and corrected HDM, and nearby TG records. The location of the selected passes is shown in the top-right panel [Modified from **Publication II**]. 43

Figure 16. Spatial distribution of the *Bias* of the a) original and b) corrected HDM with respect to SA-derived DT. Green dashed rectangles denote noticeable patterns of differences [Modified from **Publication II**]. 44

Figure 17. Annual mean dynamic topography shown for the original Nemo-Nordic model in the top row and the corrected HDM in the bottom row, along with the corresponding TG-based MDTs marked by circles. The original HDM has been adjusted by -18.6 cm to use consistent colour scaling with the corrected HDM for each year [Modified from **Publication II**]. 45

Figure 18. Flowchart of **Method II** for the HDM correction and vertical referencing it to a common vertical datum, as utilized for both SA and TG observations [Modified from **Publication IV**]. 46

Figure 19. Utilizing the DL model to correct HDM dynamic topography and vertical reference the HDM to a specific geodetic reference frame [Modified from **Publication IV**].48

Figure 20. Internal structure of the DL model with $k = 4$, $f_s = 2$, and $nf = 16$ for simplicity in display. The causal convolution blocks are shown on the right-hand side [from **Publication IV**]. 49

Figure 21. Sequential feature elimination for selecting optimal input variables. Variables are removed stepwise from left to right based on the elimination criterion. The solid blue and red lines are the average $RMSE_{\epsilon}$ resulting from five repeats of the training processes, with dotted lines representing one standard deviation from the average. The green line represents the R-Squared result of each elimination iteration. The variable set of the best solution is highlighted in blue font [from **Publication IV**]. 52

Figure 22. DL model performance. a) Location of tide gauge stations utilized in this study and their division into training, validation, and test sets. b) Performance of HDM error prediction at the tide gauge stations. Triangles and circles represent RMSE and R-Squared values, respectively, using separate colourbar [Modified from **Publication IV**]. 53

Figure 23. Time series of the actual (ϵ) and predicted HDM errors ($\hat{\epsilon}$) at three sample stations (10, 26, and 31) in top row, residuals are in middle row, and the FFT of actual HDM errors and residuals in the bottom row [from **Publication IV**]. 54

Figure 24. Bias between HDM and observations. a) Histogram of the difference between original/corrected HDM and TG measurements. b) Histogram of the $Bias_{HDM}$ with respect to the TG and SA data [Modified from **Publication IV**]. 55

Figure 25. A sample time instant of HDM correction for 18-Aug-2019, at 10:00. a) original Nemo-Nordic model reduced by $RefBias$, along with TG readings and SA measurement (pass No. 272 and cycle No. 48) at the corresponding time instant, b) predicted HDM error based on Equation (23), c) the corrected HDM, and d) along the SA track comparison between modelled and observed DTs [Modified from **Publication IV**]. 56

Figure 26. Spatial distribution of the a) *Bias* of the original HDM, b) *Bias* of the corrected HDM, c) $RMSE$ of the original HDM, and d) $RMSE$ of the corrected HDM [from **Publication IV**]. 57

Figure 27. Monthly mean of the HDM errors (ϵ) for the period from January 2017 to June 2021. 58

Figure 28. Decomposing ALS data and comparing with HDM. a) DT derived from ALS and original/corrected HDM along the flight track observation epoch 10 May 2018, at 9:30. b) FFT of the ALS profile along the track, along with the low-passed filtered signal (shown in panel a). c) High-frequency signal recorded by ALS, which indicates the wind-generated wave fluctuations, and its FFT in panel (d)..... 59

Figure 29. Overlay of DTs from the ALS point cloud and the corrected HDM at the observation epoch, in L-EST97 coordinate system. 60

Figure 30. Flowchart of the retrieval of directional wave spectra from the ALS point cloud [Modified from **Publication III**]. 61

Figure 31. Statistical stability of the wave spectral density. a) Standard errors (Equation 35) against various sample sizes for a selected fragment and wave direction 75°. b) Wavenumber spectra corresponding to the sample size of 300 [from **Publication III**]. 62

Figure 32. Frequency wave spectrum for a segment in the middle of the ALS track: a) in different direction, b) in the dominant direction. The power spectral density derived from the ALS point cloud, the buoy, and the WAM model is compared in panel (b) [Modified from **Publication III**]. 63

Figure 33. Dominant wave directions and wavelengths derived from ALS point cloud along the flight trajectory. The background contour represents the bathymetry obtained from GEBCO_2020 [Modified from **Publication III**]. 64

Figure 34. Comparing wave parameters peak period (top row), significant wave height (middle row), and wave direction (bottom row) derived from ALS point cloud and the WAM model. Comparison between the model and buoy observations for a period of 24 hours are also demonstrated [Modified from **Publication III**]..... 65

List of Tables

Table 1. National height systems complying with BSCD2000, along with their regional geoid models and permanent tide systems.	22
Table 2. Summary of the DL model and the chosen hyperparameters for training, with default values applied to the remaining parameters. C, T, and B represent dimensions of channel, time, and batch, respectively.	50
Table 3. List of the input variables used for feature selection.....	51

References

- Abdullah, N., Wijaya, D.D., Meilano, I., Kuntjoro, W., Tanuwijaya, Z., Abdillah, M. and Nurzaman, F., 2023. An Investigation of the On-board Microwave Radiometer of Satellite Altimetry for Studying the Atmosphere Variability. doi:10.21203/rs.3.rs-3200138/v1.
- Adebisi, N., Balogun, A.L., Min, T.H. and Tella, A., 2021. Advances in estimating Sea Level Rise: A review of tide gauge, satellite altimetry and spatial data science approaches. *Ocean & Coastal Management*, 208, p. 105632. doi:10.1016/j.ocecoaman.2021.105632.
- Afrasteh, Y., Slobbe, D.C., Sacher, M., Verlaan, M., Jahanmard, V., Klees, R., Guarneri, H., Keyzer, L., Pietrzak, J., Snellen, M. and Zijl, F., 2023. Realizing the European Vertical Reference System using model-based hydrodynamic leveling data. *Journal of Geodesy*. doi:10.1007/s00190-023-01778-2.
- Afrasteh, Y., Slobbe, D.C., Verlaan, M., Sacher, M., Klees, R., Guarneri, H., Keyzer, L., Pietrzak, J., Snellen, M. and Zijl, F., 2021. The potential impact of hydrodynamic leveling on the quality of the European vertical reference frame. *Journal of Geodesy*, 95, pp. 1–18. doi:10.1007/s00190-021-01543-3.
- Ågren, J., Liebsch, G. and Mononen, J., 2023. Specification of the Baltic Sea Chart Datum 2000 (BSCD2000). Available online: https://bshc.famosproject.eu/wp-content/uploads/CDWCWG_Specification-of-the-Baltic-Sea-Chart-Datum-2000.pdf (accessed on 7 August 2023).
- Ågren, J., Strykowski, G., Bilker-Koivula, M., Omang, O., Mårdla, S., Forsberg, R., Ellmann, A., Oja, T., Liepins, I., Parseliunas, E. and Kaminskis, J., 2016. The NKG2015 gravimetric geoid model for the Nordic-Baltic region, in: Presented in the 1st Joint Commission 2 and IGFS Meeting International Symposium on Gravity, Geoid and Height Systems. Thessaloniki, Greece, pp. 19–23.
- Alenius, P., Myrberg, K. and Nekrasov, A., 1998. The physical oceanography of the Gulf of Finland: a review. *Boreal Environ. Res*, 3(2), pp. 97–125.
- Andersen, O.B., Nielsen, K., Knudsen, P., Hughes, C.W., Bingham, R., Fenoglio-Marc, L., Gravelle, M., Kern, M. and Polo, S.P., 2018. Improving the coastal mean dynamic topography by geodetic combination of tide gauge and satellite altimetry. *Marine Geodesy*, 41(6), pp. 517–545. doi:10.1080/01490419.2018.1530320.
- Arheimer, B., Dahné, J., Donnelly, C., Lindström, G. and Strömqvist, J., 2012. Water and nutrient simulations using the HYPE model for Sweden vs. the Baltic Sea basin— influence of input-data quality and scale. *Hydrology research*, 43(4), pp. 315–329. doi:10.2166/nh.2012.010.
- Armitage, T.W., Kwok, R., Thompson, A.F. and Cunningham, G., 2018. Dynamic topography and sea level anomalies of the Southern Ocean: Variability and teleconnections. *Journal of Geophysical Research: Oceans*, 123(1), pp. 613–630. doi:10.1002/2017JC013534.
- Axell, L. and Liu, Y., 2016. Application of 3-D ensemble variational data assimilation to a Baltic Sea reanalysis 1989–2013. *Tellus A: Dynamic Meteorology and Oceanography*, 68(1), p. 24220. doi:10.3402/tellusa.v68.24220.
- Baker, C.M., Moulton, M., Palmsten, M.L., Brodie, K., Nuss, E. and Chickadel, C.C., 2023. Remotely sensed short-crested breaking waves in a laboratory directional wave basin. *Coastal Engineering*, 183, p. 104327. doi:10.1016/j.coastaleng.2023.104327.

- Baldi, P. and Sadowski, P.J., 2013. Understanding dropout. *Advances in neural information processing systems*, 26.
- Bartlett, M.S., 1948. Smoothing periodograms from time-series with continuous spectra. *Nature*, 161(4096), pp. 686–687. doi:10.1038/161686a0.
- Bian, C., Jing, Z., Wang, H., Wu, L., Chen, Z., Gan, B. and Yang, H., 2023. Oceanic mesoscale eddies as crucial drivers of global marine heatwaves. *Nature Communications*, 14(1), p. 2970. doi:10.1038/s41467-023-38811-z.
- Bingham, R.J., Haines, K. and Hughes, C.W., 2008. Calculating the ocean's mean dynamic topography from a mean sea surface and a geoid. *Journal of Atmospheric and Oceanic Technology*, 25(10), pp. 1808–1822. doi:10.1175/2008JTECHO568.1.
- Bjorck, N., Gomes, C.P., Selman, B. and Weinberger, K.Q., 2018. Understanding batch normalization. *Advances in neural information processing systems*, 31.
- Björkqvist, J.V., Lukas, I., Alari, V., van Vledder, G.P., Hulst, S., Pettersson, H., Behrens, A. and Männik, A., 2018. Comparing a 41-year model hindcast with decades of wave measurements from the Baltic Sea. *Ocean Engineering*, 152, pp. 57–71. doi:10.1016/j.oceaneng.2018.01.048.
- Chang, I., Kim, Y.H., Jin, H., Park, Y.G., Pak, G. and Chang, Y.S., 2023. Impact of satellite and regional in-situ profile data assimilation on a high-resolution ocean prediction system in the Northwest Pacific. *Frontiers in Marine Science*, 10, p. 1085542. doi:10.3389/fmars.2023.1085542.
- Cheng, Y., Andersen, O.B. and Knudsen, P., 2012. Integrating non-tidal sea level data from altimetry and tide gauges for coastal sea level prediction. *Advances in Space Research*, 50(8), pp. 1099–1106. doi:10.1016/j.asr.2011.11.016.
- Delpeche-Ellmann, N., Mingelaité, T. and Soomere, T., 2017. Examining Lagrangian surface transport during a coastal upwelling in the Gulf of Finland, Baltic Sea. *Journal of Marine Systems*, 171, pp. 21–30. doi:10.1016/j.jmarsys.2016.10.007.
- Delpeche-Ellmann, N., Giudici, A., Rätsep, M. and Soomere, T., 2021. Observations of surface drift and effects induced by wind and surface waves in the Baltic Sea for the period 2011–2018. *Estuarine, Coastal and Shelf Science*, 249, p. 107071. doi:10.1016/j.ecss.2020.107071.
- Denys, P.H., Beavan, R.J., Hannah, J., Pearson, C.F., Palmer, N., Denham, M. and Hreinsdottir, S., 2020. Sea level rise in New Zealand: The effect of vertical land motion on century-long tide gauge records in a tectonically active region. *Journal of Geophysical Research: Solid Earth*, 125(1). doi:10.1029/2019JB018055.
- Durand, M., Fu, L.L., Lettenmaier, D.P., Alsdorf, D.E., Rodriguez, E. and Esteban-Fernandez, D., 2010. The surface water and ocean topography mission: Observing terrestrial surface water and oceanic submesoscale eddies. *Proceedings of the IEEE*, 98(5), pp. 766–779. doi: 10.1109/JPROC.2010.2043031.
- Ekman, M., 1989. Impacts of geodynamic phenomena on systems for height and gravity. *Bulletin Géodésique*, 63, pp. 281–296. doi:10.1007/BF02520477.
- Ekman, M. and Mäkinen, J., 1996. Mean sea surface topography in the Baltic Sea and its transition area to the North Sea: A geodetic solution and comparisons with oceanographic models. *Journal of Geophysical Research: Oceans*, 101(C5), pp. 11993–11999. doi:10.1029/96JC00318.
- Ellmann, A., 2005. Two deterministic and three stochastic modifications of Stokes's formula: a case study for the Baltic countries. *Journal of Geodesy*, 79(1), pp. 11–23. doi:10.1007/s00190-005-0438-1.

- Ellmann, A., Märdla, S. and Oja, T., 2019. The 5 mm geoid model for Estonia computed by the least squares modified Stokes's formula. *Survey review*. doi:10.1080/00396265.2019.1583848.
- Featherstone, W.E. and Filmer, M.S., 2012. The north-south tilt in the Australian Height Datum is explained by the ocean's mean dynamic topography. *Journal of Geophysical Research: Oceans*, 117(C8). doi:10.1029/2012JC007974.
- Filmer, M.S., Hughes, C.W., Woodworth, P.L., Featherstone, W.E. and Bingham, R.J., 2018. Comparison between geodetic and oceanographic approaches to estimate mean dynamic topography for vertical datum unification: evaluation at Australian tide gauges. *Journal of Geodesy*, 92(12), pp. 1413–1437. doi:10.1007/s00190-018-1131-5.
- Fokker, P.A., Van Leijen, F.J., Orlic, B., Van Der Marel, H. and Hanssen, R.F., 2018. Subsidence in the Dutch Wadden Sea. *Netherlands Journal of Geosciences*, 97(3), pp. 129–181. doi:10.1017/njg.2018.9.
- Friedrichs, C.T. and Wright, L.D., 1995. Resonant internal waves and their role in transport and accumulation of fine sediment in Eckernförde Bay, Baltic Sea. *Continental Shelf Research*, 15(13), pp. 1697–1721. doi:10.1016/0278-4343(95)00035-Y.
- Gruber, T., Ågren, J., Angermann, D., Ellmann, A., Engfeldt, A., Gisinger, C., Jaworski, L., Kur, T., Marila, S., Nastula, J. and Nilfouroushan, F., 2022. Geodetic SAR for Height System Unification and Sea Level Research—Results in the Baltic Sea Test Network. *Remote Sensing*, 14(14), p. 3250. doi:10.3390/rs14143250.
- Gruno, A., Liibus, A., Ellmann, A., Oja, T., Vain, A. and Jürgenson, H., 2013, October. Determining sea surface heights using small footprint airborne laser scanning. In *Remote Sensing of the Ocean, Sea Ice, Coastal Waters, and Large Water Regions 2013* (Vol. 8888, pp. 178–190). SPIE. doi:10.1117/12.2029189.
- Guyon, I. and Elisseeff, A., 2003. An introduction to variable and feature selection. *Journal of machine learning research*, 3(Mar), pp. 1157–1182.
- Heiskanen, W.A. and Moritz, H., 1967. *Physical geodesy*. *Bulletin Géodésique (1946-1975)*, 86(1), pp. 491–492. doi:10.1007/BF02525647.
- Hieronimus, M., Hieronymus, J. and Arneborg, L., 2017. Sea level modelling in the Baltic and the North Sea: The respective role of different parts of the forcing. *Ocean Modelling*, 118, pp. 59–72. doi:10.1016/j.ocemod.2017.08.007.
- Hodgson, M.E. and Bresnahan, P., 2004. Accuracy of airborne lidar-derived elevation. *Photogrammetric Engineering & Remote Sensing*, 70(3), pp. 331–339. doi:10.14358/PERS.70.3.331.
- Hordoir, R., Axell, L., Höglund, A., Dieterich, C., Fransner, F., Gröger, M., Liu, Y., Pemberton, P., Schimanke, S., Andersson, H. and Ljungemyr, P., 2019. Nemo-Nordic 1.0: a NEMO-based ocean model for the Baltic and North seas—research and operational applications, *Geosci. Model Dev.*, 12, pp. 363–386. doi:10.5194/gmd-12-363-2019.
- Hughes, C.W. and Bingham, R.J., 2008. An oceanographer's guide to GOCE and the geoid. *Ocean Science*, 4(1), pp. 15–29. doi:10.5194/os-4-15-2008.
- Hünicke, B. and Zorita, E., 2006. Influence of temperature and precipitation on decadal Baltic Sea level variations in the 20th century. *Tellus A: Dynamic Meteorology and Oceanography*, 58(1), pp. 141–153. doi:10.1111/j.1600-0870.2006.00157.x.

- Hwang, P.A., Walsh, E.J., Krabill, W.B., Swift, R.N., Manizade, S.S., Scott, J.F. and Earle, M.D., 1998. Airborne remote sensing applications to coastal wave research. *Journal of Geophysical Research: Oceans*, 103(C9), pp. 18791–18800. doi:10.1029/98JC00895.
- Hwang, P.A., Wang, D.W., Walsh, E.J., Krabill, W.B. and Swift, R.N., 2000a. Airborne measurements of the wavenumber spectra of ocean surface waves. Part I: Spectral slope and dimensionless spectral coefficient. *Journal of physical oceanography*, 30(11), pp. 2753–2767. doi:10.1175/1520-0485(2001)031<2753:AMOTWS>2.0.CO;2.
- Hwang, P.A., Wang, D.W., Walsh, E.J., Krabill, W.B. and Swift, R.N., 2000b. Airborne measurements of the wavenumber spectra of ocean surface waves. Part II: Directional distribution. *Journal of Physical Oceanography*, 30(11), pp. 2768–2787. doi:10.1175/1520-0485(2001)031<2768:AMOTWS>2.0.CO;2.
- IAG, 1984. Resolutions adopted by the international association of Geodesy: the XVIIIth general assembly. *Bull. Geodesique* 58, pp. 309–323. doi:10.1007/BF02519005.
- Ihde, J., Augath, W. and Sacher, M., 2002, August. The vertical reference system for Europe. In *Vertical Reference Systems: IAG Symposium Cartagena, Colombia, February 20–23, 2001* (pp. 345–350). Berlin, Heidelberg: Springer Berlin Heidelberg. doi:10.1007/978-3-662-04683-8_64.
- Jahanmard, V., Delpeche-Ellmann, N. and Ellmann, A., 2021a. Realistic dynamic topography through coupling geoid and hydrodynamic models of the Baltic Sea. *Continental Shelf Research*, 222, p. 104421. doi:10.1016/j.csr.2021.104421.
- Jahanmard, V.; Delpeche-Ellmann, N.; Ellmann, A, 2021b. Machine learning prediction for filling the interruptions of tide gauge data using a least square estimation method from nearest stations. In *Geodesy for A Sustainable Earth, Scientific Assembly of the International Association of Geodesy, Abstract Book: Scientific Assembly of the International Association of Geodesy; Chinese Society for Geodesy: Beijing, China*.
- Jahanmard, V., Delpeche-Ellmann, N. and Ellmann, A., 2022a. Towards realistic dynamic topography from coast to offshore by incorporating hydrodynamic and geoid models. *Ocean Modelling*, 180, p. 102124. doi:10.1016/j.ocemod.2022.102124.
- Jahanmard, V.; Delpeche-Ellmann, N.; Ellmann, A, 2022b. Examining Mean Dynamic Topography Using Geodetic and Oceanographic Approaches for the Baltic Sea, In *Nordic Geodetic Commission General Assembly, 5th–8th of September 2022, Copenhagen, Denmark*.
- Jahanmard, V., Varbla, S., Delpeche-Ellmann, N. and Ellmann, A., 2022c. Retrieval of directional power spectral density and wave parameters from airborne LiDAR point cloud. *Ocean Engineering*, 266, p.112694. doi:10.1016/j.oceaneng.2022.112694
- Jahanmard, V., Hordoir, R., Delpeche-Ellmann, N. and Ellmann, A., 2023a. Quantification of Hydrodynamic Modelling Sea Level Bias Utilizing Deep Learning and Synergistic Integration of Data Sources. *Ocean Modelling*.
- Jahanmard, V., Delpeche-Ellmann, N. and Ellmann, A., 2023b. Absolute dynamic topography through synergizing sea level data sources utilizing a common and stable reference surface. *XXVIII General Assembly of the International Union of Geodesy and Geophysics (IUGG), Berlin*. doi:10.57757/IUGG23-1756.

- Jakimavičius, D., Kriaučiūnienė, J. and Šarauskienė, D., 2018. Assessment of wave climate and energy resources in the Baltic Sea nearshore (Lithuanian territorial water). *Oceanologia*, 60(2), pp. 207–218. doi:10.1016/j.oceano.2017.10.004.
- Johannessen, J.A., Raj, R.P., Nilsen, J.E.Ø., Pripp, T., Knudsen, P., Counillon, F., Stammer, D., Bertino, L., Andersen, O.B., Serra, N. and Koldunov, N., 2014. Toward improved estimation of the dynamic topography and ocean circulation in the high latitude and Arctic Ocean: The importance of GOCE. *The Earth's Hydrological Cycle*, pp. 661–679. doi:10.1007/978-94-017-8789-5_9.
- Jönsson, B., Döös, K., Nycander, J. and Lundberg, P., 2008. Standing waves in the Gulf of Finland and their relationship to the basin-wide Baltic seiches. *Journal of Geophysical Research: Oceans*, 113(C3). doi:10.1029/2006JC003862.
- Julge, K., Gruno, A., Ellmann, A., Liibus, A. and Oja, T., 2014, May. Exploring sea surface heights by using Airborne Laser Scanning. In 2014 IEEE/OES Baltic International Symposium (BALTIC) (pp. 1–7). IEEE. doi:10.1109/BALTIC.2014.6887853.
- Kärnä, T., Ljungemyr, P., Falahat, S., Ringgaard, I., Axell, L., Korabel, V., Murawski, J., Maljutenko, I., Lindenthal, A., Jandt-Scheelke, S. and Verjovkina, S., 2021. Nemo-Nordic 2.0: Operational marine forecast model for the Baltic Sea. *Geoscientific Model Development*, 14(9), pp. 5731–5749. doi:10.5194/gmd-14-5731-2021.
- Ke, H., Wang, A., Lei, J., Wu, J., Wang, Z. and Zhang, S., 2020. Establishment of Seamless Chart Datum and Vertical Datum Transformation for Hydrography with a Combining Geoid, Sea Surface Topography, and Ocean Tide Model in Prydz Bay, Antarctica. *Journal of Coastal Research*, 105(SI), pp. 204–209. doi:10.2112/JCR-SI105-043.1.
- Kniebusch, M., Meier, H.M. and Radtke, H., 2019. Changing salinity gradients in the Baltic Sea as a consequence of altered freshwater budgets. *Geophysical Research Letters*, 46(16), pp. 9739–9747. doi:10.1029/2019GL083902.
- Knudsen, P., Andersen, O. and Maximenko, N., 2021. A new ocean mean dynamic topography model, derived from a combination of gravity, altimetry and drifter velocity data. *Advances in Space Research*, 68(2), pp. 1090–1102. doi:10.1016/j.asr.2019.12.001.
- Knudsen, P., Bingham, R., Andersen, O. and Rio, M.H., 2011. A global mean dynamic topography and ocean circulation estimation using a preliminary GOCE gravity model. *Journal of Geodesy*, 85, pp. 861–879. doi:10.1007/s00190-011-0485-8.
- Krauss, W. and Brügge, B., 1991. Wind-produced water exchange between the deep basins of the Baltic Sea. *Journal of Physical Oceanography*, 21(3), pp. 373–384. doi:10.1175/1520-0485(1991)021<0373:WPWEBT>2.0.CO;2.
- Lagemaa, P., Elken, J. and Kõuts, T., 2011. Operational sea level forecasting in Estonia. *Estonian Journal of Engineering*, 17(4), p. 301. doi:10.3176/eng.2011.4.03.
- Lehmann, A. and Hinrichsen, H.H., 2000. On the thermohaline variability of the Baltic Sea. *Journal of Marine Systems*, 25(3-4), pp. 333–357. doi:10.1016/S0924-7963(00)00026-9
- Lehmann, A. and Myrberg, K., 2008. Upwelling in the Baltic Sea—A review. *Journal of Marine Systems*, 74, pp. S3–S12. doi:10.1016/j.jmarsys.2008.02.010.
- Leppäranta, M. and Myrberg, K., 2009. *Physical oceanography of the Baltic Sea*. Springer Science & Business Media. doi:10.1007/978-3-540-79703-6.
- Li, Z., Guo, J., Ji, B., Wan, X. and Zhang, S., 2022. A review of marine gravity field recovery from satellite altimetry. *Remote Sensing*, 14(19), p. 4790. doi:10.3390/rs14194790.

- Liblik, T. and Lips, U., 2019. Stratification has strengthened in the Baltic Sea—an analysis of 35 years of observational data. *Frontiers in Earth Science*, 7, p. 174. doi:10.3389/feart.2019.00174.
- Liebsch, G., Schwabe, J., Varbla, S., Ågren, J., Teitsson, H., Ellmann, A., Forsberg, R., Strykowski, G., Bilker-Koivula, M., Liepiņš, I., Paršeliūnas, E., Keller, K., Vestøl, O., Omang, O., Kaminskis, J. N., Wilde-Piórko, M., Pырchla, K., Olsson, P.-A., Förste, C., Ince, E. S., Somla, J., Westfeld, P., Hammarklint, T., 2023. Release note for the BSCD2000 height transformation grid. *The International Hydrographic Review*, 29(2), pp. 194–199. doi:10.58440/ihr-29-2-n11.
- Liu, Z. and Frigaard, P., 1999. Generation and analysis of random waves.
- Lou, R., Lv, Z. and Guizani, M., 2022. Wave height prediction suitable for maritime transportation based on green ocean of things. *IEEE transactions on artificial intelligence*. doi:10.1109/TAI.2022.3168246.
- Mäkinen, J. and Ihde, J., 2009. The permanent tide in height systems. In *Observing our changing earth* (pp. 81–87). Springer Berlin Heidelberg. doi:10.1007/978-3-540-85426-5_10.
- Mäkinen, J., 2021. The permanent tide and the international height reference frame IHRF. *Journal of Geodesy*, 95(9), p. 106. doi:10.1007/s00190-021-01541-5.
- Mardani, N., Suara, K., Fairweather, H., Brown, R., McCallum, A. and Sidle, R.C., 2020. Improving the accuracy of hydrodynamic model predictions using Lagrangian calibration. *Water*, 12(2), p. 575. doi:10.3390/w12020575.
- Marshall, J., Hill, C., Perelman, L. and Adcroft, A., 1997. Hydrostatic, quasi-hydrostatic, and nonhydrostatic ocean modeling. *Journal of Geophysical Research: Oceans*, 102(C3), pp. 5733–5752. doi:10.1029/96JC02776.
- Matthäus, W. and Ulrich Lass, H., 1995. The recent salt inflow into the Baltic Sea. *Journal of Physical Oceanography*, 25(2), pp. 280–286. doi:10.1175/1520-0485(1995)025<0280:TRSIT>2.0.CO;2.
- Mintourakis, I., Panou, G. and Paradissis, D., 2019. Evaluation of ocean circulation models in the computation of the mean dynamic topography for geodetic applications. Case study in the Greek seas. *Journal of Geodetic Science*, 9(1), pp. 154–173. doi:10.1515/jogs-2019-0015.
- Morrow, R., Fu, L.L., Rio, M.H., Ray, R., Prandi, P., Le Traon, P.Y. and Benveniste, J., 2023. Ocean circulation from space. *Surveys in Geophysics*, pp. 1–44. doi:10.1007/s10712-023-09778-9.
- Mostafavi, M., Delpeche-Ellmann, N. and Ellmann, A., 2021. Accurate sea surface heights from Sentinel-3A and Jason-3 retracker by incorporating high-resolution marine geoid and hydrodynamic models. *Journal of Geodetic Science*, 11(1), pp. 58–74. doi:10.1515/jogs-2020-0120.
- Mostafavi, M., Delpeche-Ellmann, N., Ellmann, A. and Jahanmard, V., 2023. Determination of accurate dynamic topography for the baltic sea using satellite altimetry and a marine geoid model. *Remote Sensing*, 15(8), p. 2189. doi:10.3390/rs15082189.
- Myrberg, K. and Soomere, T., 2013. The Gulf of Finland, its hydrography and circulation dynamics. In *Preventive Methods for Coastal Protection: Towards the Use of Ocean Dynamics for Pollution Control* (pp. 181–222). Heidelberg: Springer International Publishing. doi:10.1007/978-3-319-00440-2_6.

- Nordman, M., Kuokkanen, J., Bilker-Koivula, M., Koivula, H., Häkli, P. and Lahtinen, S., 2018. Geoid validation on the Baltic Sea using ship-borne GNSS data. *Marine Geodesy*, 41(5), pp. 457–476. doi:10.1080/01490419.2018.1481160.
- Oord, A.V.D., Dieleman, S., Zen, H., Simonyan, K., Vinyals, O., Graves, A., Kalchbrenner, N., Senior, A. and Kavukcuoglu, K., 2016. Wavenet: A generative model for raw audio. arXiv preprint arXiv:1609.03499. doi:10.48550/arXiv.1609.03499.
- Ophaug, V., Breili, K. and Gerlach, C., 2015. A comparative assessment of coastal mean dynamic topography in Norway by geodetic and ocean approaches. *Journal of Geophysical Research: Oceans*, 120(12), pp. 7807–7826. doi:10.1002/2015JC011145.
- Orseau, S., Huybrechts, N., Tassi, P., Kaidi, S. and Klein, F., 2021. NavTEL: Open-source decision support tool for ship routing and underkeel clearance management in Estuarine Channels. *Journal of Waterway, Port, Coastal, and Ocean Engineering*, 147(2), p. 04020053. doi:10.1061/(ASCE)WW.1943-5460.0000610.
- Ostanciaux, E., Husson, L., Choblet, G., Robin, C. and Pedoja, K., 2012. Present-day trends of vertical ground motion along the coast lines. *Earth-Science Reviews*, 110(1-4), pp. 74–92. doi:10.1016/j.earscirev.2011.10.004.
- Parker, K., Erikson, L., Thomas, J., Nederhoff, K., Barnard, P. and Muis, S., 2023. Relative contributions of water-level components to extreme water levels along the US Southeast Atlantic Coast from a regional-scale water-level hindcast. *Natural Hazards*, pp. 1–30. doi:10.1007/s11069-023-05939-6.
- Passaro, M., Müller, F.L., Oelsmann, J., Rautiainen, L., Dettmering, D., Hart-Davis, M.G., Abulaitijiang, A., Andersen, O.B., Høyer, J.L., Madsen, K.S. and Ringgaard, I.M., 2021. Absolute Baltic Sea level trends in the satellite altimetry era: A revisit. *Frontiers in Marine Science*, 8, p. 647607. doi:10.3389/fmars.2021.647607.
- Passaro, M., Rautiainen, L., Dettmering, D., Restano, M., Hart-Davis, M.G., Schlembach, F., Särkkä, J., Müller, F.L., Schwatke, C. and Benveniste, J., 2022. Validation of an empirical subwaveform retracking strategy for SAR altimetry. *Remote Sensing*, 14(16), p. 4122. doi:10.3390/rs14164122.
- Pettersson, H., Kahma, K.K. and Tuomi, L., 2010. Wave directions in a narrow bay. *Journal of Physical Oceanography*, 40(1), pp. 155–169. doi:10.1175/2009JPO4220.1.
- Pfeffer, J. and Allemand, P., 2016. The key role of vertical land motions in coastal sea level variations: A global synthesis of multisatellite altimetry, tide gauge data and GPS measurements. *Earth and planetary science letters*, 439, pp. 39–47. doi:10.1016/j.epsl.2016.01.027.
- Pytharouli, S., Chaikalis, S. and Stiros, S.C., 2018. Uncertainty and bias in electronic tide-gauge records: Evidence from collocated sensors. *Measurement*, 125, pp. 496–508. doi:10.1016/j.measurement.2018.05.012.
- Rajabi-Kiasari, S., Delpeche-Ellmann, N. and Ellmann, A., 2023. Forecasting of absolute dynamic topography using deep learning algorithm with application to the Baltic Sea. *Computers & Geosciences*, p. 105406. doi:10.1016/j.cageo.2023.105406.
- Rathore, N., Rathore, P., Basak, A., Nistala, S.H. and Runkana, V., 2021, December. Multi Scale Graph Wavenet for Wind Speed Forecasting. In *2021 IEEE International Conference on Big Data (Big Data)* (pp. 4047–4053). IEEE. doi:10.1109/BigData52589.2021.9671624.

- Raucoules, D., Le Cozannet, G., Wöppelmann, G., De Michele, M., Gravelle, M., Daag, A. and Marcos, M., 2013. High nonlinear urban ground motion in Manila (Philippines) from 1993 to 2010 observed by DInSAR: implications for sea-level measurement. *Remote sensing of environment*, 139, pp. 386–397. doi:10.1016/j.rse.2013.08.021.
- Räämet, A. and Soomere, T., 2010. The wave climate and its seasonal variability in the northeastern Baltic Sea. *Estonian Journal of Earth Sciences*, 59(1). doi:10.3176/earth.2010.1.08.
- Reusch, T.B., Dierking, J., Andersson, H.C., Bonsdorff, E., Carstensen, J., Casini, M., Czajkowski, M., Hasler, B., Hinsby, K., Hyytiäinen, K. and Johannesson, K., 2018. The Baltic Sea as a time machine for the future coastal ocean. *Science Advances*, 4(5), p. eaar8195. doi:10.1126/sciadv.aar8195.
- Rosentau, A., Muru, M., Gauk, M., Oja, T., Liibus, A., Kall, T., Karro, E., Roose, A., Sepp, M., Tammepuu, A. and Tross, J., 2017. Sea-level change and flood risks at Estonian coastal zone. *Coastline Changes of the Baltic Sea from South to East: Past and Future Projection*, pp. 363–388. doi:10.1007/978-3-319-49894-2_16.
- Rummel, R., 2002. Global unification of height systems and GOCE. In *Gravity, Geoid and Geodynamics 2000: GGG2000 IAG International Symposium Banff, Alberta, Canada July 31–August 4, 2000* (pp. 13–20). Springer Berlin Heidelberg. doi:10.1007/978-3-662-04827-6_3.
- Rytkönen, J., Siitonen, L., Riipi, T., Sassi, J. and Sukselainen, J., 2002. Statistical analyses of the Baltic maritime traffic. VTT Technical Research Centre of Finland.
- Santamaría-Gómez, A., Gravelle, M., Collilieux, X., Guichard, M., Míguez, B.M., Tiphaneau, P. and Wöppelmann, G., 2012. Mitigating the effects of vertical land motion in tide gauge records using a state-of-the-art GPS velocity field. *Global and Planetary Change*, 98, pp. 6–17. doi:10.1016/j.gloplacha.2012.07.007.
- Saraceno, M., Strub, P.T. and Kosro, P.M., 2008. Estimates of sea surface height and near-surface alongshore coastal currents from combinations of altimeters and tide gauges. *Journal of Geophysical Research: Oceans*, 113(C11). doi:10.1029/2008JC004756.
- Schall, J., Löcher, A., Kusche, J., Rietbroek, R. and Sudau, A., 2016. Consistency of geoid models, radar altimetry, and hydrodynamic modelling in the North Sea. *Marine Geodesy*, 39(3-4), pp. 223–237. doi:10.1080/01490419.2016.1152334.
- Schwabe, J., Ågren, J., Liebsch, G., Westfeld, P., Hammarklint, T., Mononen, J. and Andersen, O.B., 2020. The Baltic Sea Chart Datum 2000 (BSCD2000): Implementation of a common reference level in the Baltic Sea. *The international hydrographic review*, (23), pp. 63–82.
- Sea Ice modelling Integrated Initiative (SI3) – The NEMO sea ice engine, NEMO Sea Ice Working Group, Scientific Notes of Climate Modelling Center, 31, ISSN 1288-1619 Institut Pierre-Simon Laplace (IPSL), doi:10.5281/zenodo.1471689, 2019.
- Sjöberg, L. E., & Bagherbandi, M., 2017. Applications and comparisons of LSMSA and RCR. In L. E. Sjöberg, & M. Bagherbandi, *Gravity Inversion and Integration*, pp. 181–202. Cham: Springer. doi:10.1007/978-3-319-50298-4_6
- Slobbe, D.C., Klees, R. and Gunter, B.C., 2014. Realization of a consistent set of vertical reference surfaces in coastal areas. *Journal of Geodesy*, 88, pp. 601–615. doi:10.1007/s00190-014-0709-9.
- Slobbe, D.C., Verlaan, M., Klees, R. and Gerritsen, H., 2013. Obtaining instantaneous water levels relative to a geoid with a 2D storm surge model. *Continental Shelf Research*, 52, pp. 172–189. doi:10.1016/j.csr.2012.10.002.

- Soomere, T. and Keevallik, S., 2001. Anisotropy of moderate and strong winds in the Baltic Proper. *Proc. Estonian Acad. Sci. Eng*, 7(1), pp. 35–49.
- Soomere, T., 2003. Anisotropy of wind and wave regimes in the Baltic Proper. *Journal of Sea Research*, 49(4), pp. 305–316. doi:10.1016/S1385-1101(03)00034-0.
- Soomere, T., Behrens, A., Tuomi, L. and Nielsen, J.W., 2008. Wave conditions in the Baltic Proper and in the Gulf of Finland during windstorm Gudrun. *Natural Hazards and Earth System Sciences*, 8(1), pp. 37–46. doi:10.5194/nhess-8-37-2008.
- Soomere, T. and Quak, E. eds., 2013. Preventive methods for coastal protection: towards the use of ocean dynamics for pollution control. Springer Science & Business Media.
- Srinivasan, M. and Tsonos, V., 2023. Satellite Altimetry for Ocean and Coastal Applications: A Review. *Remote Sensing*, 15(16), p. 3939. doi:10.3390/rs15163939.
- Staneva, J., Alari, V., Breivik, Ø., Bidlot, J.R. and Mogensen, K., 2017. Effects of wave-induced forcing on a circulation model of the North Sea. *Ocean Dynamics*, 67, pp. 81–101. doi:10.1007/s10236-016-1009-0.
- Staneva, J., Wahle, K., Günther, H. and Stanev, E., 2016. Coupling of wave and circulation models in coastal–ocean predicting systems: a case study for the German Bight. *Ocean Science*, 12(3), pp. 797–806. doi:10.5194/os-12-797-2016.
- Steffen, H. and Wu, P., 2011. Glacial isostatic adjustment in Fennoscandia—a review of data and modeling. *Journal of geodynamics*, 52(3-4), pp. 169–204. doi:10.1016/j.jog.2011.03.002.
- Stokes, G. G., 1849. On the variation of gravity on the surface of the Earth. *Transactions of the Cambridge Philosophical Society*, 8, pp. 672–695.
- Sun, K., Wang, L., Xu, B., Zhao, W., Teng, S.W. and Xia, F., 2020. Network representation learning: From traditional feature learning to deep learning. *IEEE Access*, 8, pp. 205600–205617. doi:10.1109/ACCESS.2020.3037118.
- Sutherland, P., Brozena, J., Rogers, W.E., Doble, M. and Wadhams, P., 2018. Airborne remote sensing of wave propagation in the marginal ice zone. *Journal of Geophysical Research: Oceans*, 123(6), pp. 4132–4152. doi:10.1029/2018JC013785.
- Suursaar, Ü., Kullas, T. and Otsmann, M., 2002. A model study of the sea level variations in the Gulf of Riga and the Väinameri Sea. *Continental Shelf Research*, 22(14), pp. 2001–2019. doi:10.1016/S0278-4343(02)00046-8.
- Suursaar, Ü. and Sooäär, J., 2007. Decadal variations in mean and extreme sea level values along the Estonian coast of the Baltic Sea. *Tellus A: Dynamic Meteorology and Oceanography*, 59(2), pp. 249–260. doi:10.1111/j.1600-0870.2006.00220.x.
- Tebaldi, C., Ranasinghe, R., Vourdoukas, M., Rasmussen, D.J., Vega-Westhoff, B., Kirezci, E., Kopp, R.E., Srivier, R. and Mentaschi, L., 2021. Extreme sea levels at different global warming levels. *Nature Climate Change*, 11(9), pp. 746–751. doi:10.1038/s41558-021-01127-1.
- Undén, P., Rontu, L., Jarvinen, H., Lynch, P., Calvo Sánchez, F.J., Cats, G., Cuxart, J., Eerola, K., Fortelius, C., García-Moya, J.A. and Jones, C., 2002. HIRLAM-5 scientific documentation.
- Varbla, S., Ellmann, A. and Delpeche-Ellmann, N., 2020. Validation of marine geoid models by utilizing hydrodynamic model and shipborne GNSS profiles. *Marine Geodesy*, 43(2), pp. 134–162. doi:10.1080/01490419.2019.1701153.

- Varbla, S., Ellmann, A. and Delpeche-Ellmann, N., 2021. Applications of airborne laser scanning for determining marine geoid and surface waves properties. *European Journal of Remote Sensing*, 54(1), pp. 558–568. doi:10.1080/22797254.2021.1981156.
- Varbla, S., Ågren, J., Ellmann, A. and Poutanen, M., 2022. Treatment of tide gauge time series and marine GNSS measurements for vertical land motion with relevance to the implementation of the Baltic Sea Chart Datum 2000. *Remote Sensing*, 14(4), p. 920. doi:10.3390/rs14040920.
- Varbla, S. and Ellmann, A., 2023. Iterative data assimilation approach for the refinement of marine geoid models using sea surface height and dynamic topography datasets. *Journal of Geodesy*, 97(3), p. 24. doi:10.1007/s00190-023-01711-7.
- Vestøl, O.; Ågren, J.; Steffen, H.; Kierulf, H.; Tarasov, L. NKG2016LU: A new land uplift model for Fennoscandia and the Baltic region. *J. Geod.* 2019, 93, pp. 1759–1779. doi:10.1007/s00190-019-01280-8.
- Walsh, E.J., Hancock III, D.W., Hines, D.E., Swift, R.N. and Scott, J.F., 1985. Directional wave spectra measured with the surface contour radar. *Journal of physical oceanography*, 15(5), pp. 566–592. doi:10.1175/1520-0485(1985)015<0566:DWSMWT>2.0.CO;2.
- Weisse, R., Dailidienė, I., Hünicke, B., Kahma, K., Madsen, K., Omstedt, A., Parnell, K., Schöne, T., Soomere, T., Zhang, W. and Zorita, E., 2021. Sea level dynamics and coastal erosion in the Baltic Sea region. *Earth System Dynamics*, 12(3), pp. 871–898. doi:10.5194/esd-12-871-2021.
- Welch, P., 1967. The use of fast Fourier transform for the estimation of power spectra: a method based on time averaging over short, modified periodograms. *IEEE Transactions on audio and electroacoustics*, 15(2), pp. 70–73. doi:10.1109/TAU.1967.1161901.
- Woodworth, P.L., Gravelle, M., Marcos, M., Wöppelmann, G. and Hughes, C.W., 2015. The status of measurement of the Mediterranean mean dynamic topography by geodetic techniques. *Journal of Geodesy*, 89, pp. 811–827. doi:10.1007/s00190-015-0817-1.
- Woodworth, P.L., Hughes, C.W., Bingham, R.J. and Gruber, T., 2012. Towards worldwide height system unification using ocean information. *Journal of Geodetic Science*, 2(4), pp. 302–318. doi:10.2478/v10156-012-0004-8.
- Wöppelmann, G. and Marcos, M., 2016. Vertical land motion as a key to understanding sea level change and variability. *Reviews of Geophysics*, 54(1), pp. 64–92. doi:10.1002/2015RG000502.
- Wöppelmann, G., Miguez, B.M., Bouin, M.N. and Altamimi, Z., 2007. Geocentric sea-level trend estimates from GPS analyses at relevant tide gauges world-wide. *Global and Planetary Change*, 57(3-4), pp. 396–406. doi:10.1016/j.gloplacha.2007.02.002.
- Wöppelmann, G., Zerbini, S. and Marcos, M., 2006. Tide gauges and Geodesy: a secular synergy illustrated by three present-day case studies. *Comptes Rendus Geoscience*, 338(14-15), pp. 980–991. doi:10.1016/j.crte.2006.07.006.
- Wunsch, C. and Stammer, D., 1998. Satellite altimetry, the marine geoid, and the oceanic general circulation. *Annual Review of Earth and Planetary Sciences*, 26(1), pp. 219–253. doi:10.1146/annurev.earth.26.1.219.
- Zhang, M., Kujala, P. and Hirdaris, S., 2022. A machine learning method for the evaluation of ship grounding risk in real operational conditions. *Reliability Engineering & System Safety*, 226, p. 108697 doi:10.1016/j.ress.2022.108697.

Acknowledgements

This thesis research received support from grants provided by the Estonian Research Council, “Development of an iterative approach for near-coast marine geoid modelling by using re-tracked satellite altimetry, in-situ and modelled data” [grant number PRG330] and “Development of continuous DYNAmic vertical REference for maritime and offshore engineering by applying machine learning strategies /DYNAREF/” [grant number PRG1785]. Additional funding sources are listed in corresponding sections of Publications.

I would like to express my heartfelt gratitude to my supervisor and co-supervisor, Artu Ellmann and Nicole Delpeche-Ellmann for dedicating their time, providing support, and granting me valuable opportunities during my academic journey. I would also like to extend my sincere appreciation to Cornelis Slobbe and Robinson Hordoir for their gracious hospitality during my visiting study. Their invaluable advice and profound insights have significantly contributed to the quality of my work. I also want to thank to my colleagues and other co-authors, Sander Varbla, Majid Mostafavi, and Saeed Rajabi-Kiasari for their support and assistance throughout my doctoral program.

Lastly, I wish to convey my profound gratitude to my family for their unwavering support and encouragement. In particular, I am extremely grateful to my wife, Samira, whose contributions are beyond measure. Without her understanding and steadfast support, I have doubts whether the successful completion of this work would have been possible.

Abstract

Developments Towards Deriving Realistic Dynamic Topography by Synergizing High-Resolution Geoid with Sea Level Data

Synergistic integration of various sea level sources (tide gauges, satellite altimetry and hydrodynamic models – HDM, etc.) is important for many marine and engineering applications to achieve the required accuracy from coastline to offshore. The data fusion amongst the different sources, however, can be challenging due to: (i) varying spatial and temporal resolutions, (ii) the utilization of different vertical datums, and (iii) various sources having their own measurement/modelling errors. The geoid (the equipotential surface of Earth's gravity field) is presently the best and most realistic vertical datum that can be utilized to represent sea level variations. Expressing sea level variation relative to the geoid yields realistic ocean dynamic topography estimates from coast to offshore. Accordingly, this study demonstrates that realistic dynamic topography can be achieved by synergizing the various sea level sources by means of mathematical and computing algorithms.

Hydrodynamic models are one of the important sources of sea level data due to their spatio-temporal resolution, however, they are limited by a vertical datum bias and also by modelling errors. Two methodologies to improve HDMs are explored in this study. The first method determines and eliminates the HDM datum bias with respect to the actual sea level by using a dense network of geoid-referred tide gauges, hence serving as the ground truth. The TG data at the coast is compared to the initial HDM values and the determined bias is eliminated by employing different interpolation methods (e.g., linear, thin plate spline regression and inverse distance weighted). The second method employs a deep learning model, that is trained to find the inter-relations between a group of input spatio-temporal variables and HDM modelling errors at the locations of tide gauges. So that once these HDM modelling errors are corrected it becomes possible to confirm the HDM offshore improvements by using satellite altimetry data. Both methods were examined in the Baltic Sea region.

The vertical datum bias of the HDM was calculated to be 18.3 ± 1.9 cm, then to be eliminated. The deep learning model application shows promising potential in identifying HDM modelling errors. When compared to tide gauges and satellite altimetry data the corrected HDM significantly improved the RMSE of instantaneous dynamic topography from 7.6 and 6.5 cm to 3.4 and 4.1 cm, respectively. Satisfactorily, the HDM correlation coefficient with respect to tide gauge data improved from 0.93 to 0.98. A comparative assessment between sea level sources revealed inconsistencies and problematic regions, such as the eastern Gulf of Finland, Bothnian Sea, and southwestern Baltic Sea. Although a preliminary investigation attributed most errors to the geoid model, further investigations are needed to address inconsistencies in the participating datasets.

Lühikokkuvõte

Merepinna realistliku dünaamilise topograafia saavutamine täppisgeoidi ja meretaseme andmete kooskasutamisel

Kõrge ruumilise ja ajalise lahutatavuse tõttu on hüdrodünaamilised mudelid üks olulisi meretaseme andmestikke, kuid neile on paraku ka omane vertikaaldaatumi süstemaatiline nihe ja modelleerimisvead. Käeolevas uurimistöös kasutatakse kahte HDM-i parandamise meetodikat. Esimene meetod tuvastab ja elimineerib HDM-i nihkeväärtused tegeliku merepinna suhtes. Selleks kasutatakse veemõõdujaamade võrku, mille mõõtmistulemuste lähtepinnaks on ühtne geoidimudel. Veemõõdujaamade andmeid rannikul võrreldakse algse HDM väärtustega, misjärel tuvastatud nihe elimineeritakse erinevate interpoleerimismeetodite (nt lineaarne, õhukese plaadi splaini regressioon ja kaalutud pöördkaugus) abil. Teine meetod kasutab süvaõppe mudelit, mis on treenitud leidma veemõõdujaamade asukohtades vastastikuseid seoseid ruumilis-ajaliste sisendmuutujate ja HDM-i modelleerimisvigade vahel. HDM-i modelleerimisvigade parandamise järgselt on võimalik HDM-i täiustusi tõestada satelliitaltimeetria avamere mõõtmisandmetega. Mõlemat meetodit rakendati Läänemere piirkonnas.

HDM-i vertikaaldaatumi nihkeks saadi $18,3 \pm 1,9$ cm, misjärel see elimineeriti. Süvaõppe mudeli rakendamine on paljutõotav HDM modelleerimisvigade tuvastamiseks. Võrreldes veemõõdujaamade ja satelliitaltimeetria mõõtmise andmetega parandas korrigeeritud HDM märkimisväärselt dünaamilise topograafia keskruutvigade väärtuseid vastavalt $7,6 \rightarrow 6,5$ cm ning $3,4 \rightarrow 4,1$ cm. Ka paranes HDM-i ja veemõõdujaamade andmete korrelatsioonikoefitsient $0,93$ -lt $0,98$ -le. Meretaseme andmestike võrdlev hindamine viitas probleemsetele piirkondadele Soome lahe idaosas, Botnia meres ja Läänemere edelaosas. Kuigi esialgne uurimine omistas enamiku vigadest geoidimudelile, on osalevate andmestike ebakõlade kõrvaldamiseks vaja täiendavaid uuringuid.

Appendix 1

Publication I

Jahanmard, V., Delpeche-Ellmann, N., Ellmann, A. (2021). Realistic Dynamic Topography Through Coupling Geoid and Hydrodynamic Models of the Baltic Sea. *Continental Shelf Research*, 222. doi:10.1016/j.csr.2021.104421.



Contents lists available at ScienceDirect

Continental Shelf Research

journal homepage: www.elsevier.com/locate/csr

Realistic dynamic topography through coupling geoid and hydrodynamic models of the Baltic Sea

Vahidreza Jahanmard^{a,*}, Nicole Delpeche-Ellmann^b, Artu Ellmann^a

^a Department of Civil Engineering and Architecture, Tallinn University of Technology, Ehitajate tee 5, 19086, Tallinn, Estonia

^b Department of Cybernetics, School of Science, Tallinn University of Technology, Akadeemia tee 21, 12618, Tallinn, Estonia

ARTICLE INFO

Keywords:

Sea level
Dynamic topography
Hydrogeodesy
Vertical reference datum
Baltic sea
Gulf of Finland

ABSTRACT

Accurate and compatible sea level data are now more important than ever before, especially in semi-enclosed sea areas that are highly exploited and surrounded by many countries, such as the Baltic Sea. Obtaining accurate sea level data is however, not only hindered by resolution deficiencies and systematic and random errors from the various available sources (e.g. satellite altimetry (SA), tide gauges (TG), hydrodynamic models (HDM), etc.), but most importantly by variations in and insufficient knowledge of the vertical reference datums. This study demonstrates that by incorporating the geoid (equipotential surface of the earth, that represents a stable vertical datum) along with a network of tide gauges and hydrodynamic models it is possible to obtain accurate and realistic sea level data.

A simplified method is developed that calculates the bias between TG and HDM and identifies an optimum time period to be utilized, given the associated accuracy required. A bias period of 0–6 h results in a standard deviation of less than 5 cm at all participating TG stations. The method is tested in the estuarine water body of the Gulf of Finland (in the eastern section of the Baltic Sea). Results show that without the bias correction, the mean dynamic topography from a westerly to easterly direction along the gulf, varied from -12.7 to -8.2 cm (a difference of 4.5 cm) whilst after bias correction the model varied from 18 cm to 25.4 cm (a difference of 7.4 cm). Both these scenarios demonstrate an increasing eastward trend. Nevertheless, a major difference in quantification exists and to a first approximation, this may vary by as much as a factor of almost 2. The analysis also intrinsically identified critical areas where drastic changes in dynamic topography occur and the associated seasons. Thus, the utilization of more stable vertical reference, such as the geoid, displays promising results, that essentially allows better quantification of more realistic parameters (e.g. sea level trends, extreme value analysis etc.). In addition, it allows identification of hydrodynamic modelling imperfections and that a coherent compatibility with other sources of sea level data (e.g. SA, Global Navigational Satellite Systems etc.) is now possible. This accuracy and conformity in sea level data are urgently required for a comprehensive understanding of climate change, marine engineering and navigation applications.

1. Introduction

Various applications such as navigation, engineering and climate studies now require accurate and reliable sea level data, with sub-decimetre accuracy and most importantly, a static and internationally recognized vertical reference datum (Gaior, 2008; Omstedt and Hansson, 2006). Obtaining accurate sea level data, however, can be challenging, for various sources such as tide gauges (TG), satellite altimetry (SA), shipborne and airborne Global Navigation Satellite Systems (GNSS) profiles and hydrodynamic models (HDM) are often utilized.

These sources have different resolutions (in both space and time) and dissimilar or unknown vertical reference datums.

Out of all the available sources, HDM tends to provide the best spatial and temporal resolution relative sea level changes. They are based on a series of Navier-Stokes mathematical equations, that are driven by meteorological and hydrological data that attempt to model reality (Lehmann, 1995; Ophaug et al., 2015). The marine areas in actuality can be unpredictably turbulent and thus revealing modelling imperfections. The most relevant and alarming limitation though, is that the HDM vertical reference datum is often inconsistent and undisclosed (Slobbe

* Corresponding author.

E-mail address: vahidreza.jahanmard@taltech.ee (V. Jahanmard).

<https://doi.org/10.1016/j.csr.2021.104421>

Received 2 December 2020; Received in revised form 24 March 2021; Accepted 30 March 2021

Available online 6 April 2021

0278-4343/© 2021 Published by Elsevier Ltd.

et al., 2014).

On the other hand, TG data due to their reliability, long time span of data history and availability of temporal resolution are often assumed in many studies to portray the ‘true’ sea surface. The spatial coverage of TG tends to be limited to the coastal boundary, thus not representable for the offshore areas. It is also quite common for the vertical reference datum of marine areas (and thus TG) to refer to a chart datum, that most commonly represents tidal observation (e.g. some historic mean sea level (MSL), lowest astronomic tide (LAT), etc.) or a physical model such as the geoid (IHO, 2020). The tidal observation method is most customarily utilized by many countries for their definition of chart datum. This however, is not anymore an ideal method, for the derived chart datum can vary over different time span and depending on the country/community the sea level data may be referred to differently defined vertical datums. For instance, the Baltic Sea countries use several different vertical reference datum definitions (Schwabe et al., 2020) and in such a dynamic marine area where integration is essential, this can create inconsistency and incompatibility in the sea wide marine research.

Instead it is applicable and now common that TG stations are inter-connected through a national height network by high-precise levellings (Kollo and Ellmann, 2019; Slobbe et al., 2014). In the past, precise levellings were exclusively used for defining a nationwide or continental vertical datum. Currently, many countries consider instead development and implementation of a gravity-based height reference system, e.g. (Ellmann et al., 2020; Li et al., 2016; Véronneau and Huang, 2016), where the definition of vertical datum is realized through geoid (i.e. the shape of the equipotential ocean surface under the influence of the gravity and rotation of Earth alone) modelling. The geoid represents the vertical datum, the natural “zero”, so to speak, for physically meaningful heights and depths, and also to the tide gauge readings. Note also that the sea level variations with respect to the geoid yields dynamic topography (DT). The advantage of the geoid is that (unlike to scarcely located levelling benchmarks) it is a continuous equipotential surface,

hence it can be used for GNSS based heighting not only in land, but also offshore. The geoid is static, it is not “waving” over time (unlike MSL) and represents the natural vertical datum that should ideally be used as zero for the tide gauge readings. In this regard, the Baltic Sea Chart Datum 2000 (BSCD2000) is being implemented in this region as a geodetic reference system based on the European spatial and vertical reference systems (i.e. ETRS89 and EVRS2000) to unify chart datum of the Baltic Sea countries (Schwabe et al., 2020). Thus, it is more applicable to validate the different data and model sources against the geoid referred TG data (Liebsch et al., 2002; Varbla et al., 2020a; and 2020b). This validation should identify any bias between sources with respect to the vertical datum in addition to other systematic and random errors.

Thus, considering both the advantages and disadvantages of TG and HDM it appears logical to synergize the two data sources. As a result, focus of this study is on exploring the use of a more static and appropriate vertical reference frame such as the geoid, for validating the HDM results. A somewhat similar approach has been examined to realize the geoid as the vertical height reference and for storm surge modelling in the Dutch part of the North Sea (Slobbe et al., 2014; and 2013).

As mentioned above the difference between TG measurements and HDM often results in a bias. The significance of the bias between HDM and the vertical datum is frequently overlooked. This bias includes both model errors (e.g. mathematical approximations, uncertainty in initial and boundary conditions, etc.) and also vertical reference differences. This can essentially be composed of high- and low-frequency components. It is expected that the low-frequency component to compose of the vertical datum differences, thus being to some degree almost constant. This however is not always the case, for the bias can change with time and space. In this study a deeper exploration is made with quantifying the bias especially with respect to both the time-domain and space-domain. Quantification of the bias is a major component in correcting the HDM results to a more accurate and realistic DT estimates.

Once the bias correction is implemented in the HDM a Mean Dynamic Topography (MDT) can be calculated in any offshore location,

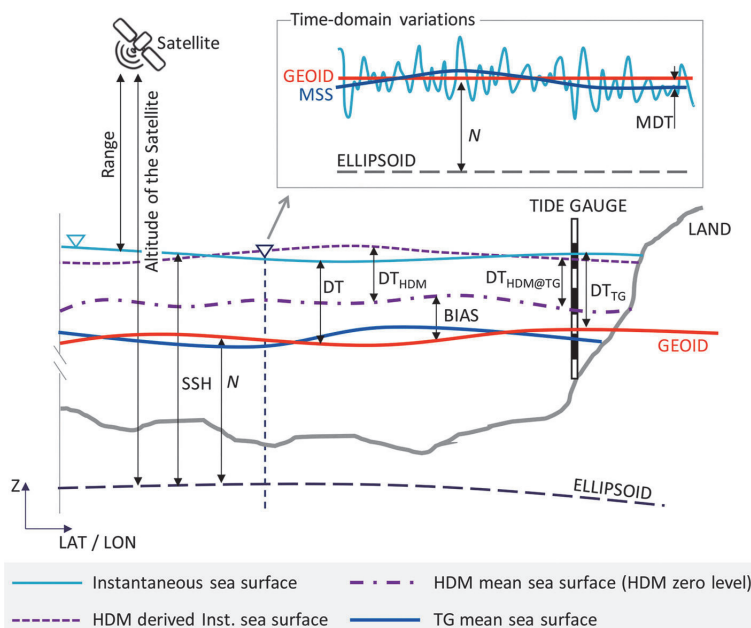


Fig. 1. Inter-relationships between hydrodynamic parameters and involved principal data types (satellite altimetry, tide gauges, hydrodynamic and geoid models) and the different vertical reference datums. For the used symbols and abbreviations please refer to the main text body.

which illustrates realistic changes in mean sea level values, extreme values, geostrophic currents etc. Note that the MDT is usually considered to be the difference between the mean sea surface and the geoid (Fig. 1). There are two ways in which the MDT can be calculated. Firstly by a geodetic approach, whereby knowledge of the mean sea surface (MSS) is derived from satellite altimetry or tide gauges records referred to a precise geoid model. The second and ocean approach utilizes HDM based sea level data (Idzanović et al., 2017). In this study we shall utilise a combined approach for we are not only interested in the DT at the coastal area but also extending in the offshore. This is to our knowledge, the first attempt of such a synergized exploration in the study area (Baltic Sea) and it is expected that similar forthcoming developments can be adapted internationally.

The eastern section of the Baltic Sea, the Gulf of Finland is used as a case study due to availability of a high density network of tide gauges, whose zero mark is referred to the geoid based national vertical datum (Kollo and Ellmann, 2019). The study area is also surrounded by three countries (Finland, Estonia and Russia) thus it is a very active and dynamic marine area. The vertical datum for Estonian tide gauges is EH2000 and the national height system in Finland is N2000, which both coincide with the BSCD2000. These characteristics make it an ideal area for testing out the method. It is the intention in this paper, to demonstrate the importance of incorporating of a static vertical reference surface such as the geoid into the marine applications and research.

This study utilizes eighteen TG stations along with two regional HDM (Nemo-Nordic and HBM-EST) for the Baltic Sea to examine: (i) the time and spatial domain changes of the bias in between the TG readings and the corresponding HDM estimates, (ii) development of a robust method that can be used for correction of the derived bias, that also retains the accuracy required and (iii) the contribution that correction of the bias has on the results in terms of instantaneous DT and MDT, not only at the TG locations but also in the offshore domain.

The organization of the present study is as follows. In Sec.2, the developed methodology is explained. In Sec. 3 the study area Gulf of Finland, Baltic Sea is described. In Sec.4, the different data sources utilized are highlighted, and the method of bias determining is explored. Sec. 5 presents the results of the bias and corrected HDM. A discussion on the method implemented and the results are presented in Sec. 6. Section 7 summarizes the main results and relevance of the paper.

2. General methodology

Several different sources of sea level data exist that are referred to different reference surfaces. Satellite altimetry and GNSS buoys both derive sea surface heights (SSH) that refer to geodetic reference ellipsoid. The TG records are usually given with respect to the geoid based vertical datum, yielding the near-shore dynamic topography (DT) values. Hence, at locations with coordinates (ϕ, λ) the ellipsoid referred SSH is obtained as follows (cf. also Fig. 1).

$$SSH(\phi, \lambda) = DT(\phi, \lambda) + N(\phi, \lambda) \quad (1)$$

where N is a ‘static’ geoid height referred to a geodetic reference ellipsoid.

Conversely, HDM often provides sea level variations with respect to an arbitrary vertical datum. Essentially, these are equivalent to DT, but not referred to the geoid. Due to this similarity, we denote the HDM derived sea level variations as DT_{HDM} . One of the most common vertical reference datums utilized by HDMs is the MSL (its exact definition can vary amongst models). The MSL is usually calculated from repeated SSH measurements for a suitable time period (Kakkuri and Poutanen, 1997). Thus many of the available sources tends to refer to a time changing vertical reference datum (e.g. LAT, MSL). It should be noted that the selected time span to calculate MSL may affect the estimation of this vertical reference. For most applications this ever-changing vertical datum is not sufficiently accurate and reliable. Instead, as mentioned

above, the focus of this study utilizes a static vertical reference surface such as the equipotential surface of the geoid to be utilized for referring the HDM data.

This study intends to calculate accurate DT anywhere offshore by correcting the HDM embedded sea level estimates. Therefore, the bias of HDM’s dynamic topography (DT_{HDM}) can be corrected by the network of TG records.

In practice, the HDM model bias is usually determined as the difference between the mean value of HDM at the tide gauge location ($\overline{DT}_{HDM@TG}$) and TG records within a certain time interval. Thus the dynamic topography bias is obtained as follows:

$$Bias_{HDM@TG} = \overline{DT}_{TG} - \overline{DT}_{HDM@TG} \quad (2)$$

where \overline{DT}_{TG} is the mean of dynamic topography during a certain time period (could also be a time instant) at the TG location. In previous studies (Lagemaa et al., 2011), the backward moving average (BMA) method (a simple low-pass filter) had been commonly used to correct the low-frequency bias of models, whereas the high-frequency DT fluctuations (e.g. period less than 7 days) were ignored by accepting some error. In this study we will show how the $Bias_{HDM@TG}$ estimates change by selecting different filter sizes, whereas this bias becomes unstable beyond certain threshold. In order to obtain $Bias_{HDM@TG}$, the previous studies compared the low-frequency part of the HDM time series with the near-coast TG records. Therefore, the time-domain bias ($TDBias$) at a m -th TG station is obtained from the following equation:

$$TDBias_{m,k}(i) = \frac{1}{k+1} \sum_{j=-k}^0 [DT_{TG_m}(i+j) - DT_{HDM@TG_m}(i+j)], \quad i > k \quad (3)$$

where i is the time index (i.e. in this study, 2014.01.01 00:00 denotes $i = 1$), j is a counter for summation, and k is the window-size of BMA, which will be investigated in the time-domain bias section (Sec. 4.3). The term of $DT_{HDM@TG}$ is the DT_{HDM} at the closest HDM node to the TG station. In the case $k = 0$, the instantaneous bias ($TDBias_{k=0}$) is calculated, which is the HDM exact bias with respect to the TG records. The corrected DT_{HDM} near m -th TG station ($DT_{HDM@TG}^{corr}$) at the time instant t is computed as follows:

$$DT_{HDM@TG_m}^{corr}(t) = DT_{HDM@TG_m}(t) + TDBias_m(t) \quad (4)$$

In order to select proper sample size (k) to correct the model, the residual standard deviation ($ResidSD$) is examined to determine $DT_{HDM@TG}^{corr}$ with required uncertainty. The $ResidSD$ for different k can be obtained as follows:

$$ResidSD_m(k) = \sqrt{\frac{\sum_{j=k+1}^n (\epsilon_{m,j} - \bar{\epsilon}_m)^2}{n - k - 1}} \quad (5)$$

where n is the total number of data at a particular location (e.g. $n = 2 \times 365 \times 24 = 17520$ for two years hourly DT data). In this equation, the $ResidSD$ is calculated based on the selecting windows-size of BMA. For instance, $n - (14 \times 24) = 17184$ data instances are used to calculate the $ResidSD$ of the corrected model by $k = 14$ days. The term of ϵ is the residual value of $DT_{HDM@TG}^{corr}$ with respect to the TG records, and $\bar{\epsilon}$ denotes the mean of ϵ (both depend on moving window k), which is calculated as follows:

$$\bar{\epsilon}_m(k) = \frac{1}{n-k} \sum_{j=k+1}^n \epsilon_{m,j} = \frac{1}{n-k} \sum_{j=k+1}^n [DT_{TG_m}(j) - DT_{HDM@TG_m}^{corr}(j)] \quad (6)$$

The $ResidSD$ can be utilized to assess the quality of $TDBias$ correction by different windows of the BMA method. Moreover, we will show why we favor using instantaneous $TDBias$ correction ($k = 0$) rather than a low-frequency correction (e.g. $k = 14$ days) in the time-domain bias section (Sec. 4.3).

Note that the calculated $TDBias$ by Eq. (3) is realistically applicable

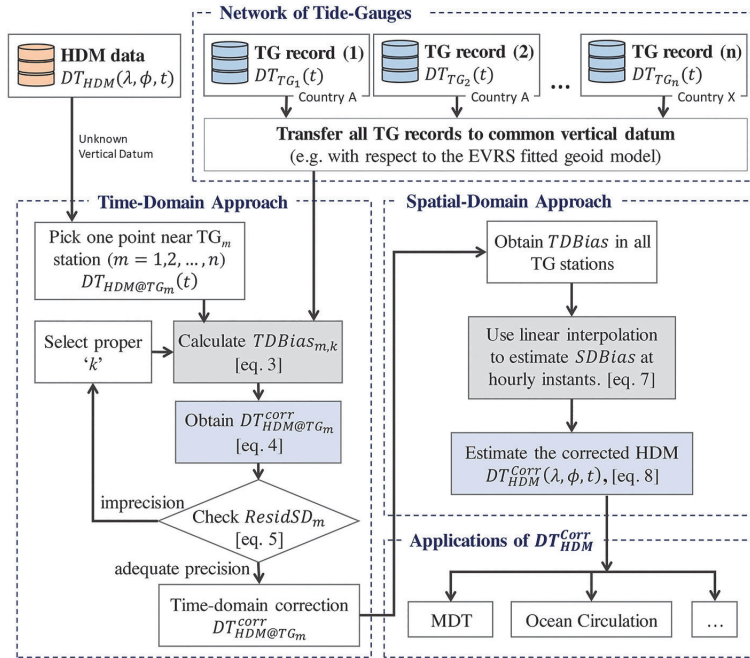


Fig. 2. Flowchart of the spatio-temporal correction of DT_{HDM} by using a network of geoid related tide-gauges.

near individual TG station. To calculate the bias in the offshore area a linear interpolation between the dense network of TG stations is employed, especially since the tide gauge stations are located on either side of the gulf. Such a method may not always perform well at the open sea, therefore more offshore data are needed to obtain and confirm the accurate $SDBias$ at the open sea. Hence, the spatial-domain bias ($SDBias$) can be numerically estimated (e.g. using a standard linear interpolation) inside the TG network loop ($DT_{HDM@TG_m}^{corr}$) at hourly instances t ,

$$SDBias(\phi, \lambda, t) = \text{interp}[\phi_{TG_m}, \lambda_{TG_m}, TDBias_{m,k}(t), \phi, \lambda] \quad (7)$$

and subsequently, the DT_{HDM}^{corr} is computed anywhere offshore with coordinates (ϕ, λ) as follows:

$$DT_{HDM}^{corr}(\phi, \lambda, t) = DT_{HDM}(\phi, \lambda, t) + SDBias(\phi, \lambda, t), t > t(k) \quad (8)$$

The schematic chart of the methodology applied to obtain DT_{HDM}^{corr} (at the HDM grid-points) is shown in Fig. 2. According to this process, the



Fig. 3. Location of the used tide-gauges (Table 1) in the study area (Gulf of Finland). The inset contains the location of the study area (enclosed by the red rectangle) in the Baltic Sea region.

HDM is examined near the tide gauge stations in the time domain, where the TG records are valid. The result allows to assess the pattern of the *TDBias* and determine the acceptable 'k' for this bias.

3. Study area

The Baltic Sea (BS) is a micro-tidal, semi-enclosed sea located in northern Europe and bounded by nine coastal countries (Fig. 3). An estuarine type of environment exists whereby large freshwater input from continental rivers and salty water intrusions from the Atlantic Ocean through the narrow connection (via Danish Straits) with the North Sea leads to the formation of the strongly stratified water column. The average water depth of the BS is approximately 52 m. It is usual in the winter months for parts of the BS to become ice-covered, especially in the northern and eastern sections. The dominant wind direction in this area is south-westerly however it is quite common for northerly winds to also be prevalent (Soomere and Keevallik, 2001). The winter and autumn seasons tend to have the strongest winds and highest waves (Jakimavičius et al., 2018).

There exist several components that affect the sea level in this water body. In terms of a long-term effect it is expected that the global sea level change (due to thermal sea water expansion and melting of glaciers) will influence the Baltic Sea level. The variation in temperature, precipitation and evaporation is expected to mostly influence on a decadal time scale. There are suggestions that temperature and precipitation may account for 15% of the sea level variability in winter and as much as 35% in summer to (Hünicke and Zorita, 2006).

For short term influences (yearly, seasonally, daily etc.) variation in the water balance caused by water exchange in the Danish Straits e.g. saltwater intrusions from the Atlantic (Major Baltic Inflow) that are driven by atmospheric conditions may cause drastic sea level changes. For example, in 1993 within 21 days the inflow raised the mean sea level by 70 cm (Matthaus and Lass, 1995). The last major intrusion occurred in December 2014 (Schimanke et al., 2014). As expected, river runoff also affects the water balance, with the biggest freshwater contributor being the Neva river located on eastern side of the Baltic Sea (Myrberg and Soomere, 2013). The decrease in sea ice days is also expected to change the dynamics of the sea level in the Baltic sea (Rosentau et al., 2017). There are some localized events that affect the sea level on much shorter time frame, for example in terms of weeks, daily and even hourly. Most of these events tends to be influenced by the meteorological factors especially the winds that can be strongly anisotropic in the Baltic Sea (Soomere, 2003). For instance, storm surges (Suursaar and Sooäär, 2007) and coastal upwellings (Delpeche-Ellmann et al., 2017) are quite prevalent in the Baltic Sea with a more or less seasonal trend.

The focus of this study is on the Gulf of Finland (cf. Fig. 3) which is in the easternmost section of the Baltic Sea. The gulf is a narrow and elongated sea with a length of approximately 400 km and width varying from 48–135 km. The mean water depth is around 37 m (maximum depth is 123 m). Water exchange occurs with the adjacent basin through an interplay of estuarine and wind-driven processes and also frequent storm waves generated in the open sea that penetrate into the gulf. Therefore it is expected that many of the components affecting sea level in the Baltic Sea mentioned above will also influence the gulf.

An overall cyclonic type circulation exists with a surface import along the Estonian coast and an export along the northern Finnish coast (Myrberg and Soomere, 2013). There also exists evidence of cross shore-transport occurring at particular locations that are influenced by the winds, underlying layers dynamics and coastal upwellings that frequent mostly during the summer months (Delpeche-Ellmann et al., 2018; and 2017; Soomere et al., 2011). These dynamics also expected to spatially influence the short-term sea level variability.

Strong westerly winds are known for increasing water levels especially in the eastern section where it creates a tilt of water surface (Pindsoo and Soomere, 2020). For instance for the years 2014–2017 the mean sea surface topography increases eastwards in the gulf by

approximately 10 cm (Kollo and Ellmann, 2019). There are thoughts that a change in the wind regime (wind direction and storminess) may be influencing the mean sea level and extreme maxima found in the easternmost sections of the Gulf with a rate of 8–10 mm/yr. For instance, extreme events such as storm surges may be more prominent in the coastal areas e.g. St. Petersburg area and Pärnu Bay area (Fig. 3) and in the low-lying areas such as the west Estonian bays (Suursaar and Sooäär, 2007). These extreme events are expected to occur on a shorter time scale.

Therefore, there exist many suggestions and thoughts with respect to the changes occurring in the Baltic Sea mean and extreme sea level and even water volume. With the changing wind patterns, sea ice days combined with vertical land crust movements has led to various point of view in the changes that takes place in different parts of the BS. Thus, the method to be explored in this study may bring some clarity to realistically quantifying the sea level estimates.

4. Method and data

4.1. Geoid referred tide gauge data

A network of 14 + 4 Estonian and Finnish tide gauge stations were utilized for obtaining the hourly in-situ sea level data (see Fig. 3 and Table 1). The zero marks of the utilized Estonian TG stations coincide with a recent high-resolution (0.01×0.02 arc-deg) regional geoid model EST-GEOID2017 (Ellmann et al., 2020). The geoid model is fitted to the national realization of the EVRS vertical datum, EH2000, the zero level of which is the Normaal Amsterdams Peil (NAP) and complies with BSCD2000. The Finnish TG records are converted from the national "theoretical mean sea level" standard (FMI, 2020a) into the national height system N2000, which is the Finnish realization of the EVRS and coincides with BSCD2000 as well. Further principles on processing of TG data can be obtained from Kollo and Ellmann (2019).

Land uplift due to postglacial rebound (PGR) increases northwards from 0.2 (Häädemeeste, TG-12) to 3.5 mm/year (Turku, TG-18) to 1.7 mm/year (Hamina, TG-15) according to model NKG2005LU (Ågren and Svensson, 2007). For the sake of rigourity, the tide gauge records were corrected for this vertical displacement.

Thus, all TG records express DT_{TG} with respect to the geoid model. The Estonian TG network are operated by the Estonian Environmental Agency (EEA, 2020) and can be sourced from: <http://ilmateenistus.ee>. The Finnish TG data were obtained from the Finnish Meteorological Institute tide gauge network data (FMI, 2020b) and can be sourced from <https://ilmatiiteenlaitos.fi>. The characteristics of the used TG stations are represented in Table 1.

A comparison between the annual 2014 and 2015 TG data reveals that, on average, the 2015 mean sea level (MSL) within the study area increased by 21 cm, and the standard deviation (SD) by 5 cm from 2014 to 2015. This denotes large inter-annual sea level variability, possibly depending on the factors that influence the water balance (e.g. Baltic inflows, storminess, presence of sea ice etc.). In general, the SD remains within 18–29 cm, whereas the larger SD is expected to be associated with the rougher sea conditions at individual TG stations. Higher annual SD may thus hint at the stormier years. The smaller SD estimates may also reveal sea sheltered locations of certain tide gauges. This possibly signifies the rapidly changing sea conditions, which, as mentioned in the introduction, the TG records can reflect these conditions only at the near shore, however offshore conditions are expected to be different. Hence the TG stations standalone cannot serve as the reference dataset, and instead, a reliable HDM can be used offshore.

4.2. Hydrodynamic model

The two HDM utilized in this study were the Nemo-Nordic developed by Swedish Meteorological and Hydrological Institutes (Hordoir et al., 2019) which was obtained in forecast mode, and the HBM-EST

Table 1

The Estonian and Finnish TG stations are listed from 1 to 14 and 15 to 18, respectively (cf. Fig. 3). The MSL refers to EVRS vertical datum.

TG No.	TG Name	Longitude arc-degree	Latitude arc-degree	MSL2014 [cm]	SD 2014 [cm]	MSL2015[cm]	SD 2015 [cm]
TG-01	Narva-Jõesuu	28.0421	59.4690	15.3	23.4	38.5	28.8
TG-02	Kunda	26.5417	59.5210	12.6	22.0	36.0	27.1
TG-03	Loksa	25.7072	59.5844	13.7	21.4	35.3	26.3
TG-04	Rohuneeme	24.7912	59.5589	8.5	21.2	30.7	25.5
TG-05	Pirita	24.8208	59.4688	8.3	20.9	28.8	25.3
TG-06	Dirhami	23.4969	59.2084	8.4	20.5	29.4	24.8
TG-07	Haapsalu	23.5274	58.9580	8.3	21.8	30.3	27.0
TG-08	Heltermaa	23.0471	58.8655	12.8	21.3	36.6	25.0
TG-09	Ristna	22.0551	58.9212	8.9	20.1	28.9	24.7
TG-10	Virtsu	23.5112	58.5722	9.7	22.1	31.2	27.0
TG-11	Pärnu	24.4778	58.3865	11.1	25.5	35.3	30.6
TG-12	Häädemeeste	24.4636	58.0374	10.6	23.7	30.7	27.6
TG-13	Roomassaare	22.5037	58.2172	8.4	20.6	29.0	25.1
TG-14	Ruhnu	23.2635	57.7835	14.3	22.1	33.8	25.9
TG-15	Hamina	27.1792	60.5627	11.0	22.3	33.5	28.6
TG-16	Helsinki	24.9562	60.1536	9.2	19.8	30.0	25.6
TG-17	Hanko	22.9765	59.8228	8.1	18.7	27.3	23.8
TG-18	Turku	22.1005	60.4282	6.6	18.4	25.5	23.8

Table 2

Basic properties of the Baltic Sea HDM set-ups (cf. Hordoir et al., 2019; Lagema et al., 2011).

	Nemo-Nordic	HBM-EST
Atmospheric forcing	Combination of hourly ECMWF LL01 and Arome data	HIRLAM
Horizontal grid resolution	2 NM	0.5 NM
Vertical grid resolution	56	50
Temporal resolution	One hour	One hour
Open boundary forcing	ECMWF forecast data	NOAMOD ^a
Ice modelling	Yes (LIM3)	Yes
River runoff	HYPE	HBV
Vertical datum	Not specified	Not specified
Grid nodes in study area	2952	10507

^a North Atlantic MODEL; a storm surge model.

developed by the Marine Systems Institute (Lagema et al., 2011) which was in operational mode and obtained from the Estonian Marine area Information System (EMIS): <http://emis.msi.ttu.ee>. The main model characteristics of two HDMs are compared in Table 2.

The Nemo-Nordic is a three-dimensional ocean-ice coupled model of

the Baltic and the North Sea, that is based on the NEMO ocean engine. A nonlinear explicit free surface method is utilized, with a time-splitting approach that computes a barotropic and a baroclinic mode, as well as the interaction between them. A horizontal resolution of 2 nautical miles was utilized and a z-vertical coordinate system whereby the vertical resolution is adapted to the physical properties of the Baltic and North seas. There exist 56 vertical levels with the upper levels each having a thickness of approximately 3 m.

The boundary conditions play a vital role in the prediction of sea level data. For Nemo-Nordic, two open boundaries are utilized: a meridional one in the western part of the English Channel and a zonal one set between Scotland and Norway. In terms of the atmospheric forcings a combination of hourly European Centre for Medium-Range Weather Forecasts data (ECMWF LL01, 9 km) and Application of Research to Operations at Mesoscale data (AROME, 2.5 km) was utilized. River discharge data were obtained from Hydrological Predictions for the Environment (HYPE) and sea ice data from Louvain-la-Neuve sea ice model (LIM3) (Hordoir et al., 2019). Nemo-Nordic data is available with an hourly time step. The bathymetry of the model was obtained from the General Bathymetric Chart of the Oceans (GEBCO-2014) Grid. The actual vertical datum used to represent the sea level in the models is however not exactly specified. We will show that the HDM used vertical datum is changing both temporally and spatially. Due to need for the actual absolute values it becomes imperative to reduce the zero of models to a stable vertical reference datum. Fig. 4 (left) shows the

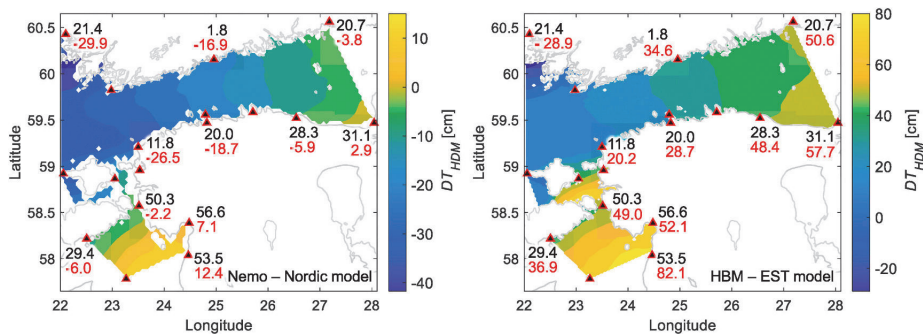


Fig. 4. Comparing dynamic topography DT_{HDM} of Nemo-Nordic (left) and HBM-EST (right) models that referred to the different vertical reference surfaces at an arbitrary time instant: 15 Mar 2014 15:00 UTC. The red values refer to the $DT_{HDM|TG}$ nearby TG stations, whereas the black values are the corresponding DT_{TG} referred to the EVRS vertical datum.

modelled DT_{HDM} of this model in an arbitrary time instant over the study area.

The HBM-EST model is currently used for mostly operational sea level forecast in Estonian marine water and plays a crucial role in the short-term prediction of the sea level in marginal seas and coastal areas. The core of the model system is a 3-dimensional baroclinic eddy-resolving circulation model. This model provides horizontal resolution of 0.5 nautical miles. This model is divided into 50 vertical layers, with the thickness of each layer 4 m in the upper 80 m, and slowly increasing towards the greater depths. The temporal resolution of the model is 1 h. The HBM-EST atmospheric forcings are sourced by the high-resolution limited area model (HIRLAM) with hourly time step and horizontal resolution of 22 km. The open boundary of the HBM-EST model is located at the Danish Straits, i.e. the western edge of the Baltic Sea. The daily data from the river runoff model HBV (Hydrologiska Byråns Vattenbalansavdelning) is used for freshwater inflow (Funkquist and Kleine, 1999; Lagemaal et al., 2011). Fig. 4 (right) shows the simulated DT_{HDM} of HBM-EST at an arbitrary time instant over the study area.

4.3. Time-domain bias approach

In order to determine the differences between the DT_{HDM} and DT_{TG} , the model grid point located closest to the TG stations are selected and extracted to produce the $DT_{HDM@TG}$ time-series. This was performed for all 18 used TG stations. An example of time-series and the difference between them (instantaneous $TDBias$ according to Eq. (3)) are shown in Fig. 5 at the easternmost Narva-Jõesuu station. Observe that this bias is actually not constant, it varies from 0 to 100 cm and -80–30 cm in Nemo-Nordic and HBM-EST model over the years 2014–2015, respectively. Notice also sudden peaks of the $TDBias$ estimates, whereas the seasonality of the bias is obvious with peaks in the winter and spring seasons. This may reflect problems with sea-ice modelling or atmospheric forcings in the Nemo-Nordic and also the fact that the HBM-EST is in operational model with some quality controls being performed using certain in-situ TG stations.

As can be seen in Fig. 5, the instantaneous $TDBias_{k=0}$ of the models has both a high- and low-frequency components. Previous studies have also observed the bias in models to exist and have usually solved the problem by focusing on the low-frequency part of the $TDBias$ by utilizing the moving average method as a low-pass filter that uses a particular time period (Lagemaal et al., 2011; Varbla et al., 2020a).

We examine this period further by employing an autocorrelation

function as a useful tool for periodicity detection and finding time dependent patterns that can be utilized to calculate a proper moving average window ‘ k ’ for this method (cf. Eq. (3)). The autocorrelation is calculated as a function of the time-lag (τ) which can be expressed as follows:

$$R_{xx}(\tau) = E[x_t x_{t-\tau}^*] \tag{9}$$

where E denotes the expected value operator of time series x , whereas x is the standardized error of HDM with respect to the tide gauge station (i.e. $TDBias$, where $k = 0$). The asterisk denotes complex conjugation.

The autocorrelation of the error for the two models has been illustrated in Fig. 6, which shows that the time series of error have two main periods: 2-week and daily. These periodic can possibly be due to the short-term unpredictability of some periodic phenomena that models are unable to account for. Although the longer periods of error (e.g. seasonal period can be seen more in the Nemo-Nordic model) may have the same reason, they can also illustrate the problem of models due to the use of unrealistic vertical reference surface. In the present study, we investigate the $ResidSD$ of low-frequency correction by different window-size of BMA (cf. Eq. (5)). Therefore, according to Fig. 6, the 2-weeks can be the largest suitable window-size for low-frequency correction, and selecting the k larger than 2-week will result in an additional bias in the corrected model. In this sense, the calculated 2-week is an optimal compromise between the accuracy and computational effort.

Fig. 7 illustrates the smoothed dynamic topography (left column) with a 14-days BMA method, the low-frequency bias ($TDBias_{k=14 \text{ days}}$) of models (middle column), and corrected models versus TG records near the 4 stations. The corresponding average $ResidSD$ for Nemo-Nordic and HBM-EST models are 4.8 cm and 7.1 cm, respectively. Examination of the difference between the smoothed tide gauge records and HDM (low-frequency bias) shows several interesting characteristics: (i) that the $TDB_{k=14 \text{ days}}$ is not constant during the time, thus the large value of ‘ k ’ such as seasonal and annual bias-correction could be very erroneous if ever applied, (ii) From the Nemo-Nordic model an under-estimation trend is observed whilst for HBM-EST an over-estimation is present and (iii) the high-frequency component of the signal is not present, thus important characteristics related to the immediate/rapid dynamics at a location in time may be lost. This detail is very important for some applications (e.g. navigation, storm surges prediction etc.).

Whilst application of only the low-frequency bias produces

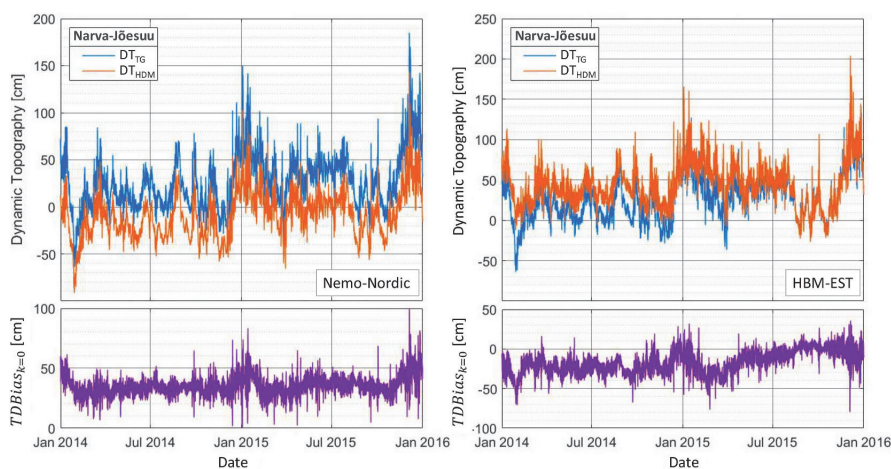


Fig. 5. An example of DT_{TG} , DT_{HDM} from Nemo-Nordic (left) and HBM-EST (right) in location of Narva-Jõesuu station (top). The instantaneous $TDBias$ between HDM and TG are shown in bottom.

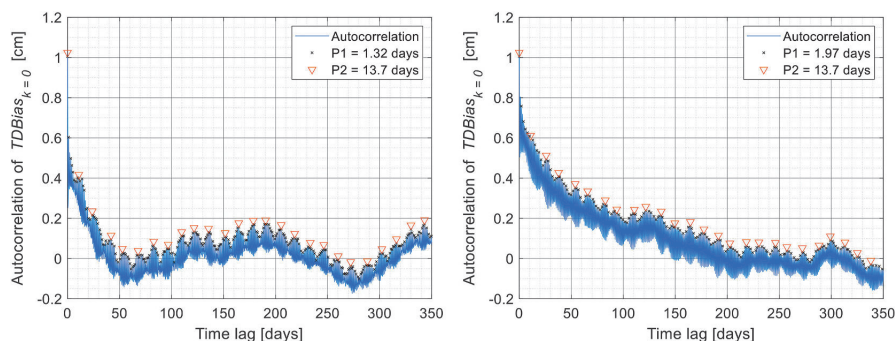


Fig. 6. The autocorrelation of $TDBias_{k=0}$ (instantaneous difference between TG and HDM) of Nemo-Nordic (left) and HBM-EST (right) at the Narva-Jõesuu TG station. The observed peaks suggest a periodicity in the $TDBias_{k=0}$. Two dominant periods, P1 and P2, are identified in both models.

reasonable results for some application, we observed that there still exist some discrepancies. The calculated $ResidSD$ is still too large for the aimed accuracy (5 cm) and the high frequency component is now smoothed out.

The magnitude of the $TDBias_{k=14 \text{ days}}$ also varies amongst the different TG stations (Fig. 8). The bias of HBM-EST model for the different stations is more concentrated than Nemo-Nordic model. This hints towards a better spatial performance of the HBM-EST model in the study area. Notice that in the Nemo-Nordic model the Narva-Jõesuu and Pärnu stations appears to have a larger $ResidSD$ than other TG stations (Fig. 9). It also reveals that not only a $TDBias$ exists but also that of a spatial-domain bias ($SDBias$). This comparison is also useful for providing spatial distribution of the stations that may require further investigation.

Figs. 7 and 8 show that the $ResidSD$ between corrected model and the actual TG observation can represent the quality of $TDBias$ correction near the tide-gauge stations. The question still remains on determining the appropriate time period (window-size) that should be used for allowing the required accuracy. Hence, Fig. 9 illustrates this criterion (Eq. (5)) and the mean of residual values versus using different time interval 'k' for all the stations.

Fig. 9 displays that in order to correct the models with high precision (uncertainty less than 5 cm), the window-size of BMA should be selected smaller than 6-h. Thus, it is reasonable to prefer an instantaneous approach ($k = 0$) since it does not require much more effort in terms of computational capabilities and allows better precision. It should be noted that a 6-h filtering window is also a reasonable quantification especially under storm events, when the water level changes rapidly and this is reflected at the tide gauges stations located at the coast but not always reflected by the hydrodynamic models. This is to be examined in future studies.

Fig. 9 also displays that the mean of residual for window-size longer than 14-days does not equal to zero and this was also showed in Fig. 7 (right) with large $ResidSD$ being present even after the $TDBias$ correction. Thus, a $TDBias$ correction with $k > 14$ days appears to be inaccurate and imprecise. Hence the 14 days is the longest time period for the averaging that can be allowed. Thus, we have identified an appropriate time period that can be utilized for the $TDBias$ and its associated errors. Note that with a low-frequency bias correction approach, whilst appropriate for many forecasting studies and other applications, some useful details are still lost concerning the high frequency component. Thus, in this study we explore an instantaneous $TDBias$ (exact bias, where $k = 0$) approach to calculate corrected $DT_{HDM@TG_m}^{corr}$.

5. Results

So far, the $TDBias$ is valid only near the coast in the vicinity of the TG.

This bias however is expected to change from the TG locations in an along-shore and offshore directions due to changing sea conditions. Due to the dense network of tide gauges available and their locations (on either side of the gulf) a reasonable assumption can be that the bias of the models more or less changes linearly in spatial directions. Henceforth a spatial linear interpolation between the TG stations can provide a suitable estimation of a spatial-domain bias ($SDBias$) in the offshore areas. The method is not perfect, but it allows a first approximation of the offshore bias over the entire study area. Based on $SDBias$ the resulting DT_{HDM}^{corr} was also calculated for each time step correlating with the model setup. The instantaneous (exact) $TDBias$ estimates at the eighteen TG stations (Fig. 3) have been utilized to obtain spatial interpolation to the offshore areas. Examples of the results obtained for the $SDBias$ and DT_{HDM}^{corr} are now presented below.

5.1. Spatial-domain bias correction

The $SDBias$ were computed for all grid nodes of the model and from these calculations the corrected models are determined by Eq. (8). An example of DT_{HDM} , $SDBias$ and the DT_{HDM}^{corr} for both HDMs, at a particular time-instant (15 Mar 2014, 15:00 UTC) is shown in (Fig. 10).

At this time instant the winds were mostly blowing from the north-east (Fig. 10) so it is intuitively expected that a higher sea level will occur on the Estonian coast. Both models (uncorrected and corrected, Fig. 10) and the DT_{TG} data display more or less this trend. Observe, however, that from the uncorrected model DT_{HDM} results (Fig. 10a and d) it is quite visible that the vertical reference datum differs between the two models. Thus, emphasizing once more the need for the models to have a common vertical reference datum. Also observe that, the discrepancies change spatially due to varying $SDBias$ (Fig. 10b and e). Such observations were also displayed in Sec. 4.3, for all the TG stations but now similar patterns are also shown for the offshore areas.

For this time instant, the magnitude of $SDBias$ for Nemo-Nordic is larger on Estonian side (41.4 cm, TG-03 (Loksa)) than on the Finnish side (18.7 cm, TG-16 (Helsinki)). Whilst for the HBM-EST model the DT_{HDM} is larger on the on Finnish side (-33 cm, TG-16 (Helsinki)) than that of the Estonian side (8.4 cm, TG-03 (Loksa)). In this example the $SDBias$ of both models display different trends on both coasts. This emphasized the complexity of the two different model configurations (e.g. atmospheric forcing, boundary conditions etc.) for it was shown in Sec. 4.3 that Nemo-Nordic model tends to underestimate and HBM-EST model overestimate the actual DT. Thus it is expected that on some occasions the trend of the bias between both models to differ. Regardless, after the $SDBias$ correction has been applied the DT_{HDM}^{corr} of both models (Fig. 10c and f) are quite similar with some slight differences and most importantly they now refer to a common vertical datum.

The DT_{HDM}^{corr} of both models whilst now visually quite similar also

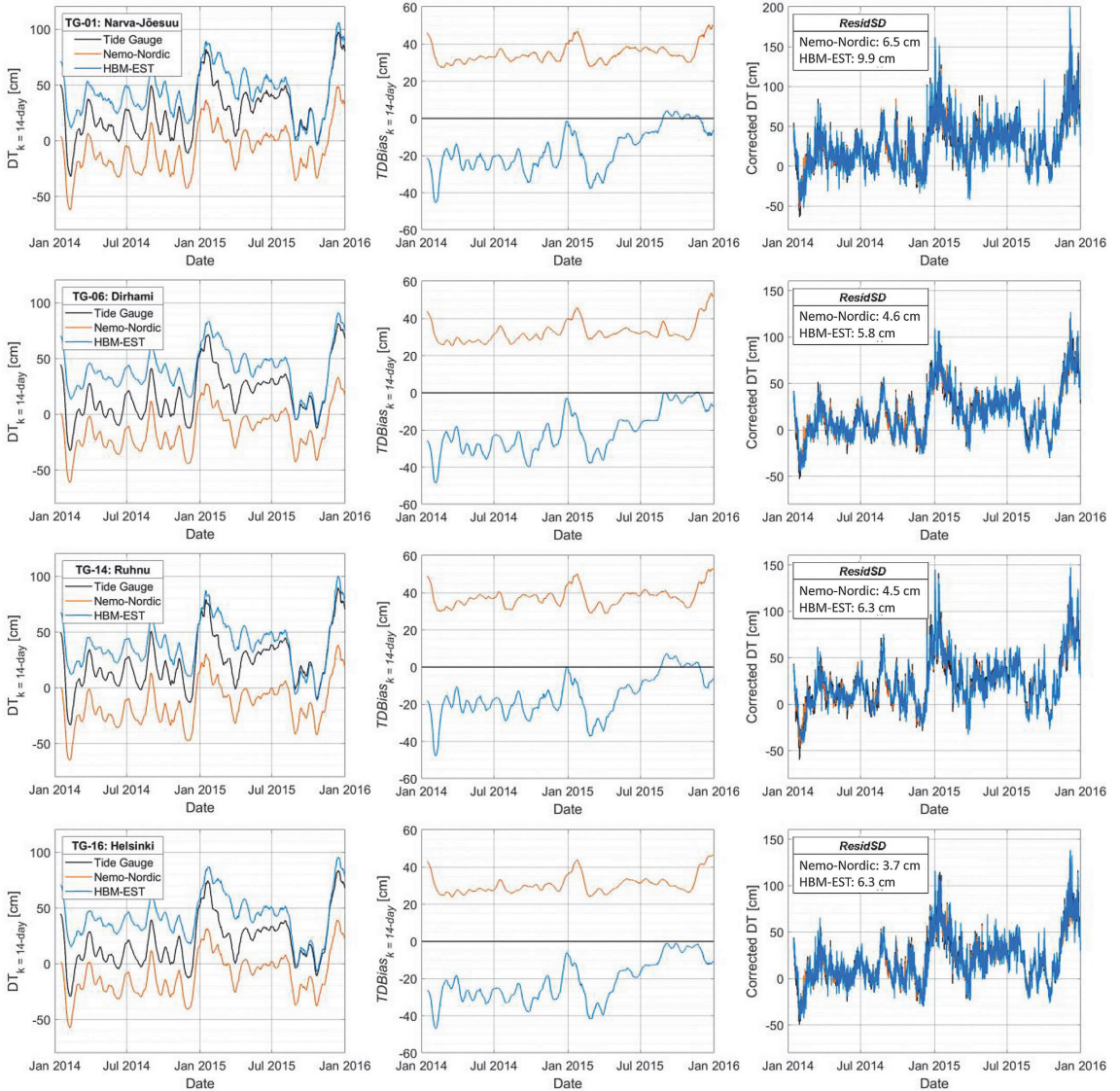


Fig. 7. The low-frequency time-domain correction of model with the $k = 14$ - day backward moving average method: The low-frequency record of TG and models (left column), low-frequency bias (middle column), the zero line denotes the TG record as reference, and instantaneous records of TG and corrected models using the 14-day BMA method (right column). Each row represents a tide gauge station: Narva-Jõesuu, Dirhami, Ruhnu, and Hamina (from top to bottom respectively). For their locations see Fig. 2. $ResidSD$ is standard deviation of error between DT_{HDM}^{corr} and DT_{TG} .

showed some slight differences. Comparison of these differences (Fig. 11a) shows that the DT_{HDM}^{corr} of the two models yield relatively small differences with respect to each other on 15 Mar 2014 15:00 UTC (cf. Fig. 10). The average spatial standard deviation of discrepancies between two model (in the same mesh grid that contains 2952 nodes) is 5.7 cm with a range from -35 to 5 cm. Note that this time-instant was deliberately chosen to show, that the largest discrepancy between the two models occurs in the west entrance of the gulf. This may be a result of the challenging conditions of the archipelago area, which is situated north-west from the anomaly in question, or due to some feature that is under/overestimated in set up of one of the models (see Table 2).

It should be noted that the distribution of spatial discrepancy between models changes in time. Examination of the average spatial standard deviation during the years 2014–2015 shows that the average spatial SD remains within 0.5 – 7.0 cm (Fig. 11b). It is important to note that the highest differences occur in the winter and spring months (Fig. 11b). These differences between the Nemo-Nordic and the HBM-EST and the times and location that they occur gives useful hints on possible improvements that can be made in the HDM model set up (e.g. sea ice modelling, atmospheric forcings). Similar observations were also made with the TDBias calculated for Narva-Jõesuu station (Sec. 4.3, Fig. 5).

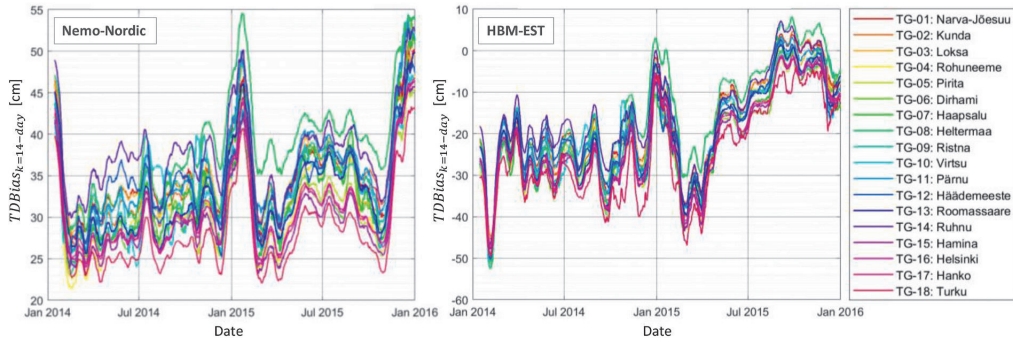


Fig. 8. The $TDBias_{k=14\text{-day}}$ of each model in different measurement stations.

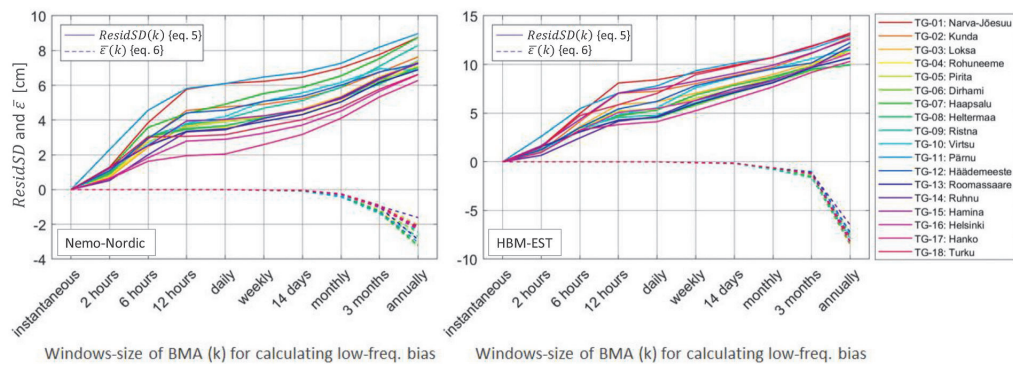


Fig. 9. The residual standard deviation ($ResidSD$) and mean of residual value ($\bar{\epsilon}$) between DT_{HDM}^{corr} and DT_{TG_n} in different stations during the years 2014–2015 versus the window-size (k) of BMA.

The seasonal snapshots at random time instances highlight some particular interesting features (Fig. 12 and Fig. 13). Firstly, from a seasonal perspective the DT_{HDM}^{corr} of both models agree reasonably well and show major improvements from the DT_{HDM} . For instance, the isolines of the corrected model (Figs. 12 and 13 (right)) agree much better than that of the uncorrected model (Figs. 12 and 13 (left)). This is also highlighted in Fig. 11b where a maximum average spatial SD of 7 cm was achieved, with the summer months showing the lowest difference, whereas the largest differences are attributed to the winter season.

Secondly, the bias to DT ratio in Nemo-Nordic is two (i.e. four times larger than the HBM-EST ratio 0.47), and this makes the shape of $SDBias$ (the quality of interpolation) more important in the DT correction. Hence, the models with a lower bias to the DT ratio provides better DT estimates.

Thirdly, and as expected, the DT varies seasonally and this is emphasized in Figs. 10, 12 and 13, where the range at Narva-Jõesuu station (Figs. 10 and 12) varied from 31.1 cm in Mar, 12 cm in Jul, -3.8 cm in Oct, and 90.1 cm in Jan. Whilst this just emphasizes particular time instances it is possible that calculation of a seasonal DT will illustrate some of the seasonal patterns and ranges that may exist (see Sec. 5.2). These snapshots also display the importance of the atmospheric forcings and possibly sea ice days which obviously influences the DT. Fig. 12 (right) and Fig. 13 (right) also display that the unidirectional and persistent winds can affect the sea level heights to tilt from one side of the gulf to opposite one. The anisotropy of the winds (in terms of magnitude and direction) can also display a variety of different sea level trends spatially. Thus, having stable vertical reference datum can actually allow deeper insight into some of the issues with the HDM

modelling. This can be performed iteratively using a combination of different sources.

To demonstrate the areal correlation between the deviation of the bias and variation of the corrected DT, the spatial distribution of the standard deviation (SD) of $SDBias$ as well as corrected DT of both models are illustrated in Fig. 14. As can be seen, the HBM-EST has a bigger variation in $SDBias$ than Nemo-Nordic (top-left), which can imply that Nemo-Nordic provides more precise results than HBM-EST. Moreover, both HDMs provide bigger dispersion in the bias on the Estonian side than the Finnish side, which is worth considering from the perspective of modelling. By comparing the spatial distribution of the standard deviation of the corrected DT, almost similar isoline and magnitude can be seen in the open sea area.

According to Fig. 14, the standard deviation of $SDBias$ almost increases in a southerly direction, while the standard deviation of corrected DT increases from the west to the east direction. However, the higher standard deviation of the bias is coincident with the larger variation of the corrected DT in some places, such as the Narva-Jõesuu and Pärnu TG stations where the rivers discharge to the sea.

5.2. Mean dynamic topography

So far knowledge on the $TDBias$ and $SDBias$ allows us to calculate DT_{HDM}^{corr} and as a result of temporal averaging we can also obtain the Mean Dynamic Topography (MDT). Recall the DT represents the sea level that deviates from the geoid. Since the ocean is influenced by winds and tides the DT is expected to vary on different time scales and spatially. It is expected however that persistent or semi/persistent dynamics pattern

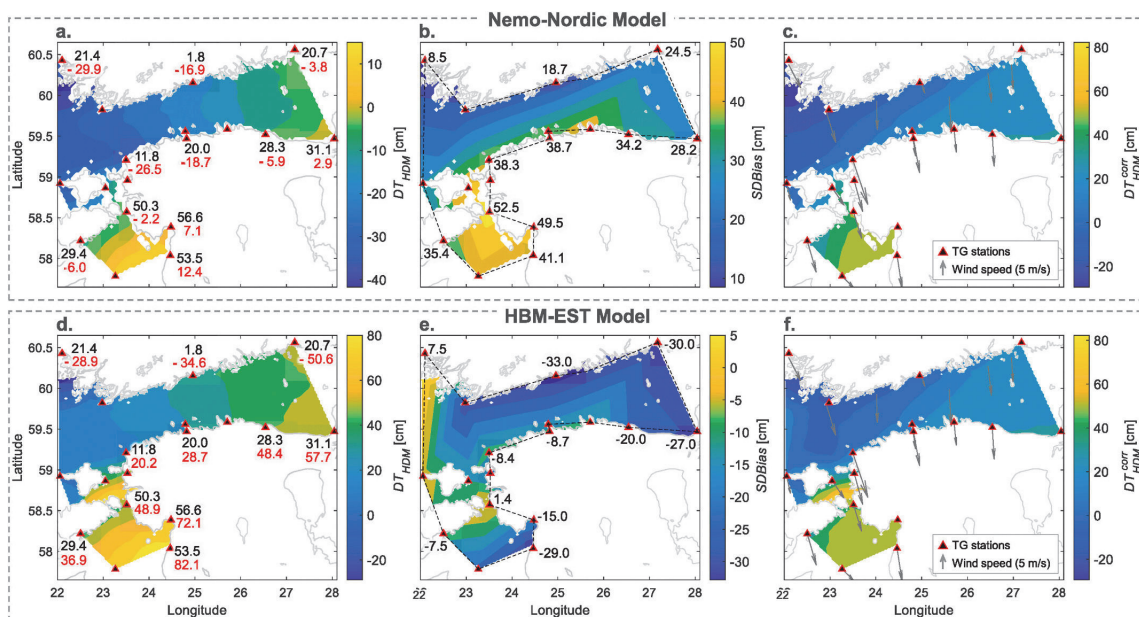


Fig. 10. Correcting process of Nemo-Nordic (top row) and HBM-EST (bottom row) model at the same time instant: 15 Mar 2014 15:00 UTC: uncorrected model DT_{HDM} (left column), the spatial-domain bias $SDBias$ (middle column), and corrected dynamic topography DT_{HDM}^{corr} (right column). The black and red values refer to TG records and HDM at some of the stations (denoted by triangles), respectively. The grey arrows demonstrate the measured wind velocity and direction at the same time; source of wind data: (EEA, 2020; FMI, 2020a).

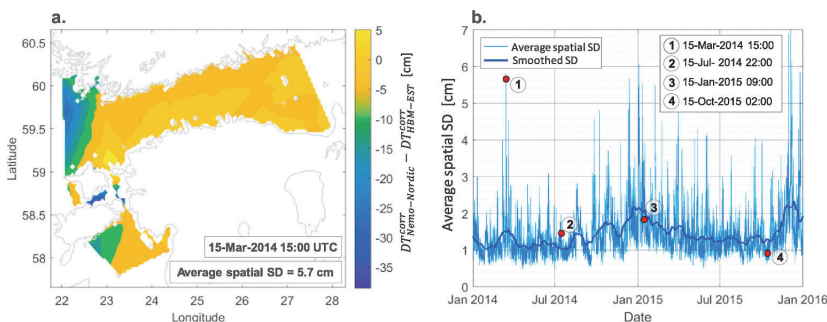


Fig. 11. a. Difference between corrected dynamic topography DT_{HDM}^{corr} of two models (cf. Fig. 10) at the selected time instant, and b. the variation of average spatial SD between corrected DT during the years 2014–2015. The red dots are relevant to the four arbitrary time-instants of Figs. 10, 12 and 13.

characteristics would be revealed by the MDT over different time scales (seasonal, annual etc.).

The uncorrected and corrected MDT for different time periods (bi-annual, annual, seasonal) are calculated for the years 2014–2015 using the DT_{HDM} and DT_{HDM}^{corr} for each MDT gridpoint with location ϕ, λ ,

$$MDT_{HDM}(\phi, \lambda, t) = \frac{\sum_{i=1}^n DT_{HDM}(\phi, \lambda, i)}{n} \quad (10)$$

$$MDT_{HDM}^{corr}(\phi, \lambda, t) = \frac{\sum_{i=1}^n DT_{HDM}^{corr}(\phi, \lambda, i)}{n} \quad (11)$$

respectively, where n denotes the total number of involved hourly time instances t . For instance, $n = 2 \times 365 \times 24 = 17520$ for two years

hourly DT data.

The MDT estimates will be compared with previous studies of MDT_{TG} in the study area using tide gauge data only (Kollo and Ellmann, 2019). This time scale of two years is perhaps too short to reasonably identify any semi-persistent seasonal or annual trends. It instead allows evaluation of the success of model correction and agreement between both used HDM.

To illustrate the effect of having a stable vertical reference datum (the geoid) the MDT_{HDM} of uncorrected models are compared to MDT_{HDM}^{corr} in Figs. 15 and 16. In both models, the MDT increases from southwest to northeast with obvious variations with respect to each other. Examination of the MDT_{HDM}^{corr} also displays a general increase from west to east, however there is intrinsically major difference between the patterns and

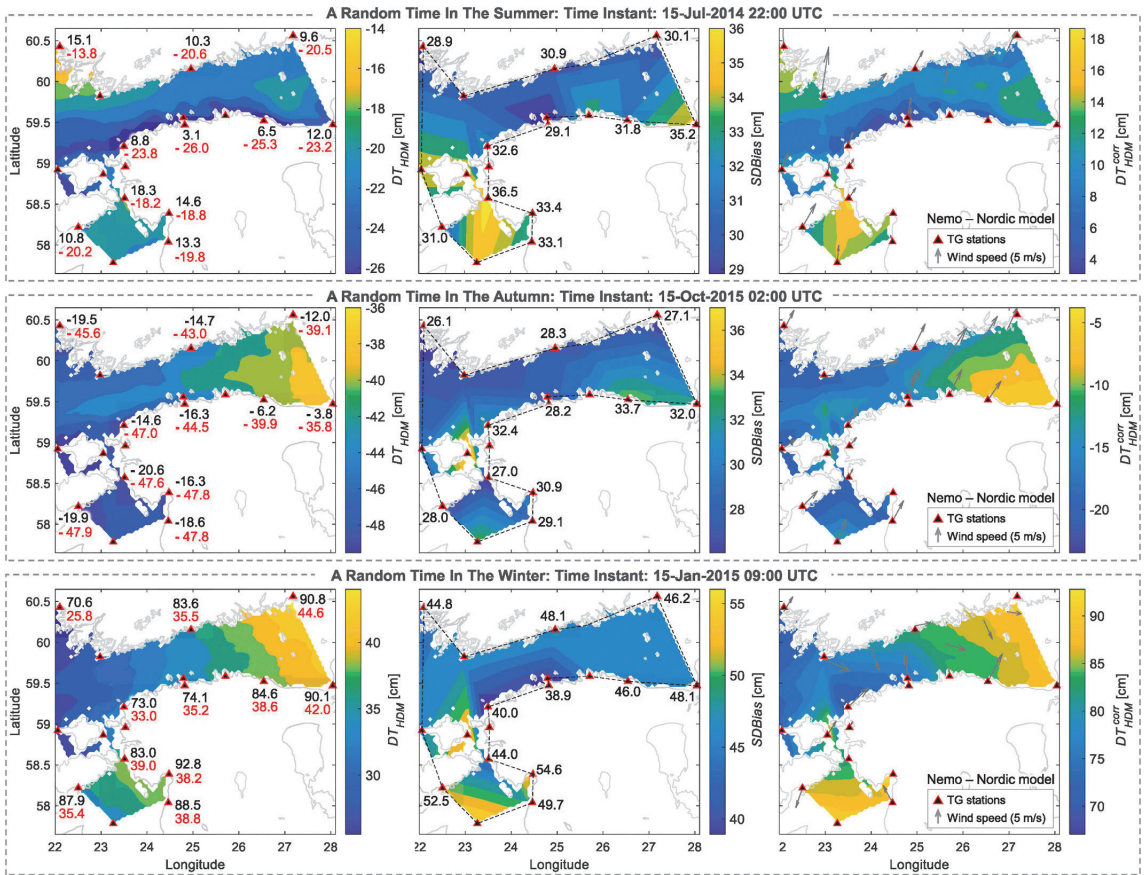


Fig. 12. Instantaneous DT_{HDM} of Nemo-Nordic model (left column), the $SDBias$ (middle column), and the DT_{HDM}^{corr} (right column) at three random time-instants. The black and red values refer to TG records and HDM at the stations (denoted by triangles), respectively. The grey arrows demonstrate the measured wind velocity and direction at the same time (EEA, 2020; FMI, 2020a).

shape between that of the MDT_{HDM} and MDT_{HDM}^{corr} (Figs. 15 and 16). MDT_{TG} studies at individual tide gauge stations performed by Kollo and Ellmann (2019) also showed similar results to that of the corrected MDT_{HDM}^{corr} (Fig. 16). After correction the range of difference between MDT_{HDM}^{corr} of Nemo-Nordic and HBM-EST decreases to 5 cm with a standard deviation of 0.5 cm, which signifies a good agreement between the two corrected models (Fig. 16c).

The method is of course an approximation. Observe in Fig. 16 around Hiiumaa island (longitude 23°, latitude 59°–59.5°) there is an unreasonably sharp DT anomaly. This is due to the $SDBias$ value being larger relative to the uncorrected DT_{HDM} . As a consequence, the shape of interpolation function affects the DT_{HDM}^{corr} pattern, especially in the Nemo-Nordic model (Fig. 12). This shows that the linear interpolation method utilized for $SDBias$ estimation by Eq. (7) may not always be sufficient.

Longitudinal variations of MDT are illustrated by a simple transect along the gulf, see Fig. 17. As can be seen, the corrected MDT_{HDM}^{corr} of both models increases eastwards with the relatively same pattern, with a difference between them of less than 1 cm. The MDT slope more or less represents the outward circulation of the gulf from east to west direction on the Finnish side (Myrberg and Soomere, 2013). Similar patterns have also been observed in Kollo and Ellmann (2019) using only tide gauge data. Moreover, Pindsoo and Soomere (2020), who examined the extreme water levels, also observed an increasing trend in the eastern

section.

Whilst the MDT shows an increasing trend to the easternmost side of the gulf, there appears however to be a sharp change around longitude 25.5° within the vicinity of tide gauge station (TG-4) Rohuneeme and (TG-3) Lokska (on the Estonian side) northwards to the Finnish coast. It is also noticeable that the uncorrected models MDT_{HDM} gradient remains unnoticed (is smoothed out). Thus, this Lokska-Helsinki “bottleneck” (denoted by the red rectangle in Fig. 17) needs to be confirmed by further analysis in the offshore domain. This can be accomplished by incorporating by an analysis of long-term satellite altimetry SSH data-series.

Further examination of the seasonal MDT of the transect in 2014 (Fig. 17) shows that during the winter and spring season the largest change with respect to other seasons in gradient occurs from west to east (this change is around 2.5 cm in winter and 3.5 cm in spring). This seasonality highly suggests that both atmospheric forcings (e.g. winds) and precipitation trends (e.g. snow melt, river discharge) may contribute to this increase on the extreme eastern section of the gulf.

As show above the gulf is known for having seasonal dynamics that shall influence the DT (Sec. 3). Thus, the seasonal MDT shows a variation from season to season and from year to year (Fig. 18, cf. Table 1). Notice that in 2014 the MDT was much lower in the winter season than it was in 2015. In the 2014/2015 ice season the maximum ice extent was

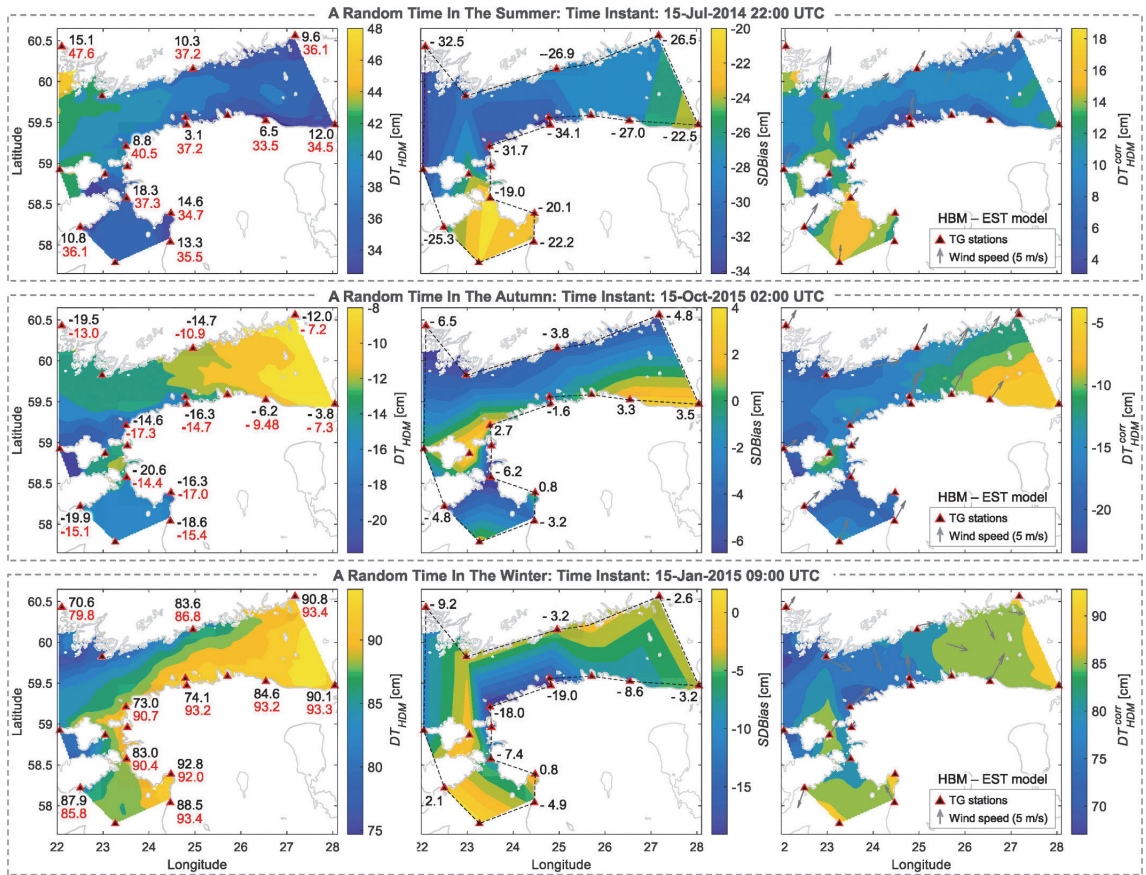


Fig. 13. Instantaneous DT_{HDM} of HBM-EST model (left column), the $SDBias$ (middle column), and the DT_{HDM}^{corr} (right column) at three random time-instant. The black and red values refer to TG records and HDM at the stations (denoted by triangles), respectively. The grey arrows demonstrate the measured wind velocity and direction at the same time (EEA, 2020; FMI, 2020a).

recorded to be one of the lowest ever since 1957, thus the lack of sea ice may have contributed to the increased MDT in 2015. Also, in December 2014 one of the strongest Major Baltic Inflow (MBI) occurred (since 1951) in the Baltic Sea and it was observed that it took approximately 9 months for it to propagate into the gulf (Liblik et al., 2018). The effect this would have had directly or indirectly on the sea level variability is still unclear. Nevertheless, the decrease of sea ice combined with storminess and perhaps MBI may have influenced the increase in seasonal MDT observed in 2015.

6. Discussion

Although HDM provide reasonable trends of the dynamics of the ocean, the question remains on their accuracy and thus reliability (i.e. precision vs accuracy). In this study we have shown that by calculating the difference between dynamic topography (DT) at land bounded TG (fitted to the geoid) and HDM data we can essentially obtain a combined bias (consisting of $SDBias$ and $TDBias$) that changes spatially and temporally. The results displayed both a high- and low-frequency components. The reasoning for this combined bias depends on the HDM model configuration and most importantly vertical reference datum issues (Slobbe et al., 2014).

Previous studies have adopted a method that corrects for the low

frequency $TDBias$ component over a particular period using an averaging method (e.g. backward moving average (Lagemaa et al., 2011)). Our detailed examination on the $TDBias$ for both HDM shows that using an averaging period of 0–6 h results in a standard deviation of less than 5 cm at all TG stations (Fig. 9). A longer time period can also be utilized, however exception stations of Narva-Jõesuu and Pärnu displayed an increased standard deviation of 5–10 cm. One of the possible reasons for these stations having such a lower accuracy, could be attributed to the fact that these stations are located in such coastal geomorphology areas, that are often influenced by local short-term storm surges episodes (Sec. 3). Thus, the HDM models may experience some difficulty in forecasting the DT at these locations.

Thus, to a first approximate we adopted an instantaneous $TDBias$ correction that accounts for both high- and low-frequency components of the $TDBias$. The analysis shows that the corrected DT_{HDM}^{corr} results yield quite different quantities compared to that of the uncorrected DT_{HDM} (Figs. 15–17). For instance, the MDT_{HDM} range from west to east (Fig. 17) in the uncorrected model was from -12.7 cm to -8.2 cm (a maximum difference of 4.5 cm) whilst in the corrected model MDT_{HDM}^{corr} varied from 18 cm to 25.4 cm (a maximum difference of 7.4 cm). This is almost a factor of two difference. The MDT_{HDM}^{corr} results from west to east of the gulf show similarity in quantification of values with previous work performed by Suursaar and Soõäär (2007), who

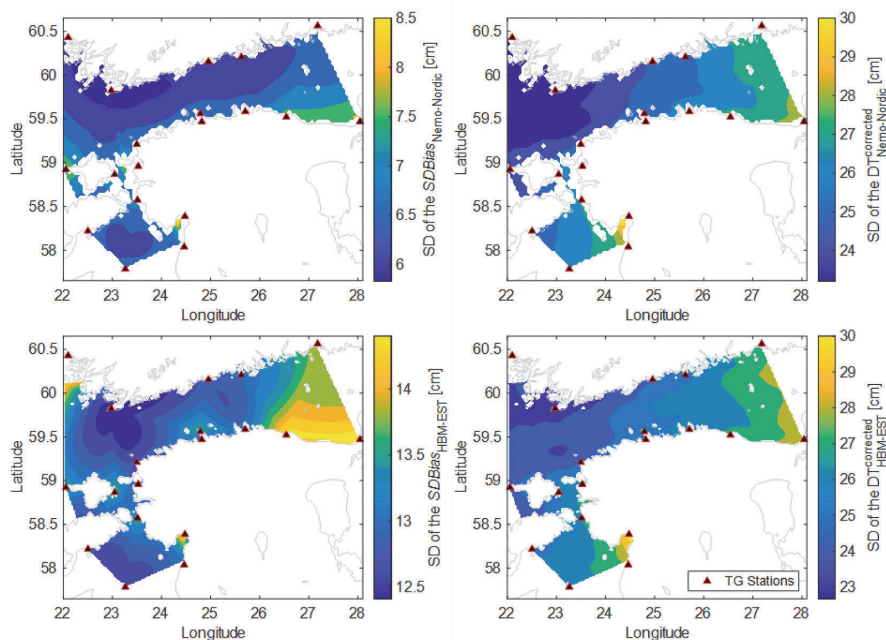


Fig. 14. The spatial distribution of the standard deviation of the SDBias (left column) and corrected DT (right column) from Nemo-Nordic model (top row) and HBM-EST model (bottom row).

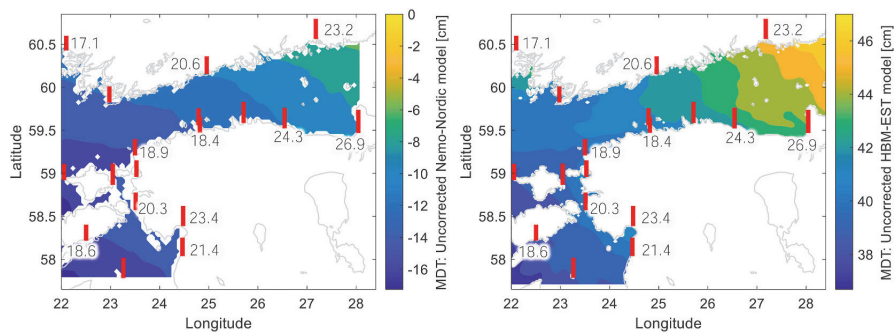


Fig. 15. Uncorrected mean dynamic topography (MDT_{HDM}) in the eastern part of Baltic Sea from Nemo-Nordic (left) and HBM-EST (right) model for the entire 2014–2015 period. The red bars and adjacent numbers demonstrate the actual MDT_{TG} at the TG locations.

investigated coastal tide gauges along the Estonian coast over the period 1842–2005. Even though there was a difference in quantification, both MDT_{HDM}^{corr} and MDT_{HDM} show that the highest value of MDT is in the southeast of the gulf, which is a well known feature also observed in other studies (Kakkuri and Poutanen, 1997; Kollo and Ellmann, 2019; Pindsoo and Soomere, 2020; Wolski et al., 2014).

Correction of the HDM also allowed not only quantification of more realistic DT values but we were able to actually identify the specific areas where the steepest MDT change occurs i.e. the Rohuneeme and Loks (Fig. 17, red rectangle) and also the potential season that this may occur i.e. the winter and spring season. With the latter hinting of properties of the wind, sea ice days and possible precipitation playing a major role in the high MDT in the east of the gulf. These results, though based on a short period (two years), still demonstrate that the patterns and changes observed (seasonally, yearly, etc.) can potentially be

utilized (especially using a long time series of data) as indicators of possible drivers of climate change and identification of critical areas. As a result, the newest contribution of this present study is that we can now quantify realistic values of MDT not only limited to the tide gauge locations but also for the offshore area.

The DT_{HDM}^{corr} results (Fig. 16), although rational intrinsically, revealed some of the improvements that can be applied in the method. For instance, the use of a $TDBias_{k=0}$ (instantaneous correction) may potentially be problematic for some localized events (e.g. wave setup, wave run up, coastal upwellings, etc.) that influence the coastal area but may not be affected in the offshore domain. This however can be resolved by the utilization of other data sources to validate the offshore DT values (e.g. GNSS buoy and satellite altimetry). Also, implementation of a larger averaging period e.g. 6–24 h may be more realistic in the $TDBias$ correction during stormy events.

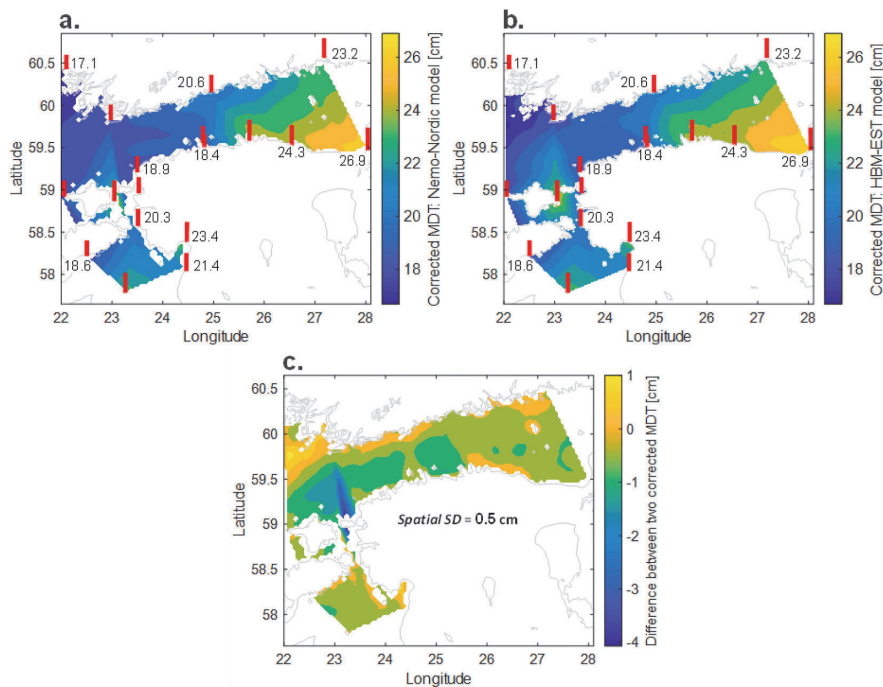


Fig. 16. Corrected mean dynamic topography MDT_{HDM}^{corr} calculated from Nemo-Nordic and HBM-EST model during the years 2014–2015 (top-left and -right, respectively), and the difference between them (bottom). The red bars and adjacent numbers demonstrate the actual MDT_{TG} at the TG locations. The spatial standard deviation of difference between two HDM models is 0.5 cm.

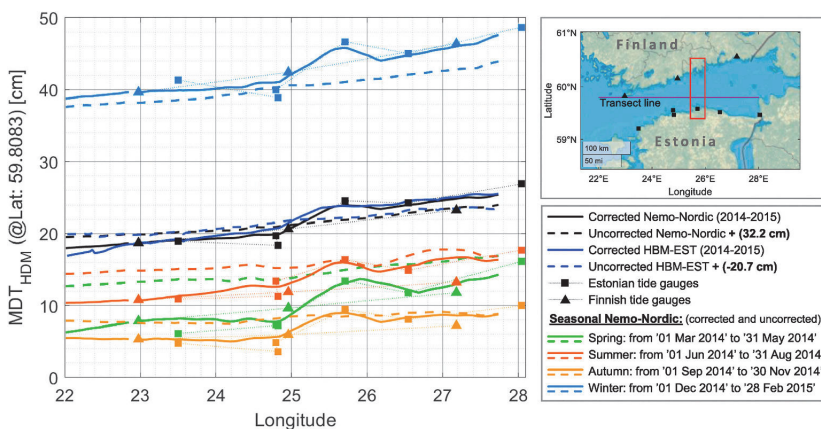


Fig. 17. MDT along a transect line at latitude 59.8083 that compares the corrected (solid lines), uncorrected (dashed lines), and tide gauges (square and triangle markers). Black and dark-blue lines represent the MDT during the years 2014–2015 for Nemo-Nordic and HBM-EST, respectively. To make the MDT trends comparable, uncorrected Nemo-Nordic and HBM-EST have been shifted by 32.2 cm and -20.7 cm (which are the mean differences of corrected and uncorrected model), respectively. The seasonal pattern of the MDT along the transect for the Nemo-Nordic is also represented by solid (corrected) and dashed (shifted uncorrected) lines. The red rectangle in the inset indicates the Loka-Helsinki bottleneck.

Due to the availability of TG data both on the Estonian and Finnish coast (with a distance between them 48–135 km), for determination of $SDBias$ we adopted a linear interpolation method, that is performed for the offshore areas. The method whilst appropriate and performs well showed on some occurrences obvious discrepancies. As was illustrated in Fig. 16c (around longitude 23°) where an obviously erratic DT anomaly was present, due to an interpolation problem. In such circumstances the availability of offshore sea level data would be useful for assisting with the method. Thus, the $SDBias$ interpolation method can be improved for future studies.

The analysis of the present study also indirectly revealed potential (spatial and temporal) problems in the HDMs which can be improved for future forecasting. For example, comparison of the DT_{HDM}^{corr} (Fig. 11) showed possible locations of discrepancies and also the times of larger standard deviation of HDM error. This hints of potential improvements in the models (e.g. due to better sea ice modelling, precipitation, atmospheric forcings etc.). Essentially the method described in this study can be utilized for any given HDM model and provided that tide gauge records and accurate high-resolution geoid model are available. Thus using a static vertical reference frame such as the geoid provides more

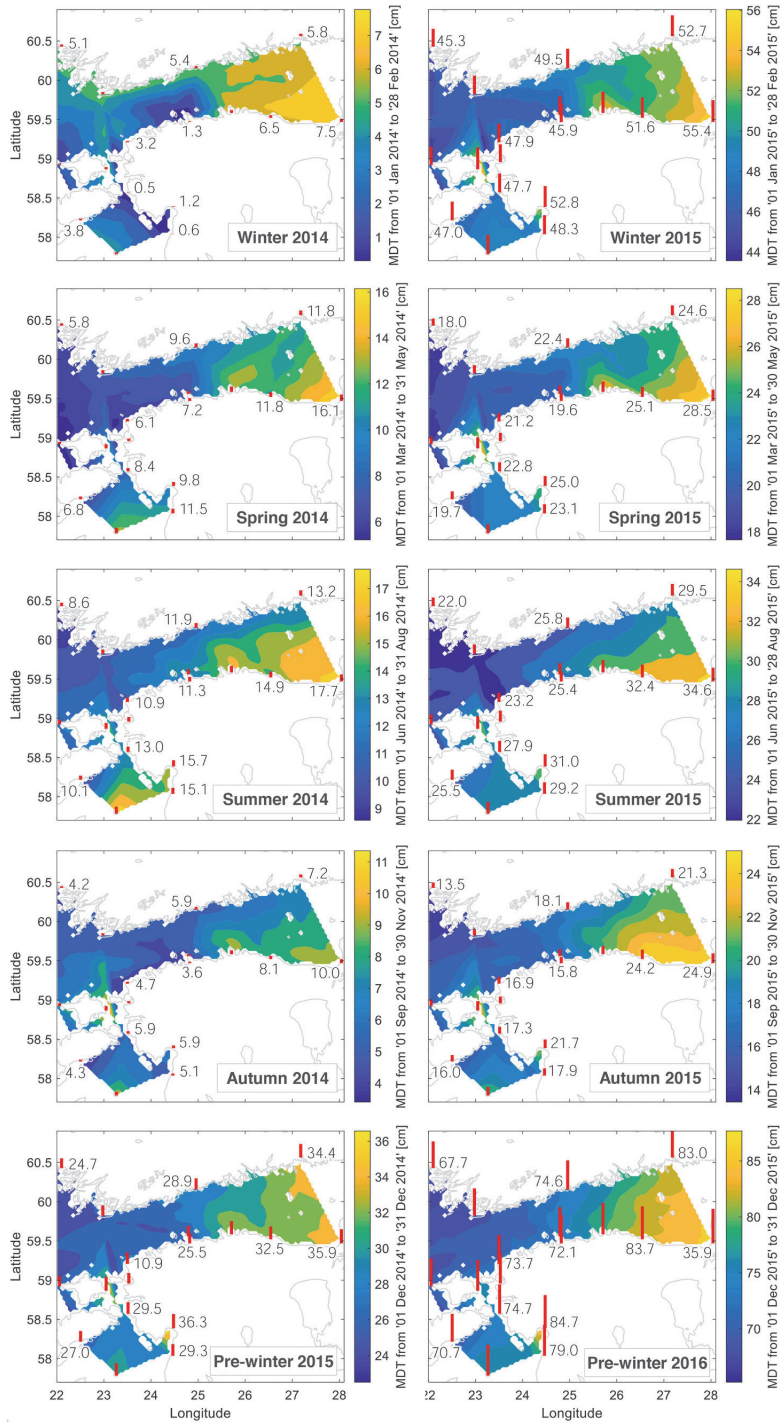


Fig. 18. The seasonal MDT_{TGM}^{corr} from Nemo-Nordic model during the years from 2014 (left column) to 2015 (right column). The red bars and adjacent numbers demonstrate the seasonal MDT_{TG} . Note that the winter and pre-winter last two months and one month, respectively.

accurate results and thus improves the applicability and efficiency of using HDM.

One of the major advantages of HDM's vertical datum to be referred to the geoid is that the results can now be utilized to incorporate with GNSS sensor equipped buoys and satellite altimetry datasets. This can be used both as a collective dataset or as validation of the data sources in the offshore domain. Thus, the space-borne data-points act as offshore reference points, i.e. a sort of offshore tide-gauge stations. Note that these in-situ GNSS and SA datasets are usually expressed with respect to a reference ellipsoid, thus the sea surface heights are derived (Fig. 1). For determining the DT-s a high resolution and accurate marine geoid model is required, see Eq. (1). Thus the developed method can be applied for identifying and eliminating the HDM biases offshore, yielding adequate DT estimates over the area of interest. Hence the involvement of these additional datasets can be improved by the developed method. It is also expected, that with new and emerging satellite missions (such as Sentinel 3, Sentinel 6, Surface Water and Ocean Topography (SWOT)) future developments are expected to occur in this direction. One of the key components however, to incorporate these emerging sea surface height data sources shall be knowledge on a high resolution and accurate marine geoid.

Adaptation to the geoid not only allows better DT estimates but it also allows accuracy and compatibility to the vertical datum between the offshore and onshore. This is very useful for marine engineering, navigation and climate studies. There is an urgent need for accurate dynamic topography data. For instance, in shipping the under-keel clearance (UKC) of vessels should be within half-decimeter accuracy. Also, with respect to climate studies, it is essential not only to know the trends of rising sea level and extreme events but also to obtain accurate estimates of these rates and to refer calculations to a common international vertical datum. Moreover, half-decimeter accurate sea surface data indirectly provide information on the Earth's gravity field that can be used to improve marine geoid solutions (Varbla et al., 2020a).

The method presented in this study is the first step in potentially adopting an integrated approach for determining accurate DT offshore. This method can potentially be applied in other study areas. There exist future improvements that can be made especially related to the HDM bias modelling and the incorporation of other sea level data in the marine areas and better interpolation methods.

7. Concluding remarks

This study demonstrated that utilization of the geoid as a static vertical reference datum for hydrodynamic models provides more realistic dynamic topography estimates DT_{HDM}^{corr} than the original DT_{HDM} . Whereby the difference without and after the HDM bias corrections can improve the MDT estimates by as much as a factor of two. The developed method utilized land bounded tide gauge records, i.e. excluding offshore reference points. The extension of this method to the offshore by future inclusion of GNSS sources and satellite altimetry data allows a substantial and accurate sea level database to be obtainable with the key components. However, to incorporate these emerging sea surface height data sources shall be knowledge on a high resolution and accurate marine geoid.

The question of the availability and access to the marine geoid models remains. Since most countries have established and are aiming at a gravity-based height reference system where the vertical datum is realized through geoid modelling, it would be an advancement and shall soon be implemented internationally. The Baltic Sea region countries have already developed a common geoid model NKG2015 (Ågren et al., 2016), that covers the entire Baltic Sea. In fact, currently the Baltic Sea Chart Datum 2000 (BSCD2000) is officially being adopted for Baltic Sea. It is based on the European Vertical Reference System (EVRS) definitions, to which many national height systems are already linked. The height reference surface of BSCD2000 is the equipotential surface of the Earth's gravity field, i.e. a marine geoid model (Schwabe et al., 2020).

The availability of such a regionally unified reference system enables other marine data products (such as hydrodynamic models) to be referred to the same geoid based vertical datum, thus allowing consistency and accuracy amongst the various sea level sources. Hence, this study demonstrated a glimpse of the possible forthcoming benefits that can be obtained by now adapting to the geoid, especially with the growing inter-relationships between various disciplines (e.g. oceanography, geodesy, hydrography, geophysics etc.).

Declaration of competing interest

The authors declare that they have no known competing financial interests or personal relationships that could have appeared to influence the work reported in this paper.

Acknowledgements

The research is supported by the Estonian Research Council grants PRG330 'Development of an iterative approach for near-coast marine geoid modelling by using re-tracked satellite altimetry, in-situ and modelled data' and PRG 1129. The authors are extremely grateful to the Swedish Meteorological and Hydrological Institute (SMHI) for providing access to the model data. We are also thankful for the constructive comments made by the anonymous reviewers.

References

- Ågren, J., Strykowski, G., Bilker-Koivula, M., Omang, O., Mårdla, S., Forsberg, R., Ellmann, A., Oja, T., Liepins, I., Parselunans, E., Kaminskis, J., 2016. The NKG2015 gravimetric geoid model for the Nordic-Baltic region, in: Presented in the 1st Joint Commission 2 and IGSF Meeting International Symposium on Gravity, Geoid and Height Systems. Thessaloniki, Greece, pp. 19–23.
- Ågren, J., Svensson, R., 2007. Postglacial Land Uplift Model and System Definition for the New Swedish Height System RH 2000. *Lantmäteriverket*.
- Delpeche-Ellmann, N., Mingelaité, T., Soomere, T., 2017. Examining Lagrangian surface transport during a coastal upwelling in the Gulf of Finland, Baltic Sea. *J. Mar. Syst.* 171, 21–30. <https://doi.org/10.1016/j.jmarsys.2016.10.007>.
- Delpeche-Ellmann, N., Soomere, T., Kudryavtseva, N., 2018. The role of nearshore slope on cross-shore surface transport during a coastal upwelling event in Gulf of Finland, Baltic Sea. *Estuarine, Coastal and Shelf Science* 209, 123–135. <https://doi.org/10.1016/j.eccs.2018.03.018>.
- EEA, 2020. Coastline Stations Operated by Estonian Environmental Agency [WWW Document]. URL <http://www.ilmateenistus.ee/meri/vaatlusandmed/kogu-rannik/kaart/> (accessed 11.10.20).
- Ellmann, A., Mårdla, S., Oja, T., 2020. The 5 mm geoid model for Estonia computed by the least squares modified Stokes's formula. *Surv. Rev.* 52, 352–372. <https://doi.org/10.1080/00396265.2019.1583848>.
- FMI, 2020a. Theoretical Mean Sea Level and Geodetical Levelling Systems in Finland [WWW Document]. URL <https://en.ilmatieteenlaitos.fi/theoretical-mean-sea-level> (accessed 11.10.20).
- FMI, 2020b. The Finnish Meteorological Institute's Open Data [WWW Document]. URL <https://en.ilmatieteenlaitos.fi/open-data> (accessed 11.10.20).
- Funkquist, L., Kleine, E., 1999. HIROMB, an Introduction to an Operational Baroclinic Model for the Baltic Sea. Vol. vol. 199. Technical report, SMHI, Norrköping, Sweden.
- Galor, W., 2008. Determination of dynamic under keel clearance of maneuvering ship. *J. KONBIN* 8, 53–60. <https://doi.org/10.2478/v10040-008-0100-0>.
- Hordoir, R., Axell, L., Höglund, A., Dieterich, C., Fransner, F., Gröger, M., Liu, Y., Pemberton, P., Schimanke, S., Andersson, H., Ljungemyr, P., Nygren, P., Falahat, S., Nord, A., Jönsson, A., Lake, I., Döös, K., Hieronymus, M., Dietze, H., Löptien, U., Kuznetsov, I., Westerlund, A., Tuomi, L., Haapala, J., 2019. Nemo-Nordic 1.0: a NEMO-based ocean model for the Baltic and North seas – research and operational applications. *Geosci. Model Dev. (GMD)* 12, 363–386. <https://doi.org/10.5194/gmd-12-363-2019>.
- Hünicke, B., Zorita, E., 2006. Influence of temperature and precipitation on decadal Baltic Sea level variations in the 20th century. *Tellus, Series A: Dynamic Meteorology and Oceanography* 58, 141–153. <https://doi.org/10.1111/j.1600-0870.2006.00157.x>.
- Idžanović, M., Ophaug, V., Andersen, O.B., 2017. The coastal mean dynamic topography in Norway observed by CryoSat-2 and GOCE. *Geophys. Res. Lett.* 44, 5609–5617. <https://doi.org/10.1002/2017GL073777>.
- IHO, 2020. International Hydrographic Organization Standards for Hydrographic Surveys (S-44 Edition 6.0.0).
- Jakimavičius, D., Kraičiūniėnė, J., Šarauskienė, D., 2018. Assessment of wave climate and energy resources in the Baltic Sea nearshore (Lithuanian territorial water). *Oceanologia* 60, 207–218. <https://doi.org/10.1016/j.oceano.2017.10.004>.

- Kakkuri, J., Poutanen, M., 1997. Geodetic determination of the surface topography of the Baltic Sea. *Mar. Geodes.* 20, 307–316. <https://doi.org/10.1080/01490419709388111>.
- Kollo, K., Ellmann, A., 2019. Geodetic reconciliation of tide gauge network in Estonia. *Geophysica* 54, 27–38.
- Lagemaa, P., Elken, J., Kõuts, T., 2011. Operational sea level forecasting in Estonia. *Est. J. Eng.* 17, 301–331. <https://doi.org/10.3176/eng.2011.4.03>.
- Lehmann, A., 1995. A three-dimensional baroclinic eddy-resolving model of the Baltic Sea. *Tellus* 47, 1013–1031. <https://doi.org/10.1034/j.1600-0870.1995.00206.x>.
- Li, X., Crowley, J.W., Holmes, S.A., Wang, Y.-M., 2016. The contribution of the GRAV-D airborne gravity to geoid determination in the Great Lakes region. *Geophys. Res. Lett.* 43, 4358–4365. <https://doi.org/10.1002/2016GL068374>.
- Liblik, T., Naumann, M., Alenius, P., Hansson, M., Lips, U., Nausch, G., Tuomi, L., Wesslander, K., Laanemets, J., Viktorsson, L., 2018. Propagation of impact of the recent major baltic inflows from the eastern gotland basin to the gulf of Finland. *Frontiers in Marine Science* 5, 222. <https://doi.org/10.3389/fmars.2018.00222>.
- Liebsch, G., Novotny, K., Dietrich, R., Shum, C.K., 2002. Comparison of multitemission altimetric sea-surface heights with tide gauge observations in the Southern Baltic Sea. *Mar. Geodes.* 25, 213–234. <https://doi.org/10.1080/01490410290051545>.
- Matthaus, W., Lass, H.U., 1995. The recent salt inflow into the Baltic Sea. *J. Phys. Oceanogr.* 25, 280–286.
- Myrberg, K., Soomere, T., 2013. The Gulf of Finland, its hydrography and circulation dynamics, in: *Preventive Methods for Coastal Protection: towards the Use of Ocean Dynamics for Pollution Control*. Springer International Publishing, pp. 181–222. http://s://doi.org/10.1007/978-3-319-00440-2_6.
- Omstedt, A., Hansson, D., 2006. The Baltic Sea ocean climate system memory and response to changes in the water and heat balance components. *Continental Shelf Res.* 26, 236–251. <https://doi.org/10.1016/j.csr.2005.11.003>.
- Ophaug, V., Breili, K., Gerlach, C., 2015. A comparative assessment of coastal mean dynamic topography in Norway by geodetic and ocean approaches. *J. Geophys. Res.: Oceans* 120, 7807–7826. <https://doi.org/10.1002/2015JC011145>.
- Pindsoo, K., Soomere, T., 2020. Basin-wide variations in trends in water level maxima in the Baltic Sea. *Continental Shelf Res.* 193, 104029. <https://doi.org/10.1016/j.csr.2019.104029>.
- Rosentau, A., Muru, M., Gauk, M., Oja, T., Liibus, A., Kall, T., Karro, E., Roose, A., Sepp, M., Tammepuu, A., Tross, J., Uppin, M., 2017. Sea-level change and flood risks at Estonian coastal zone, in: *Coastal Research Library*. Springer, pp. 363–388. https://doi.org/10.1007/978-3-319-49894-2_16.
- Schimanke, S., Dieterich, C., Meier, H.E.M., 2014. An algorithm based on sea-level pressure fluctuations to identify major Baltic inflow events. *Tellus Dyn. Meteorol. Oceanogr.* 66, 23452. <https://doi.org/10.3402/tellusa.v66.23452>.
- Schwabe, J., Ågren, J., Liebsch, G., Westfeld, P., Hammanklinter, T., Mononen, J., Andersen, O.B., 2020. The Baltic sea chart datum 2000 (BSCD2000) – implementation of a common reference level in the Baltic sea. *Int. Hydrogr. Rev.* 23, 63–83.
- Slobbe, D.C., Klees, R., Gunter, B.C., 2014. Realization of a consistent set of vertical reference surfaces in coastal areas. *J. Geodes.* 88, 601–615. <https://doi.org/10.1007/s00190-014-0709-9>.
- Slobbe, D.C., Verlaan, M., Klees, R., Gerritsen, H., 2013. Obtaining instantaneous water levels relative to a geoid with a 2D storm surge model. *Continental Shelf Res.* 52, 172–189. <https://doi.org/10.1016/j.csr.2012.10.002>.
- Soomere, T., 2003. Anisotropy of wind and wave regimes in the Baltic proper, in: *Journal of Sea Research*. Elsevier, pp. 305–316. [https://doi.org/10.1016/S1385-1101\(03\)00034-0](https://doi.org/10.1016/S1385-1101(03)00034-0).
- Soomere, T., Delpeche, N., Viikmäe, B., Quak, E., Meier, M., Döös, K., 2011. Patterns of Current-Induced Transport in the Surface Layer of the Gulf of Finland. Helsinki.
- Soomere, T., Keevallik, S., 2001. Anisotropy of moderate and strong winds in the Baltic Proper. *Proc. Estonian Acad. Sci. Eng.* 7, 35–49.
- Suursaar, Ü., Sooäär, J., 2007. Decadal variations in mean and extreme sea level values along the Estonian coast of the Baltic Sea. *Tellus, Series A: Dynamic Meteorology and Oceanography*. <https://doi.org/10.1111/j.1600-0870.2006.00220.x>.
- Varbla, S., Ellmann, A., Delpeche-Ellmann, N., 2020a. Validation of marine geoid models by utilizing hydrodynamic model and shipborne GNSS profiles. *Mar. Geodes.* 43, 134–162. <https://doi.org/10.1080/01490419.2019.1701153>.
- Varbla, S., Ellmann, A., Delpeche-Ellmann, N., 2020b. Utilizing airborne laser scanning and geoid model for near-coast improvements in sea surface height and marine dynamics. *J. Coast Res.* 95, 1339. <https://doi.org/10.2112/SI95-257.1>.
- Véronneau, M., Huang, J., 2016. The canadian geodetic vertical datum of 2013 (CGVD2013). *Geomatica* 70, 9–19. <https://doi.org/10.5623/cig2016-101>.
- Wolski, T., Wiśniewski, B., Giza, A., Kowalewska-Kalkowska, H., Boman, H., Grabbi-Kaiv, S., Hammanklinter, T., Holfort, J., Lydeikaite, Z., 2014. Extreme sea levels at selected stations on the Baltic Sea coast. *Oceanologia*. Polish Academy of Sciences 259–290. <https://doi.org/10.5697/oc.56-2.259>.

Appendix 2

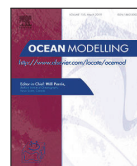
Publication II

Jahanmard, V., Delpeche-Ellmann, N., Ellmann, A. (2022). Towards Realistic Dynamic Topography from Coast to Offshore by Incorporating Hydrodynamic and Geoid Models. *Ocean Modelling*, 180. doi:10.1016/j.ocemod.2022.102124.



Contents lists available at ScienceDirect

Ocean Modelling

journal homepage: www.elsevier.com/locate/ocemod

Towards realistic dynamic topography from coast to offshore by incorporating hydrodynamic and geoid models

Vahidreza Jahanmard^{a,*}, Nicole Delpeche-Ellmann^b, Artu Ellmann^a^a Department of Civil Engineering and Architecture, Tallinn University of Technology, Ehitajate road 5, 19086 Tallinn, Estonia^b Department of Cybernetics, School of Science, Tallinn University of Technology, Akadeemia road 21, 12618 Tallinn, Estonia

ARTICLE INFO

Keywords:

Sea level
Geoid
Hydrodynamic modelling
Vertical reference datum
Hydrogeodesy
Baltic sea

ABSTRACT

One of the major factors preventing utilization of realistic sea-level data is that various sources are referred to inconsistent vertical reference datum (VRD). This study presents a methodology for deriving instantaneous and realistic sea level data from the coastal to offshore areas of the Baltic Sea, by synergizing different sources of sea level data (tide-gauge (TG), hydrodynamic model (HDM) and satellite altimetry (SA)). The key component being the geoid that links the VRD of these different sources.

HDMs are known to be a representable source of sea level data, however their VRD is often undisclosed. Therefore, they are often spatially and temporally biased with respect to in-situ data. This study demonstrates that by using geoid-referenced TG data that represents 'realistic' sea level it is possible to correct HDM, by deriving and applying a spatial bias correction. Three interpolation methods (linear, thin plate spline regression, and inverse distance weighted) are examined to derive the corrected HDM. The results showed an improvement with respect to TG data, and the annual mean dynamic topography of corrected HDM was improved by a factor of almost 1.5. Examination of the Sentinel-3A satellite along-track data also confirms the corrected HDM data to be more accurate. The methodology applied also identified problematic locations of HDM, SA and geoid data along with unreliable TG. This accuracy and conformity in sea level data are urgently required for a comprehensive understanding of climate change, marine engineering and navigation applications, which can be achieved by adapting the uniquely defined geoid for the vertical reference datum.

1. Introduction

A continuous model of accurate sea level from the coast to the offshore area with pre-defined uncertainty bounds becomes imperative for many applications, such as navigation, marine engineering, and climate studies. With better than sub-decimetres accuracy now required, the challenges of obtaining such an accurate model are hindered not only by the spatial and temporal resolution of the various sea level sources (e.g., tide gauges (TG), hydrodynamic model (HDM), shipborne and airborne Global Navigation Satellite Systems (GNSS) profiles, and satellite altimetry (SA)) but also foremost by inconsistencies in the vertical reference datums used amongst these sources (Slobbe et al., 2014; Jahanmard et al., 2021).

Hydrodynamic models, whilst capable of successfully simulating a continuous model of relative sea level, are often flawed by two major factors. The first and most relevant to this study is that, in many hydrodynamic models, there is insufficient knowledge of the vertical reference datum used (Afrasteh et al., 2021; Slobbe et al., 2014). Secondly, the HDMs are driven by mathematical equations with input sources from other models (e.g., atmospheric, river discharge, sea-ice

dynamics, etc.). Moreover, models contain underlying assumptions and approximations in the relevant model set-up (e.g., boundary conditions, parametrization and discretization techniques, etc.; Kärnä et al., 2021; Khanarmuei et al., 2021; Hieronymus et al., 2017; Zhang et al., 2016). These factors often result in many HDMs being systematically biased (both spatially and temporally) relative to observations.

Previous studies have examined the bias correction of HDM with respect to salinity and temperature (Chang et al., 2021), as well as climate models (Aung et al., 2016; Giorgi, 2019). However, the spatial and temporal bias correction related to the sea level parameter has often been overlooked. Although the HDM-derived sea level does not correspond to the in-situ observations, its simulations still represent an acceptable trend of sea level. A simple and reasonable approach that has been utilized by many studies is by calculating the correlation and standard deviation between HDM sea level and land bounded TGs (i.e., assuming the TGs refer to some defined datum) to demonstrate model assessment (Hordoier et al., 2019; Kärnä et al., 2021). Some applications also derived a bias correction by computing the difference of HDM with the TG records that refer to a desired vertical reference (Varbla et al., 2020a; Mostafavi et al., 2021). The problem becomes

* Corresponding author.

E-mail address: vahidreza.jahanmard@taltech.ee (V. Jahanmard).

complex, for numerous applications (e.g., determining realistic absolute sea level rise, climate studies, engineering design, etc.) now require accurate sea level not only in the coastal domain (i.e., within the vicinity of TG) but also in the offshore domain.

Considering that the HDM sea level bias varies both spatially and temporally (with high and low-frequency components; Jahanmard et al., 2021), this makes it challenging to obtain accurate and consistent sea level data from the coast to offshore. In Jahanmard et al. (2021), biases of the model with respect to a dense network of geoid-referenced TGs were hourly extended to the offshore using a linear interpolation method. Nevertheless, the performance of the bias correction in the offshore area remained unclear. This signals the need for a solution that also corrects the HDM data in the offshore zone so that a consistent and realistic vertical datum is utilized. Motivated by these challenges, the focus of this study is to demonstrate a novel method that corrects the HDM bias both in the coastal and offshore area using a consistent and realistic vertical datum and to demonstrate the applicability of this towards improving other related studies.

Hydrodynamic models are however not the only source of sea level data, and as mentioned above, there are other sea level sources, such as tide gauges, with defined vertical datum. Tide gauges are known historically for being one of the most reliable and accurate sources of sea level data, due to the long-time span of data collection along the earth's coastline. As a result, TG data are often considered as representative of the 'true' sea level (Jahanmard et al., 2021; Cipollini et al., 2017).

Nevertheless, there are three important limitations in using this source: (i) as mentioned above, the spatial coverage of TG tends to be restricted to the coastal boundary and thus not ideally representative for the offshore areas. (ii) As TGs usually measure relative sea level (i.e., relative to the land where the TG stations are stationary positioned), they are influenced by the vertical land movement that may occur (e.g., glacial isostatic adjustment). This signifies that, in areas affected by any land deformation, there is a need for relevant corrections to be applied in order to derive the 'true' sea level variation. Moreover, (iii) the vertical reference datum of marine areas is commonly referred to a chart datum, which is based on either a tidal observation (e.g., some historic mean sea level (MSL), lowest astronomic tide (LAT), etc.), theoretical mean sea level models (e.g., as it was used in Finland recently), or a physical model such as the geoid (Schwabe et al., 2020). Whilst sufficient to a certain degree based on the application, most of these chart datums may vary over different time periods. Also depending on the country/community, the sea level data may be referred to differently defined vertical datums. For instance, the Baltic Sea countries utilize several different vertical reference datum definitions (Table A.1) and in such a dynamic marine area where integration is essential, this can create inconsistency and incompatibility. As a result, this study proposes utilizing a common and static vertical reference, such as the geoid as a more reasonable approach.

The geoid is a shape of the equipotential ocean surface under the influence of the gravity and rotation of Earth alone. Therefore, it would be more or less a static vertical datum (unlike MSL which wavers over time) and represents the natural "zero". Note that the geoid can vary due to mass redistribution, however, this variation is usually negligible. The maximum value for the geoid rise in the Baltic Sea is around 0.6 mm/year (due to postglacial rebound; Kakkuri and Poutanen, 1997). Thanks to precise GNSS levelling, it is possible to transfer a network of TG stations to a common geoid-based vertical datum. Thus, it is more applicable to validate the different data and model sources against the geoid-referenced TG data rather than using various and MSL-based chart datums (Liebsch et al., 2002; Varbla et al., 2020a,b). This validation should identify any bias between sources with respect to the vertical datum in addition to other systematic and random errors. Thus, it seems pragmatic to use the reliable TG records (that are referred to some stable and realistic vertical datum) to fit the HDM associated sea level data to a common vertical datum (Nordman et al., 2018; Jahanmard et al., 2021).

The geoid-referenced sea level data now allows us to derive automatically dynamic topography (DT), which is physically meaningful and better quantification of a more realistic sea level (Jahanmard et al., 2021). As a result, the mean dynamic topography (MDT) can be calculated, which is the difference between the mean sea surface and the geoid (Fig. 1). Note that there are basically two approaches to calculate the MDT. First and foremost, by a geodetic approach, whereby knowledge of the mean sea surface (MSS) is derived from SA or TG records referred to a precise geoid model (Idžanović et al., 2017). The oceanographic approach (second) utilizes solely HDM-derived sea level data (Ophaug et al., 2015). In this study, we shall utilize a combined approach that employs both geodetic and oceanography methods, since we are interested in the DT not only in the coastal area but also continuing into the offshore. This is, to our knowledge, the first attempt of such a synergized exploration in the entire Baltic Sea, and it is expected that similar forthcoming developments can be adapted in other marine areas worldwide.

Based on the challenges/problems outlined above, we examine the Baltic Sea region to demonstrate an innovative and improved method that incorporates various sea level sources along with a high-resolution geoid to obtain a more realistic and accurate DT. This study area is ideal for such a demonstration due to the presence of a dense network of TGs with a common geoid-based vertical reference datum. Baltic Sea is a semi-enclosed sea, which is also fortunate to have an accurate geoid model, a realistic postglacial land uplift model, SA data that have been specially corrected for the area specific marine conditions, a three-dimensional HDM, and an agreement between nine coastal countries towards having a common marine chart datum (i.e., the Baltic Sea chart datum; Ågren et al., 2016; Ellmann et al., 2019; Vestøl et al., 2019; Schwabe et al., 2020). Therefore, a synergy of HDMs and TG records along with other data sources, such as satellite altimetry and marine geoid model, is expected to yield high-resolution realistic DT both temporally and spatially. In addition, we shall demonstrate that the method applied can also reveal the accuracy or deficiencies of the different data sources utilized.

Thus, the core component of this study is the development of a methodology that reduces the fluctuating zero level of HDM to a geoid-based vertical reference. For this purpose, the bias of the HDM is corrected by utilizing a TG network comprising 73 stations. Such an approach was first utilized in Jahanmard et al. (2021) using a simple linear approach to distribute the bias spatially. This approach, however, may be flawed because of a lack of validation in the offshore area and an insufficient assessment of the bias interpolation sensitivity. This study reduces these flaws by now including a wider sea area and denser TG network that allows the examination of three different interpolation approaches: (i) triangulation-based linear interpolation, (ii) thin plate spline regression, and (iii) inverse distance weighted. The best-derived results are then evaluated and validated by utilizing the SA data (Sentinel-3A) with respect to the NKG2015 geoid model. This validation becomes most relevant in the offshore areas, where the largest uncertainty is present.

One of the most pertinent advantages of using an identical and stable vertical datum amongst the various data sources is that accurate DT can now be determined. The method applied also significantly contributes to identifying (i) aspects of HDM modelling that require improvement (ii) SA problematic issues and (iii) aspects/locations of the geoid modelling that require improvements.

The organization of the present paper is as follows. First, the developed and general methodology is outlined. Next, the data sources are highlighted: (i) geoid-referenced tide gauge network, (ii) Nemo-Nordic HDM model, (iii) NKG2015 geoid model, and (iv) Sentinel-3A satellite altimetry data. The HDM bias correction method is described in both time and spatial domains. Then, the difference between corrected models and SA data as well as the results are presented. Finally, a discussion on the results and method is described, followed by a summary that concludes the paper.

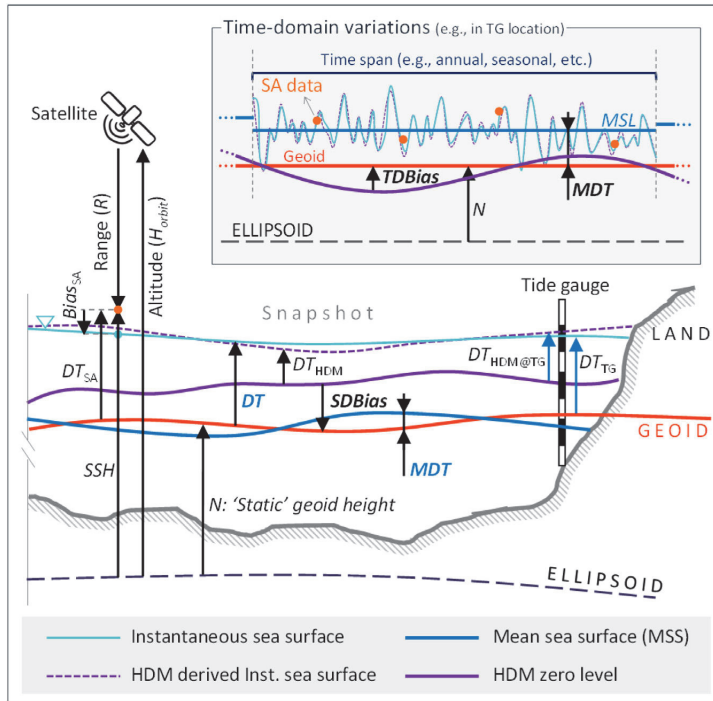


Fig. 1. Inter-relation between sea surface data sources (i.e. satellite altimetry, tide gauges, and hydrodynamic model), the different vertical reference datums and the hydrodynamic parameters. For the used symbols and abbreviations please refer to the main text body.

2. General methodology

In this study, different techniques and approaches are employed to derive the sea level from the coast and offshore. As mentioned above, one of the major challenges in obtaining accurate DT is that various data sources refer to various vertical reference datums. Apart from making it difficult to compare datasets, this inconsistency also leads to errors, particularly when inter-country/community issues arise. Thus, this section now describes an overall view of the method used to refer the vertical datum of the various sources to that of a static and common vertical datum, such as the geoid (i.e., the equipotential surface of the earth). Three principal sources of data that shall be utilized are TG, SA, and HDM data.

Fig. 1 illustrates the inter-relations between these data sources and the hydrodynamic parameters of interest in both the spatial and time domain. Recall that the TG data can be referenced to different chart datums (e.g., MSL, LAT, etc.). In the study area, the Baltic Sea Chart Datum 2000 (BSCD2000) is adopted as a geoidic reference system to unify chart datum between the surrounding countries. The chart datum is based on the common geoidic standards for height system (European Vertical Reference System; EVRS) and spatial reference system (European Terrestrial Reference System; ETRS89) in Europe. The zero level of BSCD2000 is in agreement with the Normaal Amsterdams Peil (NAP), and the chart datum coincides with the geoid surface (Schwabe et al., 2020). As previously discussed, the sea level variations with respect to the geoid surface yield dynamic topography (DT), which is more physically meaningful than sea level relative to other vertical datums (e.g., MSL, LAT; which may vary depending on definitions).

Tide gauge records, however, reflect the nearshore DT from a relative perspective (i.e., sea level variations relative to land). On the other hand, satellite altimetry (SA) measures the absolute sea level (that is, without regard to vertical land motion) in both coastal and offshore

areas. The satellite-derived sea surface height (SSH_{SA}) is relative to a geoidic reference ellipsoid (e.g., GRS 80), which can be converted to DT_{SA} as follows:

$$DT_{SA}(\varphi, \lambda) = SSH_{SA}(\varphi, \lambda) - N(\varphi, \lambda) \quad (1)$$

where N is the 'static' geoid height, a separation from the reference ellipsoid. In this study, NKG2015 as the most recent official geoid model over the Baltic countries is employed (Ågren et al., 2016).

Hydrodynamic models typically lack a well-defined vertical reference. As such, it is not straightforward to express the model-derived sea levels in a 3D coordinate system. Since the model dynamics assume zero horizontal gravity components, we denote the original (raw) HDM-derived sea level as DT_{HDM} . Despite knowing that the raw HDM is not exactly expressed relative to a geoid because the bathymetry used and prescribed sea levels along the open boundaries have not been referred to the geoid (Slobbe et al., 2013).

Therefore, since the vertical reference of the HDM is still unknown, the study focuses on determining accurate HDM-derived DT, particularly in the offshore area. In this regard, the primary objective of this study is the development of a method to correct the DT_{HDM} utilizing a stable height system reference surface (a geoid). In doing so, a geoid-referenced TG network is employed to determine and correct the bias of DT_{HDM} with respect to DT_{TG} at the location of TGs. The HDM biases are distributed to the offshore using an interpolation technique, and then the corrected HDM is examined through the DT_{SA} .

As mentioned above, due to dissimilarity in the vertical reference datums used by the DT_{HDM} and DT_{TG} , it is expected that a difference exists. This difference however changes both temporally and spatially and it is quantified in this study as a bias. Due to the characteristics of this bias, it was necessary to first derive a time-domain bias ($TDBias$) followed by a spatial-domain bias ($SDBias$). Note that firstly the $TDBias$ is determined by identifying the closest HDM grid point to that of the

TG location. The difference is then calculated between the time-mean value of HDM at the TG location ($DT_{HDM@TG}$) and DT_{TG} within a certain time interval. The backward moving average method is commonly used to correct the temporal bias of models (Jahanmard et al., 2021; Lagemaat et al., 2011):

$$TDBias_{m,k}(i) = \frac{1}{k+1} \sum_{j=-k}^0 [DT_{HDM@TG_m}(i+j) - DT_{TG_m}(i+j)], i > k \quad (2)$$

where m denotes a specific TG station, and k is the window length of the moving average. In this formulation, i is the index of time vector (ordinal number) that according to the temporal resolution of HDM and TG records, is increasing hourly. Obviously, the small amount of k yields the high-frequency error between the model and TG; and the $k = 0$ represents the instantaneous bias which is applicable for extreme cases. In this study, we require an uncertainty of less than 5 cm in order to obtain accurate sea level data. Thus, from previous studies a window length of less than 6-h is recommended (Jahanmard et al., 2021). To obtain the uncertainty of $TDBias$ in each TG station, the root mean square of errors is obtained from residuals (ϵ , which is the difference between the corrected model and raw model at the location of TG due to including the moving average filter in Eq. (2)) as follows:

$$RMSE_{m,k}(HDM, TG) = \sqrt{\frac{\sum_{j=k+1}^n (\epsilon_{m,j} - \bar{\epsilon}_m)^2}{n-k}} \quad (3)$$

where n is the number of observations at the m th station, and k , as before, is the window length of the backward moving average, which should be removed from the beginning of records for determining RMSE.

The $TDBias$ is valid only near the coast in the vicinity of the TG location. To achieve the bias through the offshore area (i.e., $SDBias$), an interpolation between the dense network of TG stations is employed:

$$SDBias_X(\varphi, \lambda, t) = \text{interp}_X[\varphi_{TG}, \lambda_{TG}, TDBias(t), \varphi, \lambda] \quad (4)$$

where interp_X is the interpolation operator, whereas X indicates the type of implemented interpolation technique. The φ_{TG} and λ_{TG} are the vector of latitude and longitude of the employed TG stations, respectively. The $SDBias$ is computed on the grid nodes of the model with vectors of latitude φ and longitude λ . Therefore, the corrected HDM is calculated accordingly:

$$DT_{HDM}^C(\varphi, \lambda, t) = DT_{HDM}(\varphi, \lambda, t) - SDBias(\varphi, \lambda, t) \quad (5)$$

The DT_{HDM}^C represents coastal and offshore values with respect to the geoid model. The various interpolation techniques (such as linear, inverse distance weighted, and thin plate spline) will be performed to determine the $SDBias$ (see Section 4.2) and the corrected model will be assessed using DT_{SA} . Note that the DT_{SA} values are often accompanied by outliers and another bias related to the TG records is also calculated (see Section 3.4). The schematic roadmap of the implemented methodology to correct the model and compare the various correction methods is shown in Fig. 2.

3. Data sets

3.1. Tide gauge dynamic topography

In this study the TG data serves as the foundation of accurate sea level data particularly with respect to deriving the time-domain bias (i.e., $TDBias$ Eq. (3)). The TG data were compiled from various sources around the Baltic Sea countries (see Table A.1). After performing quality and reliability checks, a robust network of 73 stations (from nine countries) along the coastline of the Baltic Sea was chosen. This TG dataset consists of hourly in-situ sea level data for the period December 2016–April 2020 (see Fig. 3 and Table A.1). Since different Baltic countries use different vertical datums it is essential to transfer all TG

records to an identical common vertical datum (i.e., the Baltic Sea Chart datum). The Estonian, Danish, and Swedish TGs are available with respect to their own national reference frames that are EH2000, DVR90, and RH2000, respectively. The remaining countries TG records are referred to the TGZ (except Finnish TGs that are referred to the theoretical mean sea level) that have been transferred by adding the individual conversion values. The value and reference of these conversion values and national reference frame that comply with BSCD2000 are listed in Table A.1. By these conversions, all stations are set down on a common European Vertical Reference System with an identical zero level of NAP. The permanent tide system of TG readings is the zero-tide system except for Germany, Russia, and Denmark, which are in the mean-tide and tide-free system (cf. Table A.1).

Since the Russian national height system (BHS77, Baltic Height System 1977) has not changed to the European Vertical Reference System, the zero level is shifted by adding + 19 cm to this TG station (Sacher, 2019). This offset value is an approximate difference between the Kronstadt (i.e., former zero level) and NAP.

To harmonize the permanent tide system of the TG records (specified in Table A.1) with the HDM and SA data, TG data are transferred to the mean-tide system by conversion algorithms provided by Ekman (1989). Tide gauge readings originally are relative to the TG zero mark, and then the records are reduced to the national height datums by near benchmark (e.g., BSCD2000 conversions). In the Baltic Sea, TGs' benchmark refers to NAP (EVRF2000, zero permanent tide system). In order to transform the records to the mean permanent tide system, the separation between the benchmarks and NAP height (ΔH) need to be transferred from the zero-tide to the mean-tide system. Thus (Ekman, 1989):

$$\Delta H_m = \Delta H_z + 29.6 \cdot (\sin^2 \varphi_B - \sin^2 \varphi_{NAP}) = \Delta H_z + C_{z2m} \quad \text{cm} \quad (6)$$

also for non-tide national datums (e.g., Denmark, $\gamma = 0.7$),

$$\Delta H_m = \Delta H_n + 29.6 \cdot \gamma \cdot (\sin^2 \varphi_B - \sin^2 \varphi_{NAP}) = \Delta H_n + C_{n2m} \quad \text{cm} \quad (7)$$

where φ_B is the geodetic latitude of TGs' benchmark, and φ_{NAP} is the latitude of NAP (52°22'53" in the European Terrestrial Reference System 1989). Therefore, the conversion to the mean permanent tide system (C_{z2m}) will be added to the BSCD2000 correction, and finally, TG records are corrected as follows (and the same for C_{n2m}):

$$DT_{TG_{\text{mean-tide}}} = DT_{TG_{\text{zer0-tide}}} + C_{z2m} \quad (8)$$

In addition, TGs measure relative sea level, and since in the study the absolute sea level is required, the vertical land motion (VLM) must be taken into account. Especially in the Baltic Sea where the stations are strongly affected by VLM due to the glacial isostatic adjustment. Accordingly, the land uplift increases from near zero in the southern part of the Baltic Sea to about 10 mm/year in the northern part (Vestøl et al., 2019). Fig. 4 shows the difference between long-term trends of relative and absolute sea level in an example station (Spikarna station, TG id 52) in the north of the Bothnia Sea. In this station, the relative (with respect to the land mounted TGZ) sea level trend is strongly negative (−6.7 mm/year), while the absolute (with respect to the centre of the earth) sea level trend is positive (2.2 mm/year) in this area (Madsen et al., 2019).

It should be noted that whilst the TG measurements are one of the most reliable sources of sea level data, they may contain gross errors or temporal gaps. Since these data deficiencies can disturb or decrease the quality of each analysis especially for obtaining hourly $TDBias$ (see Eq. (2)), it was necessary to identify and fill the gaps in the time series. The missing TG data have been simulated by k -nearest stations using a linear least square regression method, which results in the estimated DT with an uncertainty of 3.5 cm on average. Also, TG data screening was performed by removing spikes with residuals larger than three standard deviations.

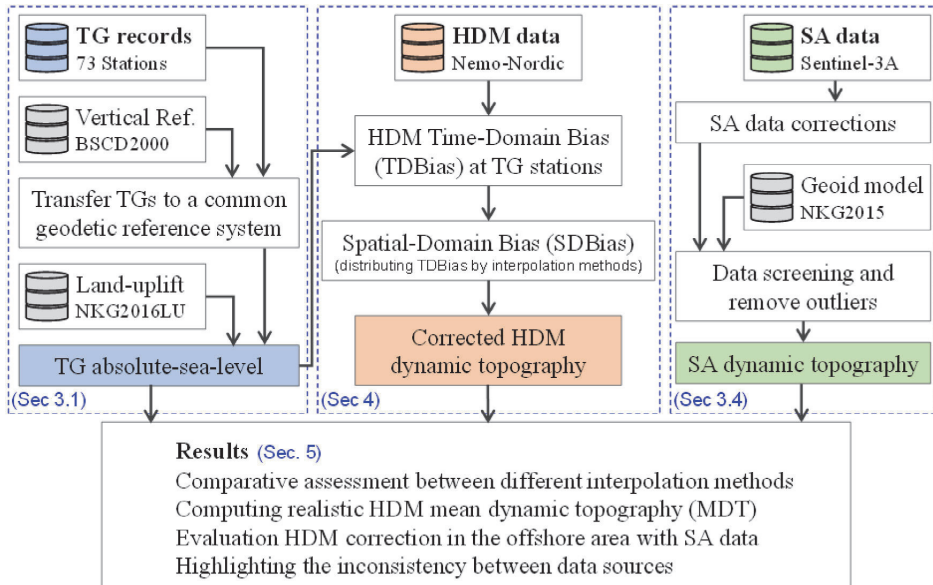


Fig. 2. Schematic roadmap of hydrodynamic model bias correction using a dense network of geoid-referential TGs, and assessment the method by satellite altimetry data.

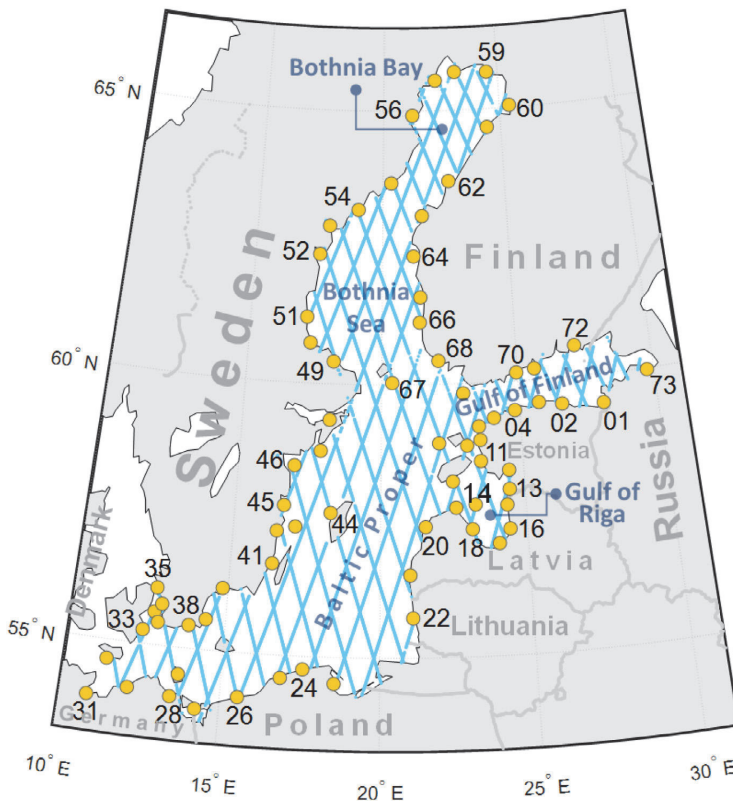


Fig. 3. Location of used tide gauge stations (yellow circles, numbered clockwise starting from the eastmost Estonian tide gauge station as shown in black in some stations) from nine countries around the Baltic Sea and ground tracks of Sentinel-3A (blue lines). See Table A.1 for more details.

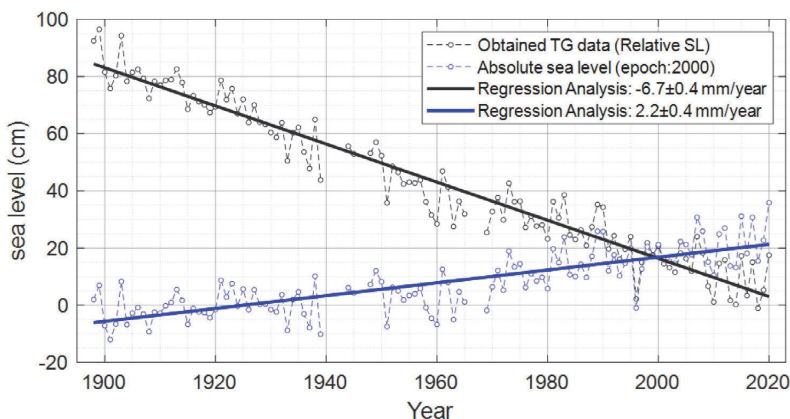


Fig. 4. Sea level trend relative to land (99% CI [-7.1, -6.3]; black) and absolute values (99% CI [1.8, 2.6]; blue) derived from Spikarna station (TG-52), where CI is confidence interval. The NKG2016LU calculated land-uplift is 8.94 mm/year in this station.

3.2. Hydrodynamic model

Nemo-Nordic is a three-dimensional coupled ocean-sea ice model of the Baltic and North Sea (Hordoïr et al., 2019) that was developed by the Swedish Meteorological and Hydrological Institute (SMHI) and originally based on the NEMO-3.6 ocean engine (Nucleus for European Modelling of the Ocean). In this study, we utilize a data assimilated version of the Nemo-Nordic model with an hourly temporal resolution and a horizontal resolution of 1 nautical mile for the period 3 December 2016–15 April 2020. The data were obtained from SMHI (SMHI, 2021) and are expected to provide sea level predictions at a higher level of quality than previous models used in the study area due to model setup settings and data assimilation techniques employed (Hordoïr et al., 2019; Kärnä et al., 2021).

A major feature of Nemo-Nordic compared to other HDM models used in the Baltic Sea is that two open boundaries are utilized: a meridional one in the western part of the English Channel and a zonal one located between Scotland and Norway. The sea level, temperature and salinity boundary conditions are obtained from ECMWF (the European Centre for Medium-range Weather Forecasts) data in the operational mode (Hordoïr et al., 2019). The model also uses a nonlinear explicit free surface method with a time-splitting approach that computes a barotropic and a baroclinic mode, as well as the interaction between them. Nemo-Nordic uses a buoyancy-extended $k-\epsilon$ turbulence model, and NEMO-3.6 is two-way coupled with the ice model LIM3.6. The atmospheric forcing is sourced from HIRLAM C11 (High-Resolution Limited Area Model) in operational mode (present model). The river discharge data are derived as daily means from Hydrological Predictions for the Environment (E-HYPE). Bathymetry data utilized in the model was sourced from the General Bathymetric Chart of the Oceans (GEBCO-2014) (Hordoïr et al., 2019).

In Hordoïr et al. (2019) a statistical comparison between measured and modelled sea level at different tide gauges in the Baltic and North seas was performed. This however was restricted to only a few stations located in the Baltic Sea for an 18-month period from July 2011 to 31 December 2012. Their results showed a high correlation between model and observations and a negative bias in terms of the representation of the low frequencies in the North Sea. For the rest of the Baltic Sea, however no major bias was identified. This study now considers a greater number of stations and from Fig. 5 which displays the sea level of the HDM at a specific time instant it is quite noticeable that a difference exists in HDM (denoted by red colour map at the location of TGs).

Therefore, the objective of this study is to evaluate and correct the Nemo-Nordic sea-level by using a geoid-referenced tide gauge network that now consists of 73 tide gauge stations. Note, however, that the

Nemo-Nordic vertical datum is not explicitly specified. As a result, we shall show in this study why the utilization of the geoid is a better approach.

3.3. Geoid model

The NKG2015, the most recent high-resolution (0.01×0.02 degrees) geoid model over the Baltic countries was developed by the Nordic Geodetic Commission in a long-term project that began in 2011 (Ågren et al., 2016). This model is based on the least-squares modification of Stokes' formula with additive corrections (LSMSA) in the framework of a remove-restore procedure. The standard deviation of this model in the 1-parameter fit to GNSS/levelling is 2.85 cm (1.5–2.0 cm on land). The coverage of the NKG2015 is from the latitude of 23N to 73N and the longitude of 0E to 34E. The geoid model refers to the GRS80 ellipsoid (ETRF2000 frame, epoch 2000.0). Note that the official NKG2015 model (that is released online) contains a 'hybrid permanent tide system' (i.e., a non-tide conversion has been added to the model to be able to use it directly for GNSS measurement). Therefore, in this study, we used the original one (NKG2015_zt), which is a pure zero-tidal model. In order to be able to use the NKG2015 for determining DT with SA data, the geoid model is transferred to mean-tide system as follows (Varbla et al., 2022):

$$N = NKG2015_zt + (0.29541 (\sin^2 \varphi - \sin^2 \varphi_{NAP}) + 0.00042 (\sin^4 \varphi - \sin^4 \varphi_{NAP})) \quad (9)$$

where φ_{NAP} is the latitude of NAP, and this equation is expressed in units of the metre.

3.4. Satellite altimetry data

Satellite altimetry (SA) is a well-known space technique used for measuring sea level data both in the offshore and coastal areas. One of the major advantages of SA that shall be employed in this study is that it tends to be a major source of data capture in the offshore areas compared to the TG data that are limited to coastal areas. In this study, we employed the Sentinel-3A (S3A) high frequency (20 Hz) along-track sea level measurements that operates in SAR mode and is based on ALES + SAR (an adapted retracking algorithm from Baltic+SEAL datasets Passaro et al., 2021). The data are captured at an across track resolution of 1.64 km and an along-track resolution of 300 m (Desjonquères et al., 2010). This dataset has been specially corrected for the coastal and sea ice conditions of the Baltic Sea and was obtained

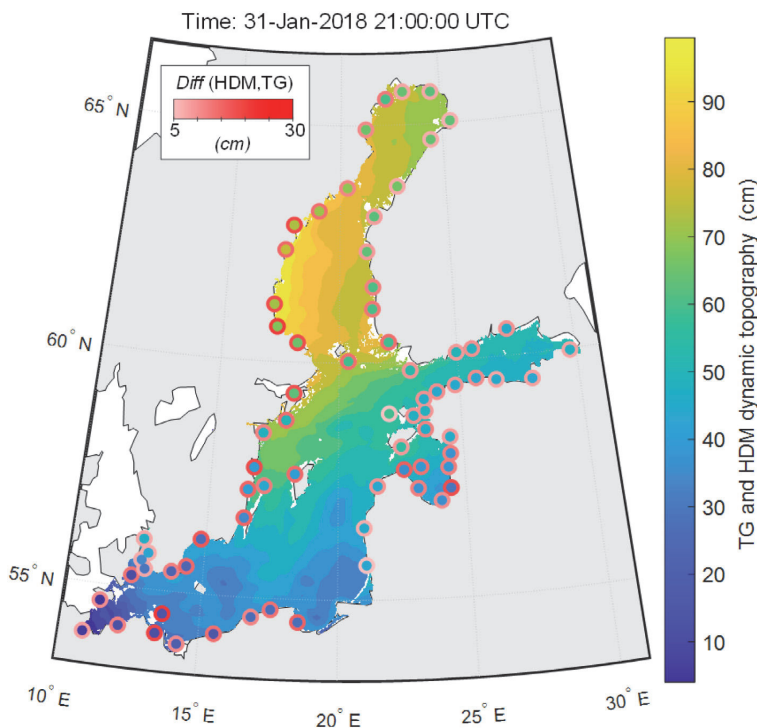


Fig. 5. Dynamic topography of the non-corrected Nemo-Nordic model (DT_{HDM}) and the TG reading (DT_{TG} , circle markers) at an arbitrary time instant: 31 January 2018 21:00 UTC. The red colour bar shows the difference between model and TG data.

from <http://balticsea.eu/data-access/>. The time period from January 2017 to June 2019 (33 cycles, with a repeat period of 27 days) which covers 39 passes over the Baltic Sea (see Fig. 3) is examined.

3.4.1. Satellite altimetry corrections

From the precise knowledge of the satellite orbit height (H_{orbit}) and the SA range (R) determination (using retracking waveforms) several other corrections (atmospheric and geophysical) are applied to derive the sea surface height (SSH). Eq. (10) displays the algorithm that was implemented by default to the Baltic+ SEAL products (Passaro et al., 2021):

$$SSH_{BS} = H_{orbit} - (R + WTC + DTC + i_{iono} + SSB + DAC + SET + PT + ROC) \quad (10)$$

where SSH_{BS} is obtained by default from the S3A data (Baltic+ SEAL project), which referred to Topex/Poseidon reference ellipsoid. The wet tropospheric (WTC), dry tropospheric (DTC), and ionospheric (i_{iono}) are atmospheric propagation corrections due to radar pulse passing through Earth's atmosphere. Sea state bias (SSB), dynamic atmospheric correction (DAC), solid Earth tide (SET), along with pole tide (PT) are classified in the geophysical corrections, which refer to the systematic geophysical effects that can be modelled and corrected. The radial orbit error (ROC) is a new correction that was derived and is based on multi-mission cross-calibration to ensure a consistent combination of all different altimetry missions (Bosch et al., 2014).

Since we will compare the SA data reduced for DAC with HDM data that does not, the default DAC correction must be cancelled by adding it back to the SSH_{BS} . Similar approach was also performed in other studies (Madsen et al., 2019; Rautiainen et al., 2020; Passaro et al., 2021). Note that the ocean tide corrections (OT) are not included in the SSH_{BS} (Eq. (10)), since the tides in the Baltic Sea are generally

small (less than 10 cm) (Samuelsson and Stigebrandt, 1996). All other geophysical corrections (i.e., SET and PT) remain to obtain identical measurements with TG records and HDM.

The DT_{SA} is formed by referencing the SSH_{BS} to a geoid model (i.e., NKG2015). The SA data are referred to the Topex/Poseidon reference ellipsoid (ITRF2008, mean permanent tide system). Hence, in the case that the geoid height N (Eq. (9)) is to be used together with SA data, the SSH_{BS} and N must be referred to the same reference ellipsoid and coordinate system. For this purpose, the SA data were transformed to the GRS80 and ETRF2000 through three steps: (i) conversion of the SA data to geocentric coordinates (X, Y, Z), (ii) transformation of the data from ITRF2008 to ETRF2000 (Altamimi, 2018), and (iii) converting back the data to the geodetic coordinate according to the GRS80 reference ellipsoid. Finally, the DT_{SA} is computed accordingly:

$$DT_{SA}(\varphi, \lambda, t) = (SSH_{BS}(\varphi, \lambda, t) + DAC(\varphi, \lambda, t) + h_{offset}(\varphi, \lambda, t)) - N(\varphi, \lambda) \quad (11)$$

where h_{offset} is the conversion values from Topex/Poseidon reference ellipsoid (ITRF2008) to the GRS80 (ETRF2000).

3.4.2. Satellite altimetry outlier removal

Outliers may be present in the SA data due to land contamination, presence of industrial infrastructure (wind turbines, platforms, etc.), turbulent waters, etc. especially near the coast. As a result, a three-step data screening procedure was applied for the outlier removal: (i) Obvious outliers that are outside of the ± 3 m range were removed. According to time-history of other sources, DT_{SA} larger than ± 3 m is physically impossible and distorts the SA statistical parameters.

This is followed by, (ii) a moving median with a window length of 1 NM was applied along the tracks, and the SA data more than

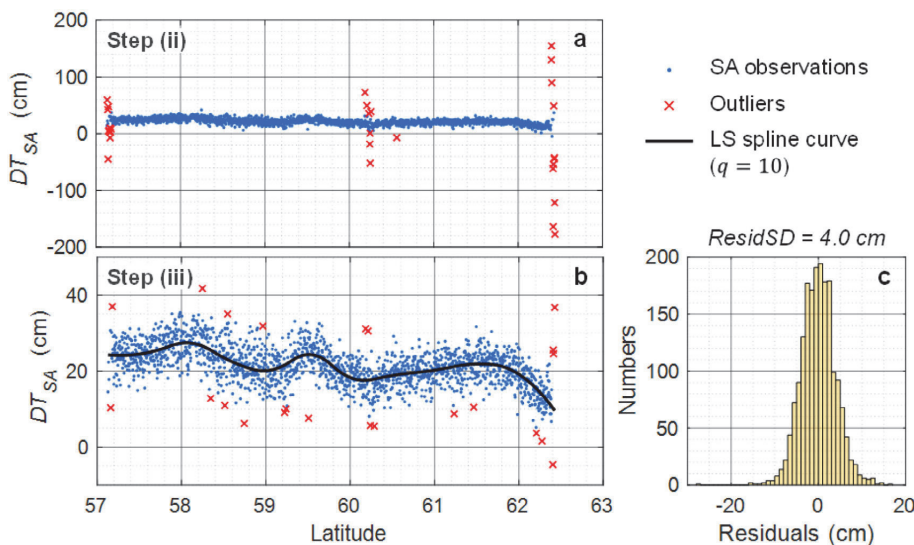


Fig. 6. An example of the second (a) and third (b) step of data screening process on the Sentinel-3A Pass No.55 and Cycle No.35. The residuals between SA observations and LS spline curve are shown in subplot (c).

four local scaled MAD (median absolute deviation) away from the local median within the sliding windows have been deleted as the coarse random errors (shown in red marker in Fig. 6a). And finally (iii) the DT_{SA} of each track was filtered by 3 standard deviation (i.e., outside of the 99.7% confidence interval) from the least-square (LS) spline approximation (shown in red marker in Fig. 6b). To determine the LS spline curves for each track, a piecewise quadratic polynomial with q knots was applied accordingly:

$$DT_{SA_j}(x) = a_0 + a_1\varphi + a_2\varphi^2, \quad j = 1, 2, \dots, q \quad (12)$$

where j denotes the index of knots and q is the number of polynomial pieces (Neitzel et al., 2019). This approximation allows the DT_{SA} to approach the coast fairly as much as the SA data is available. Note that the value of q varies for each pass and cycle depending on the ground-track length and instantaneous sea surface shape. Therefore, the number of polynomial pieces (q) was calculated using an optimization method to minimize residual standard deviation ($ResidSD$) for each pass/cycle. For this purpose, the $ResidSD$ is determined accordingly:

$$ResidSD = \sqrt{\frac{\sum_{i=1}^n (\epsilon_i - \bar{\epsilon})^2}{n-1}} \quad (13)$$

where ϵ and $\bar{\epsilon}$ are the residual between the SA data and LS spline curve and mean of residuals, respectively. The $ResidSD$ is obtained over the n data points along-track (blue dots in Fig. 6b).

Fig. 7 shows all $ResidSD$ s according to Eq. (13) based on compilation of all the passes (Fig. 7a) and all the cycles (Fig. 7b). According to Fig. 7a, the large $ResidSD$ amounts belong to short ground tracks that are within the vicinity of land (i.e., Pass No. 44-1, 158-2, 425-1, 500-1, 625-2, and 756). It also can be observed that Bothnia Bay (i.e., Pass No. 197-2, 311-2, 386-1, 425-2, and 739-2) has a large dispersion in the $ResidSD$, which can be due to sea ice conditions in the winter months. The median of $ResidSD$ for all passes and cycles is 3.6 cm. This examination of the SA data proves that the SA data are reasonably consistent and can be used for validation of DT_{HDM}^C . It also hints and identifies possible problematic (time-wise) cycles. For instance, periodic pattern is evident with an increase in the late winter and early spring (cycles 14, 28, 29, 41) which indicates a greater dispersion of SA observations in these seasons (see Fig. 7b).

3.4.3. Cycle mean dynamic topography

To give a better assessment of the model's performance in the offshore, the cycle-mean of DT ($CycleMDT$) was obtained along the SA tracks. Since the cycle period of S3A is 27 days, the $CycleMDT$ can make a contrast with hourly MDT of the HDM and TGs. Moreover, it is possible to reduce the contribution of low-quality cycles (i.e., cycles with high $ResidSD$, according to Fig. 7) by using weighted mean:

$$CycleMDT(\varphi, \lambda, Cycle) = \frac{\sum_{i=1}^C DT(\varphi, \lambda, i) \cdot w_i(Pass)}{\sum_{i=1}^C w_i(Pass)} \quad (14)$$

with

$$w_i(Pass) = \frac{1}{ResidSD(Pass, i)} \quad (15)$$

where C is the number of SA Cycles (i.e., $C = 33$ for the period January 2017–June 2019), and $ResidSD$ is the residual standard deviation according to Fig. 7. The $CycleMDT$ was also determined for the HDM and TG data similar to SA (that is, at the time of SA cycles using a linear interpolation and similar weight (Eq. (15)) used for SA). The HDM data were extracted at the coordinates of the SA data points via bilinear interpolation.

4. Method for examining time and spatial domain biases

4.1. Time-domain bias approach

As mentioned above, a difference in various sources of sea level is expected at similar locations due to: (i) the dissimilarity in the vertical reference datum utilized and (ii) the limitations of the methods employed in capturing sea level. Given that we have taken the perspective of the TG data represents the 'truth' within the coastal area, then to obtain the difference between DT of the HDM and TG records, the closest grid point of HDM to the TG locations (less than 4 km in most stations) are selected and extracted to produce the $DT_{HDM@TG}$ time-series for all 73 used stations. Thus, this difference referred to as $TDBias$ is determined according to Eq. (2) by using a 6-h moving average filter that gives an uncertainty of less than 6 cm with respect to the TG records, cf. Fig. 8b. For instance, $TDBias$ time series for three TG stations are shown in Fig. 8a. As can be observed, the bias

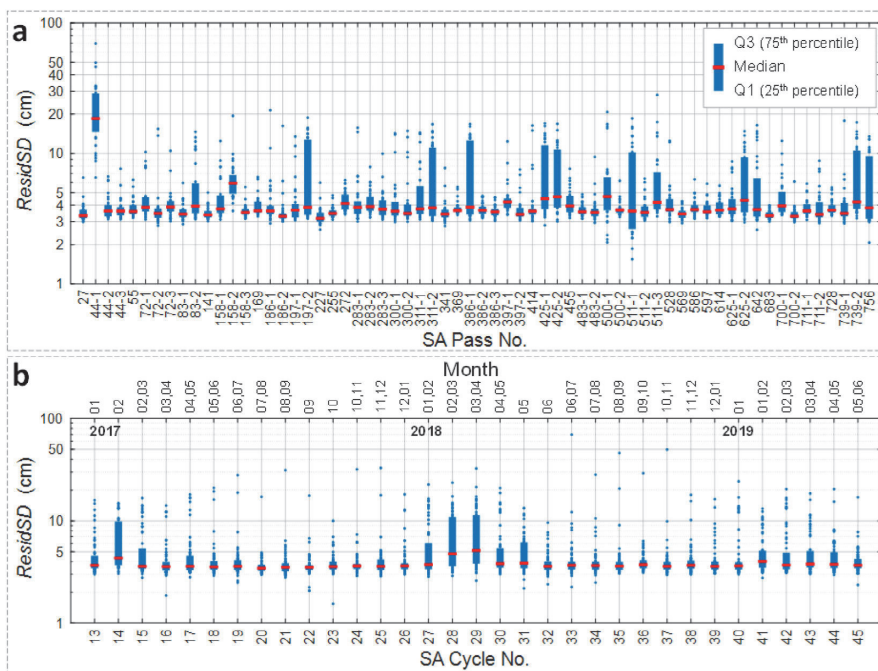


Fig. 7. The standard deviation of the residuals ($ResidSD$) of the Sentinel-3A over the Baltic Sea for the period 2017–2019 (Cycle No. 13–45) against (a) the pass number (all passes are shown in Fig. 3), as well as (b) cycle number. The vertical axes are presented on a logarithmic scale. The format of pass numbers is “{Pass No.}-x”, in which the x increments from the first part of the ground track that the satellite passed (i.e., southern part for ascending and northern part for descending tracks) according to the number of times that SA pass is interrupted by land.

is not constant in time, and it varies from around -20 to 30 cm. It is also apparent that the $TDBias$ behaves periodic, and the seasonality of bias is obvious with crest and trough in the spring and autumn seasons, respectively. The peaks in spring may be due to problems with river runoff or atmospheric forcings, which may serve as significant indicators of possible improvements for modellers.

The statistic parameter of $TDBias$ for all stations (during the period December 2016–April 2020) along with the correlation of raw Nemo-Nordic data with TG records in the course of time are illustrated in Fig. 9. It is evident that the mean of $TDBias$ at TG stations varies spatially between 5 and 16 cm with the highest values mostly occurring in the western side of the Gulf of Bothnia (Fig. 9a) and also at some distinct locations along the coast of the Baltic Sea (e.g., TG ids: 16, 28, 29, and 45) or due to their locations (e.g., mouth of river etc.) that causes them to be in disharmony with adjacent stations. Observe however that in these areas of higher bias the HDM and TG data are highly correlated (Fig. 9c). This hints that the HDM simulates similar dynamics as TG, thus the issues with the vertical datum or possibly even TG corrections are the major component contributing to the higher bias. Also observe in Fig. 9 that the model has larger standard deviation (10 cm) with respect to individual TGs in the Gulf of Riga (TG id 14) and in the eastern part of Gulf of Finland (TG id 73; see Fig. 9b). Since the surrounding TG are lower in standard deviation, this could indicate also possible issues with the TG data (e.g., insufficient corrections applied).

4.2. Spatial-domain bias approach

Since the DT_{TG} are only valid near the coast in the vicinity of the stations, computing the bias of all HDM grid points directly by Eq. (2) is not an ideal approach. Instead, given a set of $TDBias$ for a given time instant, a spatial interpolation can be employed to distribute HDM bias

over the study area. This aims to fit a surface (i.e., $SDBias$) that will best represent the spatial HDM bias. To obtain $SDBias$, the interpolation method and distance between the TG stations play key roles. The spatial interpolation is calculated based on the bias calculated between HDM and TG data at the location of stations. However, a valid DT_{HDM}^C in the open sea is indeed strongly dependent on the HDM’s performance in terms of high correlation between model and observations (i.e., truth).

In this study, the Nemo-Nordic model was corrected using three interpolation methods: (i) linear (Lin), (ii) thin plate spline regression (TPS), and (iii) inverse distance weighted (IDW). However other methods (e.g., Kriging and Least-Squares Collocation) are also commonly used in similar studies. Here, three selected interpolations with different interpolating approaches were used to demonstrate the sensitivity of the HDM correction method to the $SDBias$, and we will show that the methods provide less than a few centimetres variations in $SDBias$. To exclude possible instantaneous errors such as spikes in the TG records, a 6-h filtering window was applied as mentioned in Section 4.1. As a result, the $TDBias_{k=6-hr}$ yields a RMSE of 2.7 cm on average (see Fig. 8), which are suitable for interpolation process. The exception is for thin plate spline regression method where the instantaneous $TDBias$ was used.

The linear interpolation (Lin) can serve as a first approximation of the offshore bias (assuming the bias changes linearly over space; Jahanmard et al., 2021). The second approach, TPS, is a spline-based technique that arises from consideration of the integral of the square of the second derivative. Regarding this method, it is expected that the possible TG reading defect between stations (relative to nearby stations) is moderately relaxed. The TPS regression yielded an RMSE of 2.5 cm on average over time and at the location of the TGs after comparing corrected HDM and TG records.

The third used interpolation method is inverse distance weighted (IDW), whereby data points (stations) closer to the grid points have

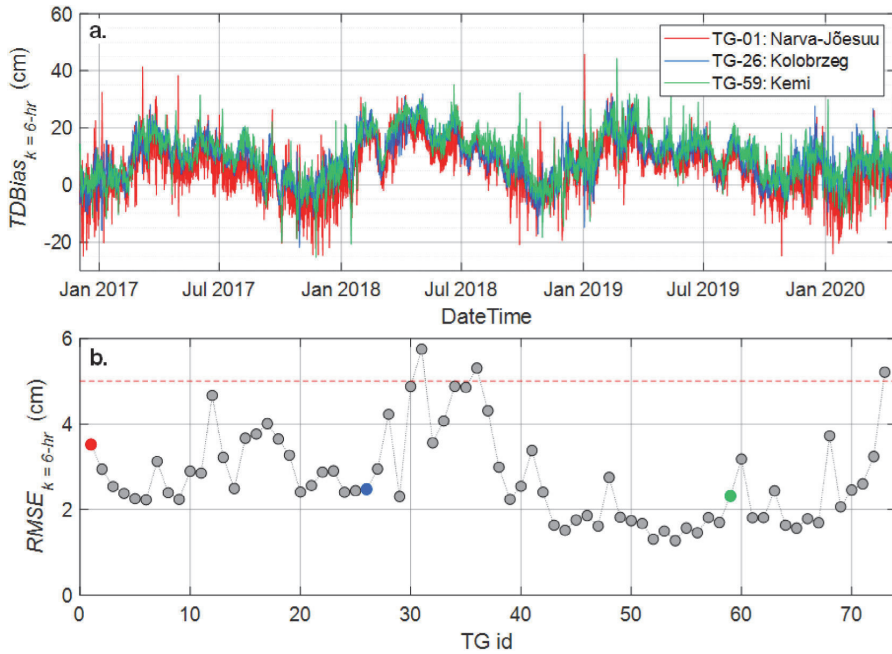


Fig. 8. The $TDBias$ time-series of Nemo-Nordic model, for example, at three TG stations with $k = 6$ -h backward moving average method (a), and the accuracy of the time-domain corrected model with respect to the DT_{TG} ($RMSE$, Eq. (3)) in the 73 used stations (b). The $RMSE$ of all stations is 2.7 cm on average. Refer to Fig. 3 and Table A.1 to see the location of stations and more details.

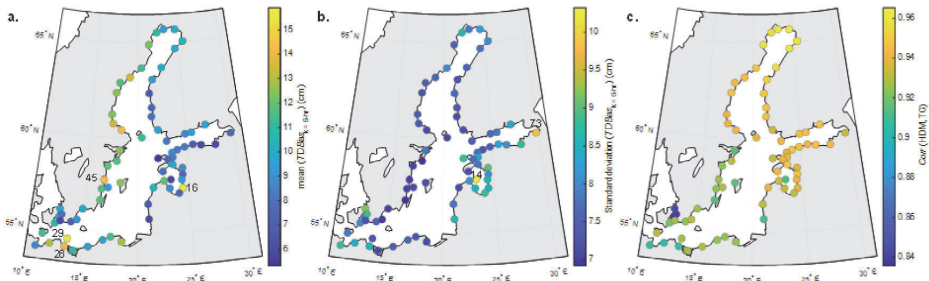


Fig. 9. (a) Mean and (b) standard deviation of the $TDBias_{k=6-hr}$, and (c) correlation between TG records and Nemo-Nordic model in the 73 used stations along the coastline of the Baltic Sea for the period December 2016–April 2020.

more effect than those which are further away. In this regard, the weighted mean is employed accordingly:

$$SDBias_{IDW}(\varphi, \lambda) = \frac{\sum_{i=1}^m w_i(\varphi, \lambda) TDBias_i}{\sum_{i=1}^m w_i(\varphi, \lambda)}, \quad \forall(\varphi, \lambda) \neq (\varphi_i, \lambda_i) \quad (16)$$

with

$$w_i = \frac{1}{D\{(\varphi, \lambda), (\varphi_i, \lambda_i)\}^2} \quad (17)$$

The subscript i denotes the TG stations, m is the number of stations (i.e., $m = 73$), and D is a distance measurement operator, which is used to measure distances on a sphere.

As an example, Fig. 10a shows the computed $SDBias$ using the above methods for a particular time instant (31 January 2018 21:00 UTC; see Fig. 5 for DT_{HDM}). In this figure, a spatial variation of model bias has been illustrated. All three methods show a more or less similar trend and range (11–26 cm), and as expected the trace of triangles’

edges are visible in the Lin interpolation method. Generally speaking, in all three interpolation methods the largest bias is associated to the western section of the Baltic Sea and also at some localized areas (due to certain TG quality issues). To evaluate the similarity and difference of those methods in the course of time, Fig. 10b represents standard deviation of range of three methods during December 2016–April 2020. Observe that in most areas the variation of the difference between methods is less than 2 cm. The largest difference occurs in the Gulf of Riga (TG id 14) where the range of three methods has the highest standard deviation of 4.2 cm in the course of time (see Fig. 10b). This also coincides with Fig. 9b that showed the same TG station also having a higher standard deviation and lower correlation than others surrounding it.

By correcting all grid data for the bias, the corrected HDM (DT_{HDM}^C) is obtained (Eq. (5)). In the following, the methods were compared with SA data, and as a result, although corrected HDMs show more

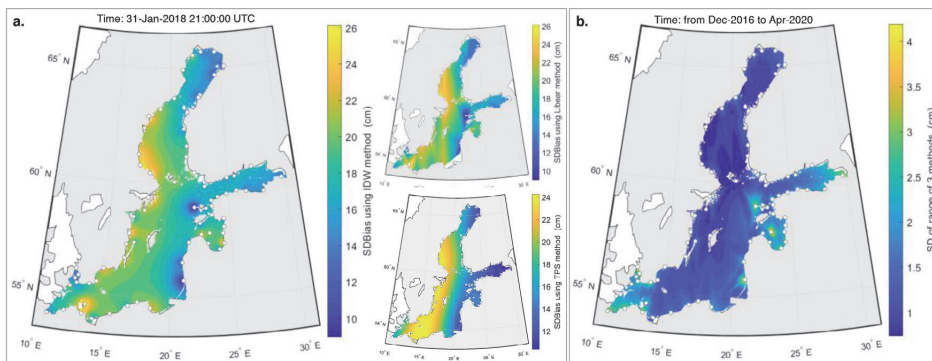


Fig. 10. (a) *SDBias* of Nemo-Nordic model for an arbitrary time instant: 31 January 2018 21:00 UTC by using linear interpolation (Lin), thin plate spline regression (TPS), and inverse distance weighted interpolation (IDW). (b) Standard deviation of range of those methods in the course of time from December 2016 to April 2020.

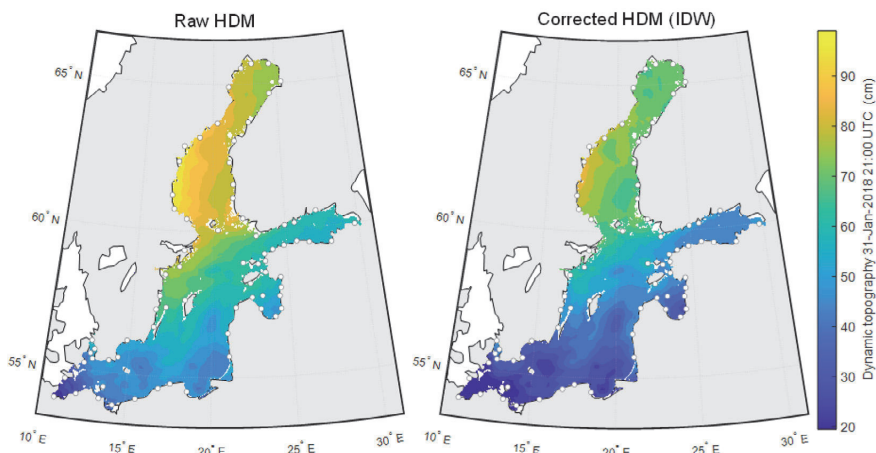


Fig. 11. Raw (left) and corrected (right) Nemo-Nordic dynamic topography by inverse distance weighted (IDW) interpolation method over the Baltic Sea for an arbitrary time instant: 31 January 2018 21:00 UTC. The circle markers indicate location of used TGs to correct HDM.

or less similar results and RMSE with respect to the DT_{SA}^C , we selected the IDW method as a preferred method to be used for correcting the model. Following this the IDW method for HDM correction is shown in all the calculations, however, we will also show in Section 5.2 that the differences between methods with respect to SA data are barely noticeable in the offshore area. The DT_{HDM}^C and raw HDM for the time instant (see Fig. 10a for *SDBias*) are presented in Fig. 11. After correction, the pattern of dynamic topography has not changed noticeably, but the range of DT_{HDM}^C has been shifted and narrowed to 5–78 cm, while the range of raw HDM was 20–100 cm at this time instant. To verify if the corrected HDM data are reliable and accurate enough, validation in the offshore areas was necessary and this was performed in this study by utilizing SA along-track data.

To illustrate the model changes in the time period of interest, the time-mean and temporal standard deviation of *SDBias* are shown in Fig. 12. The mean of *SDBias* for 41 months demonstrates that the HDM bias is roughly 10 cm with a higher value in the western Baltic Sea. This bias varies by more than 7 cm in the course of time (Fig. 12 right), which implies that long-term bias corrections (e.g., the mean of a year) are incapable to improve the model accuracy with respect to the TG data (Fig. 8a illustrates the same point). The spatial standard deviation of the mean *SDBias* (Fig. 12a) is roughly 1.3 cm. This unnoticeable amount of the spatial bias variation could indicate that the HDM uses

more or less an equipotential surface of the Earth’s gravity field as its reference, and using the term DT_{HDM} is an acceptable assumption. It is also noticeable in this figure that some stations may have zero-level problems or the HDM may not be able to simulate regional effects such as river runoff.

5. Results

5.1. Mean dynamic topography

By utilizing a network of geoid-referenced TG data along the Baltic Sea coastline, it was possible to derive a corrected hydrodynamic model dynamic topography (DT_{HDM}^C). This variable now represents sea level variations with respect to a more realistic ‘zero’ level being that of the geoid. As a result of this, it is possible to obtain a realistic Mean Dynamic Topography (MDT), over different time scales (seasonal, annual, etc.) that can reveal the persistent or semi-persistent dynamical patterns. Note that the HDM’s high temporal and spatial resolution is its advantage for this purpose compared to other datasets. The MDT is determined for different time period.

Fig. 13 illustrates the (annual) MDT for the raw and corrected HDM along with the MDT of used TGs that are shown in circles with the same colour bar at the location of stations. Particular characteristics are

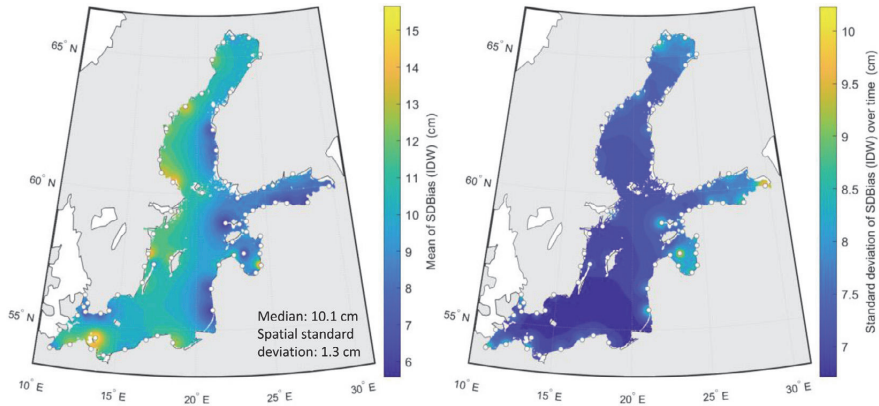


Fig. 12. The spatial distribution of the temporal mean (left) and standard deviation (right) of *SDBias* of Nemo-Nordic model for period of December 2016 to April 2020. The circle markers indicate location of used TGs.

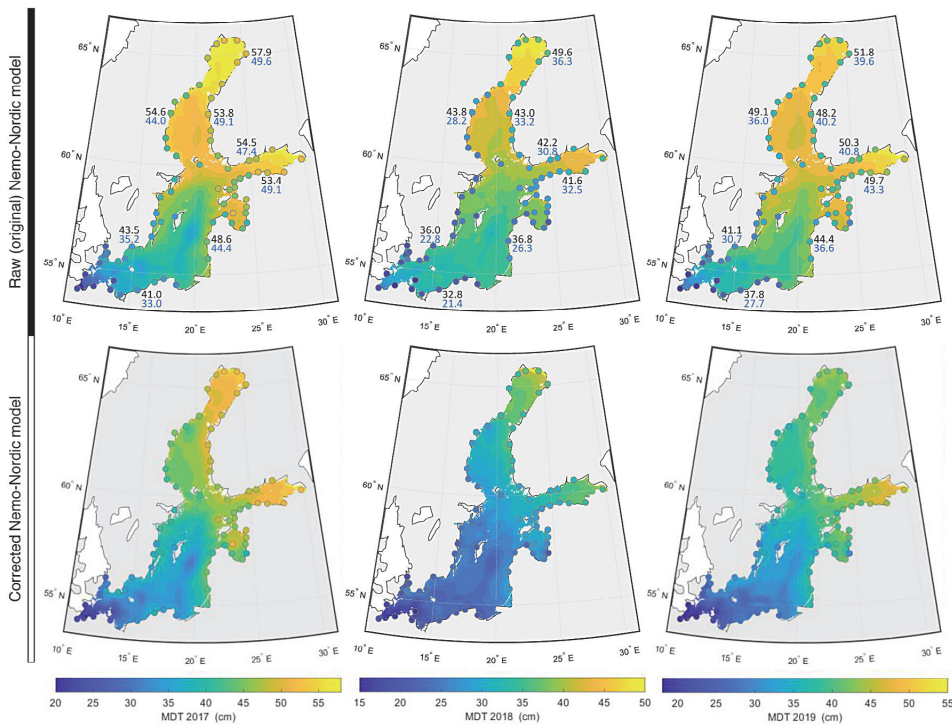


Fig. 13. Annual mean dynamic topography (MDT) of original (top row) and corrected (bottom row) Nemo-Nordic model along with MDT of selected TG records in the same color bar scale. The black and blue values in top row refer to the raw model MDT and the TG (also corrected model) MDT at some stations, respectively.

observed, for instance: (i) the raw HDM over-estimates the TG records, thus the actual values are lower; (ii) in general similar patterns of MDT is observed however there exist at particular areas a difference in patterns and trends and (iii) localized areas shows slight inconsistency in a few stations (e.g., TG id 16; as also mentioned in Section 4.1 and Fig. 9, where the *TDBias* of each station is compared to the adjacent stations) that had a higher standard deviation but lower correlation.

In general, the corrected MDT (like raw HDM) exhibits a spatial pattern, with the largest MDT in the north of the Gulf of Bothnia

and eastern section of the Gulf of Finland. This is the expected trend in the Baltic Sea (Madsen et al., 2019) which are due to freshwater accumulation and wind forces (Soomere and Quak, 2013). The annual MDT however shows much more variation in the corrected MDT than the original model. For instance, in 2019 the range of MDT is reduced almost from 37.0 (55.0-18.0) to 29.0 (46.0-17.0) cm, and the difference between the north (north of Bothnia Bay) and south (north of Poland) of the Baltic Sea has been reduced roughly 25 percent. This difference is especially noticeable in the Gulf of Bothnia, in all three years. Recall

that in the Gulf of Bothnia the highest bias was applied whether this application of a higher bias is suitable, requires further examination. For it is possible that (i) in Gulf of Bothnia (especially in its northernmost part — Bay of Bothnia) many of the TG are not exactly located at the coast but may be located more inland in riverways. So, even though they may reflect the trend of sea level, their actual value may not reflect that of the coastal sea area as was captured by the models and (ii) issues with TG corrections, that are unknown at the time of this study (e.g., offsets, vertical land movement corrections etc.). To verify however if the corrected HDM data are reliable and accurate enough, especially in the offshore areas and in the areas of higher variation in trends, a validation with SA data is performed (Section 5.2).

5.2. Validation in the offshore areas

The SA data provide an independent source of validation of the corrected HDM, especially in the offshore. Thus, we validated the raw/corrected HDMs in order to show and compare the performance of the developed methods in the offshore. However, several studies have shown that SA data may still be biased even after corrections are applied (e.g., Mostafavi et al., 2021) and an accuracy of 2–5 cm is achievable with the SA-Sentinel 3A data. We utilize the SA along-track sea level profiles that are compared with similar profiles extracted from the HDM. The corrected model was evaluated using SA data via two approaches in the offshore areas: (i) calculation/comparison of the along-track SA bias with respect to the raw/corrected HDM data (Fig. 14), and (ii) comparison of the *CycleMDT* of various datasets as defined in Section 3.4 (see Eq. (14)). In both approaches we are going to show the variation of inconsistency between HDM and SA data.

For the first approach, the SA bias with respect to each HDM data is determined accordingly:

$$Bias_{SA} = \frac{\sum_{i=1}^n (DT_{SA_i} - DT_{HDM_i}^C)}{n} \quad (18)$$

where n is the number of SA data along the track and $DT_{HDM_i}^C$ is the corrected model. For obtaining the DT_{HDM} along each pass in the desired cycle, the HDM data have coincided temporally and spatially with the SA data points with linear interpolation.

Fig. 14 shows the bias of S3A with respect to the raw HDM (in black) and corrected HDM (in green, blue, and red for Lin, TPS, and IDW method, respectively) versus the SA passes (Fig. 14a) and cycles (Fig. 14b). The comparison using all passes and cycles shows that: (i) with all three interpolation method the differences are almost negligible (that is, the model correction is insensitive to the interpolation method); (ii) The SA data agrees better with the corrected HDM (median of SA bias is roughly -1.5 cm) compared to the uncorrected (median of SA bias -13.2 cm); (iii) the scatter plot of the bias (Fig. 14c, which shows the median of the bias for the corrected HDM) identifies some passes with large biases, such as the eastern part of the Gulf of Finland with a bias of over 5 cm. These passes are however similar to the areas of higher standard deviation of *SDBias* (Fig. 12 right). Moreover, (iv) a seasonal trend is evident in the bias of the raw HDM relative to SA (as also observed in Fig. 8a relative to TG records) whereas it disappears for the corrected HDM (Fig. 14b).

The regions with a large bias require further examination, and this was performed using the *CycleMDT* approach. Thus, for the second approach of validation, a comparison with *CycleMDT* (see Eq. (14)) of all available data sources. The term *CycleMDT* is selected to make a contrast with MDT. *CycleMDT* is the average of n cycles of instantaneous SA observations, which is expected to be very close approximation to MDT.

Fig. 15 demonstrates *CycleMDT* along the three SA passes: pass no. 272, 55, and 414. According to this figure, a comparison of raw/corrected HDM, TG records, and SA data reveals that: (i) before examining the corrected HDM, the TG records and SA profiles have mostly coincided, whereas the raw HDM does not, (ii) compared to raw

HDM, corrected HDM is more consistent in magnitude as well as spatial trend with SA profiles and TG records, and (iii) the corrected HDM for Pass No. 414 (located in the eastern section of the Gulf of Finland) displays a more stable DT compared to SA. Results in this area indicate that utilizing SA data along with the geoid model (i.e., NKG2015) leads to an unrealistic DT value that fluctuates widely. This strongly suggests problems with the geoid model due to insufficient coverage of marine gravity data and validation in such locations (Ågren et al., 2016).

5.3. Identifying areas of large discrepancy

A comparison of point-to-point SA data and HDM for the entire Baltic Sea allows a broader overview for identifying problematic areas especially in the offshore areas (Fig. 16). This figure shows a point-to-point difference between *CycleMDT* of the SA data and raw (Fig. 16a) or corrected Nemo-Nordic model (Fig. 16b). This reveals possible inconsistencies between various data sources and also highlights regions with problems, especially offshore. In this study, different datasets are used: TG, HDM, SA, geoid model, and land uplift model, each of which has its own uncertainty in different conditions and regions. For instance, the SA data may contain artificial bias even after applying geophysical and atmospheric corrections.

Fig. 16a (top) clearly demonstrates the differences between HDM and SA data with an average of 11.1 cm with the highest bias occurring in the northern and eastern sections of the Baltic Sea (approx. 30.0 cm). The SA data confirm the corrected HDM with a bias of 0.1 cm, however a large difference (greater than 7.0 cm) between the corrected model and SA data is noticeable in the Gulf of Finland (as observed in Fig. 15 and Pass No. 414). The reasons for this bias requires further evaluation for future studies. The centred root mean square error (CRMSE) of the HDM before and after correction are 2.2 and 2.4 cm, respectively. Basically, the spatial comparison of differences between HDM and SA results shows the method decreases the HDM bias by roughly 11.0 cm in the offshore area.

Fig. 16 also highlights problematic areas amongst the different sources of data. For instance, there is a high discrepancy between SA and HDM (in both the raw and corrected models; shown in black) in the eastern part of the Gulf of Finland, possibly because of the geoid model deficiencies. Nearshore contaminated SA data are mostly observed in the north and centre of the Baltic Sea.

6. Discussion

The methodology employed in this study demonstrated that by utilizing a dense network of TG data that are referred to the geoid it is possible to correct the HDM bias (both temporally and spatially). Applying this bias correction allowed computation of a corrected HDM whose sea level data are now referred to the geoid and thus more or less realistic both at the coast and in the offshore domain. To evaluate whether the corrected HDM MDT results were reliable and accurate enough, the validation using SA data played an essential role in assessing this, especially in the offshore domain.

The method employed entailed initially identifying the temporal bias and then using this temporal bias along with three interpolation techniques, to obtain the spatial bias in the HDM. Examination of the temporal bias (HDM-TG), which considers data points mainly at the coast, revealed a mean bias with a range of 5.3 to 15.9 cm (that is, the HDM tended to overestimate the results) along the Baltic Sea coast (Fig. 9). The largest bias values occur in the Gulf of Bothnia (especially the western side) and in some other localized areas that appear to be TG location dependent. Interestingly the correlation between HDM and TG was high in these areas (i.e., >0.92). In-addition the standard deviation of the temporal bias also revealed that in most TG locations a value that varied from 7–9 cm. There were however a few TG locations with a standard deviation of 10 cm, and these were located of at

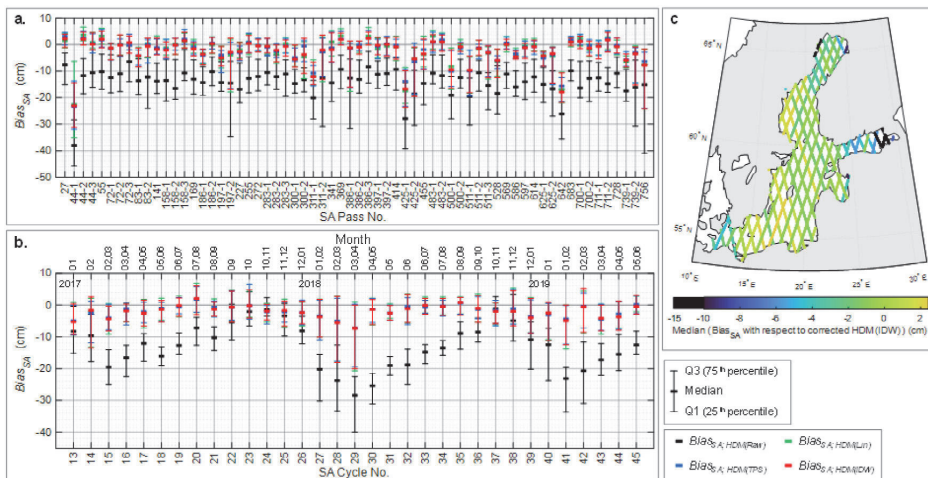


Fig. 14. Along track Sentinel-3A bias with respect to the raw/corrected Nemo-Nordic model against the (a) pass number and (b) cycle number (or month). Subplot (c) illustrates the median value of the bias for corrected HDM by IDW on each pass.

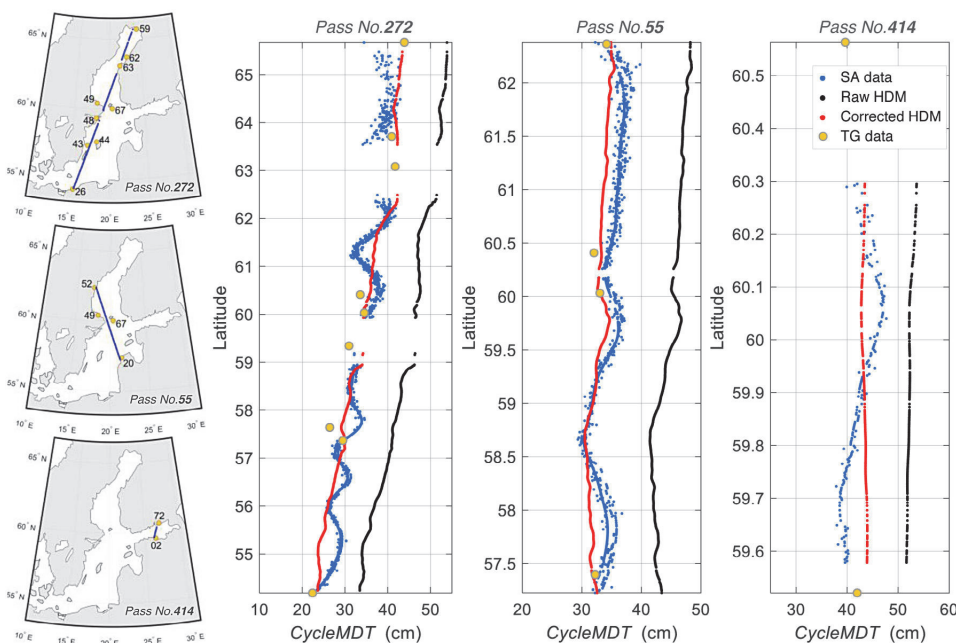


Fig. 15. Comparison of raw/corrected Nemo-Nordic model with the SA data (Sentinel-3A) and TG records via *CycleMDT* (i.e., mean of 33 cycles) in three example pass. The left column denotes the location of each passes and vicinity TGs.

the easternmost section of the Gulf of Finland at the Russian TG of Kronstadt (TG id 73, cf. Fig. 3) and also in the Estonian TG station in the Gulf of Riga at the Ruhnu station (TG id 14, cf. Fig. 3). This higher standard deviation may indicate issues with the vertical datum at these stations. These results however strongly suggest that the bias calculated between the HDM and TG consists of a combination of vertical reference issues between the HDM and TG. In addition, possible problems with TG (perhaps corrections applied, or location of TG) and HDM modelling errors may be present as was observed in Jahanmard et al. (2021). Most pertinent is that these results highlight, spatially the

critical areas/locations that require further examination/improvements both with the HDM and TG data.

To obtain the spatial bias three different interpolations methods were employed (linear, IDW and TPS) and in general results of all methods displayed similar patterns especially in the southwestern Baltic Sea (Fig. 10). As expected, three methods provide a stable *SDBias* with standard deviation of less than 2 cm in the vast majority of areas (Fig. 10b). The IDW method however displayed a more realistic trend than others (Fig. 10). In Jahanmard et al. (2021) a linear interpolation method was utilized for the Gulf of Finland, however this showed

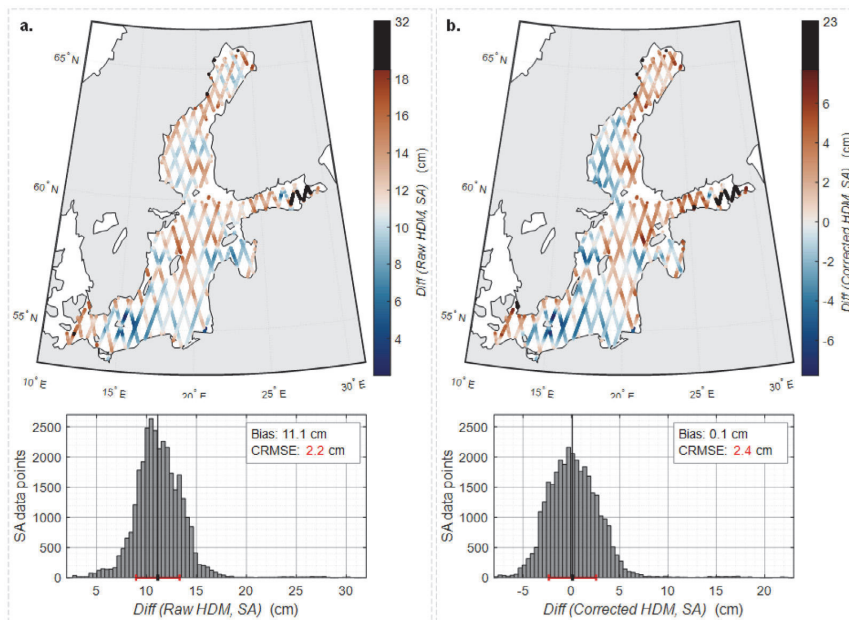


Fig. 16. Point to point comparison of *CycleMDT* of the Sentinel-3A data and Nemo-Nordic model: (a) raw model and (b) corrected model via a network of the 73 geoid referred TG records for period of January 2017 to June 2019. Bottom row indicates the histogram of these top row residuals. CRMSE is centred root mean square error that indicates with red line.

peakiness at the edges as was seen in the results of this study. Instead, now for this study, the IDW method displays an improvement that can be applied. The IDW method can further be improved for it also showed some localized discrepancy that were most likely influenced by the problems with TG data (Fig. 10). This is so for in this study the assumption was made of the TG data being ‘the truth/most realistic’. Whilst this assumption seems to perform reasonably well, the results have revealed that some TG may have some problems (e.g., location not ideal, corrections applied). Thus, the interpolation methods applied should be applied with care and checks performed with other datasets on the validity of results.

In general, the corrected HDM MDT showed an improvement (compared to uncorrected MDT) in that the high and low frequency biases (e.g., difference between reference level, seasonal bias, etc.) are eliminated by this correction, and the HDM is corrected on the scale factor of almost 1.5 in many parts of the BS, whereby the uncorrected MDT tended to overestimate the results. Given that the original HDM at the location of stations and TG records are more or less highly correlated (Fig. 9c), it was to some degree expected that a comparison of the raw and corrected HDM would show similar patterns. In general, this was the case, for most areas of the Baltic Sea showed similar patterns as calculated in other studies (e.g., Madsen et al., 2019). However the western side of the Gulf of Bothnia showed an unexpected variation compared to the raw HDM (with a difference of 5 cm from western to eastern side). This displayed, that correcting the model for the bias may also change the overall pattern of the MDT. To access whether the corrected HDM results were accurate or reliable, a validation was performed using the Sentinel-3A along-track satellite data.

This validation on whether the corrected HDM was accurate or realistic, especially in the offshore areas, was employed by comparing SA along-track data with that of the raw and corrected HDM. This comparison showed that the corrected HDM was more compatible with SA than the uncorrected HDM (Figs. 14, 15), with a bias of 0.1 cm for corrected now existing versus that of 11.1 cm for uncorrected HDM. Whilst the SA agreed better with corrected HDM, the higher differences

still existed in the Gulf of Finland region. Previous SA studies suggested that in the Baltic Sea a RMSE of 4–7 cm can be expected (Rautiainen et al., 2020; Mostafavi et al., 2021). Thus, to ascertain exactly what may be occurring in the Gulf of Finland requires further examination, for it could be a combination of HDM errors, SA and TG related problems. Further examination of the SA along-track profiles in this region revealed possible problems in geoid modelling due to sparseness of gravity data that may have affected results (Fig. 15 (Pass No. 414), Fig. 16). In Varbla et al. (2020a) this specific location was also found to have possible geoid modelling issues. In this study we employed the use of SA for validation, but it is possible for future studies to employ use of GNSS applications (Varbla et al., 2020a) or Airborne Laser scanning can be employed (Varbla et al., 2020b).

Thus, the applied methodology appears to perform reasonably well in deriving a more realistic MDT. The method however can be improved for comparison with HDM and SA data identified several key areas that require further investigation, such as Gulf of Finland, that may be affected by TG, SA, HDM or geoid modelling issues. This study assumed that TG as representative of the truth, the results however have shown that some TG may not be ideally located (e.g., installed at the mouth of rivers) or that may have had wrongly applied corrections, and this require further examination. For obtaining TG data from different countries/authorities with different protocol of measurements and instrumentation may also have errors that may be unknowingly introduced. Since the results of this study were highly dependent on the bias calculated, it is essential that: (i) TG data are consistent and accurate as can be and (ii) the computed bias needs to be valid in the offshore areas.

This study was possible due to the dense network of TG in the Baltic Sea and the agreement on employing the geoid based Baltic Sea Chart Datum. Hence, it is expected that similar approach can be applied in other marine areas. Utilization of the geoid as a vertical datum allows more realistic dynamic topography calculations and it is also more compatible with other sources of data. To some degree it is expected that deriving a corrected HDM may also lead to changes in the

Table A.1

List of tide-gauge stations from 01 to 73. The national reference frames and geoid model complying with BSCD2000 along with the reference of data providers are indicated for each country. The conversion values and land-uplift correction are listed for each individual station as well.

TG id	TG name	Latitude (arc-degree)	Longitude (arc-degree)	BSCD2000 conv.value (cm)	NKG2016LU (mm/year)	TG id	TG name	Latitude (arc-degree)	Longitude (arc-degree)	BSCD2000 conv. value (cm)	NKG2016LU (mm/year)
1. Estonia						Data provider emodnet-physics.eu					
Datum EH2000 (zero-tide system)						Ref. of conversion values –					
Geoid model EST-GEOID2017						32	Rodby	11.3500	54.6500	000.0	0.23
Data provider EEA (2021)						33	Rodvig	12.3728	55.2542	000.0	0.62
Ref. of conversion values Ellmann et al. (2019)						34	Dragor	12.6833	55.6000	000.0	0.91
01	Narva-Jõesuu	28.0421	59.4691	000.0	1.70	7. Sweden					
02	Kunda	26.5417	59.5210	000.0	2.35	Datum RH2000 (zero-tide system)					
03	Loksa	25.7072	59.5845	000.0	2.74	Geoid model SWEN17-RH2000					
04	Pirita	24.8208	59.4689	000.0	2.85	Data provider SMHI (2021)					
05	Paldiski	24.0493	59.3508	000.0	3.02	Ref. of conversion values –					
06	Dirhami	23.4969	59.2084	000.0	3.09	35	Helsingborg S.	12.6870	56.0446	000.0	1.22
07	Haapsalu	23.5274	58.9580	000.0	2.72	36	Barsebäck	12.9033	55.7564	000.0	1.05
08	Heltermaa	23.0471	58.8656	000.0	2.85	37	Skanör	12.8294	55.4167	000.0	0.77
09	Ristna	22.0552	58.9212	000.0	3.46	38	Ystad Sjö	13.8257	55.4227	000.0	0.79
10	Roomassaare	22.5038	58.2172	000.0	2.25	39	Simrishamn	14.3578	55.5575	000.0	0.89
11	Virtsu	23.5113	58.5723	000.0	2.23	40	Karlskrona S.	14.8213	56.1542	000.0	1.44
12	Pärnu	24.4820	58.3875	000.0	1.71	41	Kalmar Sjö	16.3888	56.6713	000.0	1.93
13	Häädemeeste	24.4636	58.0375	000.0	1.41	42	Oskarshamn	16.4781	57.2750	000.0	2.68
14	Ruhnu	23.2635	57.7835	000.0	1.50	43	Ölands N. U.	17.0972	57.3661	000.0	2.73
2. Latvia						44	Visby	18.2844	57.6392	000.0	2.88
Datum LAS2000,5 (zero-tide system)						45	Västervik Sjö	16.6747	57.7482	000.0	3.32
Geoid model EST-GEOID2017						46	Arkö	16.9607	58.4843	000.0	4.34
Data provider LVGMCL (2021a)						47	Landsort Norra	17.8589	58.7689	000.0	4.62
Ref. of conversion values LVGMCL (2021b)						48	Loudden Sjö	18.1373	59.3413	000.0	5.34
15	Salacgrīva	24.3536	57.7553	-484.0	1.21	49	Forsmark	18.2108	60.4086	000.0	6.75
16	Skulte	24.4094	57.3158	-485.0	0.88	50	Bönan Sjö	17.3186	60.7384	000.0	7.26
17	Daugavgrīva	24.0233	57.0594	-485.0	0.74	51	Ljusne Sjö	17.1452	61.2067	000.0	7.91
18	Mērsrags	23.1328	57.3347	-484.0	1.09	52	Spikarna	17.5311	62.3633	000.0	8.94
19	Kolka	22.5928	57.7372	-483.0	1.63	53	Lunde Sjö	17.8764	62.8865	000.0	9.21
20	Ventspils	21.5344	57.3956	-483.0	1.56	54	Skagsudde S.	19.0119	63.1906	000.0	9.48
21	Liepāja	20.9994	56.5156	-483.0	0.85	55	Holmsund S.	20.3331	63.6803	000.0	9.51
3. Lithuania						56	Furuögrund	21.2306	64.9158	000.0	9.44
Datum LAS07 (zero-tide system)						57	Strömören S.	22.2383	65.5497	000.0	9.12
Geoid model LIT15G						58	Kalix-Storön	23.0961	65.6969	000.0	8.90
Data provider EPA (2021)						8. Finland					
Ref. of conversion values BOOS (2021)						Datum N2000 (zero-tide system)					
22	Klaipėda	21.0811	55.7302	-487.4	0.23	Geoid model FIN2005N00					
4. Poland						Data provider FMI (2021a)					
Datum PL-EVRF2007-NH (zero-tide system)						Ref. of conversion values FMI (2021b)					
Geoid model PL_geoid-2011						59	Kemi	24.5153	65.6734		8.60
Data provider IMGW-PIB (2021)						60	Oulu	25.4182	65.0403		8.30
Ref. of conversion values BOOS (2021)						61	Raahe	24.4071	64.6663		8.71
23	Gdynia	18.5552	54.5177	-491.3	0.00	62	Pietarsaari	22.6896	63.7086		8.95
24	Leba	17.5505	54.7634	-491.3	0.20	63	Vaasa	21.5712	63.0815		8.79
25	Ustka	16.8538	54.5880	-491.4	0.13	64	Kaskinen	21.2148	62.3440		8.31
26	Kolobrzeg	15.5534	54.1866	-490.2	-0.06	65	Mäntyluoto	21.4634	61.5944		7.44
27	Swinoujście	14.2543	53.9084	-491.5	-0.18	66	Rauma	21.4258	61.1335		6.81
5. Germany						67	Föglö	20.3848	60.0319		5.70
Datum DHHN92 (mean-tide system)						68	Turku	22.1005	60.4283		5.41
Geoid model GCG2016						69	Hanko	22.9766	59.8229		4.16
Data provider BSH (2021)						70	Helsinki	24.9562	60.1536		3.69
Ref. of conversion values BOOS (2021)						71	Porvoo	25.6251	60.2058		3.44
28	Greifswald	13.4461	54.0928	-500.0	-0.09	72	Hamina	27.1792	60.5628		3.04
29	Sassnitz	13.6431	54.5108	-500.0	0.09	9. Russia					
30	Warnemünde	12.1033	54.1697	-500.0	0.00	Datum BHS77 (mean-tide system)					
31	Travemünde	10.8722	53.9581	-500.0	-0.12	Geoid model –					
6. Denmark						Data provider emodnet-physics.eu					
Datum DVR90 (tide-free system)						Ref. of conversion values Sacher (2019)					
Geoid model DKgeoid12						73	Kronstadt	29.7500	59.9667	+19.0	1.40

dynamics of the marine area (e.g., salinity, temperature, circulation). The focus of this study however has been on achieving a realistic sea level component that is comparable with other sources of data.

For future studies it is possible to examine in an iterative approach the corrected HDM results with other components of the HDM model (e.g., currents, salinity etc.). Consequently, the results of this study

demonstrate progress toward the utilization of a more realistic DT that has a valuable contribution to marine engineering and climate studies.

7. Concluding remarks

This study has demonstrated a methodology that allows derivation of realistic dynamic topography both in the coastal and offshore areas of the Baltic Sea. This was possible by the synergizing of tide gauge, hydrodynamic and satellite altimetry data, with the geoid being the key component that linked the vertical reference datum amongst them.

In most areas of the Baltic Sea the trend of the corrected DT agreed reasonably well with the general dynamics of the study area and also that of other studies. The annual mean dynamic topography of corrected HDM was improved by a factor of almost 1.5 (for example 2019, the uncorrected MDT was 50 cm and after correction was 35 cm in the Gulf of Bothnia). In such a busy and dynamic marine environment of the Baltic Sea, realistic DT allows better application on quantification for marine engineering (e.g., pipeline construction, offshore infrastructure etc.) and climate studies application.

Incidentally however the methodology allowed identification of: (i) potential problematic areas and seasons of HDM models that requires improvement; (ii) tide gauges that may not be reliable for various reasons (e.g., location not ideal for representing the coastal environment or questionable corrections that may have been applied); (iii) areas of satellite altimetry along-track passes that may be challenging even after outlier removal and (iv) areas that geoid model were not adequately represented.

Thus, the methodology shows an advancement and improvement towards our understanding of the marine environment and also the data sources being utilized. In addition, the assimilation of observed sea levels (from tide gauge, satellite altimetry, etc.) into a hydrodynamic model requires that the model refers to the same vertical reference datum as the observed sea levels. Hence, this vertical reference unification between model and observations enables possibilities to have a more effective implementation of the data assimilation technique for modelled dynamic topography and enhances HDM performance. The method however can be improved for the satellite altimetry to confirm particular questionable areas (e.g., eastern part of the Gulf of Finland). The validation in the offshore areas using satellite altimetry showed promising results. Thus, in future studies the utilization of other sources of offshore sea level data such as GNSS surveys and buoys and airborne laser scanners can also be explored. In addition, it is possible for future studies to use the results of the corrected HDM to improve on other data components of the HDM (e.g., currents, salinity etc.) in an iterative approach.

CRedit authorship contribution statement

Vahidreza Jahanmard: Conceptualization, Methodology, Validation, Formal analysis, Writing – original draft, Visualization. **Nicole Delpeche-Ellmann:** Conceptualization, Validation, Supervision, Writing – review & editing, Project administration. **Artu Ellmann:** Conceptualization, Validation, Supervision, Writing – review & editing, Project administration, Funding acquisition.

Declaration of competing interest

The authors declare that they have no known competing financial interests or personal relationships that could have appeared to influence the work reported in this paper.

Acknowledgements

The research is supported by the Estonian Research Council grants PRG330 ‘Development of an iterative approach for near-coast marine geoid modelling by using re-tracked satellite altimetry, in-situ and modelled data’ and PRG1129. The authors are extremely grateful to the Swedish Meteorological and Hydrological Institute (SMHI) for providing access to the model data, the Baltic+ SEAL project team for granting access to the Sentinel-3A dataset, and tide-gauge data providers: The Estonian Environment Agency (EEA), Finnish Meteorological Institute (FMI), Latvian Environment, Geology and Meteorology Centre (LVGMCL), Institute of Meteorology and Water Management (IMGW-PIB), Federal Maritime and Hydrographic Agency (BSH), and SMHI. We are also thankful for the constructive comments made by the anonymous reviewers.

Appendix

See Table A.1.

References

- Afrasteh, Y., Slobbe, D.C., Verlaan, M., Sacher, M., Klees, R., Guarneri, H., Keyzer, L., Pietrzak, J., Snellen, M., Zijl, F., 2021. The potential impact of hydrodynamic leveling on the quality of the European vertical reference frame. *J. Geod.* 95, 1–18. <http://dx.doi.org/10.1007/s00190-021-01543-3>.
- Ågren, J., Strykowski, G., Bilker-Koivula, M., Omang, O., Mårdla, S., Forsberg, R., Ellmann, A., Oja, T., Liepins, I., Parselūnas, E., Kaminskis, J., 2016. The NKG2015 gravimetric geoid model for the nordic-baltic region. In: Presented in the 1st Joint Commission 2 and IGFS Meeting International Symposium on Gravity, Geoid and Height Systems. Thessaloniki, Greece. pp. 19–23.
- Altamimi, Z., 2018. EUREF Technical Note 1: Relationship and Transformation Between the International and the European Terrestrial Reference Systems. *Publicato da EUREF*.
- Aung, M.T., Shrestha, S., Weesakul, S., Shrestha, P.K., 2016. Multi-model climate change projections for belu river basin, myanmar under representative concentration pathways. *J. Earth Sci. Clim. Change* 7.
- BOOS, 2021. Mean sea level (MSL) in different height systems. Retrieved from http://www.boos.org/wp-content/uploads/mwreg_boos.pdf.
- Bosch, W., Dettmering, D., Schwatke, C., 2014. Multi-mission cross-calibration of satellite altimeters: constructing a long-term data record for global and regional sea level change studies. *Remote Sens.* 6, 2255–2281. <http://dx.doi.org/10.3390/rs6032255>.
- BSH, 2021. Federal maritime and hydrographic agency. Germany. Retrieved from <https://www.bsh.de/>.
- Chang, J., Hart, D.R., Munroe, D.M., Curchitser, E.N., 2021. Bias correction of ocean bottom temperature and salinity simulations from a regional circulation model using regression kriging. *J. Geophys. Res.: Oceans* 126. <http://dx.doi.org/10.1029/2020jc017140>.
- Cipollini, P., Calafat, F.M., Jevrejeva, S., Melet, A., Prandi, P., 2017. Monitoring sea level in the coastal zone with satellite altimetry and tide gauges. *Integrative Study of the Mean Sea Level and Its Components* 35–59.
- Desjonquères, J.D., Carayon, G., Steunou, N., Lambin, J., 2010. Poseidon-3 radar altimeter: new modes and in-flight performances. *Mar. Geod.* 33, 53–79. <http://dx.doi.org/10.1080/01490419.2010.488970>.
- EEA, 2021. Coastline stations operated by estonian environmental agency. Estonia. Retrieved from [http://ilmateenistus.ee/meri/vaatlus\(and\)med/kogu-rannik/kaart/](http://ilmateenistus.ee/meri/vaatlus(and)med/kogu-rannik/kaart/).
- Ekman, M., 1989. Impacts of geodynamic phenomena on systems for height and gravity. *Bulletin Géodésique* 63, 281–296. <http://dx.doi.org/10.1007/bf02520477>.
- Ellmann, A., Mårdla, S., Oja, T., 2019. The 5 mm geoid model for estonia computed by the least squares modified Stokes's formula. *Surv. Rev.* 52, 352–372. <http://dx.doi.org/10.1080/00396265.2019.1583848>.
- EPA, 2021. Environmental protection agency of Lithuania. Lithuania. Retrieved from <https://gamta.lt/>.
- FMI, 2021a. The finnish meteorological institute's open data. Finland. Retrieved from <https://en.ilmatiiteenlaitos.fi/open-data>.
- FMI, 2021b. Theoretical mean sea level and geodetical levelling systems in Finland. Finland. Retrieved from <https://en.ilmatiiteenlaitos.fi/theoretical-mean-sea-level>.
- Giorgi, F., 2019. Thirty years of regional climate modeling: where are we and where are we going next? *J. Geophys. Res.: Atmos.* 124, 5696–5723. <http://dx.doi.org/10.1029/2018jd030094>.
- Hieronymus, M., Hieronymus, J., Arneborg, L., 2017. Sea level modelling in the baltic and the north sea: The respective role of different parts of the forcing. *Ocean Model.* 118, 59–72. <http://dx.doi.org/10.1016/j.ocemod.2017.08.007>.

- Hordoir, R., Axell, L., Höglund, A., Dieterich, C., Fransner, F., Gröger, M., Liu, Y., Pemberton, P., Schimanke, S., Andersson, H., Ljungemyr, P., Nygren, P., Falahat, S., Nord, A., Jönsson, A., Lake, I., Döös, K., Hieronymus, M., Dietze, H., Löptien, U., Kuznetsov, I., Westerlund, A., Tuomi, L., Haapala, J., 2019. Nemo-nordic 1.0: a NEMO-based ocean model for the Baltic and north seas – research and operational applications. *Geosci. Model Dev.* 12, 363–386. <http://dx.doi.org/10.5194/gmd-12-363-2019>.
- Iđžanović, M., Ophaug, V., Andersen, O.B., 2017. The coastal mean dynamic topography in Norway observed by CryoSat-2 and GOCE. *Geophys. Res. Lett.* 44, 5609–5617. <http://dx.doi.org/10.1002/2017GL073777>.
- IMGW-PIB, 2021. Institute of meteorology and water management. Poland. Retrieved from <https://imgw.pl/>.
- Jahanmard, V., Delpêche-Ellmann, N., Ellmann, A., 2021. Realistic dynamic topography through coupling geoid and hydrodynamic models of the Baltic sea. *Cont. Shelf Res.* 222, 104421. <http://dx.doi.org/10.1016/j.csr.2021.104421>.
- Kakkuri, J., Poutanen, M., 1997. Geodetic determination of the surface topography of the Baltic sea. *Mar. Geod.* 20 (4), 307–316. <http://dx.doi.org/10.1080/01490419709388111>.
- Kärnä, T., Ljungemyr, P., Falahat, S., Ringgaard, I., Axell, L., Korabel, V., Murawski, J., Maljutenko, I., Lindenthal, A., Jandt-Scheelke, S., Verjovkina, S., Lorkowski, I., Lagema, P., She, J., Tuomi, L., Nord, A., Huess, V., 2021. Nemo-nordic 2.0: operational marine forecast model for the Baltic sea. *Geosci. Model Dev.* 14, 5731–5749. <http://dx.doi.org/10.5194/gmd-14-5731-2021>.
- Khanarmuei, M., Mardani, N., Suara, K., Sumihar, J., Sidle, R.C., McCallum, A., Brown, R.J., 2021. Assessment of an ensemble-based data assimilation system for a shallow estuary. *Estuar. Coast. Shelf Sci.* 257, 107389.
- Lagema, P., Elken, J., Kõuts, T., 2011. Operational sea level forecasting in Estonia. *Estonian J. Eng.* 17, 301–331. <http://dx.doi.org/10.3176/eng.2011.4.03>.
- Liebsch, G., Novotny, K., Dietrich, R., Shum, C.K., 2002. Comparison of multimission altimetric sea-surface heights with tide gauge observations in the southern Baltic sea. *Mar. Geod.* 25, 213–234. <http://dx.doi.org/10.1080/01490410290051545>.
- LVGMCL, 2021a. Latvian environment, geology and meteorology centre. Latvia. Retrieved from <https://meteo.lv/hidrologija-datu-meklesana/>.
- LVGMCL, 2021b. Latvian environment, geology and meteorology centre. Latvia. Retrieved from <https://meteo.lv/hidrologijas-staciju-karte/>.
- Madsen, K.S., Høyer, J.L., Suursaar, Ü., She, J., Knudsen, P., 2019. Sea level trends and variability of the Baltic sea from 2D statistical reconstruction and altimetry. *Front. Earth Sci.* 7. <http://dx.doi.org/10.3389/feart.2019.00243>.
- Mostafavi, M., Delpêche-Ellmann, N., Ellmann, A., 2021. Accurate sea surface heights from sentinel-3A and Jason-3 retracers by incorporating high-resolution marine geoid and hydrodynamic models. *J. Geodetic Sci.* 11, 58–74. <http://dx.doi.org/10.1515/jogs-2020-0120>.
- Neitzel, F., Ezhov, N., Petrovic, S., 2019. Total least squares spline approximation. *Mathematics* 7, 462. <http://dx.doi.org/10.3390/math7050462>.
- Nordman, M., Kuokkanen, J., Bilker-Koivula, M., Koivula, H., Häkli, P., Lahtinen, S., 2018. Geoid validation on the Baltic sea using ship-borne GNSS data. *Mar. Geod.* 41, 457–476. <http://dx.doi.org/10.1080/01490419.2018.1481160>.
- Ophaug, V., Breili, K., Gerlach, C., 2015. A comparative assessment of coastal mean dynamic topography in Norway by geodetic and ocean approaches. *J. Geophys. Res.: Oceans* 120, 7807–7826. <http://dx.doi.org/10.1002/2015jc011145>.
- Passaro, M., Müller, F., Dettmering, D., Abulaitjiang, A., Rautiainen, L., Scarrott, R.G., Chalçon, E., Sweeney, M., 2021. BALTIC+ Theme 3 Baltic+ SEAL (Sea Level) Product Handbook. European Space Agency, <http://dx.doi.org/10.5270/esa.BalticSEAL.PH1.1>.
- Rautiainen, L., Särkkä, J., Tuomi, L., Müller, F., Passaro, M., 2020. Baltic+ SEAL: Validation Report. ESA EO, <http://dx.doi.org/10.5270/esa.balticseal.vrv2.2>.
- Sacher, M., 2019. The European vertical reference system (EVRS)–development and latest results. *Geophys. Res. Abstr.* 21.
- Samuelsson, M., Stigebrandt, A., 1996. Main characteristics of the long-term sea level variability in the Baltic sea. *Tellus A* 48, 672–683. <http://dx.doi.org/10.1034/j.1600-0870.1996.t01-4-00006.x>.
- Schwabe, J., Ågren, J., Liebsch, G., Westfeld, P., Hammanklint, T., Mononen, J., Andersen, O.B., 2020. The Baltic sea chart datum 2000 (BSCD2000): Implementation of a common reference level in the Baltic sea. *Int. Hydrogr. Rev.* 63–83.
- Slobbe, D.C., Klees, R., Gunter, B.C., 2014. Realization of a consistent set of vertical reference surfaces in coastal areas. *J. Geod.* 88, 601–615. <http://dx.doi.org/10.1007/s00190-014-0709-9>.
- Slobbe, D.C., Verlaan, M., Klees, R., Gerritsen, H., 2013. Obtaining instantaneous water levels relative to a geoid with a 2D storm surge model. *Cont. Shelf Res.* 52, 172–189. <http://dx.doi.org/10.1016/j.csr.2012.10.002>.
- SMHI, 2021. Swedish meteorological and hydrological institute. Sweden. Retrieved from <https://www.smhi.se/>.
- Soomere, T., Quak, E. (Eds.), 2013. Preventive Methods for Coastal Protection: Towards the Use of Ocean Dynamics for Pollution Control. Springer Science & Business Media.
- Varbla, S., Ågren, J., Ellmann, A., Poutanen, M., 2022. Treatment of tide gauge time series and marine GNSS measurements for vertical land motion with relevance to the implementation of the Baltic sea chart datum 2000. *Remote Sens.* 14 (4), 920. <http://dx.doi.org/10.3390/rs14040920>.
- Varbla, S., Ellmann, A., Delpêche-Ellmann, N., 2020a. Validation of marine geoid models by utilizing hydrodynamic model and shipborne GNSS profiles. *Mar. Geod.* 43, 134–162. <http://dx.doi.org/10.1080/01490419.2019.1701153>.
- Varbla, S., Ellmann, A., Delpêche-Ellmann, N., 2020b. Utilizing airborne laser scanning and geoid model for near-coast improvements in sea surface height and marine dynamics. *J. Coast. Res.* 95, 1339. <http://dx.doi.org/10.2112/SI95-257.1>.
- Vestøl, O., Ågren, J., Steffen, H., Kierulf, H., Tarasov, L., 2019. NKG2016LU: a new land uplift model for Fennoscandia and the Baltic region. *J. Geod.* 93, 1759–1779. <http://dx.doi.org/10.1007/s00190-019-01280-8>.
- Zhang, Y.J., Stanev, E.V., Grashorn, S., 2016. Unstructured-grid model for the north sea and Baltic sea: validation against observations. *Ocean Model.* 97, 91–108. <http://dx.doi.org/10.1016/j.ocemod.2015.11.009>.

Appendix 3

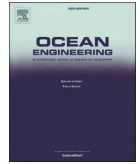
Publication III

Jahanmard, V., Varbla, S., Delpeche-Ellmann, N., Ellmann, A. (2022). Retrieval of directional power spectral density and wave parameters from airborne LiDAR point cloud. *Ocean Engineering*, 266. doi:10.1016/j.oceaneng.2022.112694.



Contents lists available at ScienceDirect

Ocean Engineering

journal homepage: www.elsevier.com/locate/oceaneng

Retrieval of directional power spectral density and wave parameters from airborne LiDAR point cloud

Vahidreza Jahanmard^{a,*}, Sander Varbla^a, Nicole Delpeche-Ellmann^b, Artu Ellmann^a

^a Department of Civil Engineering and Architecture, Tallinn University of Technology, Ehitajate Road 5, 19086, Tallinn, Estonia

^b Department of Cybernetics, School of Science, Tallinn University of Technology, Akadeemia Road 21, 12618, Tallinn, Estonia

ARTICLE INFO

Keywords:

Directional power spectral density
Spatial wave spectrum
Airborne laser scanner
Wave direction
Significant wave height
Baltic sea

ABSTRACT

Increasing magnitude and frequency of extreme events (e.g., floods, waves, storms), along with the demands of shipping (e.g., increasing vessel sizes) and marine engineering (e.g., intensified port development), can compromise operations and result in economic and human loss. Consequently, a re-examining and better understanding of the sea surface topography and, in particular, surface ocean waves is now imperative. Quantifying surface ocean waves' properties can often be a complex procedure based on the source of measurements and the technique used. For instance, airborne laser scanning (ALS) can provide a high-resolution dataset of 3D spatial sea surface topography with a point cloud density around 6 p/m^2 and vertical accuracy of 5–15 cm, from which properties of surface waves can be derived. This study explores a novel method to enhance ALS-derived directional spatial wave spectrum by sampling from the point cloud and adjusting the standard error. As a result, wave parameters such as significant wave height, peak period, wavelength, and dominant wave direction can be obtained. The method was tested in the eastern section of the Baltic Sea. The wave spectra retrieved from ALS were validated with a nearby wave buoy, wave model and an alternative direct geometrical method from a previous study. These comparisons demonstrated good agreement with the significant wave height and peak period having mean differences of 0.10 m and 0.0 s; 0.09 m and 0.2 s; 0.20 m and 0.8 s compared with the buoy, wave model and direct method, respectively. The ALS-detected dominant wave direction varied from 60.0° to 97.0° , whereas the corresponding estimates for the buoy and regular wave model were 86.5° and 78.9° – 83.8° , respectively.

1. Introduction

Retrieval of the spatial spectra of sea surface waves, which tend to change under the influence of various factors (e.g., wind, water depth, fetch, vessels), is essential for solving numerous fundamental and applied problems of modern oceanology (Phillips, 1980; Monin and Krasitsky, 1985; Bondur, 2004). In particular, monitoring waves is essential for the safety and performance analysis of vessels and marine structures (Chen et al., 2021; Abaei et al., 2018; Jahanmard et al., 2015). Moreover, measuring and understanding ocean waves' properties also contribute to the quantification of coastal processes (erosion and sediment transport), as well as the validation and calibration of wave models and relevant sensors (Vieira et al., 2020). Various sources of in situ measurements (e.g., wave buoys and pressure sensors), remote sensing (satellite imagery and altimetry, airborne laser scanning – ALS, etc.), and wave models are often employed (Huang and Chen, 1998; Sun et al.,

2005; Bondur et al., 2016; Soomere, 2022) to obtain the parameters and power spectra of sea waves. Nevertheless, derivation of the surface waves' properties can be a complex procedure. Recent technological advances in wave measurement sources also require a deeper re-examination of the methods employed. Thus, this study developed a method applicable for an airborne LiDAR (light detection and ranging) acquired dense 3D point cloud to determine the parameters of ocean surface waves.

Airborne laser scanning technology has advanced over the years to provide high-resolution mapping using active ranging, where the LiDAR sensor emits short laser pulses and registers returning reflections from a surface. Such a technique is primarily used for dry land topography mapping, and its vertical accuracy is estimated at 5–15 cm depending on the measured surface and configuration during the time of acquisition (Huising and Gomes Pereira, 1998; Sande et al., 2010). Several studies that have used ALS for marine applications (Gruno et al., 2013; Zlinszky

* Corresponding author.

E-mail address: vahidreza.jahanmard@taltech.ee (V. Jahanmard).

<https://doi.org/10.1016/j.oceaneng.2022.112694>

Received 26 April 2022; Received in revised form 20 September 2022; Accepted 22 September 2022

Available online 11 October 2022

0029-8018/© 2022 Elsevier Ltd. All rights reserved.

et al., 2017; Sutherland et al., 2018; Varbla et al., 2021) have demonstrated that similar accuracy can also be achieved for sea surface measurements. An improved characteristic is that modern LiDAR systems can provide high-quality data regardless of marine conditions (Varbla et al., 2021). The high pulse repetition rate, low beam divergence (i.e., yielding a small and crisp footprint), and slow platform speed of ALS enable covering a wide swath by deflecting laser pulses from the nadir perpendicular to the flight direction (Zlinszky et al., 2017). As a result, a dense and highly accurate 3D point cloud of the sea surface is generated using the active ranging. This allows the determination of the wavenumber spectrum that defines waves' propagation direction and wavelength (Hwang et al., 1998; Walsh et al., 1985). In addition, using a combination of active ranging, passive imaging, and video recording, the properties of breaking waves and white cap coverage can also be established (Hwang et al., 1998).

It is challenging to infer the directional distribution of waves from typical in situ wave measurements positioned at a single location (such as pitch-and-roll buoys or wave gauge arrays; Hwang et al., 2000a). Instead, the ALS-captured 3D point cloud of ocean surface topography could be a more reliable data source. This study focuses on ALS data to obtain a directional wave spectrum. Previous studies estimated the directional wavenumber spectrum using a 2D fast Fourier transform (FFT) on an ALS data segment with an implicit homogeneous process assumption (Sutherland et al., 2018; Hwang et al., 2000a). For example, in Hwang et al. (2000a, 2000b), nine segments of the ALS track (each segment covering an area of 0.25×1.5 km) were combined to retrieve the one-directional spatial wave spectrum along the flight direction, in which the wave field was quasi-steady (i.e., the wave variation could be ignored along the 14 km long stretch). An alternative approach utilized by Vrbancich et al. (2011) and Varbla et al. (2021) directly employs the measured sea surface geometry to derive waves' properties. The latter, however, can be time-consuming and cannot be fully automated, thus introducing a human factor to data processing.

Note that the sea surface is described by quickly changing random variations. According to the stochastic theory of turbulence, it is possible to model the sea surface as a horizontally homogeneous and stationary random field by selecting sufficient spatial and temporal scales. For wave field observations, the scale in the order of 10 km and 30 min or longer may be desirable for considering homogeneous (i.e., spatial invariance) and stationary (i.e., temporal invariance) processes, respectively (Hauser et al., 2005; Goda, 2000). However, the wave conditions in the strong current shear or near coastal areas (shallow water waves) can be very inhomogeneous (Goda, 2000). Also, with rapidly advancing technologies (e.g., satellite, ALS, etc.) that collect data at varying spatial and temporal scales, it becomes necessary to re-explore traditional methods with these new specifications.

Contrary to often used satellite images (such as high-resolution (0.65–1 m) QuickBird and Ikonos satellite images; Bondur et al., 2016), the data corridor width limitation of ALS point clouds can be challenging for deriving sea surface wave parameters (good quality data are obtained within a kilometre). Thus, the required statistical stability of the wave parameters is not easily obtained, whereas this limitation has not been addressed in earlier studies (Huang et al., 2012; Sutherland et al., 2018). As a result, this study shows an alternative new approach developed for deriving sea waves' parameters and power spectral density using ALS.

Instead of using 2D FFT (Romero and Melville, 2010; Lenain and Melville, 2017), the method developed in this study uses averaging of one-dimensional periodograms for each direction of interest, allowing to derive the spectral estimate of a stationary process (Bartlett, 1948; Welch, 1967). With such an approach, wave parameters can be retrieved using the spatial limitations of the ALS data (particularly considering the limited data corridor width), where 2D FFT may be an obfuscation rather than a recovery of information. The method employed in this study also corrects for the Doppler effect (due to relative flight speed and direction) on the retrieved spectra in each wave direction.

As a result, the spatial wave spectrum, which portrays the energy of the wave components relative to the wavenumber, can be determined in various directions. Also, by using the dispersion relationship, the frequency wave spectrum can be derived (Bondur et al., 2016). This transformation from the spatial domain to the frequency domain enables comparisons with buoy observations, a well-established method for measuring wave characteristics over time, thus providing a basis for data validation. The results are also compared with the WAM (cycle 4.6.2) wave model for the Baltic Sea (sourced from: <https://copernicus.eu>) and an alternative method from a previous study (Varbla et al., 2021). Therefore, this study demonstrates a reconstruction of the directional wave spectrum using ALS-derived point cloud data.

The paper is structured as follows. First, the study area and the employed dataset are described in Section 2. Next, in Section 3, the method is outlined in three steps: (i) determining the power spectral density of the extracted signal, (ii) providing a robust spatial wave spectrum and addressing the homogeneous wave condition, and (iii) deriving frequency wave spectrum. Sections 4 and 5 present and discuss the computational and validation results. Also, a comparison between measured wave characteristics, buoy observations, and the WAM model is demonstrated. The paper concludes with a brief summary in Section 6.

2. Case study

The developed methodology will be presented using ALS survey data collected in the Gulf of Finland, located in the easternmost section of the Baltic Sea (Fig. 1). For demonstrating the benefits and applicability of the developed approach, theoretical principles shall first be outlined in Section 3, supported by the results using the described dataset.

The Gulf of Finland is a narrow and elongated basin with a length of approximately 400 km and a width varying from 48 to 135 km. The mean water depth of the gulf is around 37 m (maximum depth is 123 m). In the study area, the average depth is around 70 m, which satisfies the deep-water condition based on the linear wave theory. In the Gulf of Finland, the wave characteristics include: (i) mean significant wave heights (SWH) of around 0.5–1.0 m (Nikolkina et al., 2014), and (ii) the extreme wave height and period of around 6 m and 8–11 s, respectively, at the entrance of the gulf, and correspondingly 4 m and 6–8 s in its eastern part (Räämet et al., 2010). The geometry and bathymetry of the northern Baltic Sea can steer the wave and current direction, especially into the gulf. The wind and wave direction difference in the gulf can also be up to 50° (Pettersson et al., 2010). In semi-sheltered seas, such as the Gulf of Finland, small changes in the wind direction can lead to significant spatio-temporal variations in the wave climate (Najafzadeh et al., 2021). An examination of wind, waves, and surface currents shows that wind and surface waves largely govern surface drift (Delpeche-Ellmann et al., 2021).

A marine ALS survey was performed on 10.05.2018 in the Gulf of Finland (Fig. 1) by employing the Estonian Land Board's survey plane Cessna Grand Caravan 208B mounted RIEGL VQ-1560i LiDAR Scanning System. The system operated with a pulse repetition rate of 1 MHz at the wavelength of 1064 nm. An operational flight altitude of around 1200 m yielded ca 1000–1200 m wide sea surface height (SSH) data corridor and LiDAR footprint diameter of 0.3 m. The average point cloud density was estimated at 2.9 p/m² (6.2 p/m² for the central 100 m of the swath). Varbla et al. (2021) reconstructed from these ALS measurements instantaneous SSH grids (to reduce data noise and improve subsequent data processing performance), one of which is now employed in this study (cf. Fig. 1; the open-access data is available from Varbla et al., 2020). The central 500 m wide data corridor is used here, neglecting poorer quality data at the edges. The data spatial resolution is 1 m, which allows extracting wave profiles in various directions with a sampling interval from 1 m (for directions 0° and 90°) to 1.4 m (for 45° and 135°, using linear interpolation). These data represent the basis for testing the developed method.

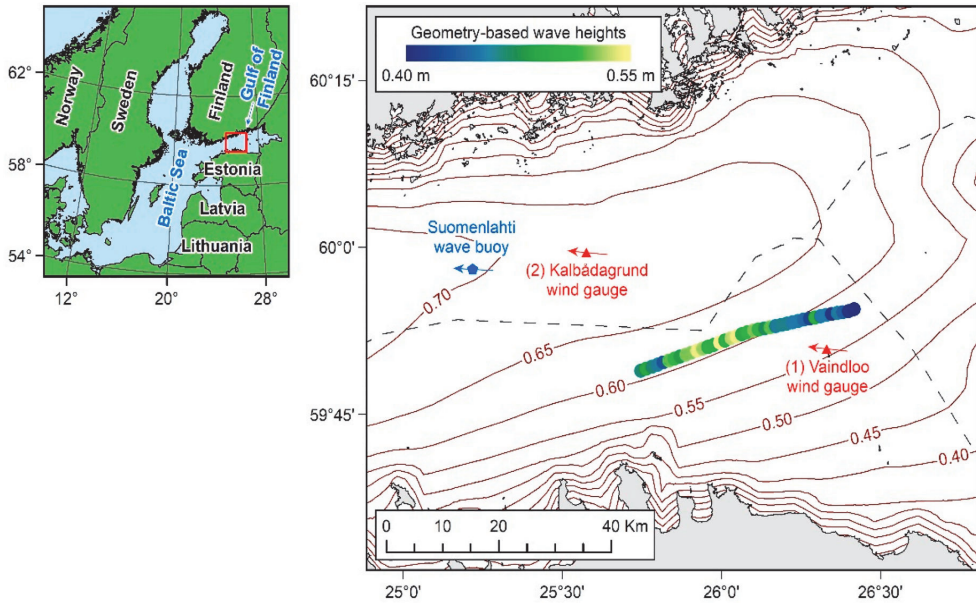


Fig. 1. The study area and ALS flight trajectory over the Gulf of Finland on 10.05.2018 at around 09:35 UTC. The colours of the trajectory show the geometry-based mean wave heights (averaged within fragments' boundaries) derived by Varbla et al. (2021). Isolines depict significant wave heights of the WAM wave model at 09:00 UTC. Coloured arrows show wave and wind directions during the ALS survey at the closest observation stations.

3. Method

3.1. Directional spatial wave spectrum

ALS point cloud datasets usually extend over vast distances, thus making it unfeasible to use such data directly. Hence, the division of point clouds into several fragments can be an initiative to (i) extract

wave profiles with almost the same length in all directions, (ii) eliminate the influence of very low-frequency sea level variations and geoid slope to achieve pure wave profiles (i.e., with Gaussian distribution and zero mean in all directions), and (iii) keep stable wave direction that may change over longer distances due to spatial variations in wind regime and water depth.

Here, the fragmentation was performed by 1×1 km squares. Fig. 2

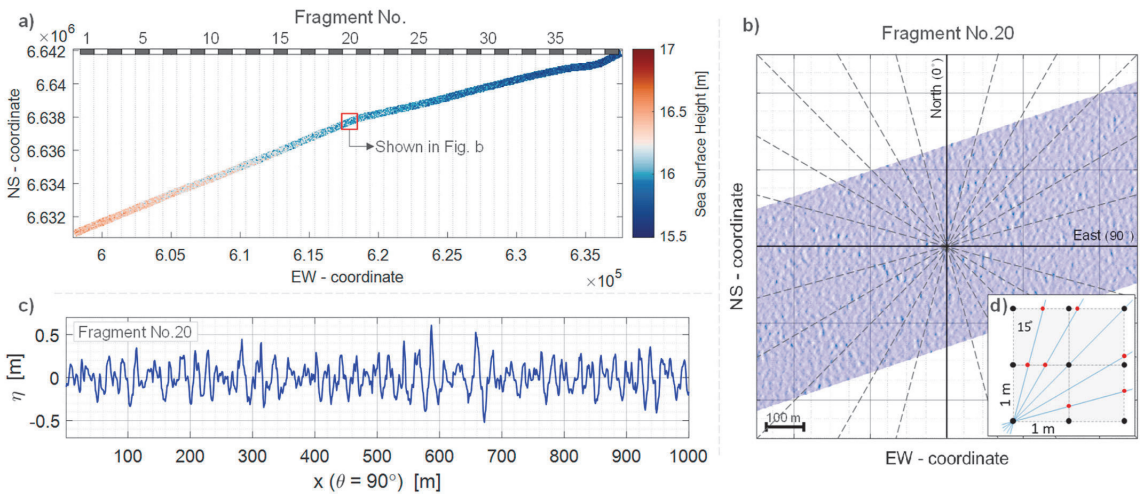


Fig. 2. a) The reconstructed 1×1 m resolution ALS point cloud in terms of SSH values, and b) a sample 1×1 km point cloud fragment (the rectangular NS and EW coordinates are given in the Estonian Lambert-EST97 map projection coordinate system). Black lines mark the wave profile directions that cross the fragment's center (the centre is henceforth named a sample point). In c), an example wave profile (η) is shown in the east-west direction ($\theta = 90^\circ$). Inset d) shows a schematic of grided ALS data (black dots) and resampling in different directions (red dots).

sub-plots (a) and (b) show the used ALS dataset and an example fragment, respectively. Sea surface height profiles were then extracted for directions (denoted θ) from 0° to 165° with a 15° step. Note that the shortest profile (roughly perpendicular to flight direction) is ca 500 m in length, which is sufficient to derive the peak wavenumber in the study area. The construction of wave profiles from such SSH data requires the vertical reference to be transferred from the reference ellipsoid (e.g., GRS80) to the sea surface by subtracting the fraction mean SSH (\overline{SSH}) from ALS measured instantaneous SSH:

$$\eta = SSH - \overline{SSH} \quad (1)$$

where η denotes the wave surface. The mean SSH was determined for all profiles separately. An example of the derived wave profile is presented in Fig. 2c.

Possible outliers in the wave records were detected by discarding data points with a high changing rate (i.e., the difference between $\eta(x_j)$ and $\eta(x_{j-1})$, which was estimated over a single wave profile) exceeding ± 3 -fold standard deviations (estimated separately for each profile). The discarded wave records were filled in by using spline interpolation. Moreover, resampling using linear interpolation was employed to increase the sampling frequency of wave records (directions other than 0° and 90°) to keep the peak wavenumber (k_p) of the 1D spatial spectra apart from the aliasing frequency. As a result, the minimum sampling frequency of the used wave records is thus 0.7 m^{-1} , which is suitable for the case study. Note that the Nyquist frequency for this sampling rate is 0.35 m^{-1} , corresponding to the wavelength of 2.86 m.

Using the periodogram method (Kawauchi et al., 2009), the spatial wave spectrum can be determined by employing the derived profiles. However, it is essential to note here that long enough wave profiles are required to determine a stable wave spectrum of a homogeneous process. Otherwise, the resulting wave spectrum may be unsatisfactory as two nearby profiles may give highly varying results due to the randomness of the sea waves.

Before applying the discrete Fourier transform (DFT), it may be desirable to modify the discontinuities at the records' two endpoints by using a cosine taper data window (Liu and Frigaard, 1999):

$$W(x) = \begin{cases} \frac{1}{2} \left(1 - \cos \frac{10\pi \bullet x}{X_0} \right), & 0 \leq x \leq \frac{X_0}{10} \\ 1.004, & X_0 \leq x \leq \frac{9X_0}{10} \\ \frac{1}{2} \left(1 + \cos \frac{10\pi \left(x - \frac{9X_0}{10} \right)}{X_0} \right), & \frac{9X_0}{10} \leq x \leq X_0 \end{cases} \quad (2)$$

where X_0 is wavelength equal to the length of the wave profile (estimated separately for each direction θ). Therefore:

$$\eta' = \eta(x) \bullet W(x) \quad (3)$$

Note that the sampling interval (δx ; i.e., data spatial resolution) and length of the wave profile differ for each direction. Such a variation leads to different wavenumber resolutions in the 1D spectra, which makes it challenging to represent the directional spectrum. Hence, zero values were added to the two ends of wave profiles to facilitate equal wavenumber resolution. The number of added zero values to each end was defined as half of the difference between the required length of each direction (N) and the length of the obtained wave profiles. The parameter N was computed for each direction as follows:

$$N = \frac{N_T}{\delta x} \quad (4)$$

where N_T is the target length of the wave profile with a sampling interval of 1 m. Here, a target length of 1200 m was selected based on the min-

imum length that keeps all data. The DFT for spatial wave records is then computed for each direction as:

$$Y_m = \sum_{n=1}^N \eta'_n e^{-ik_m n \delta x} \delta x = \delta x \sum_{n=1}^N \eta'_n e^{-\frac{2\pi i m n}{N}} \quad (5)$$

with

$$k_m = \frac{2\pi m}{N \delta x}, m = 1, 2, \dots, N \quad (6)$$

where term k is the wavenumber vector with a size of m (note that $k = 2\pi/\lambda$, where λ is wavelength). As a result, the one-sided spatial spectrum is determined as:

$$\chi(k_m) = \frac{2}{2\pi N \delta x} |Y_m|^2 \quad (7)$$

Fig. 3 illustrates the derived spatial wave spectrum of fragment No.20 (refer to Fig. 2 for its location), where the 1D spectra are computed for 12 directions (values between selected directions were approximated via linear interpolation). Notice that there appears to be no difference between the computed wave directions and their opposite directions (i.e., θ and $\theta + 180$). Hence, more information is required to distinguish between these two angles than a single snapshot of the sea surface (shown in Fig. 2b), such as a meteorological station measured wind direction in that region. In Section 4, the wind rose of nearby stations is used to compare and identify the wave direction.

As mentioned above, the short length of wave profiles obtained from ALS (for example, ca 527 m for 0° and 1000 m for 90° azimuthal direction) is insufficient to reach a stable power spectral density function. In Fig. 3, one such poor estimate of the directional spectrum is demonstrated that cannot be interpreted for determining wave parameters. Thus, in this study, a more robust approach was developed to derive the spatial wave spectrum, which relies on augmenting the wave spectrum by accumulating wave information from parallel profiles (allowed by the high-resolution ALS point cloud), where the final results are obtained by averaging periodograms (Bartlett, 1948).

3.2. Enhancement of the directional spatial wave spectrum

Using a single ALS wave profile (in each direction) may not provide satisfactory results due to the randomness of the sea waves and the constraint of ALS spatial coverage (recall, in this study, a 500 m wide

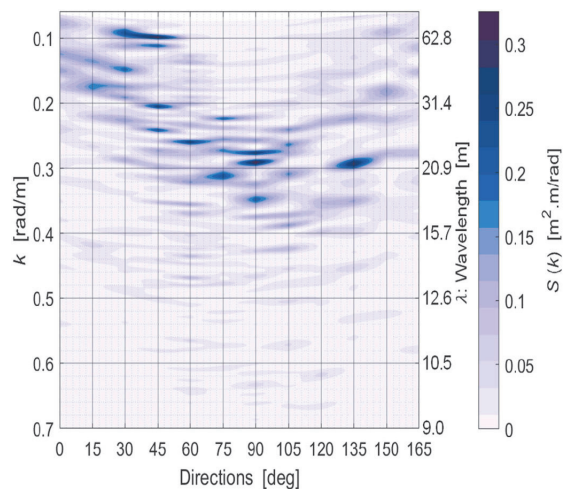


Fig. 3. Spatial wave spectrum of sea waves in various directions for fragment No.20 (i.e., a $1 \times 1 \text{ km}$ area).

data corridor is used). Hence, there is a need to include more information about sea surface variations to determine a more reliable spatial wave spectrum. For this purpose, the spectrum computations were repeated by selecting random (using random sampling method) sample points (i.e., elementary events) within a pre-defined data sampling area of an initial point cloud fragment (e.g., fragment No.20 as shown in Fig. 2b). In this study, the size of the sampling area was defined as 300×300 m (notice the red square in Fig. 4), whereby the area was centred at the centre of an initial point cloud fragment. This procedure is demonstrated in Fig. 4 for fragment No.20, where the i -th moving sample point is selected by random coordinate increments Δy_i and Δx_i . In other words, based on the initial point cloud fragment, a new set of randomly selected moving fragments was defined. Note that the moving fragments retrieve sample wave records over the whole ALS point cloud dataset (cf. Fig. 2a), as was described in Section 3.1.

The random sampling was conducted until stable sample size n was obtained, where n denotes the number of times a spatial wave spectrum was generated based on a moving point cloud fragment. As a result, a robust spatial wave spectrum can be obtained with a desirable standard error (SE) based on the central limit theorem:

$$X(k) = \frac{1}{n} \sum_{i=1}^n X_i(k) \quad (8)$$

An experiment with $R = 100$ sample sets (where a sample set consists of n sample points) was constructed to determine the SE and to show the ability of the method to determine the directional power spectral density by averaging parallel wave profiles. As the spectrum's peak $X(k_p)$, associated with the peak wavenumber, has the highest sensitivity and variability, the maximum SE can be expected to occur in peak wavenumber (i.e., k_p). Therefore:

$$SE = \sqrt{\frac{\sum_{r=1}^R (X_r(k_p) - \mu)^2}{R}} \quad (9)$$

where μ is the mean of the estimated 100 values of $X(k_p)$. This experiment was conducted for n values from 1 to 1000, as shown in Fig. 5. Here, the sample points were selected randomly within the area of 300×300 m. Alternatively, the sample points can also be selected using

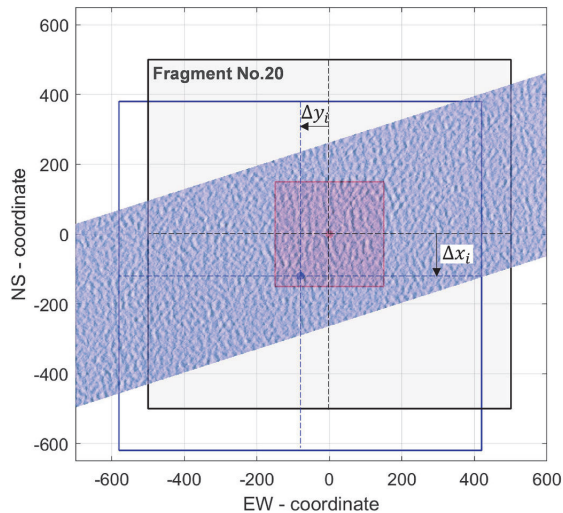


Fig. 4. An example of a moving fragment (blue square) by picking i -th moving sample point (with coordinate increments Δy_i and Δx_i relative to the initial sample point) within the data sampling area (red square) of an initial target fragment (black square).

equal spacing, which requires the determination of an optimal spacing for all directions. Such a method can be explored in future studies.

The described experiment is demonstrated in Fig. 5a for fragment No.20 that uses various sample sizes n of the point cloud in the direction $\theta = 75^\circ$. It can be noticed that the SE decreases rapidly until the sample size reaches 100 samples, whereby the mean spectrum's peak appears to stabilize when $n > 100$. According to the presented results (also considering the region and sea state during the ALS survey), the sample size of 300 can provide a spatial wave spectrum with a SE of less than $0.01 \text{ m}^2 \cdot \text{m}/\text{rad}$, which is roughly 5% of the $X(k_p)$. Thus, the sample size of 300 was determined suitable for the current study. In Fig. 5b are shown (with red colour) all $R = 100$ generated sample sets' spectrums (according to Eq. (8), where $n = 300$) and the mean of these (with blue colour). It is apparent that the peak wavenumber (k_p) remains similar for all sample sets, whereas more significant variation can be seen for other wavenumber values. Note that the experiment was also conducted in other directions, resulting in similar outcomes. Thus, only the 75° azimuth example is shown here.

It is essential to note that to have a meaningful comparison between SEs associated with various sample sizes n (cf. Fig. 5a), the peak wavenumber (k_p) was selected according to the largest n (i.e., 1000) and used as a constant to determine the $X(k_p)$. Furthermore, due to the sensitivity of the spectrum's peak, it is necessary to reduce SE to determine a stable dominant wave direction. Since the dominant wave direction also influences neighbouring directions, a large SE may cause significant variation in various iterations' determined dominant wave directions. Therefore, the developed method can provide a solution for determining homogeneous sea wave condition from ALS data to obtain a robust spatial wave spectrum.

Since the measurements were conducted on a moving platform, the spatial spectrum is calculated based on the derived/encountered wavenumber (k_e). Thus, there is a shift between the computed and true wavenumber due to the Doppler effect (Δk). The wavenumber is corrected by considering aircraft speed (v_a) and direction relative to the chosen wave profile (Walsh et al., 1985):

$$\Delta k = \frac{\sqrt{g \cdot \tanh kd} / k}{v_a \cdot \cos \mu} \quad (10)$$

and

$$\Delta k = k_e - k \quad (11)$$

where d is water depth (roughly 70 m), and μ is the angle between flight and wave direction. The flight speed was approximately 62 m/s, and for fragment No.20, the flight azimuth was 71.5° (directions may vary slightly between fragments). Since Δk is small, a two-step estimation can be performed using computed k (i.e., k_e) as a first approximation (Walsh et al., 1985). Then, a better estimate of k is obtained by Eq. (11). In the second iteration, Δk is determined by substituting the estimated k into Eq. (10).

3.3. Frequency wave spectrum

Contrary to the afore-described spatial wave spectrum, the frequency wave spectrum is used more commonly and is easier to interpret for engineering applications. In this regard, the conversion from spatial spectra to frequency spectra can be valuable. Such a conversion can also enable comparisons with well-proven in situ (such as an offshore buoy) data, thus allowing validation of the ALS-derived results.

The frequency spectrum $S(\omega)$ of wave amplitude portrays the distribution of wave energy at a single point over the angular frequency ω . On the other hand, the spatial spectrum $X(k)$ represents the distribution of waves at a given time over the wavenumbers k . These two approaches have different physical senses and rely on different measurement techniques. Hence, to link the two domains (spatial and temporal) of the sea waves, the dispersion relationship can be used (Goda, 2000):

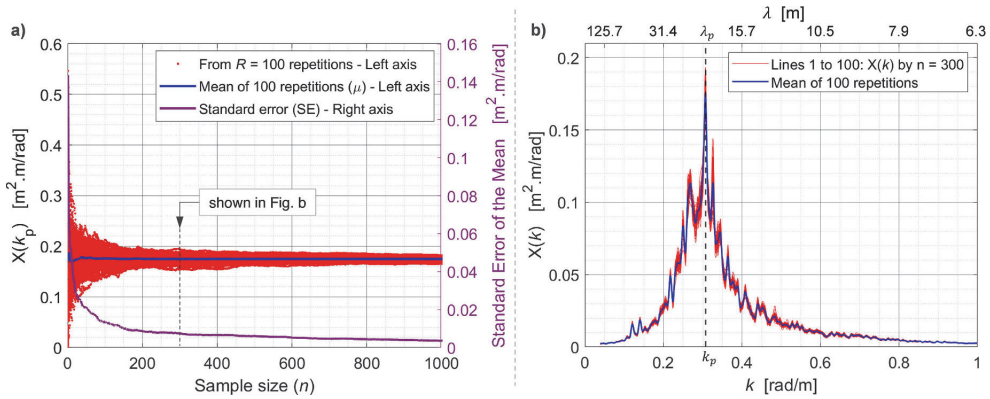


Fig. 5. a) Standard error (SE) of the mean spectrum's peak associated with sample size for fragment No.20 in a selected direction 75°. The SE was determined from 100 sample sets. In b) is shown the associated spatial wave spectrum for $n = 300$.

$$\omega = \sqrt{kg \cdot \tanh kh} \quad (12)$$

where g is the acceleration of gravity, and h water depth. In deep water (where $h > 0.5\lambda$), Eq. (12) can be simplified to:

$$\omega = \sqrt{kg} \quad (13)$$

The well-known relation between the angular frequency ω and wave period T is:

$$T = 2\pi/\omega \quad (14)$$

Considering the requirement that an equal amount of wave energy must be contained in the corresponding intervals of Δk and $\Delta\omega$, the dispersion relationship allows the derivation of the correlation between the spatial and frequency wave spectra (Bondur et al., 2016) as:

$$S(\omega) = X(k(\omega)) \cdot \frac{dk(\omega)}{d\omega} \quad (15)$$

In addition, SWH can theoretically be estimated from the obtained spectrum:

$$SWH = 4\sqrt{m_0} \quad (16)$$

where m_0 is the zero moment (the area under the spectral curve):

$$m_0 = \int_0^\infty S(\omega)d\omega = \int_0^\infty X(k)dk \quad (17)$$

In this study, the JONSWAP standard wave spectrum (cf. Goda, 2000) was used to compare a nearby buoy observed SWH and peak wave period to the ALS-derived frequency wave spectrum.

The developed method for obtaining wave parameters from airborne LiDAR point cloud is summarized in Fig. 6 flowchart.

4. Results

The distribution of wave energy in various directions of each fragment was determined according to the robust wave spectra method described in Section 3.2. Two nearby wind gauges (Vaindloo and Porvoo Kalbådagrund stations; cf. Fig. 1 for their locations) were used to distinguish between the opposite directions of waves (as indicated in Section 3.1). Fig. 7a illustrates the spatial wave spectrum for the point cloud fragment No.20 in various directions from 0° to 165° with an increment of 15°, where it is aligned with wind direction (Fig. 7b). It can be observed in Fig. 7a that the peak of wave energy occurred in the direction of about 75°, which represents the dominant wave direction. A more detailed dominant wave direction of 72° can be estimated by

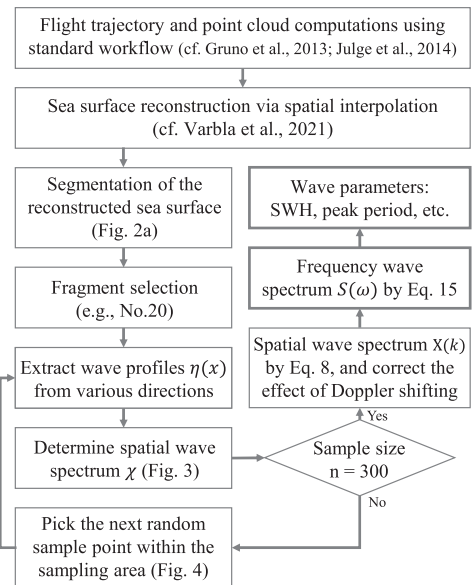


Fig. 6. Schematic flowchart of the method for retrieving spatial wave spectrum from an airborne LiDAR point cloud.

fitting a curve on the spectrum's peaks (dashed line in Fig. 7a). This direction almost agrees with the Suomenlahti wave buoy direction of 86.5° (sourced from: <https://ilmatieteenlaitos.fi>; notice in Fig. 1 that the buoy is roughly 40 km from the profile) and 82.5° determined by the WAM model at the time of the ALS campaign. The ALS-derived peak wavenumber k is 0.31 rad/m, and the corresponding peak wavelength ($\lambda = 2\pi/k$) is 20.6 m.

As discussed in Section 3.3, the dispersion relationship enables the transformation of the spatial wave spectrum to the frequency spectrum. Fig. 8a presents the directional frequency wave spectrum corresponding to the spatial spectrum in Fig. 7a. It can be observed that the peak frequency of the existing wave condition is well captured. The peak frequency and period of the dominant wave direction are 1.73 rad/s and 3.63 s, respectively. Buoy observed peak period of 3.65 s and the model-obtained 3.56 s are in good agreement with the ALS-derived value.

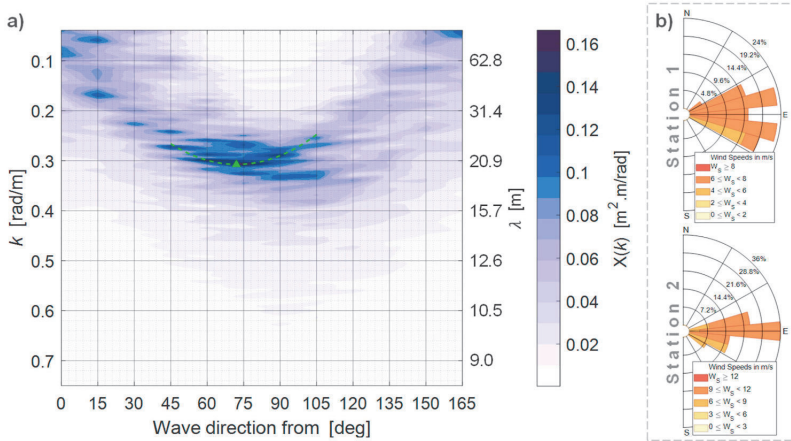


Fig. 7. a) Directional spatial wave spectrum of fragment No.20 in various directions (the dashed line represents the fitted curve on the spectrum's peaks) and b) the wind roses of wind gauge stations 1 and 2 (denoted in Fig. 1) during the 24 h leading up to the ALS campaign. As there were no westerly winds during that time span, only the eastern halves of the wind roses are shown.

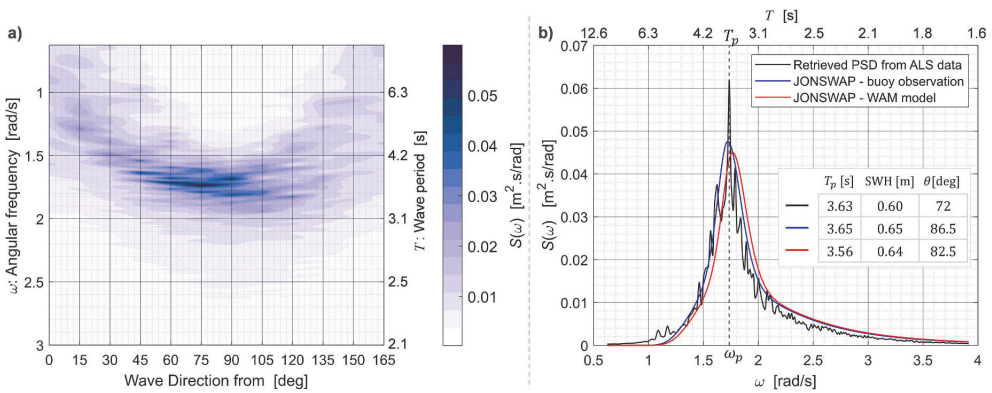


Fig. 8. a) Directional frequency wave spectrum of fragment No.20 in various directions and b) comparison between ALS-derived wave spectrum and standard wave spectrum of the Suomenlahti wave buoy and the model-obtained wave parameters.

In Fig. 8b, the ALS-derived frequency wave spectrum is compared to the JONSWAP standard wave spectrum related to the buoy measured and WAM model determined SWH and peak period of the dominant wave direction. In general, there appears to be a good agreement

between them. The SWH computed from fragment No.20 in the dominant direction ($\theta_d = 72^\circ$) is 0.60 m (cf. Eq. (16)). This value appears to agree well with wave heights (cf. Fig. 1) derived by an alternative approach that reconstructs the waves' geometry (Varbla et al., 2021),

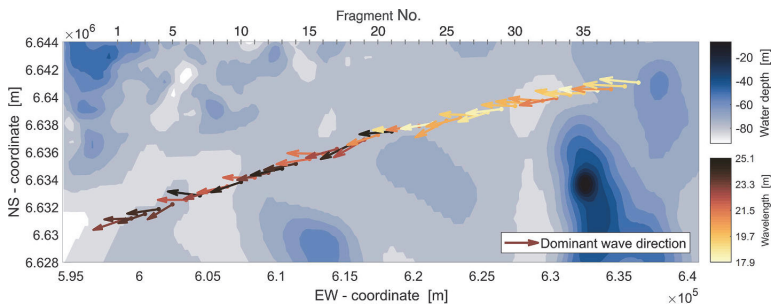


Fig. 9. The derived dominant wave directions and wavelengths (λ) of the ALS point cloud fragments (see Fig. 2) along with bathymetry data (GEBCO_2020; sourced from: <https://gebcoset.org/>).

suggesting that the obtained SWH represents the actual geometry well. The corresponding values from buoy observations and the WAM model are 0.65 m and 0.64 m, respectively. The slight discrepancy between ALS-derived value and buoy observations could be caused due to the distance between the buoy and the flight trajectory (refer to Fig. 1). Fig. 8b also shows that the wave direction is well-identified relative to its opposite direction. Due to Doppler shifting and flight direction, if the opposite direction were selected, the measured peak period would deviate from the buoy and WAM model by moving to the left.

The derived dominant wave directions and wavelengths along the flight trajectory are presented in Fig. 9. As can be seen, the dominant directions fluctuate between fragments. Such differences could be caused by a specific physical phenomenon (such as variation in the wind, currents, or water depth), or computational errors, which require further research. The estimated peak wavelengths vary between 17.9 and 25.1 m along the trajectory. On average, the wavelengths are around 21.3 m.

Fig. 10 compares the ALS-derived wave parameters with the hourly WAM wave model (spatial resolution of one nautical mile). The model data were extracted at the coordinates of the fragments' centres at 9:35 UTC (i.e., the ALS flight time) via bilinear interpolation. In addition, the modelled wave parameters at the location of the Suomenlahti wave buoy are also compared. The uncertainty of the hourly model data relative to the buoy observations during 24 h (i.e., on 10 May 2018) is also marked in the figure. These values for the peak period, SWH, and dominant wave direction are 0.23 s, 0.05 m, and 7.4° , respectively. The comparison also reveals a mean difference between modelled wave parameters and observations, which equal correspondingly -0.1 s, -0.12 m, and 10.0° .

According to the comparison in Fig. 10, the LiDAR-based method appears to be well supported by the modelled estimates along the flight trajectory with a mean difference (MD) and residual standard deviation (ResidSD) of a) 0.2 s and 0.1 s for the peak period, b) -0.09 m and 0.03 m for the SWH, and c) -0.5° and 10.0° for dominant wave

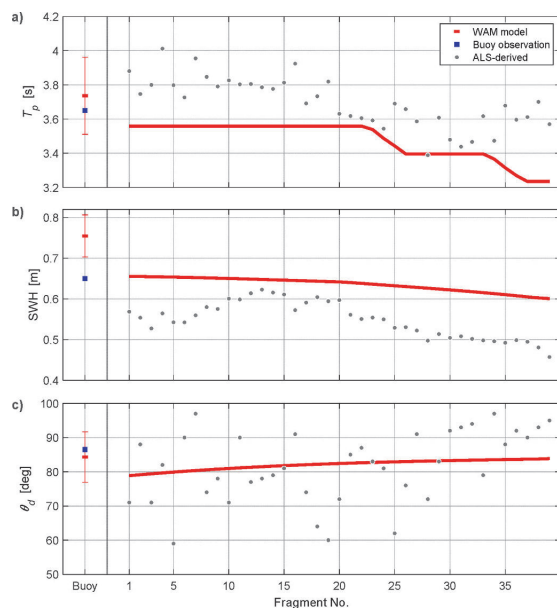


Fig. 10. Comparison between ALS-derived, buoy observed, and WAM model-based wave parameters: a) peak period, b) significant wave height, and c) dominant wave direction. The vertical bars indicate the estimated uncertainty of the WAM model at the location of the wave buoy.

direction, respectively (cf. Table 1). Note that the ALS-derived results are more scattered than the WAM model data because the former is based on instantaneous observations that contain sampling variation. Since the ALS data represents an instantaneous sea state, it can be concluded that ALS-derived data products are more sensitive to local conditions and hence more realistic. Also, since ECMWF's ERA5 wind model with an hourly output and spatial resolution of 0.28° (i.e., 16.8 nautical miles) is used to force the wave model, the model variation appears smoother than ALS results due to the limitation of the wind model resolution (Lindgren et al., 2021; Hersbach and Dee, 2016). The values of Fig. 10 are also listed in Table 1 and compared additionally with the direct geometrical method provided by Varbla et al. (2021). The results of Varbla et al. (2021) are assumed to represent mean waves. For comparability, the wave heights and periods were transformed to SWH ($SWH = 1.56 \cdot \bar{H}$) and peak period ($T_p \approx 1.2 \cdot \bar{T}$), respectively.

Finally, Fig. 11 shows a comparison between ALS-derived spectrum and model-based standard wave spectrum for fragments No.13 and 28, suggesting in general a rather good agreement. According to Fig. 10, the retrieved spectrum shows the best SWH match with the wave model for fragment No.13, while T_p agrees poorly. On the other hand, notice that the opposite is true for fragment No.28 (cf. Fig. 10).

5. Discussion

This study demonstrated that different methods can be employed to obtain parameters and power spectra of sea waves using an ALS-measured 3D point cloud. One of the challenges of using ALS data with existing wave theory has been the spatial limitations. For instance, at best, ALS can provide accurate along-track data where the across-track data corridor is at the scale in the order of a kilometre. Nevertheless, a scale in the order of 10 km of the random field of surface waves is typically required to satisfy statistical stability. This study showed that a spatial wave spectrum could be obtained utilizing the periodogram method and discrete Fourier transform (using a snapshot of SSH in a 1×1 km area). The results, however, proved to be unsatisfactory and unstable due to the randomness of the sea surface (Fig. 3). Note that PSD is meant for homogenous wave profiles.

Therefore, a robust spatial wave spectrum method was developed that uses random sampling for selecting sample points within a pre-defined data sampling area to determine a more reliable spatial wave spectrum (see Section 3.2). It was revealed (Fig. 5a) that the standard error improves significantly by increasing the sample size. This allowed examining the homogeneity condition and retrieval of long enough wave profiles to reach a stable power spectral density function for ALS-measured point clouds. The random sampling method involves more information about the desired irregular random sea waves by adding parallel wave profiles instead of increasing the spatial length of the profile. Note that the sample points may also be selected using equal spacing and this method can be explored in future studies.

In this study, a sample size of 300 was estimated sufficient to achieve a standard error of less than 5% of the spectrum's peak in any direction. Hence, the directional spatial wave spectrum was computed by employing a sample size of 300 (see Fig. 7), which in comparison to Fig. 3, provides an improved stable spectrum utilizing limited spatial coverage of ALS data. Such a directional spectrum can allow the detection of the dominant wave direction, which corresponds to the maximum wave energy. Similarly, the peak wavelength of around 20.6 m in the dominant wave direction could be detected (see an example in Fig. 7).

The computed spectrum of the dominant wave direction was validated using data from a nearby buoy. Since ALS and buoy use different measurement techniques resulting in different physical quantities, the spatial wave spectrum of ALS data was transformed to the frequency wave spectrum using the dispersion relationship. Such a transformation made the two datasets comparable (Fig. 8). The ALS-derived significant

Table 1

Obtained wave parameters: peak period (s), significant wave height (m), and dominant wave direction (°) by using the presented method, WAM model, and direct geometrical (Varbla et al., 2021) method. The MD ± ResidSD of each dataset with respect to (w.r.t.) other sources are also presented.

No.	Latitude	Longitude	ALS-derived			WAM model			Varbla et al. (2021)		
			T_p	SWH	θ_d	T_p	SWH	θ_d	T_p	SWH	θ_d
01	59.8070	25.7622	3.9	0.57	71.0	3.6	0.66	78.9	2.8	0.72	81.5
02	59.8099	25.7802	3.7	0.55	88.0	3.6	0.66	79.2	2.9	0.77	81.2
03	59.8126	25.7982	3.8	0.53	71.0	3.6	0.65	79.4	2.9	0.72	76.7
04	59.8155	25.8162	4.0	0.56	82.0	3.6	0.65	79.6	2.9	0.70	77.8
05	59.8184	25.8341	3.8	0.54	59.0	3.6	0.65	79.9	2.8	0.67	77.7
06	59.8211	25.8521	3.7	0.54	90.0	3.6	0.65	80.1	3.0	0.81	75.4
07	59.8238	25.8701	4.0	0.56	97.0	3.6	0.65	80.4	2.9	0.80	72.9
08	59.8266	25.8881	3.8	0.58	74.0	3.6	0.65	80.6	2.9	0.75	75.9
09	59.8291	25.9061	3.8	0.58	78.0	3.6	0.65	80.8	3.0	0.81	75.4
10	59.8317	25.9240	3.8	0.60	71.0	3.6	0.65	80.9	3.0	0.81	77.9
11	59.8344	25.9420	3.8	0.60	90.0	3.6	0.65	81.1	3.1	0.84	77.9
12	59.8373	25.9600	3.8	0.61	77.0	3.6	0.65	81.3	3.0	0.83	79.3
13	59.8397	25.9780	3.8	0.62	78.0	3.6	0.65	81.5	3.0	0.78	80.5
14	59.8426	25.9960	3.8	0.62	79.0	3.6	0.65	81.6	2.9	0.78	77.3
15	59.8454	26.0140	3.8	0.61	81.0	3.6	0.65	81.8	3.0	0.86	79.1
16	59.8485	26.0321	3.9	0.57	91.0	3.6	0.65	82.0	3.0	0.78	83.4
17	59.8514	26.0501	3.7	0.59	74.0	3.6	0.64	82.1	3.1	0.84	79.9
18	59.8540	26.0681	3.7	0.60	64.0	3.6	0.64	82.2	3.1	0.84	77.5
19	59.8569	26.0861	3.8	0.59	60.0	3.6	0.64	82.4	3.0	0.77	81.8
20	59.8598	26.1041	3.6	0.60	72.0	3.6	0.64	82.5	3.0	0.78	81.4
21	59.8617	26.1221	3.6	0.56	85.0	3.6	0.64	82.6	3.0	0.81	83.7
22	59.8635	26.1401	3.6	0.55	87.0	3.6	0.64	82.7	3.1	0.78	85.5
23	59.8647	26.1580	3.6	0.55	83.0	3.5	0.64	82.8	2.9	0.73	86.6
24	59.8660	26.1760	3.5	0.55	81.0	3.5	0.63	82.8	2.9	0.81	85.6
25	59.8675	26.1939	3.7	0.53	62.0	3.4	0.63	82.9	2.9	0.70	83.9
26	59.8690	26.2119	3.7	0.53	76.0	3.4	0.63	83.0	2.9	0.72	83.3
27	59.8707	26.2298	3.6	0.52	91.0	3.4	0.63	83.0	3.0	0.72	85.5
28	59.8722	26.2478	3.4	0.50	72.0	3.4	0.63	83.1	2.9	0.70	83.5
29	59.8740	26.2658	3.6	0.51	83.0	3.4	0.62	83.2	2.9	0.70	85.9
30	59.8757	26.2837	3.5	0.50	92.0	3.4	0.62	83.3	2.9	0.69	84.2
31	59.8772	26.3017	3.4	0.51	93.0	3.4	0.62	83.3	2.8	0.66	89.0
32	59.8784	26.3197	3.5	0.50	94.0	3.4	0.62	83.4	3.0	0.77	88.5
33	59.8799	26.3376	3.6	0.50	79.0	3.4	0.62	83.5	2.9	0.70	89.2
34	59.8816	26.3556	3.5	0.50	97.0	3.4	0.61	83.5	2.9	0.70	88.3
35	59.8826	26.3735	3.7	0.49	88.0	3.3	0.61	83.6	2.9	0.63	88.5
36	59.8839	26.3915	3.6	0.50	92.0	3.3	0.61	83.6	2.9	0.70	91.0
37	59.8845	26.4094	3.6	0.49	90.0	3.2	0.60	83.7	2.9	0.67	91.5
38	59.8859	26.4274	3.7	0.48	93.0	3.2	0.60	83.7	2.6	0.63	92.4
39	59.8885	26.4454	3.6	0.46	95.0	3.2	0.60	83.8	2.8	0.63	91.2
Mean of the 39 fragments			3.7	0.55	81.5	3.5	0.64	82.0	2.9	0.75	82.8
w.r.t. ALS-derived results			–	–	–	–0.2	0.09	0.5	–0.8	0.20	1.2
						±0.1	±0.03	±10.0	±0.2	±0.04	±9.3
w.r.t. WAM model			0.2	–0.09	–0.5	–	–	–	–0.6	0.11	0.7
			±0.1	±0.03	±10.0				±0.1	±0.05	±4.1
w.r.t. wave buoy (cf. Fig. 1)			0.0	–0.10	–5.0	–0.2	–0.01	–4.5	–0.7	0.10	–3.7
T_p	SWH	θ_d	±0.1	±0.04	±10.4	±0.1	±0.02	±1.4	±0.1	±0.06	±5.1
3.7	0.65	86.5									

wave height and peak wave period were 0.60 m and 3.63 s, respectively, whereby the corresponding buoy-observed control values were 0.65 m and 3.65 s. The measured wind speed (7 m/s on average) and direction (from the east) were quasi-steady 24 h before the ALS campaign. These results reveal a good agreement, given that there was a distance of about 40 km between the buoy and ALS flight trajectory (Fig. 1).

The results were also compared with the WAM model along the flight trajectory (Fig. 10). This comparison represents an almost good agreement between the model and ALS-derived wave parameters with a (spatial) mean difference of 0.09 m for the SWH, 0.2 s for the peak period, and 0.5° for the dominant wave direction (see Table 1). The most variation between the ALS results and the WAM model appears in the dominant wave direction estimates. Hence, it is essential to consider that the WAM model provides generalized information about the wavefield, whereas more realistic ALS-derived results are more sensitive to local conditions representing instantaneous sea state. Note also the difference between the WAM model and buoy data (at the buoy location), which is 0.10 m for the SWH, 0.9 s for the peak period, and 2.2° for the dominant

wave direction (cf. Fig. 10).

In Varbla et al. (2021) study, the parameters of surface waves were derived directly from the ALS-measured sea surface geometry. The determined significant wave heights (for the dataset also used in this study) were estimated to be around (on average) 0.75 m, peak period 2.9 s, and wave directions 83°. Statistical comparisons with the results of this study are presented in Table 1. Comparison with the developed method shows systematic differences in significant wave heights and peak periods of around 0.20 m and 0.8 s by average, respectively, which could be due to the different methods employed. However, it should be noted that the significant wave heights estimated by the Varbla et al. (2021) direct method and the method employed in this study agree equally well with the wave buoy and WAM model, although the systematic differences are opposite signed (cf. Table 1). Also, the wave directions estimated by Varbla et al. (2021) appear to show slightly better agreement with the wave buoy and WAM model than this study's results.

In addition to the wind-generated surface waves, Varbla et al. (2021)

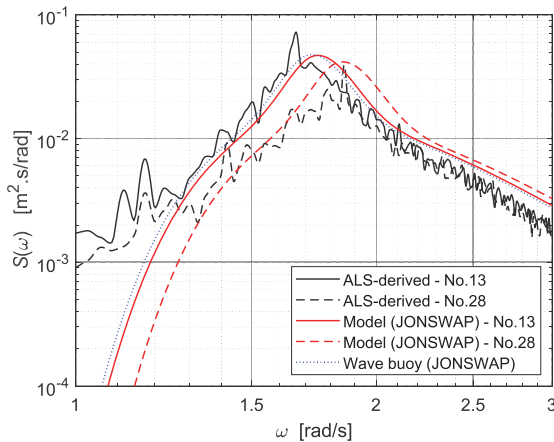


Fig. 11. The ALS-derived spectrum compared to the model-based and buoy-obtained (cf. Fig. 1 for buoy location) standard wave spectrum for fragments No.13 and 28 on a logarithmic scale.

showed that the ALS measurements for another nearby flight trajectory also detected lower frequency swells in the background. Most interestingly, these swells with wavelengths of approximately 30–40 m and wave heights of 0.05–0.12 m had a wave direction that differed from surface wind waves by roughly 40°. Since the portion of swell waves in this dataset is small, these waves are not clearly detectable in the wave spectra. However, two peaks in Fig. 8b around the frequency of 1.1 rad/s suggest the existence of these waves. The first and second swell waves are identified in the spectra with directions from around 195° and 165° (directions are established based on the Doppler shifting and relation to the peaks in Fig. 8b), where the wavelengths are 57 m and 157 m, respectively. The WAM model provides the direction and wave height of the primary swell wave to be 221° and 0.01 m, respectively, and the secondary swell wave height to be approximately zero.

The developed approach provides the directional PSD of the sea waves by considering the entire wave frequency content using the random sampling method, while the direct method suggested by Varbla et al. (2021) yields wave heights and -lengths through data filtering in predefined directions, whereas wave randomness was not considered. In the direct method, the desired wave directions are determined by relying on visual inspection.

Hwang et al. (2000a, 2000b) presented a wave spectrum utilizing 2D FFT with ALS data over an area of around 0.25×1.5 km. Comparatively speaking, the developed method detects the dominant wave direction by addressing the ALS spatial coverage limitation (which results in insufficient lengths of wave profiles) using a random sampling technique, while Hwang et al. (2000a, 2000b) combined nine segments (i.e., 0.25×14 km, where the flight had been aligned approximately with the wave direction) to compute the one-dimensional wavenumber spectrum. They also examined buoy data to show that the wave climate was quasi-steady during the flight, making the spatial wave spectrum determination feasible. In the present study, the directional wave spectrum is obtained for each fragment (which allows us to determine wave parameters such as wave direction) regardless of the angle between the dominant wave and flight directions. Thus, the developed approach presents significant methodological improvements.

6. Conclusions

This study showed that it is possible to retrieve frequency content and power spectral density from ALS-measured 3D point cloud of SSH by using the periodogram method and a random sampling approach. Wave

parameters, such as the dominant wave direction, significant wave height, and peak wave period, can be obtained. For instance, in the presented example of fragment No.20, the measured dominant wave direction was 72°, significant wave height 0.60 m, and peak wave period 3.63 s. Compared to the other methods utilizing ALS (e.g., Hwang et al. (2000a, 2000b) or a direct reconstruction of the wavefield geometry), the method proposed in this study showed that the procedure could retrieve directional wave spectrum accurately for each segment of ALS point cloud stand-alone, which yields the dominant wave direction and other wave parameters. The random selection approach was used in this study to examine the assumption that the wave field is homogeneous over spatial scales without involving other data sources. Future studies can explore using non-random equal spacing selection instead of random selection to reduce the complexity of the method.

Although ALS technology can be somewhat expensive compared to some alternative sensors (e.g., wave buoys, pressure sensors, satellites), it has significant benefits, such as portability, fast 3D data acquisition over vast distances, and most importantly, the potential to provide dense point cloud datasets with high measurement accuracy. The ALS technology could thus be of interest to industry, government, and research. The 3D data capture of the spatial domain also allows a deeper insight into a better understanding of the surface ocean waves, which is necessary for our changing climate and advances in marine engineering and shipping.

CRedit authorship contribution statement

Vahidreza Jahanmard: Conceptualization, Methodology, Validation, Formal analysis, Writing – original draft, Visualization. **Sander Varbla:** Conceptualization, Methodology, Validation, Formal analysis, Writing – review & editing, Visualization. **Nicole Delpeche-Ellmann:** Conceptualization, Validation, Supervision, Writing – review & editing, Project administration. **Artu Ellmann:** Conceptualization, Validation, Supervision, Writing – review & editing, Project administration, Funding acquisition.

Declaration of competing interest

The authors declare that they have no known competing financial interests or personal relationships that could have appeared to influence the work reported in this paper.

Data availability

Data will be made available on request.

Acknowledgements

The research is supported by the Estonian Research Council grants “Development of an iterative approach for near-coast marine geoid modelling by using re-tracked satellite altimetry, in situ and modelled data” [grant number PRG330] and “Wave dynamics for coastal engineering and management: the advantages and challenge of the Lagrangian perspective” [grant number PRG1129]. The two anonymous reviewers are thanked for their constructive comments.

References

- Abaei, M.M., Arzaghi, E., Abbassi, R., Garaniya, V., Chai, S., Khan, F., 2018. A robust risk assessment methodology for safety analysis of marine structures under storm conditions. *Ocean Eng.* 156, 167–178. <https://doi.org/10.1016/j.oceaneng.2018.02.016>.
- Bartlett, M.S., 1948. Smoothing periodograms from time-series with continuous spectra. *Nature* 161 (4096), 686–687. <https://doi.org/10.1038/161686a0>.
- Bondur, V.G., 2004. *Aerospace methods in modern oceanology. New ideas in oceanology* 1, 55–117.

- Bondur, V.G., Dulov, V.A., Murynin, A.B., Yurovsky, YuYu, 2016. A study of sea-wave spectra in a wide wavelength range from satellite and in-situ data. *Izvestiya Atmos. Ocean. Phys.* 52 (9), 888–903. <https://doi.org/10.1134/s0001433816090097>.
- Chen, C., Sasa, K., Prpić-Orsić, J., Mizojiri, T., 2021. Statistical analysis of waves' effects on ship navigation using high-resolution numerical wave simulation and shipboard measurements. *Ocean Eng.* 229, 108757 <https://doi.org/10.1016/j.oceaneng.2021.108757>.
- Delpeche-Ellmann, N., Giudici, A., Rätsep, M., Soomere, T., 2021. Observations of surface drift and effects induced by wind and surface waves in the Baltic Sea for the period 2011–2018. *Estuarine, Coastal and Shelf Science* 249, 107071. <https://doi.org/10.1016/j.ecss.2020.107071>.
- Goda, Y., 2000. Random seas and design of maritime structures. In: *Advanced Series on Ocean Engineering, second ed.* World Scientific, ISBN 981-02-3256- X.
- Gruno, A., Liibus, A., Ellmann, A., Oja, T., Vain, A., Jürgenson, H., 2013. Determining sea surface heights using small footprint airborne laser scanning. *SPIE Proceedings*. In: *Remote Sensing of the Ocean, Sea Ice, Coastal Waters, and Large Water Regions 2013*, vol. 8888. SPIE, pp. 178–190. <https://doi.org/10.1117/12.2029189>.
- Hauser, D., Kahma, K., Krogstad, H.E., Lehner, S., Monbaliu, J.A., Wyatt, L.R., Action, C. O.S.T., 2005. Measuring and Analysing the Directional Spectra of Ocean Waves. Office for Official Publications of the European Communities, Luxembourg, p. 485. <https://doi.org/10.25607/OBP-811>.
- Hersbach, H., Dee, D., 2016. *ERA5 Reanalysis Is in Production*, ECMWF Newsletter, vol. 147. ECMWF, Reading, UK.
- Huang, M.-C., Chen, J.-Y., 1998. Wave direction analysis from data buoys. *Ocean Eng.* 25 (8), 621–637. [https://doi.org/10.1016/s0029-8018\(97\)00036-x](https://doi.org/10.1016/s0029-8018(97)00036-x).
- Huang, Z.-C., Reineman, B.D., Lenain, L., Melville, W.K., Middleton, J.H., 2012. Airborne lidar measurements of wave energy dissipation in a coral reef lagoon system. *J. Geophys. Res.: Oceans* 117 (C3). <https://doi.org/10.1029/2011jc007203>.
- Huising, E.J., Gomes Pereira, L.M., 1998. Errors and accuracy estimates of laser data acquired by various laser scanning systems for topographic applications. *ISPRS J. Photogrammetry Remote Sens.* 53 (5), 245–261. [https://doi.org/10.1016/s0924-2716\(98\)00013-6](https://doi.org/10.1016/s0924-2716(98)00013-6).
- Hwang, P.A., Walsh, E.J., Krabill, W.B., Swift, R.N., Manizade, S.S., Scott, J.F., Earle, M. D., 1998. Airborne remote sensing applications to coastal wave research. *J. Geophys. Res.: Oceans* 103 (C9), 18791–18800. <https://doi.org/10.1029/98JC00895>.
- Hwang, P.A., Wang, D.W., Walsh, E.J., Krabill, W.B., Swift, R.N., 2000a. Airborne measurements of the wavenumber spectra of ocean surface waves. Part I: spectral slope and dimensionless spectral coefficient. *J. Phys. Oceanogr.* 30 (11), 2753–2767. [https://doi.org/10.1175/1520-0485\(2001\)031<2753:AMOTWS>2.0.CO;2](https://doi.org/10.1175/1520-0485(2001)031<2753:AMOTWS>2.0.CO;2).
- Hwang, P.A., Wang, D.W., Walsh, E.J., Krabill, W.B., Swift, R.N., 2000b. Airborne measurements of the wavenumber spectra of ocean surface waves. Part II: directional distribution. *J. Phys. Oceanogr.* 30 (11), 2768–2787. [https://doi.org/10.1175/1520-0485\(2001\)031<2768:AMOTWS>2.0.CO;2](https://doi.org/10.1175/1520-0485(2001)031<2768:AMOTWS>2.0.CO;2).
- Jahanmard, V., Diznab, M.A.D., Mehdigholi, H., Tabeshpour, M.R., Seif, M.S., 2015. Performance-based assessment of steel jacket platforms by wave endurance time method. *Ships Offshore Struct.* 12 (1), 32–42. <https://doi.org/10.1080/17445302.2015.1099245>.
- Kawauchi, H., Ueno, K., Sato, M., Fanz, C., Hiraoka, R., 2009. Comparative study of ocean wave height estimation with power spectral density function by three methods. *Math. Phys. Fisheries Sci.* 7, 70–89.
- Lenain, L., Melville, W.K., 2017. Measurements of the directional spectrum across the equilibrium saturation ranges of wind-generated surface waves. *J. Phys. Oceanogr.* 47 (8), 2123–2138. <https://doi.org/10.1175/JPO-D-17-0017.1>.
- Lindgren, E., Tuomi, L., Huess, V., 2021. Product User Manual for Baltic Sea Physical Reanalysis Product BALTICSEA_REANALYSIS_WAV_003_015. Copernicus Marine Service (CMEMS). <https://doi.org/10.48670/moi-00014>.
- Liu, Z., Frigaard, P., 1999. In: *Generation and Analysis of Random Waves*, first ed. Aalborg University.
- Monin, A.S., Krasitsky, V.P., 1985. *Phenomena on the Surface of the Ocean*. Gidrometeoizdat, Leningrad, p. 375.
- Najafzadeh, F., Kudryavtseva, N., Soomere, T., 2021. Effects of large-scale Atmospheric circulation on the Baltic Sea wave climate: application of the EOF method on multi-mission satellite altimetry data. *Clim. Dynam.* 57 (11), 3465–3478. <https://doi.org/10.1007/s00382-021-05874-x>.
- Nikolkina, I., Soomere, T., Raamet, A., 2014. Multidecadal ensemble hindcast of wave fields in the Baltic Sea. In: 2014 IEEE/OES Baltic International Symposium (BAL TIC. IEEE, pp. 1–9. <https://doi.org/10.1109/baltic.2014.6887854>.
- Pettersson, H., Kahma, K.K., Tuomi, L., 2010. Wave directions in a narrow bay. *J. Phys. Oceanogr.* 40 (1), 155–169. <https://doi.org/10.1175/2009jpo4220.1>.
- Phillips, O.M., 1980. *The Dynamics of the Upper Ocean*. Cambridge Univ. Press, Cambridge.
- Räätmet, A., Soomere, T., Zaitseva-Pärnaste, I., 2010. Variations in extreme wave heights and wave directions in the north-eastern Baltic Sea. *Pro Proceedings of the Estonian Academy of Sciences* 59 (2), 182. <https://doi.org/10.3176/proc.2010.2.18>.
- Romero, L., Melville, W.K., 2010. Airborne observations of fetch-limited waves in the Gulf of Tehuantepec. *J. Phys. Oceanogr.* 40 (3), 441–465. <https://doi.org/10.1175/2009JPO4127.1>.
- Sande, C., Soudarissanane, S., Khoshelham, K., 2010. Assessment of relative accuracy of AHN-2 laser scanning data using planar features. *Sensors* 10 (9), 8198–8214. <https://doi.org/10.3390/s100908198>.
- Soomere, T., 2022. Numerical simulations of wave climate in the Baltic Sea: a review. *Oceanologia*. <https://doi.org/10.1016/j.oceano.2022.01.004>.
- Sun, J., Burns, S.P., Vandemark, D., Donelan, M.A., Mahr, L., Crawford, T.L., Herbers, T. H.C., Crescenti, G.H., French, J.R., 2005. Measurement of directional wave spectra using aircraft laser altimeters. *J. Atmos. Technol.* 22 (7), 869–885. <https://doi.org/10.1175/jtech1729.1>.
- Sutherland, P., Brozena, J., Rogers, W.E., Doble, M., Wadhams, P., 2018. Airborne remote sensing of wave propagation in the marginal ice zone. *J. Geophys. Res.: Oceans* 123 (6), 4132–4152. <https://doi.org/10.1029/2018JC013785>.
- Varbla, S., Ellmann, A., Delpeche-Ellmann, N., 2020. Airborne Laser Scanning Derived Sea Surface Height Datasets in the Gulf of Finland. https://doi.org/10.17882/76491_10.05.2018.
- Varbla, S., Ellmann, A., Delpeche-Ellmann, N., 2021. Applications of airborne laser scanning for determining marine geoid and surface waves properties. *European Journal of Remote Sensing* 54 (1), 558–568. <https://doi.org/10.1080/22797254.2021.1981156>.
- Vieira, F., Cavalcante, G., Campos, E., 2020. Analysis of wave climate and trends in a semi-enclosed basin (Persian Gulf) using a validated SWAN model. *Ocean Eng.* 196, 106821 <https://doi.org/10.1016/j.oceaneng.2019.106821>.
- Vrbancich, J., Lief, W., Hacker, J., 2011. Demonstration of two portable scanning LiDAR systems flown at low-altitude for investigating coastal sea surface topography. *Rem. Sens.* 3 (9), 1983–2001. <https://doi.org/10.3390/rs3091983>.
- Walsh, E.J., Hancock III, D.W., Hines, D.E., Swift, R.N., Scott, J.F., 1985. Directional wave spectra measured with the surface contour radar. *J. Phys. Oceanogr.* 15 (5), 566–592. [https://doi.org/10.1175/1520-0485\(1985\)015<0566:DWSMWT>2.0.CO;2](https://doi.org/10.1175/1520-0485(1985)015<0566:DWSMWT>2.0.CO;2).
- Welch, P., 1967. The use of fast Fourier transform for the estimation of power spectra: a method based on time averaging over short, modified periodograms. *IEEE Trans. Audio Electroacoust.* 15 (2), 70–73. <https://doi.org/10.1109/TAU.1967.1161901>.
- Zlinszky, A., Boergens, E., Glira, P., Pfeifer, N., 2017. Airborne Laser Scanning for calibration and validation of inshore satellite altimetry: a proof of concept. *Rem. Sens. Environ.* 197, 35–42. <https://doi.org/10.1016/j.rse.2017.04.027>.

Appendix 4

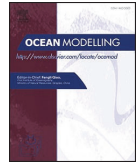
Publication IV

Jahanmard, V., Hordoir, R., Delpeche-Ellmann, N., Ellmann, A. (2023). Quantification of Hydrodynamic Model Sea Level Bias Utilizing Deep Learning and Synergistic Integration of Data Sources. *Ocean Modelling*. doi:10.1016/j.ocemod.2023.102286.



Contents lists available at ScienceDirect

Ocean Modelling

journal homepage: www.elsevier.com/locate/ocemod

Quantification of hydrodynamic model sea level bias utilizing deep learning and synergistic integration of data sources

Vahidreza Jahanmard^{a,*}, Robinson Hordoir^{b,c}, Nicole Delpeche-Ellmann^d, Artu Ellmann^a

^a Department of Civil Engineering and Architecture, Tallinn University of Technology, Ehitajate tee 5, Tallinn 19086, Estonia

^b Institute of Marine Research, Bergen, Norway

^c Bjerknes Centre for Climate Research, Bergen, Norway

^d Department of Cybernetics, School of Science, Tallinn University of Technology, Ehitajate tee 5, 12618, Tallinn, Estonia

ARTICLE INFO

Keywords:

Absolute dynamic topography
Hydrodynamic model
Deep learning network
Vertical reference datum
Hydrogeodesy
Sea level

ABSTRACT

This study demonstrates the use of machine learning strategies to examine and quantify the bias that often exists in sea level data from hydrodynamic models. The sea level bias is considered to consist of two components: (i) hydrodynamic modelling errors due to numerical modelling limitations, and (ii) a bias related to the difference between vertical datums. The goal is to accurately quantify these components, enabling the determination of absolute dynamic topography from coastal to offshore areas. The method is tested in the Baltic Sea employing a synergy of hydrodynamic models, tide gauges, and satellite altimetry.

Firstly, a multivariate deep neural network approach inspired by WaveNet is used to identify and quantify hydrodynamic modelling errors. A wrapper-type sequential feature elimination algorithm identifies seven relevant variables out of the initially considered sixteen for training the deep learning model in the Baltic Sea region. The model is trained using sixteen tide gauge records. As a result, the model predicts hydrodynamic modelling errors with a root mean squared error of 3.2 cm and 3.4 cm, and an R-Squared value of 0.82 and 0.77 for the training and test sets, respectively. Comparing the predicted and observed errors reveals localized areas where other sea level dynamics, such as seiches in the Gulf of Riga, may be of interest but were not incorporated into the deep learning model. Secondly, once the hydrodynamic modelling errors are quantified, the method allows for the determination of the vertical reference bias by comparing known and reliable observations, such as tide gauge and satellite altimetry data. The vertical reference bias is calculated to be 18.1 ± 2.9 cm.

The method significantly improves the accuracy of dynamic topography, resulting in an average root mean squared error of 4.1 cm compared with satellite altimetry and a correlation of 0.98 compared with tide gauges. This approach presents a novel way to integrate modelled and observed dynamic topography using machine learning techniques for enhancing our understanding and its applications.

1. Introduction

The synergy of various sources of sea level data, such as tide gauges (TG), satellite altimetry (SA), hydrodynamic models (HDM), Global Navigation Satellite Systems tide buoys, and airborne laser scanning, is vital to understand the marine environment in the expanding blue growth economy. This synergistic combination of diverse data sources allows determination of accurate and precise sea level from coast to offshore. This accuracy and consistency are of utmost importance for a wide range of applications, including navigation (Orseau et al., 2021), climate change (Magnan et al., 2022; Bian et al., 2023), engineering (Bitner-Gregersen et al., 2013), coastal management (Tebaldi et al.,

2021; Parker et al., 2023). The fusion of these sea level sources is not that straightforward, for several limitations exist such as: (i) different spatial and temporal resolutions; (ii) different vertical reference datums are utilized, and (iii) different errors are present based on the method of data collection (Jahanmard et al., 2022).

Hydrodynamic models tend to ideally be one of the best sources, especially in their extensive spatial and temporal data coverage. However, they are not perfect, and their major shortfalls can be grouped into two main categories. Firstly, HDMs often use an unknown/unspecified vertical datum, which leads to a vertical reference bias when compared to other sources, such as TG and SA data (Slobbe et al., 2013; Jahanmard et al., 2022). Secondly, HDMs are based on mathematical

* Corresponding author.

E-mail address: vahidreza.jahanmard@taltech.ee (V. Jahanmard).

<https://doi.org/10.1016/j.ocemod.2023.102286>

Received 20 July 2023; Received in revised form 25 September 2023; Accepted 1 November 2023

Available online 8 November 2023

1463-5003/© 2023 Elsevier Ltd. All rights reserved.

equations that rely on various inputs, models (e.g., atmospheric, river discharge), assumptions, and approximations (e.g., boundary conditions, parametrization, and discretization techniques).

The reference bias and modelling error are however quite different in nature. For simplicity, several studies have explored the HDM sea level bias as one bias component. For instance, Jahanmard et al. (2021, 2022) and Mostafavi et al. (2023) showed that by using TG data as the realistic ‘ground truth’ along with interpolation methods, it is possible to derive the bias at the coastal areas and extend it to the offshore, where the offshore domain was validated by SA observations. These results were promising with an accuracy of within 5 cm being established. It, however, did not exactly quantify the vertical reference bias of models or the bias associated with the modelling errors. Note that the method employed in these previous studies was mainly possible because an existing dense network of geoid-referenced TGs. The geoid, an equipotential surface of Earth’s gravity field, plays a key role in linking and unifying all data sources, enabling the derivation of dynamic topography (DT). As a result, DT is the instantaneous sea level relative to a particular geoid surface and represents a realistic quantification of water level variations (more details in Section 2).

This study aims to explore the discrepancies between HDM-based sea levels and observations in both time and space in a deeper manner. In this regard, we categorized them as mentioned above into two components that consist of HDM modelling errors and a bias resulting from the difference in vertical reference datums. In this study, the former will be determined using machine learning methods and TG records, and the latter will be obtained by comparing SA observations and the corrected HDM. The reference bias enables the unification of the vertical reference surfaces of the data sources for further integration and investigations.

Recently, machine learning strategies have been widely employed in various ocean applications, including data assimilation, forecasting, and gap filling (Brajard et al., 2020; Zhang et al., 2020; Arcucci et al., 2021; Meng et al., 2021; de Siqueira and de Moraes Paiva, 2021; Buizza et al., 2022; Cheng et al., 2023). In this study, a deep learning (DL) model is employed to predict HDM modelling errors, which utilizes stacks of dilated causal convolutional layers inspired by WaveNet (Oord et al., 2016). Various DL structures, including different configurations of the long short-term memory (LSTM) and other recurrent neural network (RNN) models (Hochreiter and Schmidhuber, 1997; Connor et al., 1994; Che et al., 2018), were tested for this application. Notably, the causal convolution outperformed the others in terms of performance. The advantages of the selected model include learning in the temporal dimension while maintaining temporal causality between input variables and output, as well as more efficient capture of long-range dependencies in data compared to other tested models. This approach allows us to investigate the frequency contents of HDM errors and discover causal relationships between HDM errors and input variables. Also, as TG records are considered the most reliable time series for representing the temporal variation of sea level, the DL model is trained using TGs. However, the spatial sparsity of TG stations hinders feature learning over space and the application of spatial convolutions. Hence, it is necessary for the DL model to generalize effectively over the spatial dimension. This can be attained by carefully selecting appropriate training and test sets and ensuring the model’s robustness to spatial variations during the training process.

Once the HDM modelling errors have been predicted, the corrected HDM is determined by mitigating the predicted errors from the original HDM sea level. Thus, the vertical reference bias can be determined by comparing the corrected HDM and SA data, where SA data has been corrected for a particular geoid model. SA data has been proven to be an accurate and reliable source of absolute sea level measurements from coastal to offshore areas (Abdalla et al., 2021).

Our study aims to accomplish the following objectives: (i) introducing a DL model to predict the HDM errors, resulting in the correction of HDM, (ii) identifying the important input variables that influence the error prediction, (iii) determining the reference bias between the

corrected HDM and observations using both SA and TG data, and (iv) conducting a comparative assessment between data sources to identify both the consistencies and inconsistencies. The method will be tested using the Nemo-Nordic model (Hordoir et al., 2015, 2019; Kärnä et al., 2021) over the Baltic Sea.

The study area is ideal for this examination due to its dense network of TGs with a common geoid-based Baltic Sea chart datum BSCD2000 (Schwabe et al., 2020). In addition, the availability of a high-resolution geoid model NKG2015 facilitates the derivation of SA-based dynamic topography (Ågren et al., 2016). The land uplift model NKG2016LU is also utilized to adjust the relative TG readings to the common reference epoch of 2000.0 (Vestøl et al., 2019). Note that the method can be applied to other regions worldwide in a similar manner.

The present paper is organized as follows. The background theory is presented in Section 2, then the method is outlined in Section 3. Next, the presented method is employed for an application in Section 4, and the results are presented in Section 5. Finally, a brief summary concludes the paper.

2. Background theory

Hydrodynamic models typically lack a well-defined vertical reference (Slobbe et al., 2013; Jahanmard et al., 2022). Consequently, the first question queried is which reference surface is being used to model sea levels. HDMs are typically set up using spherical coordinates (latitude φ , longitude λ , vertical component); however, regardless of the specific vertical coordinate system employed, there is an implicit vertical coordinate z in the model. It is important to note that surfaces of constant z do not accurately reflect distance from the Earth’s centre. Instead, they represent surfaces of constant geopotential W (Hughes and Bingham, 2008). Therefore, we can use the term “dynamic topography” to refer to the modelled sea levels (DT_{HDM}).

Note that HDM’s reference surface is frequently misconstrued as coinciding with the mean sea surface (MSS) (Slobbe et al., 2013). Indeed, the model’s vertical reference surface can coincide with a geoid model, which is determined through the use of gravity data and the application of Stokes’ formula. The separation between MSS and a surface of constant geopotential (i.e., the geoid surface) represents the mean dynamic topography (MDT), which allows for the computation of surface geostrophic currents.

A more accurate implementation of geoid geometry in HDMs results in differences at the 0.5 % level and is not a significant source of error in modelling (Kantha and Clayson, 2000; Hughes and Bingham, 2008). Another source of error in HDMs is the discrepancy in vertical datums used for height parameters, such as bathymetry and open boundary sea levels. This issue is addressed through an extensive calibration and validation process (Cea and French, 2012). Additionally, HDMs can contain errors stemming from topography, computational errors, time steps and modelling discretization, limitations in model resolution and parameterization schemes, and uncertainties in boundary conditions and forcing inputs (Mardani et al., 2020).

In this study, we aim to perform post-processing HDM-derived sea levels to minimize the level of errors, and then apply vertical referencing to reduce the HDM’s reference surface to a well-defined geodetic reference frame. By considering DT as the ground-truth dynamic topography that is obtained from a reliable source (e.g., TG, SA), the following relation can describe the HDM-derived dynamic topography:

$$DT(\varphi, \lambda, t) = DT_{HDM}(\varphi, \lambda, t) - E(\varphi, \lambda, t) \quad (1)$$

where E is the discrepancy between the modelled DT and the ground-truth sea level, which includes both the HDM modelling errors and a constant bias resulting from differences in zero levels between the HDM’s reference surface and a particular geoid surface. Hence, E should be divided into two terms as follows:

$$E(\varphi, \lambda, t) = \varepsilon(\varphi, \lambda, t) + RefBias \quad (2)$$

where ε is the HDM modelling error, which vary over time and space. This term occurs due to errors and limitations in the modelling. The second term, $RefBias$, is a constant value that is the difference between the geopotential surface of the HDM and a particular geoid model used for the observations. In this study, the former term will be addressed by employing a DL model to predict the HDM errors based on the TG readings (Section 3.1), and the latter term will be tackled through a comparison between the corrected HDM and SA data (Section 3.2). Note that TG readings, used as ground-truth sea level for training the DL model, may contain errors and biases compared to the actual reality. However, the DL model is able to mitigate the errors through its generalization ability along with using adequately long time series from multiple locations.

Fig. 1 shows a schematic view of the interrelation between data sources and parameters used. Note that a stable and common vertical reference surface is required to make various data sources comparable in terms of absolute dynamic topography (Jahanmard et al., 2022). In this regard, computing $RefBias$ and utilizing geoid-referenced observations can make everything consistent for combining sea level measurements from different sources.

The method for predicting the HDM errors and referencing HDM to a common vertical frame with other observations was investigated in the Baltic Sea region. This semi-enclosed sea provides an ideal study area due to the availability of the Nemo-Nordic model, a dense network of TGs with a common geoid-based vertical reference datum, a high-resolution geoid model NKG2015, and an accurate postglacial land uplift model NKG2016LU. The Baltic Sea has frequently served as a research site for investigating global climate and environmental changes, benefiting from extensive long-term marine and land-based monitoring programs (Reusch et al., 2018). This area is classified as low-salinity brackish water with a salinity range between 5 and 7 PSU, which is influenced by freshwater inputs from river runoff and net precipitation, as well as the exchange with saline water from the North Sea (Kniebusch et al., 2019). In addition, the coastal areas in this region may experience the formation of ice cover during winter.

There are four main mechanisms that cause currents in the Baltic Sea: wind stress on the sea surface, sea level atmospheric pressure gradient, horizontal density gradient resulting from temperature and salinity differences, and tidal forces. In addition, the shallow depth, averaging ca. 54 m, results in a notable damping effect on currents due to bottom friction (Soomere and Quak, 2013). The impact of astronomical tides on

the Baltic Sea is generally insignificant because of its limited co-oscillation with the open ocean. Nevertheless, locally generated tides may still contribute, and under resonance conditions, the resulting tide-induced sea level variations could become noticeable (Weisse et al., 2021). The Baltic Sea consists of several basins with several periodic dynamical processes in time scales from 1 h to 1–2 days, including seiches (less than 40 h) and inertial oscillations (Jönsson et al., 2008; Soomere and Quak, 2013). In the upcoming sections, we will provide a detailed explanation of our methodology applied in this study area.

3. Method

In this section, we describe the methodology employed for predicting the HDM modelling error using a multivariate DL model and the determination of the vertical reference bias ($RefBias$). In this regard, we used a multivariate time series prediction with the causal convolutional network to estimate the HDM modelling error ε with respect to the TG series, for which the formulations and the DL model used are described in Section 3.2. The input variables are represented in Sections 4.1 and 4.2. The determination of the $RefBias$ is described in Section 3.3, and the application of the present method and its evaluation are explained in Section 3.4. Fig. 2 shows the flowchart of this study.

3.1. HDM modelling error

Tide gauges provide continuous and high-frequency sea level measurements, and they are the most reliable and accurate estimate of sea level variations (Wöppelmann et al., 2006). Consequently, comparing hourly HDM data with TG records at station locations enables the identification of high- and low-frequency HDM errors ε with respect to observed sea levels. Although TG records provide enhanced temporal resolution, they are spatially scattered and unevenly distributed. On the other hand, SA observations offer more satisfactory spatial coverage, especially in offshore areas. Nevertheless, their repeat cycles (e.g., 27 for Sentinel-3A) are relatively large to effectively capture high-frequency HDM errors.

It should be noted that TGs typically measure water levels relative to nearby tide gauge benchmarks, which are connected to national height systems. These benchmarks may be either part of the height reference network or only connected imprecisely (Varbla et al., 2022). Therefore, TG records may contain biases from vertical datum shifts or lack a precise vertical reference unification between countries or communities. To minimize this bias in our HDM error computation, the temporal mean of differences between HDM and TG records for the entire time period at each station ($Bias$) should be eliminated from the HDM error. As a result, the HDM error ε , which serves as the target values for DL training, is determined for the i -th station as follows:

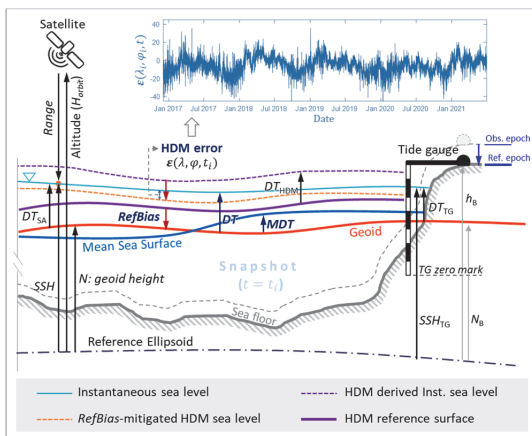


Fig. 1. A schematic diagram of interrelation between different data sources, hydrodynamic parameters and vertical reference surface.

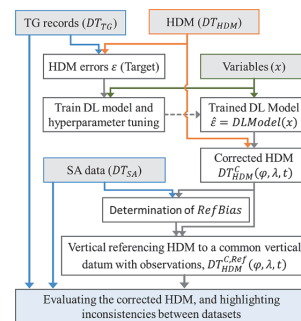


Fig. 2. Flowchart of the methodology for HDM correction and vertical referencing to a common vertical datum as used for SA and TG observations.

$$\varepsilon_i(t) = (DT_{HDM@TG_i}(t) - DT_{TG_i}(t)) - Bias_i \quad (3)$$

where i indicates the index of stations, $DT_{HDM@TG}$ is the HDM sea level series at the TG station, and obtained as follows:

$$DT_{HDM@TG_i}(t) = \text{median}(H_i(\varphi, \lambda) \cdot DT_{HDM}(\varphi, \lambda, t)) \quad (4)$$

where H_i is a binary matrix with the same size as the HDM grid, which is used to select HDM data within a small radius (e.g., 5 km) around the i -th station. In this regard, the median operator is applied to average the selected values of the HDM around the TG station. The same H is also applied to the input variables, enabling the extraction of variables at the TGs' locations for DL model training process.

In Eq. (3), removing the *Bias* from the HDM error ε is justified because the reference surface of HDMs is generally stable (Afrasteh et al., 2021, 2023). Even a slight erroneous tilt in the HDM's vertical reference can lead to significant water fluxes that must be in equilibrium with open boundary inputs. Therefore, these artificial fluxes can cause instability in modelling, which modelers usually remedy through model calibration.

3.2. Utilizing deep learning model for predicting HDM errors

The HDM error ε is expected to consist of different components that are most likely to be predictable both in time and space. Hence, predicting modelling errors is possible to investigate through convolutional neural networks that have been successfully applied in various applications, such as reconstructing sea surface dynamics (Fablet et al., 2023), oceanic eddy detection (Du et al., 2019), predicting sea levels (Liu et al., 2020; Rajabi-Kiasari et al., 2023), and forecasting wave fields (Bai et al., 2022). In this study, we utilized a DL model with temporal dilated causal convolution layers inspired by WaveNet (Oord et al., 2016), which is also employed in a wide range of fields, such as ocean wave height prediction (Lou et al., 2022), wind speed forecasting (Rathore et al., 2021), and nonlinear system identification (Yuan et al., 2023).

Unlike ordinary convolutions, causal convolution is unidirectional (1D), which is particularly used in time series analysis and can efficiently model sequences in a causal manner. In this convolutional operation, the learnable parameters (i.e., weights and biases) are trained to predict the current moment using historical information within the receptive field length (R). By dilation that refers to the spacing between filter elements in a convolutional layer, the receptive field can be expanded without significantly increasing the number of parameters or computational cost. Therefore, dilated causal convolution layers are employed in this study, and the advantage of it over conventional convolutions is their ability to maintain temporal causality. As a result, the DL model can be trained at the TG locations to capture dependencies between the spatiotemporal variables and HDM errors, and consequently, to be used over the HDM domain.

The DL model consists of k blocks of causal convolutional units. Each block contains two conv1D layers with a filter size (fs), nf number of filters, and a dilation (d). This layer has two learnable parameters: weights and biases, which are trained during the training process. To enable the model to learn complex relationships between the inputs and output, Rectified Linear Unit (ReLU) activation functions are incorporated after the conv1D layers. This introduces non-linearity to the model. The utilization of batch normalization between the conv1D and ReLU layers enhances accuracy and accelerates the training process (Bjorck et al., 2018). Additionally, incorporating a dropout layer helps prevent overfitting and encourages the network to learn more robust and generalized representations (Baldi and Sadowski, 2013). Table 1 presents a summary of the block.

Fig. 3 illustrates the internal structure of the DL model used in this study on the left, while the right side shows the causal convolution blocks. For simplicity, the internal structure is shown with values of fs ,

Table 1

Summary of causal convolution blocks used in the DL model. Output shape indicates the dimension of layer output in channels (C), time steps (T), and batches (B).

Layers	Output shape	Learnable parameters #
Conv1D (Dilated causal conv.)	$32(C) \times 1(T) \times 1(B)$	Weights: $6 \times (\text{num_inp}) \times 32$ Bias: 1×32
Batch normalization	$32(C) \times 1(T) \times 1(B)$	Offset: 32×1 Scale: 32×1
ReLU activation function	$32(C) \times 1(T) \times 1(B)$	–
Dropout (probability of 0.2)	$32(C) \times 1(T) \times 1(B)$	–
Conv1D (Dilated causal conv.)	$32(C) \times 1(T) \times 1(B)$	Weights: $6 \times 32 \times 32$ Bias: 1×32
Batch normalization	$32(C) \times 1(T) \times 1(B)$	Offset: 32×1 Scale: 32×1
ReLU activation function	$32(C) \times 1(T) \times 1(B)$	–
Addition	$32(C) \times 1(T) \times 1(B)$	–
Filter size fs : 6 Number of filters nf : 32 Dilation d : 2^{k-1}		

nf , and k set to 2, 16, and 4, respectively. Following the k blocks, the feature maps, with a receptive field of R , are fed into the fully connected layers. These fully connected layers also possess two learnable parameters: weights and biases, which are also fine-tuned during the training process.

Table 2 represents the summary of the entire DL model used and the selected hyperparameters. In this study, we employed 5 blocks of the causal convolutional units, with values of fs and nf set to 6 and 32, respectively. Consequently, the receptive field of the DL model is calculated as $R = (fs - 1)(2^k - 1) + 1 = 156$ (equivalent to 6.5 days).

It should be noted that due to the sparse nature of the TG observations, feature learning over the spatial dimensions is disrupted, which results in the DL model being unable to learn in the spatial dimensions. However, incorporating spatiotemporal input variables (described in Sections 4.1 and 4.2) and utilizing causal convolutions to effectively learn from temporal dimensions with a fixed receptive field enables us to develop a DL model capable of training at TG locations and operating across the entire study domain. Therefore, it is essential to generalize the model across spatial dimensions and eliminate irrelevant variables. For this purpose, an effective spatial sample splitting strategy enables us to prevent overfitting and obtain a generalized DL model for predicting ε . In this study, 50 stations (shown in Fig. 4) are utilized, which are divided into a training set of 16 stations, a validation set of 16 stations, and a test set of 18 stations. Note that the model is trained over the temporal dimension, and selection of equal size for training and validation set allows better to control the model's generalization across spatial dimensions through a feature selection. Additionally, the goal was to use a minimal number of TG stations for training, demonstrating the model's ability to predict HDM errors in situations where a dense network of TGs is not accessible. The test stations serve only for evaluating the DL model's performance with unseen data.

3.3. Vertical reference bias

The vertical Reference bias (*RefBias*) represents the difference between the vertical reference surface of the corrected HDM and a particular geoid surface. Determining the *RefBias* enables us to reduce the zero level of a hydrodynamic model to a well-defined geodetic reference system. As a result, the modelled and observed DT s can be efficiently compared in terms of absolute values, and a common reference surface enables the synthesis various sea level sources with consistent physical definitions. For this purpose, the *RefBias* is computed

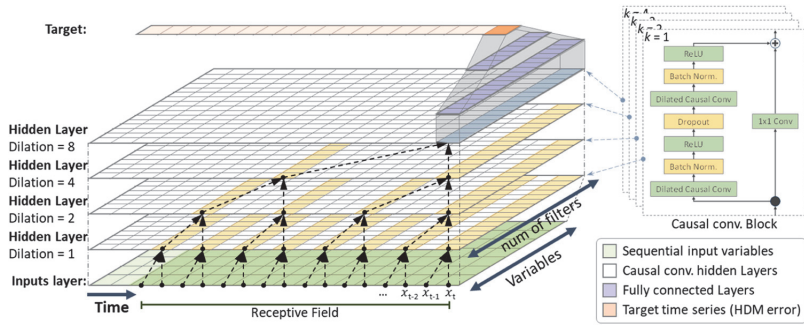


Fig. 3. Internal structure of the DL model used on the left, and the causal convolution blocks on the right.

Table 2
Summary of the DL model and selected hyperparameters for training. Default values were used for the other parameters.

Layers	Output shape	Learnable parameters #
Causal_conv_block ($k = 1$)	$32(C) \times 1(T) \times 1(B)$	Weights: 7488 Bias: 64 Offset: 64 Scale: 64
Skip_conv1D	$32(C) \times 1(T) \times 1(B)$	Weights: 224 Bias: 32
Causal_conv_block ($k = 2-5$)	$32(C) \times 1(T) \times 1(B)$	Weights: 49,152 Bias: 256 Offset: 256 Scale: 256
Fully_connected_1	$32(C) \times 1(T) \times 1(B)$	Weights: 1024 Bias: 32
Layer_normalization_1	$32(C) \times 1(T) \times 1(B)$	Offset: 32 Scale: 32
Dropout (probability of 0.2)	$32(C) \times 1(T) \times 1(B)$	-
Fully_connected_2	$16(C) \times 1(T) \times 1(B)$	Weights: 512 Bias: 32
Layer_normalization_2	$16(C) \times 1(T) \times 1(B)$	Offset: 16 Scale: 16
Fully_connected_out	$1(C) \times 1(T) \times 1(B)$	Weights: 16 Bias: 1
Regression_output	$1(C) \times 1(T) \times 1(B)$	-

Number of layers: 49
Total learnable parameters: 59,553
Optimizer: Adam
mini-batch size: 4
Number of epochs: 200
Loss function: 0.5MSE (default)
Learning rate: 0.001

as follows:

$$RefBias = \text{median}(\text{bias_op}(\varphi_{Obs}, \lambda_{Obs})) \quad (5)$$

where the median operator is employed as a robust statistic to determine the bias arising from differences between reference surfaces, and bias_op is:

$$\text{bias_op}(\varphi_{Obs}, \lambda_{Obs}) = \frac{1}{Q} \sum_{t=1}^Q (DT_{HDM}^C(\varphi_{Obs}, \lambda_{Obs}, t_{Obs}) - DT_{Obs}(\varphi, \lambda, t)) \quad (6)$$

where DT_{HDM}^C represents the corrected HDM obtained by applying the predicted ε to the original HDM, DT_{Obs} is the observed dynamic topography relative to the desired geodetic reference, and Q is the number of observations within the selected time span. Therefore, the bias_op refers to the remaining bias between the observations and the corrected HDM at the observing points $(\varphi_{Obs}, \lambda_{Obs})$. In this study, SA observations are utilized to determine $RefBias$ due to their well-distributed spatial coverage. Therefore, the DT_{SA} relative to a particular geoid model is

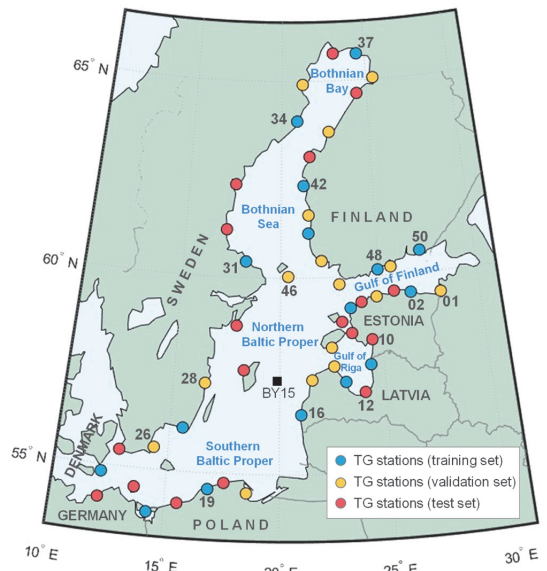


Fig. 4. Study area (Baltic Sea) and the locations of the tide gauge stations used in the study (numbered clockwise starting from the Eastmost Estonian tide gauge station, as denoted in some stations). The stations have been split into training, validation, and test sets. The location of the Gotland deep BY15 is also indicated by a black square.

determined as follows:

$$DT_{SA}(\varphi, \lambda, t) = SSH_{SA}(\varphi, \lambda, t) - N(\varphi, \lambda) \quad (7)$$

where SSH_{SA} is the SA-based sea surface height relative to a reference ellipsoid, and N is the geoid height. In this study, NKG2015, which is a high-resolution geoid model with resolution of $0.01^\circ \times 0.02^\circ$ (Ågren et al., 2016), is used to determine geoid height N . This regional geopotential model has been determined through a least-squares modification of Stokes' formula with additive corrections, resulting in a static reference surface that exhibits a standard deviation of 2.9 cm with respect to GNSS/levelling data. Note that the geoid model must be transformed to the mean permanent tide system before applying Eq. (7). For more details, we refer to Jahanmard et al. (2022).

3.4. Application of HDM correction and referencing

The DL model described above is trained using the training set. The selection of the input variables will be discussed in Section 4. Furthermore, the hyperparameters have been optimized through multiple trial and error iterations, with the details already reported in Section 3.2 (Tables 1 and 2). By leveraging the pre-trained DL model, it becomes possible to determine the HDM modelling errors ε using the spatio-temporal input variables, as follows:

$$\begin{aligned} x_f(c, t, p) &= \text{Vec}(x(c, t, \varphi, \lambda)) \\ \hat{\varepsilon}(p, t) &= \text{DLModel}(x_f(c, t, p)) \\ \hat{\varepsilon}(\varphi, \lambda, t) &= \text{Vec}^{-1}(\hat{\varepsilon}(p, t)) * G(ks, \sigma) \end{aligned} \quad (8)$$

where operators $\text{Vec}(\cdot)$ and $\text{Vec}^{-1}(\cdot)$ are used to flatten variables x and reshape the predicted HDM errors $\hat{\varepsilon}$ on the spatial dimensions, respectively (see Fig. 5). Therefore, x_f represents the input variables to the DL model, which the pre-trained model is denoted by DLModel. To suppress potential high-frequency noises that may arise from the individual determination of HDM errors at each grid point, a Gaussian spatial filter is also applied on the predicted HDM errors $\hat{\varepsilon}$ with a kernel size of $ks = 5$ nautical miles and a standard deviation of $\sigma = 2.5$ nautical miles. Symbol $*$ denotes the convolution operation, c is the dimension of the input variables/channels, and p represents the index of HDM grid data points within the study domain when the spatial dimensions are flattened by Vec operator. The performance of the DL model with respect to the TG records is evaluated using the root mean squared error (RMSE) and coefficient of determination (R^2), calculated as follows:

$$RMSE = \sqrt{\frac{1}{Q} \sum_{i=1}^Q (\hat{\varepsilon}(i) - \varepsilon(i))^2} \quad (9)$$

$$R^2 = 1 - \frac{\sum_{i=1}^Q (\hat{\varepsilon}(i) - \varepsilon(i))^2}{\sum_{i=1}^Q (\varepsilon(i) - \text{mean}(\varepsilon(i)))^2} \quad (10)$$

where Q is the number of samples within the designated time span. The RMSE and R-Squared estimates are determined for each TG station, and the performance of the training, validation, and test sets is determined by averaging the results across stations in each set. For final evaluation, the validation and test sets are merged as a test set. Finally, the corrected HDM, DT_{HDM}^C , is computed accordingly:

$$DT_{HDM}^C(\varphi, \lambda, t) = DT_{HDM}(\varphi, \lambda, t) - \hat{\varepsilon}(\varphi, \lambda, t) \quad (11)$$

Therefore, the *RefBias* would be accurately determined as per Eq. (5). As a result, the vertical referencing of the HDM is performed as follows:

$$DT_{HDM}^{C,Ref}(\varphi, \lambda, t) = DT_{HDM}^C(\varphi, \lambda, t) - \text{RefBias} \quad (12)$$

Fig. 5 illustrates the procedure of the HDM correction and its vertical referencing using the DL model and TG and SA observations.

In the Baltic Sea region, the common geoid-based chart datum BSCD2000 has been established to enhance the effective utilization of GNSS methods for accurate navigation and offshore surveying

(Schwabe et al., 2020). The BSCD2000 based zero marks of TG stations are rigorously connected to the EVRS based national height systems, also coincide with the geoid surface with the reference point of the Normaal Amsterdams Peil (NAP). The NKG2015 geoid model used along with SA data for *RefBias* determination is also based on the EVRS. This suggests that the *RefBias* associated with the TG records is expected to be similar to the one determined through SA observations, with a small margin of error (to be discussed in Section 5.2).

Note that the network of the TG stations may contain vertical datum shifts, and the marine geoid utilized may incorporate error and problematic regions (Jahanmard et al., 2022; Varbla and Ellmann, 2023). Therefore, this unification of the vertical reference between different sources of sea level allows for the determination of accurate dynamic topography and facilitates the investigation of inconsistencies between data sources. Furthermore, the corrected HDM enables the establishment of a link across the sea to connect TG zero marks, in the absence of a common height reference amongst TG stations or between countries (Afrasteh et al., 2021, 2023; Wang et al., 2023).

After applying the HDM correction, we also assess the remaining bias (*SB*) and root mean square error (*SRMSE*) at the observation points across time. The *SB* indicates how closely the corrected HDM fits the observations spatially, revealing static inconsistencies between the datasets. The *SRMSE* is a measure of the temporal variations between the modelled and observed data. Therefore:

$$\begin{aligned} SB(\varphi_{Obs}, \lambda_{Obs}) &= \frac{1}{Q} \sum_{i=1}^Q (DT_{HDM}^{C,Ref}(\varphi_{Obs}, \lambda_{Obs}, t) - DT_{Obs}(\varphi_{Obs}, \lambda_{Obs}, t)) \\ SRMSE(\varphi_{Obs}, \lambda_{Obs}) &= \sqrt{\frac{1}{Q} \sum_{i=1}^Q (DT_{HDM}^{C,Ref}(\varphi_{Obs}, \lambda_{Obs}, t) - DT_{Obs}(\varphi_{Obs}, \lambda_{Obs}, t))^2} \end{aligned} \quad (13)$$

where Q is the number of observations, and the equations are applied at the locations of all the SA and TG observations.

4. Datasets and input variables

The developed approach will be presented using the Nemo-Nordic model (Hordoir et al., 2019; Kärnä et al., 2021), fifty TG stations, and Sentinel-3A satellite altimetry data over the Baltic Sea region for the period of December 2016 to June 2021.

4.1. Hydrodynamic model

The hydrodynamic model was developed by the Swedish Meteorological and Hydrological Institute (SMHI). It is a 3D coupled ocean-sea ice model of the Baltic and North Sea, which is based on the NEMO-4.0 ocean engine (Nucleus for European Modelling of the Ocean). The model sea level is hourly with horizontal resolution of 1 nautical mile (NM). Nemo-Nordic uses a bathymetry obtained from the global GEBCO dataset (GEBCO-2014) and has two open boundaries: a meridional boundary in the English Channel between Brittany and Cornwall, and a zonal boundary between Scotland and Norway. The model uses SI³ sea ice model (Kärnä et al., 2021) and forced with the HIRLAM atmospheric

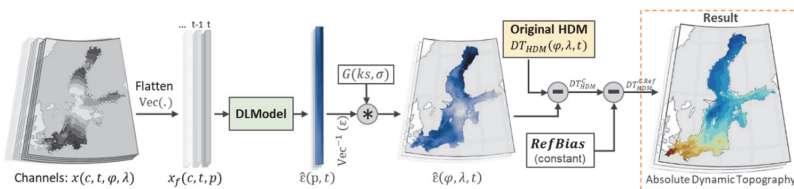


Fig. 5. Implementation of the DL model for correcting the HDM dynamic topography and vertical referencing to a particular geodetic reference frame.

forecast model data (Undén et al., 2002). River discharge data is derived from the E-HYPE daily mean (Arheimer et al., 2012). It has been demonstrated that wind waves significantly contribute to extreme sea levels (Staneva et al., 2016, 2017). However, to the best of our knowledge, Nemo-Nordic does not consider wind waves in its calculations.

4.2. Tide gauge data

Tide gauge data serves as a base for determining the HDM modelling error (ϵ). Therefore, it is important to carefully inspect and correct TG records to ensure their accuracy. In this study, hourly TG data are obtained from seven Baltic Sea countries, which are listed in detail in Table A.1 and the location of stations is indicated in Fig. 4. The TG zero marks are consistent with their national height systems complying with BSCD2000 (Schwabe et al., 2020). Since the BSCD2000 is a common geoid-based chart datum amongst the Baltic countries, TG readings can be directly expressed as dynamic topography DT_{TG} .

The Baltic Sea region is under a strong influence of the glacial isostatic adjustment (GIA) induced land uplift (Vestøl et al., 2019). It is therefore necessary to reduce TG readings into a common time-epoch through a vertical land uplift model. This has been achieved by using the NKG2016LU model for the reference epoch 2000.0 (Varbla et al., 2022). In addition, the TG zero marks must also be transformed to the mean permanent tide system. For more information about the TG treatment for this study, we refer to Jahanmard et al. (2022).

Fig. 6 shows the discrepancies (E) between the HDM and TG records according to Eq. (2) at three sample stations. This figure shows the combination of the HDM error and reference bias. Observe that: (i) E changes in time but the pattern of change is the similar at the high-lighted stations. Similar pattern was also observed for all stations and (ii) the Biases used in Eq. (3) are relatively consistent at different TG stations. This indicates that the used TGs are referenced to a common reference surface, and as a result, the HDM modelling errors (ϵ) are accounted for in Eq. (3). However, in this method, it is not necessary for the TG stations to have a common reference surface. This approach can also be employed to reference accurately the TG zero marks to a common reference surface through the corrected HDM, even without requiring a pre-existing common reference (cf. Afrasteh et al., 2021).

By removing the Biases, the frequency contents of the HDM error can be obtained using the Fast Fourier Transform (FFT), as shown in Fig. 6b. This figure emphasizes that the HDM error (ϵ) at different TG stations representing various sub-basins in the Baltic Sea consists of: (i) both

high- and low-frequency components, (ii) the variations ranging from half-day to annual errors, (iii) a consistent pattern observed across all stations, and (iv) almost similar amplitude observed (1–4 cm). The importance of these findings suggests that similar HDM errors can be reflected more or less at different stations.

4.3. Satellite altimetry

The method implemented using the DL model should also have the capability to predict the modelling error not only at other stations but also in the offshore domain. As a result, the method can also be validated using satellite altimetry sea level data. In addition, satellite data is utilized to obtain the $RefBias$ by Eq. (5).

In this study, high frequency (20 Hz) along-track sea level measurements from Sentinel-3A satellite were utilized. These measurements operate in SAR mode based on the ALES+SAR retracker. The dataset is downloaded from the EUMETSAT data centre (<https://www.eumetsat.int>). The SA mission retrieves the instantaneous sea surface height with a cycle period of 27 days and a spatial resolution of 300 m. To compare other sea level sources with SA data, the HDM and TG data are interpolated bilinearly in space to the SA data points and linearly in time to the SA time epoch to unify the time and location of measurements. Standard geophysical and atmospheric corrections have already been applied to the data. For more details, we refer to Jahanmard et al. (2022).

The satellite-based dynamic topography DT_{SA} is determined according to Eq. (7) and the NKG2015 geoid model. Note that the geoid rise regarding GIA also needs to be considered for the Baltic Sea region. The maximum geoid rise in the study domain is 0.6 mm/year in the Northern part of the Bothnian Sea (Kakkuri and Poutanen, 1997).

The satellite altimetry data also may contain enormous errors and outliers due to land contamination, sea ice, etc. (Mostafavi et al., 2023). These outliers were eliminated from the SA observations. For this purpose, the data points within 5 km from the coastlines are removed to diminish the land contamination errors. In addition, a moving median with a sliding window of one degree along the latitude and a threshold of three local scaled median absolute deviations are applied to detect the outlier data during each pass and cycle.

Considering the difference in horizontal resolution between the Nemo-Nordic and SA data sampling (300 m), it is desirable to filter out high-frequency fluctuations from the DT_{SA} . For this purpose, variations with a wavelength shorter than 10 km were filtered from the along-track SA data using a wavelet filter. Fig. A.1 shows the original and post-processed along-track SA signals for a sample pass and cycle.

4.4. Data consistency and dataflow

Datasets used in this study include Nemo-Nordic model, TG records, Sentinel-3A radar altimetry measurements, NKG2015 geoid model, NKG2016LU land uplift model and the corresponding geoid rise due to the strong influence of GIA in the region of interest, and spatiotemporal input variables that will be discussed in the following Subsection. Table 3 summarizes the spatial and temporal resolution of the datasets.

Hourly TG records are corrected for GIA vertical land motion using NKG2016LU and with the reference epoch of 2000.0. Consequently, TG

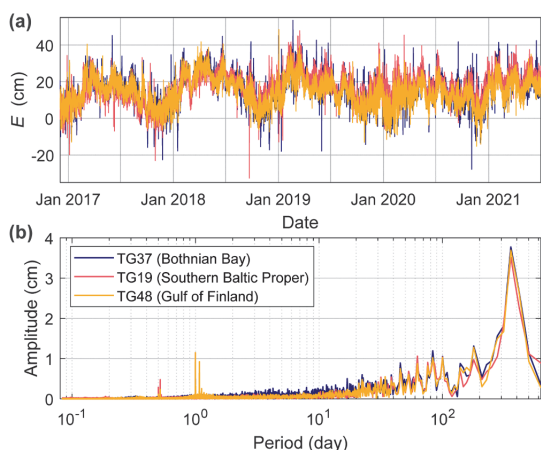


Fig. 6. (a) Discrepancy between the Nemo-Nordic and three tide gauges. The locations of the tide gauges are shown in Fig. 4. (b) Frequency contents of the corresponding signals.

Table 3

Spatial and temporal resolution of data sources in this study.

Datasets	Resolution Spatial	Temporal
Nemo-Nordic model	1 NM	Hourly
TG records	at location of stations	Hourly
Sentinel-3A	300 m along the tracks	27 days
NKG2015	$0.01^\circ \times 0.02^\circ$	–
NKG2016LU; geoid rise	$0.08^\circ \times 0.16^\circ$	–
Input variables	see Table 4	

records are compared with their nearby hourly HDM-derived sea levels to serve as the training target for the DL model. The HDM values at TG locations are extracted using Eq. (4), and the same H_S s are used for extracting the variables (see Section 4.1) to serve as the DL inputs in training process.

Pre-trained DL model are employed to predict the HDM errors across entire HDM domain using spatiotemporal variables. For this purpose, the spatial and temporal resolutions of the variables are unified with the HDM through linear interpolations.

The $RefBias$ between the reference surface of the corrected HDM and a particular geoid surface is determined by comparing the corrected HDM with DT derived from SA measurements. A secondary check was also made by comparison of the corrected HDM with TG data. Since HDMs benefit from using an equipotential surface as their vertical reference and a static bathymetry dataset in their configuration, $RefBias$ is a constant value over the study domain and in time. To determine DT from SA data by Eq. (7), the NKG2015 geoid model and geoid rise model are computed at SA data points via bilinear interpolation. Therefore, the comparison for the determination of $RefBias$ between the corrected HDM and SA-derived DTs is conducted at the SA data points and their corresponding time instants, where the corrected HDM is interpolated bilinearly in space and linearly in time to the location and time of SA measurements.

4.5. Spatiotemporal channels for DL model

In order to reconstruct the HDM error at the location of TGs and then outstretch the DL model to all HDM grid points in the study domain, the identification of relevant spatiotemporal channels (input variables) is essential. Important considerations for channel selection encompass: (i) relevance to the physical processes, (ii) predictive power for generalizing to new data, particularly in the spatial domain, (iii) availability of the channels, (iv) dimensionality of the data, and (v) addressing regularization and overfitting concerns.

The objective of training the DL model is to predict the HDM error (ϵ) over the space at each time step. In this regard, sixteen spatiotemporal variables are introduced as input variables for the DL model. The variables consist of oceanic and atmospheric parameters and some computed variables, and they are obtained from the Nemo Nordic or other data sources. In Section 4.2, we will explain a feature elimination process that allows identifying which variables contribute to the reconstruction of the HDM errors. Although deep learning approaches can reduce the impact of unrelated input variables and enhance generalization through feature learning (Sun et al., 2020), this feature elimination process is essential in this study to avoid overfitting in the spatial dimensions.

The variables obtained directly from the Nemo-Nordic include zonal and meridional wind components (U and Vwind), sea surface temperature (SST), sea surface salinity (SSS), and ice fraction (Ice-frac). Other variables are retrieved from different sources, which are interpolated bilinearly in space and linearly in time to maintain consistency in terms of dimensionality.

In addition to the wind components, the wind stress (X_s and Y_s) and Ekman pumping velocity (w-Ekman) are determined to explore potential relationships between the HDM error and these variables. It is recommended to use the wind stresses utilized by the HDM as a driving force in the momentum equations based on the bulk formulae used. However, in this study, the wind stresses are derived by multiplying a coefficient with the square of the wind speed in both the zonal and meridional directions, given the unavailability of the wind stresses used by the HDM. The w-Ekman is calculated by dividing the curl of the wind stress by the product of water density and the Coriolis parameter (Gill, 1982).

Sea surface pressure (SLP) data, known as a significant driver of sea level variations (Weisse et al., 2021), is downloaded from the CERRA dataset. Additionally, the mean total precipitation rate is obtained from

the ERA5 dataset to estimate the water column induced by precipitation (η_p) at the grid points. To account for the contribution of wind waves in the HDM modelling error, the significant wave height (SWH) of the Baltic Sea was obtained from the wave model WAM. Although there is a relatively high correlation between wind components and wave height, the SWH variable is included, and the DL model is allowed to evaluate the significance of these variables (describe in Section 4.2). It is also important to note that the challenge persists in the reconstruction of wave properties within the nearshore, archipelago regions, and narrow sub-basins (Soomere, 2023). Other used variables are introduced in the following Subsections.

4.6. Astronomical tides

The impact of astronomical tides on the Baltic Sea is typically considered minor due to limited co-oscillation with the open ocean. However, locally generated tides can still contribute, and under resonance conditions, the resulting variations in sea level induced by tides could become more noticeable. The prescribed sea levels along the Nemo-Nordic's open boundaries contain tides, but the local tidal potential effect is not included in the modelling. One could remove the tides from observations (i.e., TG and SA data) and HDM, while in this study, the tides are retained as they are, and tides variables are fed to the DL model.

In this study, eight tidal constituents, namely M2, O1, K1, S1, P1, Mf, Mm, and Ssa, are employed based on tidal analysis on TG records. The sea level induced by these constituents is determined on HDM grid points as follows:

$$\eta_a(\varphi, \lambda, t) = f_c H_c \cos(\omega_c t + (V_0 + u)_c - G_c) \quad (14)$$

where $f_c H_c$, ω_c , and G_c are the amplitude, angular velocity, and phase of harmonic constituent c , respectively. $(V_0 + u)_c$ connects the local time basis to the positions of the Sun, Moon, and Earth. The amplitudes and phases are retrieved from the FES2014 global ocean tides atlas (Carrere et al., 2015). The tidal series were computed at the grid points. To reduce the number of input channels, the series are divided into three variables: semi-diurnal (M2), diurnal (O1, K1, S1, and P1), and low tides (Mf, Mm, and Ssa).

4.7. Steric effect

Steric sea level changes occur as a result of variations in the density of the water column, leading to its expansion/contraction. The mean steric height, along with the additional barotropic contribution associated with bottom pressure, are essential components of mean dynamic topography (Siegmund et al., 2007). However, models that utilize the Boussinesq approximation, such as NEMO, conserve volume rather than mass and do not appropriately represent the steric height in modelling (NEMO Consortium, 2023). Although this approximation does not pose a significant error in the calculated flow field of the model, it is essential to consider the significant contribution of steric changes to local variations in dynamic topography over seasonal and climatic time scales.

The correction for net expansion/contraction can typically be addressed by incorporating the steric height into the water level prescribed at the open boundary (Slobbe et al., 2013). As we do not have access to the Nemo-Nordic setup and this correction is undisclosed to us, the steric height changes (η_s) can be considered as a potential input variable for predicting the HDM error. The absence of this correction in the HDM becomes more questionable, given the annual period displayed in Fig. 6b.

The steric height at a specific location is completely determined by the temperature and salinity profiles. It can be calculated directly from 3D models using the parameters available at vertical nodes. Nevertheless, given the obtained Nemo-Nordic dataset for this study includes only sea surface parameters, the observed salinity and temperature in the

Table 4

List of the input variables used for feature selection. The selected features for the final DL model training are indicated in bold, as described in Section 4.2.

	Variable	units	Sourced resolution		Data source
			Temporal	Spatial	
1	Zonal wind (Uwind)	m/s	Hourly	1 NM	Obtained from Nemo-Nordic dataset
2	Meridional wind (Vwind)	m/s	Hourly	1 NM	
3	Sea surface temperature (SST)	°C	Hourly	1 NM	Copernicus: 10.24381/cds.622a565a MTPR is downloaded from Copernicus: 10.24381/cds.adbb2d47 Copernicus; 10.48670/moi-00014 Aviso: https://www.aviso.altimetry.fr/ Monthly profiles of S and T are downloaded from SHARKweb: https://sharkweb.smhi.se/ Computed
4	Sea surface salinity (SSS)	psu	Hourly	1 NM	
5	Ice fraction (Ice-frac)	%	Hourly	1 NM	
6	Zonal wind stress (X_z)	Pa	Computed at the HDM grid points with an hourly temporal resolution using U and Vwind		
7	Meridional wind stress (Y_z)	Pa	Computed at the HDM grid points with an hourly temporal resolution		
8	Ekman pumping (w-Ekman)	m/s	Computed at the HDM grid points with an hourly temporal resolution		
9	Sea surface pressure (SLP)	Pa	3-hourly	5.5 km	
10	Precipitation water col. (η_p)	cm	Hourly	0.25°	
11	Significant wave height (SWH)	m	Hourly	2 km	
12	Semi-diurnal tide (M2)	cm	Computed at the HDM grid points with an hourly temporal resolution		
13	Diurnal tides	cm	Computed at the HDM grid points with an hourly temporal resolution		
14	Low tides	cm	Computed at the HDM grid points with an hourly temporal resolution		
15	Steric height changes (η_s)	cm	Computed at the HDM grid points with an hourly temporal resolution		
16	Sea level variability ($msdDT_{24}$)	cm	Computed at the HDM grid points with an hourly temporal resolution		

water column at station BY15 (denoted in Fig. 4) were used to estimate η_s . The steric effect variation is low-frequency, and the calculated variation can be applied uniformly across the entire study domain. Therefore, the steric height variable was determined as follows:

$$\eta_s(t) = \frac{-1}{\rho_0} \int_{-H}^0 \Delta\rho(T, S) \cdot dz \quad (15)$$

where ρ_0 is the reference density, and the density variation $\Delta\rho$ is determined by the observed temperature and salinity, in accordance with the equation of state described by Gill (1982). The computed time series of η_s is utilized for all grid points.

4.8. Resonant oscillation

The Baltic Sea is also known for its local oscillatory modes that can amplify variations in sea level (Jönsson et al., 2008). Upon initial examination of the HDM error, it is evident that certain locations, such as the Eastern part of the Gulf of Finland and the Gulf of Riga, exhibit a higher standard deviation. This increased deviation can be attributed to the resonance effect.

The frequency analysis of the HDM error (Fig. 6) indicates that a period of approximately one day is a common occurrence in these regions. In addition, in Pärnu Bay (station 10; located Northeast of the Gulf of Riga), there is also an observed period of approximately about 6-h in the HDM error, which could be related to the barotropic 5-h seiche period in the Gulf of Riga (Suursaar et al., 2002).

It is challenging to include the resonance effect and seiche as inputs for the DL model because the model cannot extract spatial features effectively (cf. Section 3.2), and these effects heavily rely on the geometry of the basins. Nevertheless, an innovative variable is defined as follows:

$$msdDT_{24}(\varphi, \lambda, t) = \text{MSD}(DT_{HDM}(\varphi, \lambda, t), 24) \cdot \tilde{S}(\varphi, \lambda) \quad (16)$$

where $msdDT_{24}$ is the moving standard deviation MSD of the HDM-based dynamic topography, using a 24-hour window size. The moving standard deviation can provide information about the amplitude of variations, and the growth of the amplitude can be inferred from an increasing $msdDT_{24}$. A location-based modification $\tilde{S}(\varphi, \lambda)$ was also applied to assist the DL model in focusing on desired locations. This parameter is the normalized mean squared of the daily standard deviation of DT_{HDM} over the designated time span, as shown in Fig. A.2. This represents a form of spatial normalization aimed at regulating the impact of this variable across different locations.

As a result, the sixteen introduced spatiotemporal variables are

summarized in Table 4. Prior to being fed into the model, the input variables were normalized. This normalization process enhances stability and facilitates faster convergence during training, which is particularly important when utilizing the Adam optimizer.

4.9. Feature selection

To ensure the robustness of the DL model for HDM error prediction, selecting variables that contribute to accurately predicting the target and excluding irrelevant variables that can potentially lead to overfitting during training is essential. By doing so, we can develop a more generalized DL model that considers the spatial dimension and gain insights into the sources of HDM error.

For this purpose, a wrapper-type sequential feature elimination algorithm was utilized to systematically eliminate variables in each iteration (Guyon and Elisseeff, 2003). The algorithm begins by training with a subset of variables and then removes a variable based on an elimination criterion. This criterion is a combination of the RMSEs from both the training and validation sets, as described in Eq. (9). Since the objective of this feature selection is spatial generalization, the training and validation sets are defined as indicated in Fig. 4.

Fig. 7 illustrates the iterations of the feature elimination process. In the first iteration, the model is trained using all variables listed in

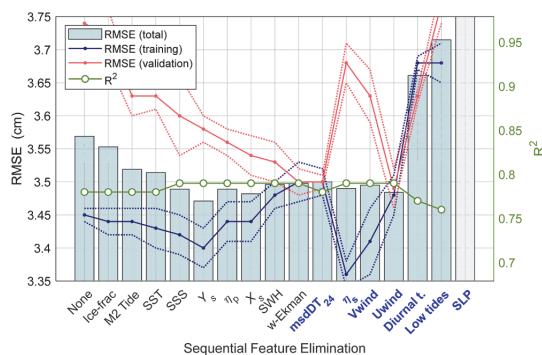


Fig. 7. Sequential feature elimination for selecting the best set of input variables. The variables are removed stepwise from left to right based on the elimination criterion. The solid blue and red lines represent the average RMSE resulting from five repeats of the training processes, with dotted lines indicating one standard deviation from the average. The green line represents the R-Squared result of each elimination iteration. The variable set of the best solution is highlighted in blue font.

Table 4, denoted by 'none' elimination. This initial training results in an RMSE of 3.57 cm and an R-Squared value of 0.78, which the RMSE serves as the elimination criterion. The iteration reveals an RMSE of 3.45 cm for the training set and 3.74 cm for the validation set, indicating overfitting. The model performs well on the training locations but struggles to effectively generalize to unseen data from other locations.

In the next iteration, sixteen DL models were trained, with each training process involving the elimination of one variable. Results demonstrate that removing the 'ice-frac' variable leads to improved model performance, resulting in an RMSE of 3.55 cm. By removing the variable, the next iteration will proceed with the remaining variables, and the next candidate for elimination is determined. These iterations continue until all variables have been removed from the set of DL model inputs.

Fig. 7 shows the results of all elimination iterations sequentially from left to right. The bars in the figure represent the resulting RMSE for each iteration, with the x-axis indicating the variable that is removed. The blue and red lines represent the RMSEs of the training set and validation set, respectively. This visual representation allows for the identification of overfitting, where the RMSE of the training set is higher than that of the validation set. To account for random variations in the elimination iterations, each training process was repeated five times, and the average RMSE was used as the elimination criterion. Dotted lines are included in the figure to represent one standard deviation for both the training and validation sets, based on the five repetitions of training.

Based on the results shown in Fig. 7, we have selected a set of important variables that demonstrate the lowest RMSE, highest R-Squared, and avoid overfitting. It is observed that by removing 'w-Ekman' from the remaining variables, the DL model demonstrates the best performance with an RMSE of 3.5 cm for both the training and validation sets and an R-Squared of 0.79. As a result, the DL model can be generalized over the spatial dimension via the following input variables: 'msdDT₂₄', 'η_s', 'Uwind', 'Vwind', 'Diurnal tides', 'Low tides', and 'SLP'. Note that other new variables can also be added to Table 4 and the feature elimination process can be repeated. However, for this study, we will proceed with the selected variables mentioned.

Given the possible limitations of the sequential feature selection/elimination approach, such as assuming feature independence and sensitivity to elimination order, alternative methods like evaluating all feature combinations (e.g., using genetic algorithms) can also be preferable. Hence, the features were also explored using the multi-objective optimization algorithm NSGA-II to find the optimal feature combination, which the number of features, RMSE, and $(1 - R^2)$ are used as the objectives to determine the Pareto front. In this study, since the optimal combination of features obtained using NSGA-II resembled that achieved through the sequential elimination method, only the sequential method is presented as the result of feature selection.

While this approach is necessary to train a spatially generalized DL model in this study, it may result in the removal of variables with localized effects, such as ice fraction, which predominantly occurs in the Northern and Eastern parts of the Baltic Sea. It is important to note that retaining localized variables may introduce challenges in model generalization. Nevertheless, we have specifically examined the ice fraction variable in locations where it occurs, and it has been excluded again during the feature elimination process, which suggests that the ice fraction variable does not contribute to predict the ϵ , and the HDM works well under the ice condition.

5. Results and discussion

5.1. HDM error prediction

The DL model for predicting the HDM error is constructed based on the architecture outlined in Section 3.2 and input variables described in Sections 4.2. The model is trained using 16 stations and evaluated on all stations (indicated in Fig. 4) for 4.5 years. The progress of the DL model

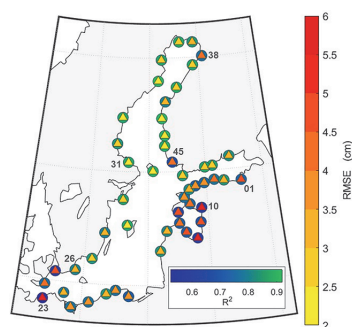


Fig. 8. Performance of the HDM error prediction at available TG stations. The RMSE values are indicated by triangles, and the R-Squared values are indicated by circles, with different colourbars representing the magnitude of the metrics.

training with 200 epochs is illustrated in Fig. A.3.

Fig. 8 illustrates the performance assessment of the HDM error predictions at various locations using the RMSE and R-Squared metrics, according to Eqs. (9) and (10). The average values for RMSE and R-Squared are 3.5 cm and 0.79, respectively. It is evident that some regions have significant RMSE values, such as the Gulf of Riga and Southwest of the Baltic Sea. Higher RMSE values may indicate issues with the HDM error prediction and DL model, such as some variables that were not considered in the analysis, and/or TG problem, for even though the observed HDM modelling error (Eq. (3)) considers the TG data to be perfect. In reality, the TG can still have some errors associated with vertical datum or the location of TG compared to HDM points (e.g., within archipelagos or complex coastal areas).

In addition, the prediction residuals indicate that the remaining errors are associated with high-frequency components, suggesting that the inclusion of additional input variables specific to these locations may be necessary. For instance, at station 10, resonance with the barotropic 5-h seiche period of the Gulf of Riga can result in amplitude growth in Pärnu Bay (Suursaar et al., 2002), which the DL model was unable to accurately predict in terms of the corresponding HDM error. Furthermore, the unique geometry of the Gulf of Riga and the bathymetry at its main entrance, the Irbe Strait, lead to distinct oscillations in this basin compared to other locations, resulting in deviations in the predicted error when generalizing the DL model (Jönsson et al., 2008). Similarly, at Eckernförde Bay TG23, sea level variation is strongly characterized by seiche-like oscillations (Friedrichs and Wright, 1995). Also, station 45 is located in the archipelago area, where the HDM may not exhibit the same performance as it does in other locations. These observations indicate that the DL model provides reasonable results but also highlights the areas where localized dynamics may be occurring, indicating high complexity in terms of resonance effects, seiches, and bathymetry (Otsmann et al., 2001; Jönsson et al., 2008).

To illustrate the performance of the DL model, the predicted ($\hat{\epsilon}$) and actual time series of the HDM error (ϵ) along with the prediction residuals are shown in Fig. 9 for three sample stations (10, 26, 31). Observe that the HDM error (ϵ) varied from -40 to $+40$ cm at station 10 located in Pärnu Bay, Gulf of Riga. The residuals, representing the remaining error after applying the DL model, range from -20 to 20 cm for this station. Also, based on the FFTs presented in the bottom row, it is evident that the DL model was unable to perfectly predict the high-frequency errors in this station. This figure also demonstrates that the high-frequency error is relatively more prominent in this station, as well as in other stations within the Gulf of Riga, compared to other locations. At station 26 located on the Southern Swedish coast, the HDM error was within the range of -20 to 20 cm, and the residuals is reduced to the range of -10 to $+10$ cm. The range and pattern observed at station 26 are similar at station 31, which is in the Northern part of the Baltic Sea.

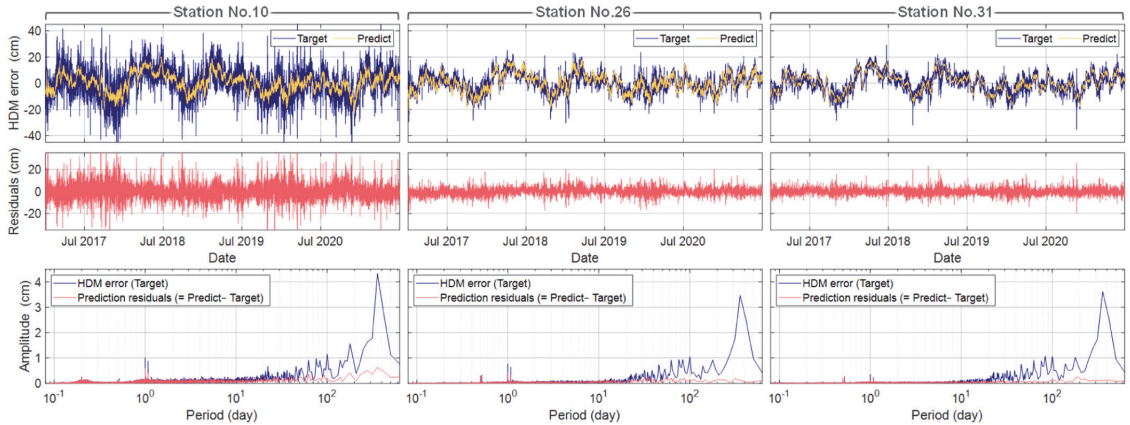


Fig. 9. Time series of both the actual (target, ϵ) and predicted HDM error ($\hat{\epsilon}$) at three sample stations (10, 26, and 31). Residuals of the predictions are depicted by the red lines. Frequency contents of the actual HDM error, along with the residuals, are illustrated in the bottom row.

As a result, the DL model was able to reduce the range of HDM errors by a factor of at least two. It is important to note that the DL model applied in this study is successful in estimating the low-frequency HDM errors, including annual and seasonal cycles. However, further efforts are required to address the high-frequency errors.

5.2. Derived reference bias using SA and TG

The utilization of the DL model allows the prediction of the HDM modelling errors (ϵ) from coast to offshore. Once this modelling error was determined, the HDM model could be corrected (Eq. (11)). The corrected HDM permits an accurate determination of the *RefBias* between HDM's reference surface and a particular geodetic reference

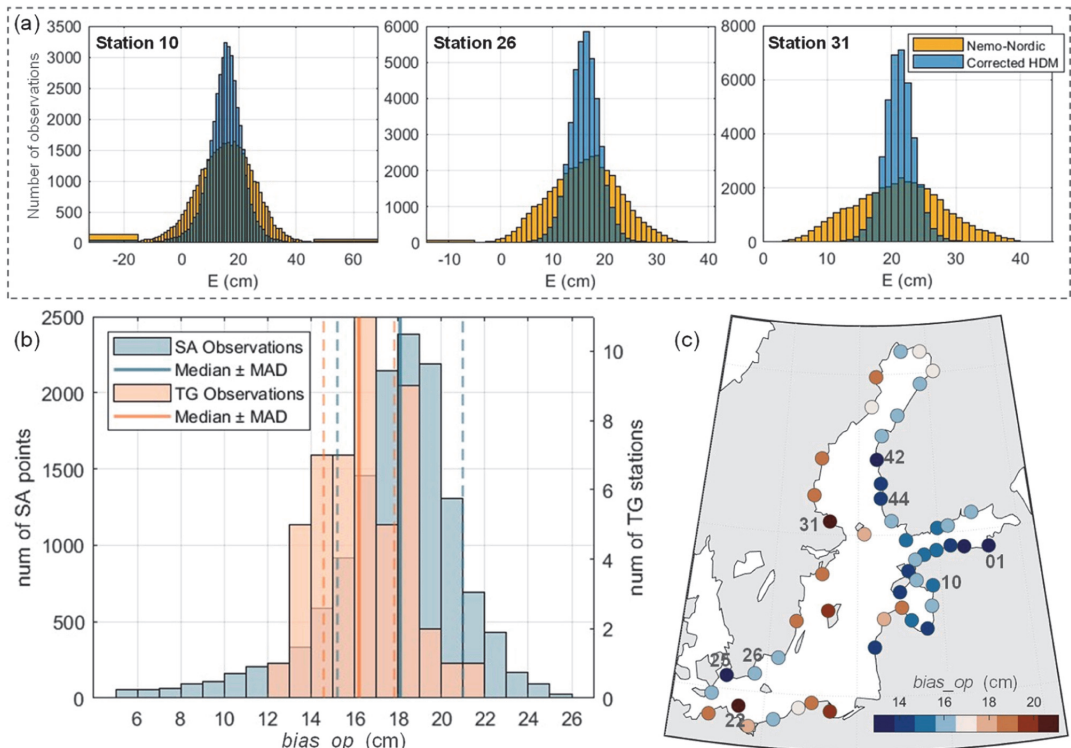


Fig. 10. (a) Histogram of difference between the HDM and TG records (according to Eq. (1)), before and after the HDM error correction. (b) Histogram of the *bias_{op}* (Eq. (6)) at the locations of the TG stations (red), and at the SA data points (blue). The spatial distribution of the bias relative to the TG records are shown in panel c.

surface according to Eq. (5). Therefore, the $RefBias$ is determined using the SA observations within a certain standard deviation as described in Section 3.3. Also, as a secondary control the $RefBias$ was also calculated using the TG data.

Firstly, we present histograms in Fig. 10a that illustrate the difference between the HDM and TG records (E from Eq. (1)) before and after the HDM correction for three sample stations. For instance, before the HDM correction, the median absolute deviation (MAD) for stations 10, 26, and 31 were measured at 7.8 cm, 5.5 cm, and 5.6 cm, respectively. However, after the correction, these values reduced to 4.5 cm, 2.3 cm, and 1.8 cm, respectively. The performance of the DL model at these stations was shown in Fig. 8. The histogram of E values vividly illustrates the improvement of the HDM-based dynamic topography, and it is important to note that the remaining errors in the corrected HDM follow a Gaussian distribution. As a result, the average of the remaining errors in the corrected HDM reflects the reference bias between the HDM and the observation (i.e., SA or TG) at the location ($\varphi_{Obs}, \lambda_{Obs}$), as described in Eq. (6).

Fig. 10b illustrates the histogram of the $bias_{op}$ at TG stations in red and at the SA data points in blue. The values of $bias_{op}$ vary from 5 to 25 cm in the SA data points and from 13 to 21 cm in the TG stations. Ideally, the $bias_{op}$ should be a constant value since both the modelled and observed sea levels are referenced to equipotential surfaces. However, due to errors in factors such as TG zero marks, geoid model, and SA measurements near the coast, the results were scattered. Therefore, the median of all the $bias_{op}$ values is an appropriate calculation to represent the vertical reference bias between the HDM and observations, referred to as $RefBias$ according to Eq. (5). The calculated $RefBias$ of the Nemo-Nordic model relative to the TG and SA datasets is calculated as 16.2 ± 1.6 and 18.1 ± 2.9 cm, respectively.

Fig. 10c also displays the spatial distribution of the $bias_{op}$ for the TG stations, highlighting the pattern of high and low bias relative to the corrected HDM. It is observed that the zero marks of TGs along the coastline of Finland and Estonia are positioned lower than the reference surface of the HDM. The presence of high values in some stations that do not harmonize with the nearby stations suggests a possible vertical datum shift in those TG stations, such as stations 22, 25, 31, and even stations 42 to 44. The absolute value of this bias in the Estonian TGs on the Gulf of Finland gradually increases from West to East. The spatial distribution of the remaining bias between the HDM and SA data will

also be presented in the following subsection (Fig. 12b).

Due to the extensive spatial coverage of the SA data compared to the TG stations, the reference bias of the Nemo-Nordic relative to the European vertical reference system ($RefBias$) has been calculated as 18.1 ± 2.9 cm. Consequently, by adjusting the Nemo-Nordic model by shifting it by this value, it becomes possible to establish a unified vertical reference surface for all data sources. As a result, comparing the values of different sea level sources in terms of absolute dynamic topography is accomplished.

5.3. Comparative assessment

The determination of the $RefBias$ facilitates the unification of the vertical reference surface between HDM dynamic topography and observations. Therefore, the HDM correction employed can be evaluated, and different data sources can be compared to identify any inconsistencies between them.

The instantaneous corrected HDM is obtained according to Fig. 5. The original Nemo-Nordic dynamic topography is also adjusted by $RefBias$ to maintain the same scale for comparison. Fig. 11 depicts the $RefBias$ -mitigated Nemo-Nordic and corrected HDM along with a pass of SA observation and TG readings for a specific time instant and using the same colourbar. This figure shows the improvement of the HDM after applying the correction. The map of HDM error represents the values and pattern of the correction used for this specific time, which ranges from 5 to 16 cm. This range and pattern vary over time. It can be observed that the corrected HDM exhibits good agreement with the SA and TG data compared to the original HDM.

The left panel also shows discrepancies along the SA track (pass No. 272 and cycle No. 48). Notable incompatibility between the corrected HDM and SA data has occurred between latitudes of 54° and 57° . This could be attributed to a part of the HDM error that the DL model was unable to resolve, or existing errors in the SA data or geoid model used. The former is a possibility if the HDM has a specific type of error in this area that cannot be explained by the input variables. The latter is also possible because the SA pass falls in the vicinity of the coastline, particularly around the latitude of 57° .

Another significant discrepancy between the HDM and SA data in Fig. 11 (left panel) is observed between latitudes of 60° and 62° . This discrepancy is attributed to the poor accuracy of the geoid model

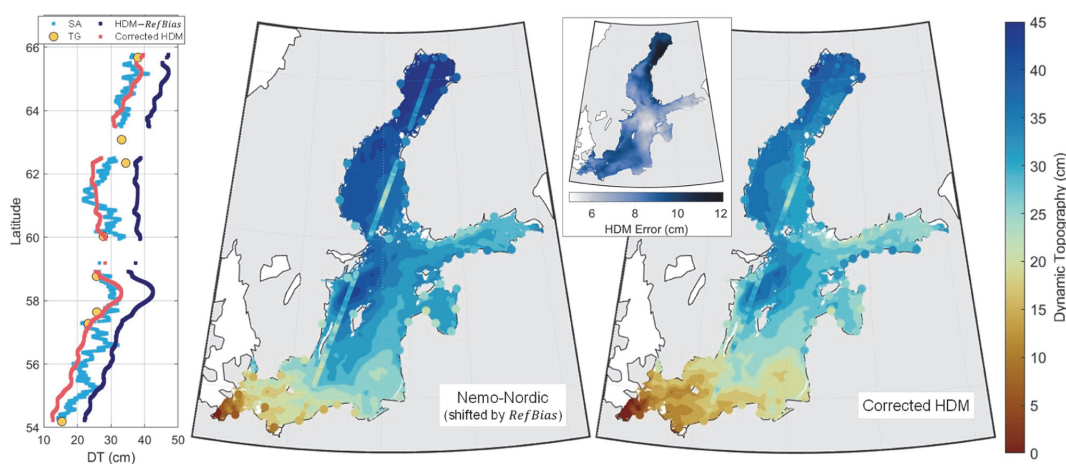


Fig. 11. A snapshot of the absolute dynamic topography for a specific time instant (18-Aug-2019 10:00) to demonstrate the HDM correction by predicted HDM error ($\bar{\epsilon}$, presented in the inset figure) using the DL model, and a comparison between the original Nemo-Nordic that shifted by the $RefBias$ and the corrected HDM. The TG and SA (pass No. 272 and cycle No. 48) observations at this specific time are also demonstrated. The left panel shows this comparison along the SA track. The colour maps used are from (Cramer, 2018).

(Jahanmard et al., 2022; Varbla and Ellmann, 2023; Mostafavi et al., 2023). Because this large variation of DT in such a limited area is not feasible, and this variation is consistently observed across all cycles of SA observations. The significant discrepancy between the corrected HDM and TG readings at latitude 62.5° is more likely due to an existing vertical datum shift in this station rather than an issue with the HDM, as can also be observed in Fig. 10c.

Fig. 12 illustrates the spatial distribution of two metrics: the remaining bias (SB) and the deviation of the HDM from observations ($SRMSE$), as determined by Eq. (13). These values are computed for both the original and corrected Nemo-Nordic model, and a comparison between two models reveals notable improvements in the corrected HDM. Fig. 12a shows the bias between the HDM and observed data, which includes the $RefBias$ along with a spatial bias that was corrected by the DL model. The $RefBias$ is indicated by the white colour in the colourbar, allowing for a direct comparison of the existing spatial bias patterns with panel b.

Fig. 12b highlights remaining inconsistencies and problematic regions after the correction process, in which three major problematic regions are marked with red rectangles: the Eastern part of the Gulf of Finland, the Bothnian Sea, and the Southwest of the Baltic Sea (Bornholm). These regions demonstrate a remaining bias exceeding ± 7 cm, which is relatively large when considering it as an average over a period of ca. 4.5 years. The first two regions have been identified as areas in which the geoid model shows inaccuracies, which is consistent with the findings of recent studies (Jahanmard et al., 2022; Varbla and Ellmann, 2023; Mostafavi et al., 2023). Also, as described in Fig. 11, the significant inconsistency observed in the southwest of the Baltic Sea requires further investigation to determine the source of the error.

Fig. 12c and 12d illustrate the spatial distribution of the root mean square error ($SRMSE$) for the original and corrected HDM, respectively. The average deviation of the original HDM from all data points is 7.6 cm with respect to TGs and 6.5 cm with respect to SA data. While these values are significantly reduced to 3.5 cm for TGs and 4.1 cm for SA data

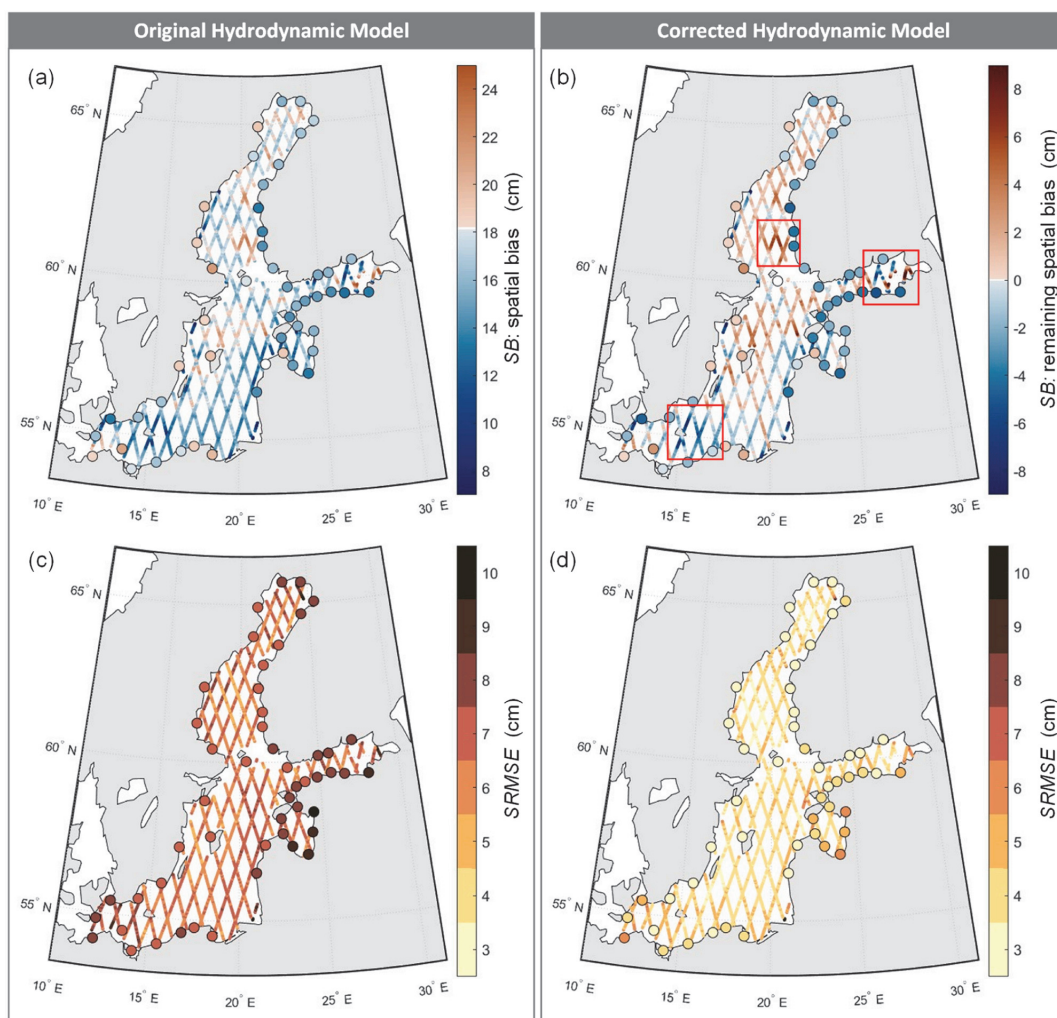


Fig. 12. (a) Spatial bias of the Nemo-Nordic model compared to the SA and TG observations based on Eq. (13). (b) Spatial bias of the corrected HDM. The white colour in (a) and (b) has been set on their $RefBias$ relative to SA observations. $SRMSE$ of original and corrected HDM based on Eq. (13) is demonstrated in (c) and (d), respectively.

after applying the DL-based HDM correction. The corrected model also shows an average increase in correlation coefficient with TG records, from 0.93 to 0.98.

6. Summary and concluding remarks

This study presented a method that utilizes a deep learning multi-variate causal convolutional network to estimate hydrodynamic modelling errors that are often associated with imperfections in the models. Quantification and identification of these HDM modelling errors, further allowed quantification of the vertical reference bias that exists in hydrodynamic models. The basic concept is that the modelling errors are predictable and characterized through causal relationships with the input variables, which are expected to extend spatially.

The DL model was trained using data from sixteen tide gauge stations, and to validate the results, another sixteen stations were used to assess the model's ability to generalize in the spatial dimension. The vertical reference bias is expected to be constant both in space and time, so once the modelling errors are determined, the vertical reference can be calculated using satellite altimetry.

As a result, the DL model followed by feature selection identified seven main input variables for predicting modelling errors: sea level pressure, diurnal and low tides, zonal and meridional wind, steric height, and sea level variability. The selected inputs were generalized for the entire Baltic Sea, but by examining areas with high RMSE, the results also identified localized phenomena causing local errors in the HDM that need to be addressed. The DL model effectively predicted the HDM error (ϵ) with the RMSE of 3.2 cm and 3.4 cm for the training and validation sets, respectively. Additionally, R-Squared values of 0.82 and 0.77 were obtained for the training set and validation set, respectively. However, additional efforts are required to relax the remaining errors in certain identified areas, such as the Gulf of Riga and the entrance of the Baltic Sea where seiches may be present and that the DL model was not able to replicate. It is worth noting that the selected variables could be further improved by collaborating with the Nemo-Nordic current developers and using the HDM outputs, such as wind stresses that the model used for its forcing and computed steric height from the HDM output. By doing so and acquiring a better knowledge of the physical model outputs, one can enhance the performance of the DL model and simplify the interpretation of feature selection.

The reference bias was calculated using both tide gauge and satellite altimetry data. The calculated reference bias of the Nemo-Nordic model relative to the tide gauge data is 16.2 ± 1.6 cm, and relative to the satellite altimetry data is 18.1 ± 2.9 cm.

Quantification of both the modelling errors and reference bias now allowed accurate calculation of HDM dynamic topography. The DL-based corrected Nemo-Nordic model indicates agreement with the fifty tide gauge records, with an RMSE of 3.5 cm and a correlation coefficient of 0.98 compared to the original HDM with an RMSE of 7.6 cm and a correlation coefficient of 0.93 for the period of December 2016 to June 2021. In addition, the RMSE of the corrected HDM compared to the

satellite altimetry measurement is noticeably improved on average from 6.5 cm to 4.1 cm across the Baltic Sea. The utilization of different sources of data also allowed identification of problematic areas, for instance in the Eastern part of the Gulf of Finland and the Bothnian Sea which may be attributed to geoid modelling problems. Whilst Southwest of the Baltic Sea (Bornholm) requires further investigation to determine the source of the error.

This study demonstrated a promising improvement in the determination of absolute dynamic topography by integrating the hydrodynamic model, tide gauge, satellite altimetry, and marine geoid model. The unification of the vertical reference between the model and observations enhances the effectiveness of data assimilation, enabling the integration of various data sources to accurately determine the absolute dynamic topography. This accuracy and consistency in sea level data are urgently required for a comprehensive understanding of climate change, marine engineering, coastal management, and navigation applications (including optimal routes and autonomous navigation). Further studies can be conducted to address and improve the problematic regions by incorporating informative variables into the deep learning model.

CRedit authorship contribution statement

Vahidreza Jahanmard: Conceptualization, Methodology, Validation, Formal analysis, Writing – original draft, Visualization. **Robinson Hordoïr:** Conceptualization, Validation, Writing – review & editing. **Nicole Delpeche-Ellmann:** Conceptualization, Validation, Writing – review & editing, Supervision. **Artu Ellmann:** Conceptualization, Validation, Supervision, Writing – review & editing, Project administration, Funding acquisition.

Declaration of Competing Interest

The authors declare that they have no known competing financial interests or personal relationships that could have appeared to influence the work reported in this paper.

Data availability

Data will be made available on request.

Acknowledgments

The research is supported by the Estonian Research Council grants PRG1785 "Development of continuous dynamic vertical reference for maritime and offshore engineering by applying machine learning strategies" and PRG1129. The authors are extremely grateful to the Swedish Meteorological and Hydrological Institute (SMHI) for providing access to the model data. We are also thankful for the constructive comments made by the anonymous reviewers.

Appendix

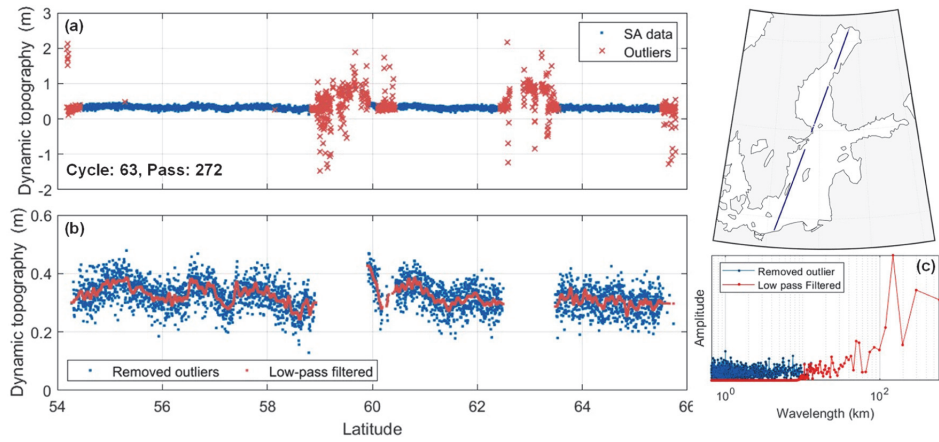


Fig. A.1. An illustration of data screening and treatment for satellite altimetry data: (a) the SA dynamic topography with outlier data points detected for Cycle No. 63 (24-Sep-2020 09:42) and Pass No. 272, which shown in the top-right panel, (b) SA data that has undergone low-pass filtering to smoothen the dynamic topography and eliminate variations with wavelengths shorter than 10 km, as they are not of interest. The frequency contents of the SA data are shown in panel (c) in the same colour scheme as panel (b).

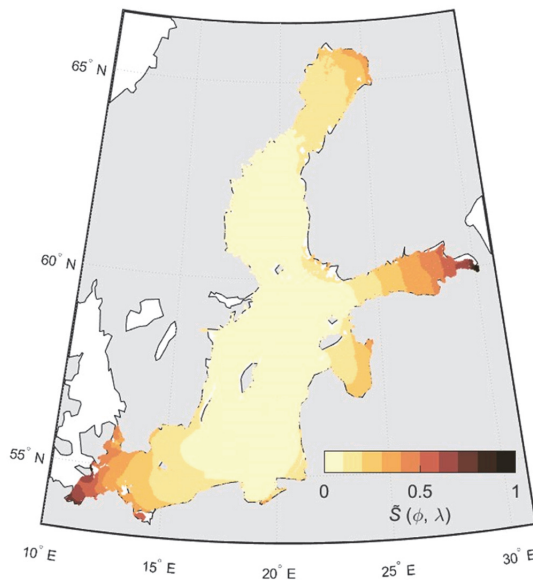


Fig. A.2. Normalized mean squared of the daily standard deviation (from 00:00 to 23:00) of DT_{HDM} for the period of 2017.0 to 2021.5 to remark locations with high daily sea level variations.

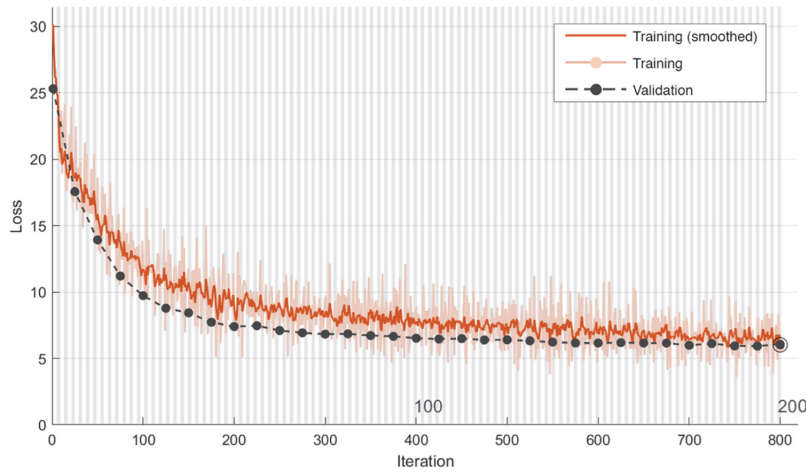


Fig. A.3. Training progress of the DL model for each mini-batch (size: 4), including a smoothed version. Learning loss function is half of the mean squared error as default. Performance on the validation set is also presented in black circles.

Table A.1

List of tide-gauge stations from 01 to 50 along with used national reference frames that comply with BSCD2000. The number of hourly NaN values for the period of December 2016 to June 2021 is also expressed.

ID	Name (Country)	Datum	Location	NaNs	ID	Name (Country)	Datum	Location	NaNs
01	Narva-Jõesuu (EE)	EH2000	(59.47, 28.04)	0	26	Simrishamn (SE)	RH2000	(55.56, 14.36)	0
02	Kunda (EE)	EH2000	(59.52, 26.54)	0	27	Kungsholmsfort (SE)	RH2000	(56.11, 15.59)	0
03	Loksa (EE)	EH2000	(59.58, 25.71)	203	28	Oskarshamn (SE)	RH2000	(57.28, 16.48)	0
04	Pirita (EE)	EH2000	(59.47, 24.82)	0	29	Visby (SE)	RH2000	(57.64, 18.28)	284
05	Paldiski (EE)	EH2000	(59.35, 24.05)	698	30	Landsort norra (SE)	RH2000	(58.77, 17.86)	40
06	Dirhami (EE)	EH2000	(59.21, 23.50)	0	31	Forsmark (SE)	RH2000	(60.41, 18.21)	0
07	Heltermaa (EE)	EH2000	(58.87, 23.05)	388	32	Ljusne sjöv (SE)	RH2000	(61.21, 17.15)	217
08	Roomassaare (EE)	EH2000	(58.22, 22.50)	0	33	Spikarna (SE)	RH2000	(62.36, 17.53)	364
09	Virtsu (EE)	EH2000	(58.57, 23.51)	0	34	Ratan (SE)	RH2000	(63.99, 20.90)	0
10	Pärnu (EE)	EH2000	(58.39, 24.48)	0	35	Furuögrund (SE)	RH2000	(64.92, 21.23)	0
11	Salacgriva (LV)	LAS2000,5	(57.76, 24.35)	0	36	Kalix-storön (SE)	RH2000	(65.70, 23.10)	166
12	Daugavgriva (LV)	LAS2000,5	(57.06, 24.02)	0	37	Kemi Ajos (FI)	N2000	(65.67, 24.52)	0
13	Mersrags (LV)	LAS2000,5	(57.33, 23.13)	0	38	Oulu Toppila (FI)	N2000	(65.04, 25.42)	0
14	Kolka (LV)	LAS2000,5	(57.74, 22.59)	0	39	Raaha Lapaluoto (FI)	N2000	(64.67, 24.41)	0
15	Ventspils (LV)	LAS2000,5	(57.40, 21.53)	0	40	Pietarsaari Leppäluoto (FI)	N2000	(63.71, 22.69)	0
16	Liepāja (LV)	LAS2000,5	(56.52, 21.00)	0	41	Vaasa Vaskiluoto (FI)	N2000	(63.08, 21.57)	0
17	Gdynia (PL)	PL-EVRF2007-NH	(54.52, 18.56)	0	42	Kaskinen Ådskär	N2000	(62.34, 21.21)	0
18	Leba (PL)	PL-EVRF2007-NH	(54.76, 17.55)	78	43	Pori Mäntyluoto K. (FI)	N2000	(61.59, 21.46)	0
19	Ustka (PL)	PL-EVRF2007-NH	(54.59, 16.85)	0	44	Rauma Petäjäs (FI)	N2000	(61.13, 21.44)	0
20	Kołobrzeg (PL)	PL-EVRF2007-NH	(54.19, 15.55)	2682	45	Turku Ruissalo S. (FI)	N2000	(60.43, 22.10)	0
21	Świnoujście (PL)	PL-EVRF2007-NH'	(53.91, 14.25)	0	46	Föglö Degerby (FI)	N2000	(60.03, 20.38)	0
22	Sassnitz (DE)	DHHN2016'	(54.51, 13.64)	5808	47	Hanko Pikku Kolalahti (FI)	N2000	(59.82, 22.98)	0
23	Warnemünde (DE)	DHHN2016	(54.17, 12.10)	5808	48	Helsinki Kaivopuisto (FI)	N2000	(60.15, 24.96)	0
24	Hesnaes (DK)	DVR90	(54.82, 12.13)	0	49	Porvoo Emäsalo V. (FI)	N2000	(60.21, 25.63)	0
25	Skanör (SE)	RH2000	(55.42, 12.83)	224	50	Hamina Pitäjansaari (FI)	N2000	(60.56, 27.18)	0

References

Abdalla, S., et al., 2021. Altimetry for the future: building on 25 years of progress. *Adv. Space Res.* 68 (2), 319–363.

Afrasteh, Y., Slobbe, D.C., Sacher, M., Verlaan, M., Jahanmard, V., Klees, R., Guarneri, H., Keyzer, L., Pietrzak, J., Snellen, M., Zijl, F., 2023. Realizing the European vertical reference system using model-based hydrodynamic leveling data. *J. Geod.* 97 (10), 1–19.

Afrasteh, Y., Slobbe, D.C., Verlaan, M., Sacher, M., Klees, R., Guarneri, H., Keyzer, L., Pietrzak, J., Snellen, M., Zijl, F., 2021. The potential impact of hydrodynamic leveling on the quality of the European vertical reference frame. *J. Geod.* 95, 1–18.

Ågren, J., Strykowski, G., Bilker-Koivula, M., Omang, O., Mårdla, S., Forsberg, R., Ellmann, A., Oja, T., Liepins, I., Parselūnais, E., Kaminskis, J., 2016. The NKG2015 gravimetric geoid model for the Nordic-Baltic region. Presented in the. In:

Proceedings of the 1st Joint Commission 2 and IGFS Meeting International Symposium on Gravity, Geoid and Height Systems. Thessaloniki, Greece, pp. 19–23.

Arcucci, R., Zhu, J., Hu, S., Guo, Y.K., 2021. Deep data assimilation: integrating deep learning with data assimilation. *Appl. Sci.* 11 (3), 1114.

Arheimer, B., Dahné, J., Donnelly, C., Lindström, G., Strömqvist, J., 2012. Water and nutrient simulations using the HYPE model for Sweden vs. the Baltic Sea basin—influence of input-data quality and scale. *Hydro. Res.* 43 (4), 315–329.

Bai, G., Wang, Z., Zhu, X., Feng, Y., 2022. Development of a 2-D deep learning regional wave field forecast model based on convolutional neural network and the application in South China Sea. *Appl. Ocean Res.* 118, 103012.

Baldi, P., Sadowski, P.J., 2013. Understanding dropout. *Adv. Neural. Inf. Process. Syst.* 26, 2814–2822.

Bian, C., Jing, Z., Wang, H., et al., 2023. Oceanic mesoscale eddies as crucial drivers of global marine heatwaves. *Nat. Commun.* 14, 2970. <https://doi.org/10.1038/s41467-023-38811-z>.

- Bitner-Gregersen, E.M., Eide, L.I., Horte, T., Skjong, R., Bitner-Gregersen, E.M., Eide, L.I., Horte, T., Skjong, R., 2013. Potential impact of climate change on design of ship and offshore structures. *Ship Offshore Struct. Des. Clim. Change Perspect.* 2, 43–52.
- Bjorck, N., Gomes, C.P., Selman, B., Weinberger, K.Q., 2018. Understanding batch normalization. *Adv. Neural. Inf. Process Syst.* 31, 7694–7705.
- Brajard, J., Carrassi, A., Bocquet, M., Bertino, L., 2020. Combining data assimilation and machine learning to emulate a dynamical model from sparse and noisy observations: a case study with the Lorenz 96 model. *J. Comput. Sci.* 44, 101171.
- Buizza, C., Casas, C.Q., Nadler, P., Mack, J., Marrone, S., Titus, Z., Le Cornec, C., Heylen, E., Dur, T., Ruiz, L.B., Heaney, C., 2022. Data learning: integrating data assimilation and machine learning. *J. Comput. Sci.* 58, 101525.
- Carrere, L., Lyard, F., Cancet, M., Guillot, A., 2015. FES 2014, a new tidal model on the global ocean with enhanced accuracy in shallow seas and in the Arctic region. In: *Proceedings of the EGU General Assembly Conference Abstracts*, p. 5481.
- Cea, L., French, J.R., 2012. Bathymetric error estimation for the calibration and validation of estuarine hydrodynamic models. *Estuar. Coast. Shelf Sci.* 100, 124–132.
- Che, Z., Purushotham, S., Cho, K., Sontag, D., Liu, Y., 2018. Recurrent neural networks for multivariate time series with missing values. *Sci. Rep.* 8 (1), 6085.
- Cheng, S., Quilodrán-Casas, C., Ouala, S., Farchi, A., Liu, C., Tandeo, P., Fablet, R., Lucor, D., Iooss, B., Brajard, J., Xiao, D., 2023. Machine learning with data assimilation and uncertainty quantification for dynamical systems: a review. *IEEE/CAA J. Autom. Sin.* 10 (6), 1361–1387.
- Connor, J.T., Martin, R.D., Atlas, L.E., 1994. Recurrent neural networks and robust time series prediction. *IEEE Trans. Neural Netw.* 5 (2), 240–254.
- Cramer, F., 2018. *Scientific Colour Maps*. Zenodo. <http://doi.org/10.5281/zenodo.1243862>.
- de Siqueira, B.V.P., de Moraes Paiva, A., 2021. Using neural network to improve sea level prediction along the southeastern Brazilian coast. *Ocean Modell.* 168, 101898.
- Du, Y., Song, W., He, Q., Huang, D., Liotta, A., Su, C., 2019. Deep learning with multi-scale feature fusion in remote sensing for automatic oceanic eddy detection. *Inf. Fusion* 49, 89–99.
- Fablet, R., Febvre, Q., Chapron, B., 2023. Multimodal 4DVarNets for the reconstruction of sea surface dynamics from SST-SSH synergies. *IEEE Trans. Geosci. Remote Sens.* 61, 1558–0644.
- Friedrichs, C.T., Wright, L.D., 1995. Resonant internal waves and their role in transport and accumulation of fine sediment in Eckernförde Bay, Baltic Sea. *Cont. Shelf Res.* 15 (13), 1697–1721.
- Gill, A.E., 1982. *Atmosphere-Ocean Dynamics* (Vol. 30).
- Guyon, I., Elisseeff, A., 2003. An introduction to variable and feature selection. *J. Mach. Learn. Res.* 3 (Mar), 1157–1182.
- Hochreiter, S., Schmidhuber, J., 1997. Long short-term memory. *Neural Comput.* 9 (8), 1735–1780.
- Hordoir, R., Axell, L., Höglund, A., Dieterich, C., Fransser, F., Gröger, M., Liu, Y., Pemberton, P., Schimanke, S., Andersson, H., Ljungemyr, P., 2019. Nemo-Nordic 1.0: a NEMO-based ocean model for the Baltic and North seas—research and operational applications. *Geosci. Model Dev.* 12, 363–386.
- Hordoir, R., Axell, L., Löptien, U., Dietze, H., Kuznetsov, I., 2015. Influence of sea level rise on the dynamics of salt inflows in the Baltic Sea. *J. Geophys. Res.: Oceans* 120 (10), 6653–6668.
- Hughes, C.W., Bingham, R.J., 2008. An oceanographer's guide to GOCE and the geoid. *Ocean Sci.* 4 (1), 15–29.
- Jahanmard, V., Delpeche-Ellmann, N., Ellmann, A., 2021. Realistic dynamic topography through coupling geoid and hydrodynamic models of the Baltic Sea. *Cont. Shelf Res.* 222, 104421.
- Jahanmard, V., Delpeche-Ellmann, N., Ellmann, A., 2022. Towards realistic dynamic topography from coast to offshore by incorporating hydrodynamic and geoid models. *Ocean Modell.* 180, 102124.
- Jönsson, B., Döös, K., Nycander, J., Lundberg, P., 2008. Standing waves in the Gulf of Finland and their relationship to the basin-wide Baltic seiches. *J. Geophys. Res. Oceans* 113, C03004.
- Kakkuri, J., Poutanen, M., 1997. Geodetic determination of the surface topography of the Baltic Sea. *Mar. Geodesy* 20 (4), 307–316.
- Kantha, L.H., Clayson, C.A., 2000. *Numerical Models of Oceans and Oceanic Processes*. Elsevier.
- Kärnä, T., Ljungemyr, P., Falahat, S., Ringgaard, I., Axell, L., Korabel, V., Murawski, J., Maljutenko, I., Lindenthal, A., Jandt-Scheelke, S., Verjovkina, S., 2021. Nemo-Nordic 2.0: operational marine forecast model for the Baltic Sea. *Geosci. Model Dev.* 14 (9), 5731–5749.
- Kniesbusch, M., Meier, H.M., Radtke, H., 2019. Changing salinity gradients in the Baltic Sea as a consequence of altered freshwater budgets. *Geophys. Res. Lett.* 46 (16), 9739–9747.
- Liu, J., Jin, B., Wang, L., Xu, L., 2020. Sea surface height prediction with deep learning based on attention mechanism. *IEEE Geosci. Remote Sens. Lett.* 19, 1–5.
- Lou, R., Lv, Z., Guizani, M., 2022. Wave height prediction suitable for maritime transportation based on green ocean of things. *IEEE Trans. Artif. Intell.* 4, 328–337.
- Magnan, A.K., Oppenheimer, M., Garschagen, M., Buchanan, M.K., Duvat, V.K., Forbes, D.L., Ford, J.D., Lambert, E., Petzold, J., Renaud, F.G., Sebesvari, Z., 2022. Sea level rise risks and societal adaptation benefits in low-lying coastal areas. *Sci. Rep.* 12 (1), 10677.
- Mardini, N., Suara, K., Fairweather, H., Brown, R., McCallum, A., Sidle, R.C., 2020. Improving the accuracy of hydrodynamic model predictions using Lagrangian calibration. *Water (Basel)* 12 (2), 575.
- Meng, L., Yan, C., Zhuang, W., Zhang, W., Yan, X.H., 2021. Reconstruction of three-dimensional temperature and salinity fields from satellite observations. *J. Geophys. Res. Oceans* 126 (11), e2021JC017605.
- Mostafavi, M., Delpeche-Ellmann, N., Ellmann, A., Jahanmard, V., 2023. Determination of accurate dynamic topography for the Baltic Sea using satellite altimetry and a marine geoid model. *Remote Sens. (Basel)* 15 (8), 2189.
- NEMO Consortium, 2023. *NEMO ocean engine: user guide*. Retrieved from NEMO website: <https://www.nemo-ocean.eu/doc/node82.html>.
- Oord, A.V.D., Dieleman, S., Zen, H., Simonyan, K., Vinyals, O., Graves, A., Kalchbrenner, N., Senior, A. and Kavukcuoglu, K., 2016. Wavenet: a generative model for raw audio. *arXiv preprint arXiv:1609.03499*.
- Orseau, S., Huybrechts, N., Tassi, P., Kaidi, S., Klein, F., 2021. NavTEL: open-source decision support tool for ship routing and underkeel clearance management in Estuarine channels. *J. Waterw. Port Coast. Ocean Eng.* 147 (2), 04020053.
- Otsmann, M., Suursaar, Ü., Kullas, T., 2001. The oscillatory nature of the flows in the system of straits and small semienclosed basins of the Baltic Sea. *Cont. Shelf Res.* 21 (15), 1577–1603.
- Parker, K., Erikson, L., Thomas, J., Nederhoff, K., Barnard, P., Muis, S., 2023. Relative contributions of water-level components to extreme water levels along the US Southeast Atlantic coast from a regional-scale water-level hindcast. *Nat. Hazards* 117, 2219–2248.
- Rajabi-Kiasari, S., Delpeche-Ellmann, N., Ellmann, A., 2023. Forecasting of absolute dynamic topography using deep learning algorithm with application to the Baltic Sea. *Comput. Geosci.* 178, 105406.
- Rathore, N., Rathore, P., Basak, A., Nistala, S.H., Runkana, V., 2021. Multi scale graph wavenet for wind speed forecasting. In: *Proceedings of the IEEE International Conference on Big Data (Big Data)*. IEEE, pp. 4047–4053.
- Reusch, T.B., Dierking, J., Andersson, H.C., Bonsdorff, E., Carstensen, J., Casini, M., Czajkowski, M., Hasler, B., Hinsby, K., Hyytiäinen, K., Johannesson, K., 2018. The Baltic Sea as a time machine for the future coastal ocean. *Sci. Adv.* 4 (5), eaar1195.
- Schwabe, J., Ågren, J., Liebsch, G., Westfeld, P., Hammarklint, T., Mononen, J., Andersen, O.B., 2020. The Baltic Sea Chart Datum 2000 (BSCD2000)—Implementation of a common reference level in the Baltic Sea. *Int. Hydrogr. Rev.* 23, 63–83.
- Siegmund, F., Johannessen, J., Drange, H., Mork, K.A., Korabel, A., 2007. Steric height variability in the Nordic Seas. *J. Geophys. Res. Oceans* 112, C12010.
- Slobbe, D.C., Verlaan, M., Klees, R., Gerritsen, H., 2013. Obtaining instantaneous water levels relative to a geoid with a 2D storm surge model. *Cont. Shelf Res.* 52, 172–189.
- Soomere, T., Quak, E., 2013. *Preventive Methods For Coastal Protection: Towards the Use of Ocean Dynamics For Pollution Control*. Springer Science & Business Media.
- Soomere, T., 2023. Numerical simulations of wave climate in the Baltic Sea: a review. *Oceanologia* 65 (1), 117–140.
- Staneva, J., Alari, V., Breivik, Ø., Bidlot, J.R., Mogensen, K., 2017. Effects of wave-induced forcing on a circulation model of the North Sea. *Ocean Dyn.* 67, 81–101.
- Staneva, J., Wahle, K., Günther, H., Stanev, E., 2016. Coupling of wave and circulation models in coastal-ocean predicting systems: a case study for the German Bight. *Ocean Sci.* 12 (3), 797–806.
- Sun, K., Wang, L., Xu, B., Zhao, W., Teng, S.W., Xia, F., 2020. Network representation learning: from traditional feature learning to deep learning. *IEEE Access* 8, 205600–205617.
- Suursaar, Ü., Kullas, T., Otsmann, M., 2002. A model study of the sea level variations in the Gulf of Riga and the Väinameri Sea. *Cont. Shelf Res.* 22 (14), 2001–2019.
- Tibaldi, C., Ranasinghe, R., Voudoukas, M., Rasmussen, D.J., Vega-Westhoff, B., Kirezci, E., Kopp, R.E., Srivier, R., Mentaschi, L., 2021. Extreme sea levels at different global warming levels. *Nat. Clim. Chang.* 11 (9), 746–751.
- Undén, P., Rontu, L., Jarvinen, H., Lynch, P., Calvo Sánchez, F.J., Cats, G., Cuxart, J., Eerola, K., Fortelius, C., García-Moya, J.A. and Jones, C., 2002. HIRLAM-5 scientific documentation.
- Varbla, S., Ellmann, A., 2023. Iterative data assimilation approach for the refinement of marine geoid models using sea surface height and dynamic topography datasets. *J. Geod.* 97 (3), 1–22.
- Varbla, S., Ågren, J., Ellmann, A., Poutanen, M., 2022. Treatment of tide gauge time series and marine GNSS measurements for vertical land motion with relevance to the implementation of the Baltic Sea Chart Datum 2000. *Remote Sens. (Basel)* 14 (4), 920.
- Vestøl, O., Ågren, J., Steffen, H., Kierulf, H., Tarasov, L., 2019. NKG2016LU: a new land uplift model for Fennoscandia and the Baltic Region. *J. Geod.* 93, 1759–1779.
- Wang, J., Qi, X., Luo, K., Li, Z., Zhou, R., Guo, J., 2023. Height connection across sea by using satellite altimetry data sets, ellipsoidal heights, astrogeodetic deflections of the vertical, and an Earth Gravity Model. *Geodesy* 14, 347–354.
- Weisse, R., Dailidiénė, I., Hünicke, B., Kahma, K., Madsen, K., Omstedt, A., Parnell, K., Schöne, R., Soomere, T., Zhang, W., Zorita, E., 2021. Sea level dynamics and coastal erosion in the Baltic Sea region. *Earth Syst. Dyn.* 12 (3), 871–898.
- Wöppelmann, G., Zerbini, S., Marcos, M., 2006. Tide gauges and Geodesy: a secular synergy illustrated by three present-day case studies. *C.R. Geosci.* 338 (14–15), 980–991.
- Yuan, W., Zhu, R., Xiang, T., Marchesiello, S., Anastasio, D., Fei, Q., 2023. Nonlinear system identification using audio-inspired WaveNet deep neural networks. *AIAA J.* 61, 1–9.
- Zhang, Z., Stanev, E.V., Grayek, S., 2020. Reconstruction of the basin-wide sea-level variability in the North Sea using coastal data and generative adversarial networks. *J. Geophys. Res. Oceans* 125 (12), e2020JC016402.

Curriculum vitae

Personal data

Name: Vahidreza Jahanmard
Date of birth: 31.01.1989
Place of birth: Kazerun, Iran
Citizenship: Iran

Contact data

E-mail: vahidreza.jahanmard@taltech.ee / jahanmard.vr@gmail.com

Education

2019–2023 Tallinn University of Technology, PhD
2012–2014 Sharif University of Technology, MSc

Language competence

Persian Native
English Fluent
Estonian Elementary

Professional employment

2023–... Tallinn University of Technology, Early-Stage Researcher
2019–2024 Tallinna Tehnikaülikool, PhD student
2014–2019 Sharif Marine Engineering Laboratory, Marine Engineer

Publications

Articles in peer-reviewed journals indexed in reputable databases (ETIS 1.1):

Jahanmard, V., Hordoir, R., Delpeche-Ellmann, N., Ellmann, A., 2023. Quantification of Hydrodynamic Model Sea Level Bias Utilizing Deep Learning and Synergistic Integration of Data Sources. *Ocean Modelling*. doi:10.1016/j.ocemod.2023.102286.

Afrasteh, Y., Slobbe, C., Sacher, M., Verlaan, M., **Jahanmard, V.**, Klees, R., Guarneri, H., Keyzer, L., Pietrzak, J., Snellen, M., Zijl, F., 2023. Realizing the European Vertical Reference System using model-based hydrodynamic leveling data. *Journal of Geodesy*, 97, 86. doi:10.1007/s00190-023-01778-2

Mostafavi, M., Delpeche-Ellmann, N., Ellmann, A., **Jahanmard, V.**, 2023. Determination of Accurate Dynamic Topography for the Baltic Sea Using Satellite Altimetry and a Marine Geoid Model. *Remote Sensing*, 15 (8), #2189. doi:10.3390/rs15082189

Jahanmard, V., Varbla, S., Delpeche-Ellmann, N., Ellmann, A., 2022. Retrieval of directional power spectral density and wave parameters from airborne LiDAR point cloud. *Ocean Engineering*, 266. doi:10.1016/j.oceaneng.2022.112694

Jahanmard, V., Delpeche-Ellmann, N., Ellmann, A., 2022. Towards Realistic Dynamic Topography from Coast to Offshore by Incorporating Hydrodynamic and Geoid Models. *Ocean Modelling*, 180. doi:10.1016/j.ocemod.2022.102124

Jahanmard, V., Delpeche-Ellmann, N., Ellmann, A., 2021. Realistic Dynamic Topography Through Coupling Geoid and Hydrodynamic Models of the Baltic Sea. *Continental Shelf Research*, 222. doi:10.1016/j.csr.2021.104421

Jahanmard, V., Diznab, M. A. D., Mehdigholi, H., Tabeshpour, M. R., Seif, M. S., 2017. Performance-based assessment of steel jacket platforms by wave endurance time method. *Ships and Offshore Structures*, 12 (1), 32–42. doi:10.1080/17445302.2015.1099245

Diznab, M. A. D., **Jahanmard, V.**, Tabeshpour, M. R., Seif, M. S., Mehdigholi, H., 2016. Wave endurance time: A new concept for structural assessment under extreme waves. *Proceedings of the Institution of Mechanical Engineers Part M Journal of Engineering for the Maritime Environment*, 230 (2), 364–377. doi:10.1177/1475090215579329

Conference abstracts (ETIS 5.2):

Jahanmard, V., Delpeche-Ellmann, N., Ellmann, A., 2023. Application of deep conditional generative adversarial networks to fill the gaps of satellite altimetry-based absolute dynamic topography. XXVIII General Assembly of the International Union of Geodesy and Geophysics (IUGG), 11-17 July, Berlin, Germany. doi:10.57757/IUGG23-1627.

Jahanmard, V., Delpeche-Ellmann, N., Ellmann, A., 2023. Absolute dynamic topography through synergizing sea level data sources utilizing a common and stable reference surface. XXVIII General Assembly of the International Union of Geodesy and Geophysics (IUGG), 11-17 July, Berlin, Germany. doi:10.57757/IUGG23-1756.

Jahanmard, V., Delpeche-Ellmann, N., Ellmann, A., 2023. Reanalysis of ocean model-based dynamic topography utilizing deep neural network and geoid-referenced observations. *Machine Learning and Data Analysis in Oceanography*, 8 to 12 May, Liège, Belgium.

Jahanmard, V., Delpeche-Ellmann, N., Ellmann, A., 2022. Assessment of hydrodynamic model sea level performance through geoid-referenced tide-gauge and satellite altimetry. The electronical abstract book, session A8.04 Ocean Health: Living Planet Symposium (LPS22), May 23-27, Bonn, Germany.

Jahanmard, V., Delpeche-Ellmann, N., Ellmann, A., 2022. Examining mean dynamic topography using geodetic and oceanographic approaches for the Baltic Sea. Session 1 – Planet Ocean and Geodesy: Nordic Geodetic Commission General Assembly: Planet Ocean and Geodesy, September 5-8, Copenhagen, Denmark.

Ellmann, A., **Jahanmard, V.**, Varbla, S., Mostafavi, M., Delpeche-Ellmann, N., 2022. Realistic coastal dynamic topography by a synergy of satellite altimetry data and marine geoid. The electronical abstract book, session A8.05 Coastal Altimetry Algorithms, Products and Applications: Living Planet Symposium (LPS22), May 23-27, Bonn, Germany.

Mostafavi, M., **Jahanmard, V.**, Rajabi-Kiasari, S., Delpeche-Ellmann, N., Ellmann, A., 2022. Absolute sea level trend forecasting using an ensemble empirical mode decomposition method for satellite altimetry data. The Nordic Geodetic Commission General Assembly 2022 in Copenhagen, poster session: Nordic Geodetic Commission

General Assembly: Planet Ocean and Geodesy, September 5-8, Copenhagen, Denmark.

Mostafavi, M., Rajabi-Kiasari, S., **Jahanmard, V.**, Delpeche-Ellmann, N., Ellmann, A., 2022. Reconstruction of dynamic topography using cyclostationary empirical orthogonal functions in the Baltic Sea. Session: Geodynamics and Earth Observation: Nordic Geodetic Commission General Assembly: Planet Ocean and Geodesy, September 5-8, Copenhagen, Denmark.

Jahanmard, V., Delpeche-Ellmann, N., Ellmann, A., 2021. Machine learning prediction for filling the interruptions of tide gauge data using a least square estimation method from nearest stations. Geodesy for a Sustainable Earth, Scientific Assembly of the International Association of Geodesy, June 28-July, Beijing, China.

Jahanmard, V., Delpeche-Ellmann, N., Ellmann, A., 2021. Development of synergized method to determine accurate sea level using satellite altimetry and high-resolution geoid model. Geodesy for a Sustainable Earth, Scientific Assembly of the International Association of Geodesy, June 28-July, Beijing, China.

Jahanmard, V., Delpeche-Ellmann, N., Ellmann, A., 2020. comparison of dynamic topography bias in HIROMB and NEMO-Nordic model by utilizing marine geoid. Geophysical Research Abstracts: EGU General Assembly, May, Vienna, Austria.

Delpeche-Ellmann, N.; Varbla, S.; **Jahanmard, V.**; Ellmann, A., 2019. Deeper insights into the validation of hydrodynamic models using a synergy of remote sensing data. Baltic Earth Workshop on Climate projections and uncertainties in the northern Baltic Sea region, November 19-20, Helsinki, Finland.

Elulookirjeldus

Isikuandmed

Nimi:	Vahidreza Jahanmard
Sünniaeg:	31.01.1989
Sünnikoht:	Kazerun, Iraan
Kodakondsus:	Iraan

Kontaktandmed

E-post:	vahidreza.jahanmard@taltech.ee / jahanmard.vr@gmail.com
---------	---

Hariduskäik

2019–2023	Tallinna Tehnikaülikool, PhD
2012–2014	Sharif University of Technology, MSc

Keelteoskus

Pärsia keel	emakeel
Inglise keel	kõrgtase
Eesti keel	algtase

Teenistuskäik

2023–...	Tallinna Tehnikaülikool, doktorant-nooremteadur
2019–2024	Tallinna Tehnikaülikool, doktorant
2014–2019	Sharif Marine Engineering Laboratory, insener

Teaduspublikatsioonide nimekiri on esitatud inglise keelse elulookirjelduse all.

ISSN 2585-6901 (PDF)
ISBN 978-9916-80-101-7 (PDF)